DEVELOPMENT, VERIFICATION, AND VALIDATION OF AN APPLIED ELEMENT METHOD SIMULATION FRAMEWORK FOR GLASS LITE FRACTURE, FRAGMENTATION, AND DEBRIS FIELD PREDICTION

by

Jonathan Michael Moss

A dissertation submitted to the faculty of
The University of North Carolina at Charlotte
in partial fulfillment of the requirements
for the degree of Doctor of Philosophy in
Civil Engineering

Charlotte

2020

Approved by:

Dr. Matthew J. Whelan

Dr. David C. Weggel

Dr. Howie Fang

Dr. Nicole L. Braxtan

Dr. Tara L. Cavalline

ABSTRACT

JONATHAN MICHAEL MOSS. Development, Verification, and Validation of an Applied Element Method Simulation Framework for Glass Lite Fracture, Fragmentation, and Debris Field Prediction. (Under the direction of DR. MATTHEW J. WHELAN)

In the aftermath of an explosive event, forensic investigators are presented the challenge of characterizing the properties of the explosive device, including the charge size and epicenter of the detonation. Although surrounding infrastructure damaged during the explosion serves as witness to the event, evidence in the form of structural damage is conventionally relegated to a qualitative analysis in favor of nonstructural evidence, such as blast residue, primarily because of the difficulty associated with accurately predicting nonlinear structural behavior under blast loading. Further, simulation of debris field formation potentially resulting from fragmentation of windows, which are commonly observed to fail during blast events, is beyond the conventional capabilities of most numerical methods for structural dynamics simulation. The primary objective of this research effort is to develop a physics-based simulation tool that is specifically capable of predicting the distribution of glass debris fields generated during blast events. Toward achieving this stated objective, a simulation framework for predicting glass lite failure probabilities and debris fields under blast loading is developed through implementation and extension of the relatively new Applied Element Method of structural analysis. Although similar to the Finite Element Method, the Applied Element Method has been demonstrated in existing literature as advantageous for simulation of complex, nonlinear structural behavior, including progressive collapse, fracture, fragmentation, and formation of debris fields, because of its unique approach to element connectivity. Development of the simulation framework is accom-

plished in four distinct phases involving verification and validation of software routines developed for simulating linear elastic static and dynamic behavior, nonlinear geometric behavior, nonlinear material constitutive behavior, and particle dynamics with element contact behavior. The predictive fidelity of the developed simulation framework for problems involving linear elastic behavior and nonlinear geometric effects is successfully verified through comparison to analytical and Finite Element models. Validation of the predictive fidelity of the simulator for problems involving complex nonlinear behavior, including fracture, fragmentation, and debris field formation, is accomplished through comparison with experimental results compiled specifically for this research effort. The experimental test program includes six open-arena blast tests performed with a small enclosure featuring a conventional fenestration system outfitted with six conventional tempered glass lite specimens. Experimental characterization of the glass lite behavior was also performed through extensive experimental modal analysis and through uniform static loading to failure of a glass lite specimen mounted in the fenestration system. In order to accurately predict the failure behavior of the glass lite specimens, the Applied Element Method is extended for the first time to simulate fracture and fragmentation of tempered glass, and, as a further component of this dissertation, is implemented with the well established Glass Failure Prediction Model to predict the failure probabilities of the glass lite specimens under static loading and open-arena blast loading. Finally, implementation of the developed simulation framework to model the experimental scenarios of open-arena blast testing indicates that the Applied Element Method is capable of predicting debris field distributions that exhibit strong qualitative agreement with the observed experimental results.

ACKNOWLEDGMENTS

I am profoundly grateful for the support I have received throughout this research effort, and I would like to thank my advisor, Dr. Matthew Whelan, for the guidance, support, and patience he has shown over the years encompassed by this project. I am appreciative of the opportunities he has provided me, and I am further grateful to Dr. David Weggel, with whom I have had the opportunity to work with extensively throughout this research effort. I would like to thank the rest of my dissertation committee members, Dr. Fang, Dr. Braxtan, and Dr. Cavalline for their insights and recommendations that have strengthened this research.

This research effort would not have been possible without funding from the National Institute of Justice through the Graduate Research Fellowship in STEM program (Grant No. 2017-R2-CX-0009). In addition, the National Institute of Justice supported the field experimentation and early development of the simulation framework through a Research and Development in Forensic Science for Criminal Justice Purposes grant (Grant No. 2014-DN-BX-K004). Experimental testing for this research effort was conducted at the University of North Carolina at Charlotte Infrastructure Security and Emergency Responder Research and Training facility in partnership with the City of Gastonia Police Department Bomb Squad, who provided for the safe purchase, handling, transportation, and detonation of the explosive components required for this research. Structural specimens for experimental testing were provided through in-kind support from local industry partners, and I would like to thank Greg Walden of GRATEC and Andy Lytle of Union Glass and Metal.

I am further grateful to my family and friends for their support and patience while I

have devoted my time to completion of this dissertation, and above all I thank God for orchestrating everything that made this research effort possible and for providing whatever was needed to overcome any obstacles along the way.

TABLE OF CONTENTS

LIST OF FIGURES

LIST OF TABLES

CHAPTER 1: INTRODUCTION

1.1 Introduction

Numerous events involving detonation of an explosive device are reported by the Bureau of Alcohol, Tobacco, Firearms, and Explosives to occur across the United States of America every year (USBDC, 2017). Due to the significant impulsive energy release associated with an explosive detonation, explosions can potentially result in a wide range of damage to both structural and non-structural infrastructure, depending primarily on the characteristics of the explosive device and the resilience of the infrastructure. The effects of an explosion can range from minor damage, such as cracking of nonstructural components due to vibrations, to complete collapse resulting from catastrophic failure of a critical structural component (National Research Council, 1995). The potentially devastating effects of a maliciously detonated explosive device are specifically evidenced in recent years by intentional bombings, with a notable example being the Alfred P. Murrah federal building, which suffered catastrophic failure of critical structural components and subsequent partial collapse during a terrorist bombing (Sozen et al., 1998). High velocity glass debris generated during the bombing was a significant source of casualties, with 40% of survivors reporting injuries caused by projected glass fragments. Notably, laceration injuries were even reported by occupants of neighboring buildings (FEMA, 2003), which underscores the hazardous nature of projected glass fragments. The explosive event further exemplifies

the vulnerability of glass windows, due to their prevalence and the brittle failure behavior of glass. It has been observed that explosions occurring in or near structures will almost certainly result in window failure (Pritchard, 1981), and the risk of injury caused by glass debris is often increased with modern infrastructure design, which frequently incorporates significant surface areas of glass windows (US Army Corps of Engineers, 2008).

In the aftermath of an explosive event, forensics investigators are often tasked with the critical challenge of reconstructing the scene of the explosion, with a key focus being determination of the strength of the explosive device and the epicenter of the detonation (Ambrosini et al., 2002, 2005; Sorensen and McGill, 2011b). Although the surrounding area and damaged structural components serve as witness to the event, structural damage is oftentimes not considered beyond a qualitative examination (Van der Voort et al., 2015). It has been noted that quantitative analysis of blast-induced structural damage using physics based simulations is typically not practical for post-blast investigations, and the impracticality of such simulations in the post-blast investigative environment stems from the complex nature of blast simulations, which conventionally necessitate high order numerical models that require advanced user knowledge (Sorensen and McGill, 2012). This is specifically true for cases of specialized behavior, such as fragmentation and debris field formation. Such cases are exceedingly difficult to model using methods such as the Finite Element Method (FEM), which is commonly employed for numerical prediction of structural response to blast loading. Although advantageous for simulating numerous scenarios of structural response to many types of loading, including blast, prediction of fracture in the FEM requires adaptation of specialized models, such as the Extended Finite Element Method (Moës et al., 1999). Further, although combined methods such as the Finite Ele-

ment Method/Discrete Element Method have been implemented to simulate fragmentation (Morris et al., 2006), the Finite Element Method alone is inhibited in its ability to predict debris field formation. It is therefore speculated that evidence in the form of structural damage, especially glass failure, is often omitted from post-blast scene reconstruction not from a lack thereof, but from the lack of a fast-running and easily implemented numerical model capable of predicting specialized cases of structural behavior, specifically fracture, fragmentation, and debris field formation under blast loading.

The overarching objective of this research is therefore development of a physics-based structural dynamics code for the simulation of glass lite failure capable of serving as a tool for post-blast forensics investigations by accurately predicting fragmentation and debris field formation during blast events. Toward achieving this objective, this research effort leverages a relatively new method of structural analysis, known as the Applied Element Method (AEM) (Tagel-Din, 1998), that has been demonstrated as potentially advantageous for problems involving fragmentation under blast loading (Tagel-Din and Rahman, 2006; Tagel-Din, 2009; Keys and Clubley, 2013; Kernicky et al., 2014; Keys and Clubley, 2017). While similar to the prevalent FEM, the AEM features a different formulation for element connectivity that more naturally accommodates prediction of nonlinear response to blast loading including fracture, fragmentation, subsequent particle dynamics, and debris field formation all within one consistent and intuitive framework.

1.2 Overview of Research Effort

Toward achieving the stated objective, this research effort seeks to develop a structural dynamics code implementing, and extending, the AEM to accommodate the prediction of

glass lite failure probabilities and debris fields formed under blast loading. The AEM was selected for this research primarily because of its demonstrated ability to model not only linear elastic static and dynamic structural response, but also highly nonlinear behavior, such as fragmentation and collision, with relative ease. The AEM is similar to the FEM in that both methods numerically represent a structure as a discretized continua of elements. However, the ability of the AEM to simulate such a wide range of structural phenomena is attributable to its unique method of connectivity between elements. Whereas the FEM implements nodal connectivity between elements, the AEM features interface springs between elements. The stiffness representation of the system is formulated by the stiffness of the individual springs, which facilitates simulation of element separation or collision by removal or introduction, respectively, of interface springs.

The prediction of the structural response of glass lites under blast loading using the AEM required the implementation of relatively advanced nonlinear capabilities in a library of software routines developed specifically for this research, as well as the introduction of new extensions of the AEM to address challenges specific to modeling tempered glass. Consequently, the AEM-based structural dynamics code was developed in four unique, increasingly advanced developmental phases. Each phase was accompanied by corresponding verification and/or experimental validation of the results generated using the developed software routines. Confirming the predictive fidelity of the simulator for each developmental phase ensured that subsequent developments would not be hindered by the possibility of prior mistakes. Each developmental phase, accompanied by its respective verification or validation, is summarized in the flowchart presented in Figure 1.1. As indicated in Figure 1.1, the structural dynamics code has been developed in the MATLAB computing

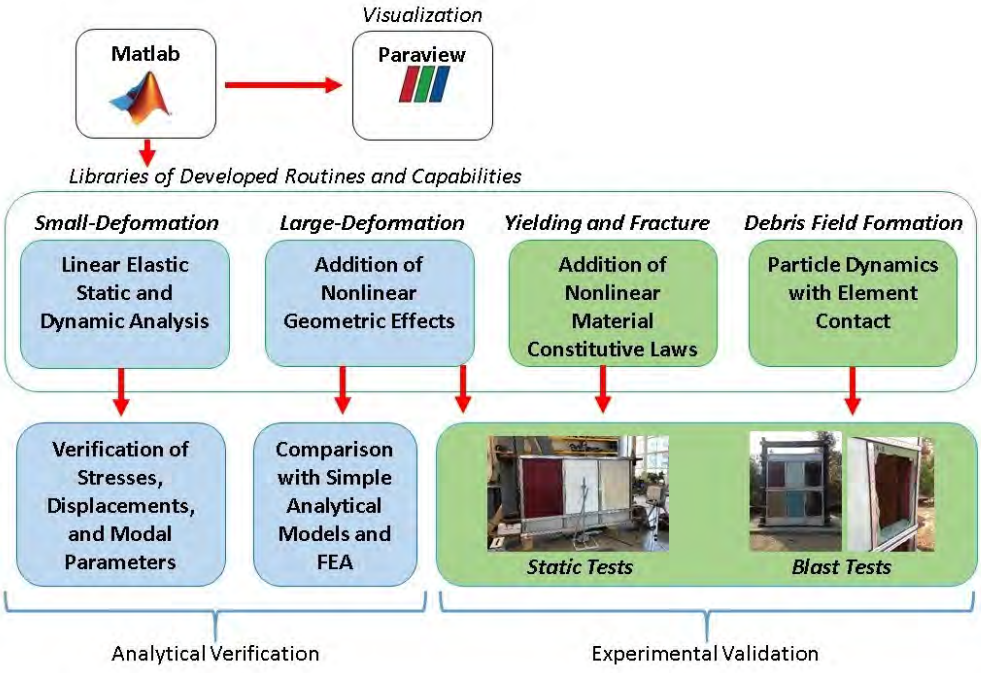

FIGURE 1.1: Phases of blast simulator development and the accompanying methods of verification and validation

environment, and post-processing and visualization of the results is accomplished in the open-source Paraview software package. Validation of the developmental phases required extensive experimentation to compile a database of results. Most notably, six open-arena blast tests on a small enclosure with a facade consisting of an array of conventional glass lite specimens were conducted for this research effort. The open-arena blast tests were designed and conducted specifically for this research, and were designed to represent a conventional facade structure, such as is often employed in commercial storefront applications, subjected to a bombing event. In order to conform with conventional construction practices, the glass lite specimens featured typical tempered glass and were mounted in the facade using conventional practices. Similarly, the explosive charges were composed of either PETN or ANFO, which are relatively common charge compositions used for military

and commercial applications, respectively (Beveridge, 2011). Each open-arena blast test varied in charge size, location, and composition in order to provide unique scenarios of debris field formation for validation of the developed simulations. An experimental static load test was further conducted to characterize the static load-deflection response and failure behavior of a glass lite specimen nominally identical to the glass lite specimens subjected to open-arena blast testing.

The first developmental phase was focused on implementation of linear elastic static and dynamic analysis capabilities into AEM software routines. Since linear elastic structural response to dynamic and static loading is predictable using established analytical models, the predictive fidelity of the first developmental phase was successfully verified through comparison to analytical models. The second developmental phase was characterized by introduction of nonlinear geometric effects, such as large displacement behavior. This developmental phase featured verification against similar FEM models and experimental validation using the results of the experimental static loading test, which exhibited geometric nonlinear behavior.

Phase three of the simulator development focused on the addition of material constitutive models into the simulation. Specifically, a fracture and fragmentation model for tempered glass was developed and implemented in the simulation. This developmental phase presented the challenge of modeling the extensive fragmentation behavior of tempered glass and is the first time a fracture model specific to tempered glass and inclusive of residual stresses from the glass tempering process has been implemented with the AEM. The AEM software routines developed in this phase were compared to experimental observations obtained during uniform static loading of a glass lite specimen in the laboratory to failure.

Furthermore, the Glass Failure Prediction Model, a probabilistic approach for predicting the likelihood of glass failure due to surface flaw distribution, was implemented for the first time using the AEM. A technique for employing the Glass Failure Prediction Model on blast loaded tempered glass using the AEM was formulated. Plausible surface flaw parameters were selected by applying this formulation to an AEM simulation of the static load test and then the individual and joint probabilities of lite failure across the six open-arena blast tests were calculated to demonstrate the approach.

The final phase of the software development was the culmination of the first three developmental phases coupled with introduction of contact modeling into the AEM simulation. The combined progress of all phases and the contact model provided the necessary components to simulate structural response to blast loading, followed by fracture, fragmentation, and debris field formation. The predictive fidelity of the AEM structural dynamics code was evaluated by comparing the simulation results to the experimentally observed debris fields generated for the different scenarios of open-arena blast testing.

1.3 Expected Contribution

Since the AEM is a relatively new method of structural analysis, research studies implementing the AEM are relatively limited. Further, there is currently only one commercially available AEM based software package. It is expected that this research effort will significantly contribute to the current knowledge base of AEM modeling by implementing the methodologies described Tagel-Din (1998) to simulate debris field formation of tempered glass lites under blast loading. Similar research efforts to model the fracture, fragmentation, and debris field formation of tempered glass lites have not been observed in the literature.

This will further serve to build the post-blast structural forensics knowledge base by evaluating the suitability of the Applied Element Method as a tool for hypothesis testing in the post-blast environment, specifically in cases involving debris field formation. As a component of this dissertation, this research effort will contribute to the current knowledge base of tempered glass failure modeling through developing and implementing a tempered glass failure model for the first time in the AEM. Further, the suitability of the AEM for probabilistic prediction of glass failure is evaluated for the first time through implementation of the well established Glass Failure Prediction Model in conjunction with the Applied Element simulations.

1.4 Dissertation Outline

The outline of this dissertation is as follows:

- Chapter 2 provides a brief overview of blast loading of structures and the current state of practice for consideration of blast induced structural damage in post-blast forensics investigations. Numerical modeling of structural response to blast loading is discussed with specific focus on simulating fracture. Challenges specific to predicting failure in glass specimens, specifically the effects of tempering, the probabilistic nature of glass failure, and the load-deflection behavior of glass lites are discussed. Lastly, case studies pertaining to the simulation of glass failure under blast loading are presented.

- Chapter 3 provides a detailed explanation of the formulation of the AEM. The methodologies employed for prediction of deformations and stress distribution during static and dynamic linear elastic behavior, nonlinear constitutive behavior, and collision

are discussed. Implementation of the described methodologies to develop an AEM based simulation framework for this research effort is described. Lastly, the predictive fidelity of the AEM based simulation framework is verified against a suite of example problems with comparison to analytical and numerical solutions.

- Chapter 4 provides a detailed description of all experimental tests performed for this research effort. Details of the experimental setups, instrumentation, and test specimens are provided, and the results of all tests are presented. Both the open-arena blast tests and laboratory uniform static load test are presented in this chapter. Furthermore, experimental modal analysis of all lites used in the research is presented to document the dynamic properties of the specimens.

- Chapter 5 provides detailed descriptions of the AEM models developed for the tempered glass lite specimens subjected to experimental testing. The chapter emphasizes the development, tuning, and validation of the boundary conditions of the model, the introduction of residual stresses from tempering into the AEM formulation, and development and implementation of a macro-scale fracture model for approximating the fragmentation of tempered glass. Further, the developed AEM models for predicting the response to static and dynamic blast loading are discussed.

- Chapter 6 describes adaptation and implementation of the Glass Failure Prediction Model, a well established probabilistic model for glass failure analysis that accounts for surface flaw distributions, in the AEM framework. Application of the probabilistic model to static simulations and simulations of open-arena blast testing are described. Lastly, the model is implemented in conjunction with the AEM simulations

described in Chapter 5 to predict the failure probability of the glass lite specimens subjected to static loading and open-arena blast testing.

- Chapter 7 presents application of the AEM structural dynamics code for the prediction of the glass debris fields formed during the open arena blast tests. Specific focus is given toward implementing a contact model and incorporating aerodynamic drag forces in the AEM simulations. Comparisons between the predicted and experimentally observed debris fields are presented both qualitatively and quantitatively.

- Chapter 8 provides a summary of key contributions and conclusions developed from this effort. Recommendations for future research are formulated.

CHAPTER 2: LITERATURE REVIEW

2.1 Blast Analysis

Explosions occurring near or within structures have been noted to cause catastrophic structural damage to both exterior and interior components, with severe cases resulting in failure and collapse (National Research Council, 1995). The risk of explosive threats has risen in recent years, and it has been reported through the Bomb Arson Tracking System developed by the Bureau of Alcohol, Tobacco, Firearms, and Explosives that the occurrence of explosions per year in the United States 2010 peaked at 1,242 in 2012 (USBDC, 2015, 2017). With the rise in explosive threats, a corresponding increase in attention has been given to the analysis and prediction of the behavior of structural components subjected to blast loading. Analysis of structural response and the level of damage incurred under blast loading requires consideration of the development of overpressures in the blast front, the dynamics of the structural system subject to the loading, and the interaction that takes place between the shock front and the response of the structure. Since the characteristics of the pressure waves generated by the explosion and their interaction with structures are critical components of such an analysis, introductions to these aspects are presented in the following sections.

2.1.1 Blast Wave Loading

Detonation of an explosive device results in the generation and subsequent propagation of a blast pressure wave away from the detonation location, or epicenter, of the explosion (Hetherington and Smith, 1994). The blast wave is the product of the detonation process of an explosive material, wherein a shock front originates and then travels through the unreacted explosive components. As the shock front moves through the unreacted explosive components, it is followed by a subsequent chemical reaction, which in turn gives way to the products of the detonation process. The blast pressure wave is a product of the detonation process, and a relationship exists between the rate of reaction of the explosive material during the detonation process and the detonation pressure (Beveridge, 2011). Notably, the rate of reaction during detonation varies across different explosive materials and therefore serves as a key descriptor of explosive types. If the rate of the reaction through the material is less than the speed of sound through the material, the explosive material is classified as a low explosive (LE). Conversely, a high explosive (HE) is characterized by a rate of reaction exceeding the speed of sound though the material (National Research Council, 1995). Examples of common low explosives include black powder and smokeless powder and notably require containment to generate explosive pressures. In contrast, high explosives, which are of greater relevance to this dissertation, do not require containment to generate a blast pressure wave (Beveridge, 2011). As the shock front moves through the unreacted material and is followed by the subsequent chemical reaction with its associated detonation products, formation and propagation of the blast wave through the surrounding environment occurs. A simplified illustration of the blast wave propagating away from the

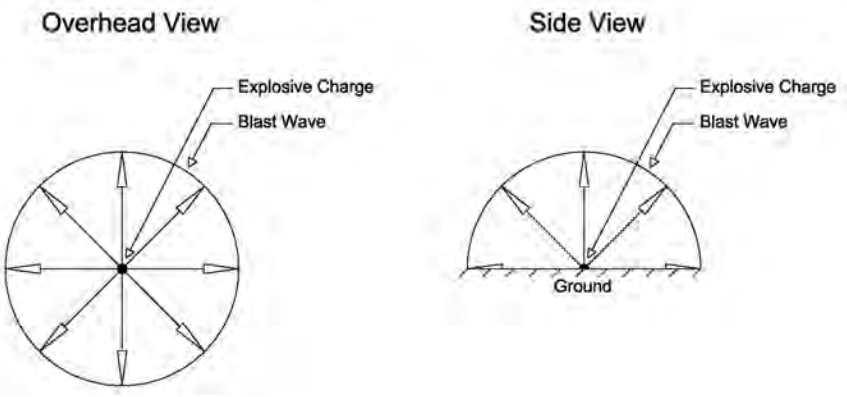

FIGURE 2.1: Simple illustration of a blast pressure wave propagating away from the location of detonation

epicenter is presented in Figure 2.1. As the pressure wave propagates radially outward from the epicenter, the blast pressure as a function of time typically exhibits a profile similar to the idealized form illustrated in Figure 2.2. As depicted, an immediate and significant increase in pressure is experienced upon arrival of the pressure wave, which is referred to as the peak overpressure. The overpressure exhibits an exponential decay that, in many cases, descends below ambient pressure as the blast wave transitions from the positive phase to the negative phase (Shukla et al., 2013). During the negative phase, a reverse in loading occurs due to the suction generated.

The peak overpressure created by the explosive device can be estimated using the trinitrotoluene (TNT) equivalence of the explosive charge, which is often used to characterize an explosive charge as its equivalent weight in TNT. The blast overpressure resulting from detonation of various quantities and types of explosive materials is often related to TNT equivalence, since extensive experimental databases have been compiled for TNT (Beveridge, 2011). The TNT equivalence, N, of an explosion can be determined by:

$$N = \left(\frac{Z_{charge}}{Z_{TNT}} \right)^3 P \tag{2.1}$$

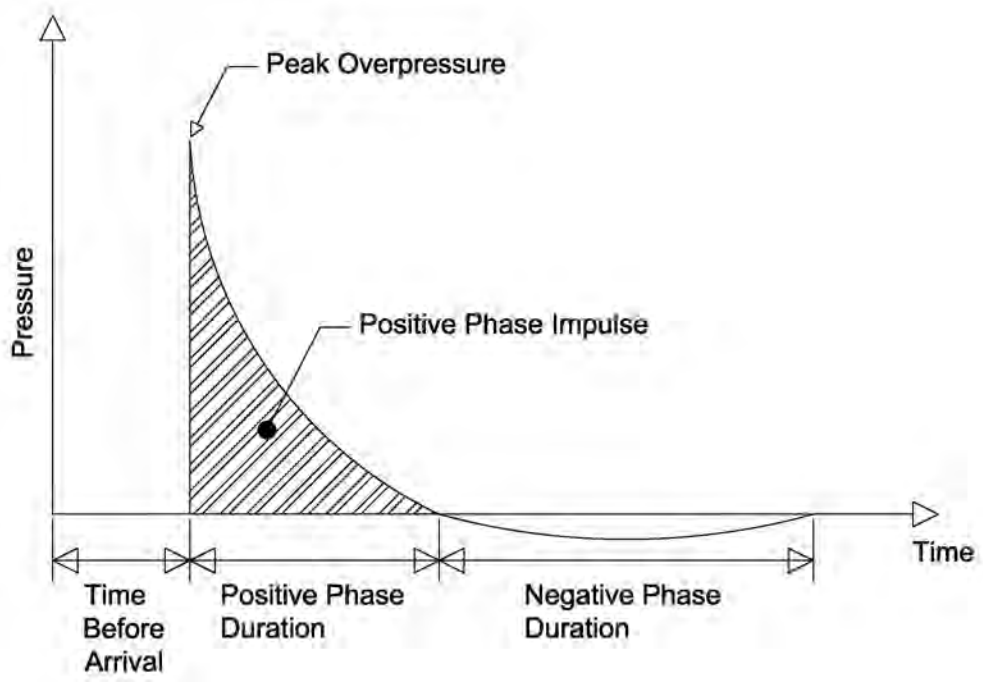

FIGURE 2.2: Typical pressure wave experienced at a fixed distance from an explosive detonation

where Z_{charge} is the scaled distance of the charge, defined as the distance to the charge divided by the cubed root of the weight of the charge, Z_{TNT} is the equivalent weight of TNT, and P is the blast overpressure.

The decay of the blast overpressure as a function of time is commonly represented numerically through modification of the Friedlander equation developed in Friedlander (1946). The modified Friedlander equation can be determined as

$$p(t) = P\left(1 - \frac{t}{T}\right)e^{\frac{-bt}{T}} \tag{2.2}$$

where $p(t)$ denotes the pressure as a function of time, P indicates the blast overpressure corresponding to the TNT equivalence, t represents the variable time, T represents the duration of the positive phase, and b is a dimensionless constant dependent on the shock strength of the blast, which is defined as the peak overpressure divided by the ambient

pressure (Baker, 1973). The blast impulse corresponding to the blast overpressure is a further characteristic of the explosive event, and the positive impulse can be calculated as the area under the pressure curve during the positive pressure phase (Beveridge, 2011). Since impulse is calculated as the integral of the overpressure, it can be seen that a high initial overpressure corresponds to a higher level of impulse. Therefore, the effects of short-duration blast events are typically more dependent on the positive phase impulse, while the overpressure plays a more significant role in long-duration blast loading (US Army Corps of Engineers, 2008). It has been noted that the effects of a blast event on the surrounding area are related to both the pressure and the impulse (Beveridge, 2011)

2.1.2 Structures under Blast

The properties of a blast wave, specifically the magnitude of the peak overpressure and the positive phase impulse, resulting from an explosive event significantly affect the response of a structure subjected to the blast wave (National Research Council, 1995). Dependent upon the size of the explosion and the location of its epicenter in relation to the various components of the structure, any combination of global deformations, local failure and fragmentation of walls or floors, or transmittance of the shock wave through structural members could potentially be experienced. Many factors, both from the perspective of dynamic structural behavior and from that of explosive characterization, are involved in the analysis of structural behavior under blast wave loading, thereby introducing a level of difficulty in modeling a blast event affecting a structure.

A critical aspect in modeling blast wave loads acting upon a structure is accurate estimation of the reflected pressures that develop as the blast pressure wave loads a structure. A

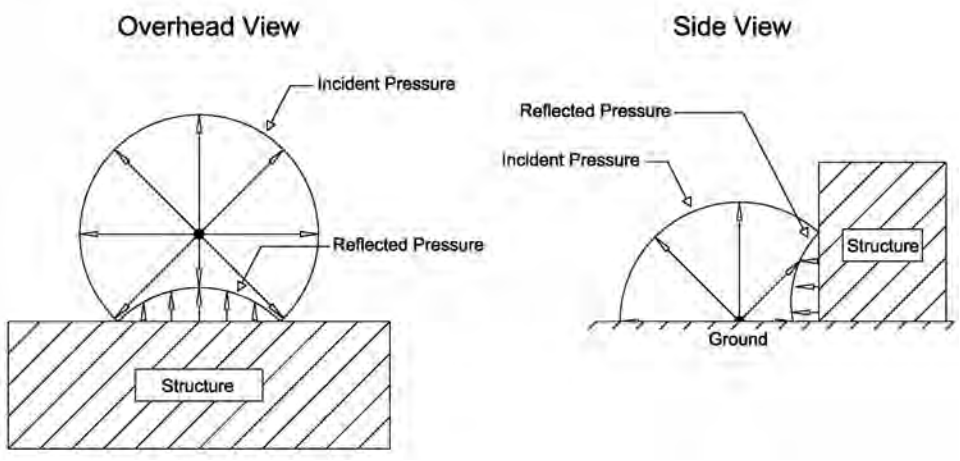

FIGURE 2.3: Simplified illustration of a blast pressure wave reflecting off of a structure

significant distinction exists between the incident pressure, which corresponds to the free-air overpressure of the blast wave, and the reflected pressure, which occurs as the blast wave is forced to reflect off of a fixed surface, such as a structure (Beveridge, 2011). The reflective interaction with the fixed surface typically results in a significant increase in amplitude compared to the initial incident pressure as the blast wave pressures amplify as they interact while reversing direction. This is exemplified through the simplified illustration presented in Figure 2.3 of a blast pressure wave impacting a structure and subsequently reflecting. The magnitude of the reflected pressure is dependent upon several factors, including the magnitude of the peak incident pressure, the angle of reflection, and the compliance of the structural surface.

An effort to characterize the reflected pressure acting on a fixed point was introduced in Kingery and Pannill (1964) and continued in Kingery et al. (1984). Through regression on a compilation of air blast parameters obtained from experimental tests with TNT, the authors empirically formulated high-order polynomial models for estimating the peak reflected overpressure, positive phase impulse, time of arrival, and duration for both incident

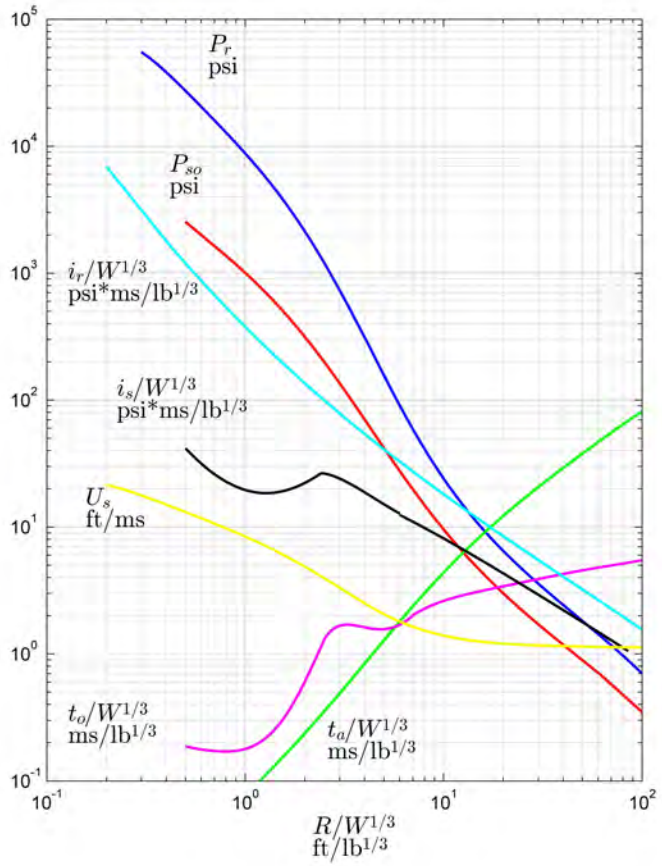

FIGURE 2.4: Polynomials for estimation of blast wave characteristics by Kingery et al. (1984)

and reflected pressures. The polynomials use the scaled distance and are presented graphically in Figure 2.4. The air blast parameters developed in Kingery et al. (1984) have been coupled with technical documents, such as the Unified Facilities Criteria (US Army Corps of Engineers, 2008), to develop pressure curves for estimation of the reflected pressure experienced under varying circumstances. Estimation of the reflected pressure in turn facilitates calculation of the loads needed to predict the structural response. It should be noted that the air blast parameters prescribed in Kingery et al. (1984) do have limitations, such as the absence of parameters describing the negative phase (Swisdak, 1994), and these limi-

tations have been attributed to the empirical nature by which the reflected pressure curves were developed.

2.2 Structural Forensics for Post-Blast Investigations

In the aftermath of a blast event and during the ensuing post-blast investigation, the surrounding area and structural components affected by the explosion serve as witness to the event and can indicate the characteristics of the explosive device. Whether the explosive event has occurred maliciously, as in the case of terrorism (National Research Council, 1995), or accidentally, as has been notably seen in the case of agricultural, specifically fertilizer, facilities (Wesevich and Olson, 2005), a post-blast forensic investigation is often carried out in the aftermath of the event. In the case of intentional or terror-related explosive events, the ultimate objective of the investigation is identification of the perpetrator of the event, with a key component of the post-blast investigative process being determination of the design of the explosive device (Beveridge, 2011). Characterization of the explosive device can provide valuable insight to forensic investigators, and a noteworthy example of this can be seen in the determination of the explosive component used in the manufacture of the device. Since many explosive components are only available through highly regulated procurement processes, determination of the utilized explosive component can narrow the field of potential origins of the device, which in turn can guide investigators toward the correct source (Beveridge, 2011). Similarly, because the blast overpressure and the corresponding structural damage are related to the size and location of the explosive device, determination of the charge size and epicenter becomes a further area of importance to the investigation. Therefore, characterization of the explosive device is a crucial step in

the post-blast forensics investigation (Ambrosini et al., 2002, 2005; Sorensen and McGill, 2011b), and, as will be seen in the literature, determination of the size and epicenter of the explosive charge is often considered a critical aspect of this step.

These key descriptors regarding the explosive charge are often determined using empirical methods and qualitative judgment based on evidence, such as blast residue, crater formation, and other observables (Sorensen and McGill, 2011b; Van der Voort et al., 2015). The prioritization of other forms of evidence over observed damage to structural components in a post-blast forensics investigation is underscored through examination of the approach to post-blast explosives identification followed by the Bureau of Alcohol, Tobacco, and Firearms (Garner et al., 1986). The importance of collection of chemical evidence for subsequent chemical analysis is emphasized, while investigative use of structural components is not mentioned.

In contrast, collection of evidence in the form of structural damage is recommended in a guide for post-blast scene investigation prepared by the National Institute for Justice (NIJ) (NIJ, 2000). Since it is a relatively brief technical guide serving essentially as a checklist for post-blast investigations, the document goes no further than to list structural damage as evidence to be collected and does not contain specific information regarding the use of the data after collection. Nonetheless, it is notable that observation and collection of structural damage data during the early stages of the investigation is recommended.

While not exclusively the case in post-blast forensic investigation, damage to surrounding structural and nonstructural building components is often not included in the forensic analysis, although it has been suggested by several authors that inclusion of structural damage could render information of significant usefulness to the investigation (Sorensen and

McGill, 2011b; Ambrosini et al., 2005). Likewise, while structural damage is conventionally not prioritized in a post-blast forensic investigation, several cases in which structural forensics have been implemented to gain insight into the explosive event have been identified. Case studies on both the use of structural analysis for post-blast investigations and on proposed methods for further integrating structural damage measurements into post-blast investigative practice are detailed in the following sections.

2.2.1 Examples of Structural Forensics in Post-Blast Investigations

A relatively early attempt at characterization of relationships between peak incident pressure and observed damage to various structural items was presented in Brasie and Simpson (1968) and adapted in Beveridge (2011). The authors detailed a number of commonly-observed damages with the corresponding range of peak overpressure that is typically required to cause the observed levels of damage. For example, it was found that glass windows typically shattered when exposed to an overpressure between 3.5 kPa (0.5 psi) and 6.9 kPa (1.0 psi), while unreinforced brick walls failed under pressure ranging from 48.3 kPa (7.0 psi) to 55.2 kPa (8.0 psi). It was further explained in Beveridge (2011) that the use of structural damage as a means of estimating the TNT equivalence of an explosive charge is facilitated through determination of the TNT equivalence corresponding to the estimated pressure required to cause the observed structural damage. However, it should be noted that the authors state that this method can often result in a significant error between the estimated and actual charge sizes, particularly with certain levels of damage, such as collapse, that are not readily correlated to a specific overpressure. This is notable, as it will be demonstrated in the following section that several authors have implemented approaches

for charge size and location estimation based on the principles incorporated in this method.

In contrast to the method of qualitative analysis explained above, a specific example of the application of structural analysis to a post-blast investigation is presented in Wesevich and Olson (2005). Although the case study was limited in detail regarding aspects of the data acquisition and analysis, the authors summarized the investigation of a fertilizer plant that experienced an accidental explosive event. The investigators utilized plastically deformed structural members as damage indicators by acquiring simple deflection measurements of the members. Nonlinear, single-degree-of-freedom models were employed to simulate the plastic deformation in each member resulting from prescribed blast loads. This methodology allowed for estimation of the actual charge properties through iterative adjustment of the charge properties in the numerical simulation until the structural results optimally correlated with the damage measurements. The authors stated that this methodology led to determination of a probable solution for the yield of the explosion.

An overview of techniques for predicting structural damage under blast loading was presented in Pape et al. (2010) as the third installment in a three part series on the effects of blast loading on structures. Through the presentation of a relatively simple case study, the authors demonstrated the application of structural analysis to a post-blast investigation. The presented case study described an explosive event in which a masonry structure was damaged by an internal explosion that destroyed two walls and damaged others. Observation of the damage led to a hypothesis that the explosion was caused by a vapor cloud formed by the accidental release of aerosol cooking oil when several cans of the substance overheated. Structural analysis was used to estimate the peak overpressure required to cause the observed structural damage. The corresponding quantity of aerosol cans required to create

the estimated overpressure was then calculated. This form of hypothesis testing confirmed that there were more than enough ruptured aerosol cans present at the blast scene to have released a vapor cloud capable of creating a peak overpressure resulting in the observed structural damage. Although the case study proved to be a relatively simple example that did not involve highly complex numerical models and is not directly comparable to the methods explored in this dissertation, it did demonstrate the use of structural analysis for post-blast hypotheses testing. However, it should be noted that the authors emphasized the importance of caution when using simple overpressure damage criteria, such as those employed in this example and those documented in Beveridge (2011). This corresponds to the similar warning regarding damage observables found in Beveridge (2011). A second case study detailed in the same research effort examined the use of Finite Element Analysis (FEA) to determine through hypothesis testing which of two possible explosive scenarios was more likely to have caused damage to a feed mill table. Although the example is of limited scope and scale, the authors explained how the results of the structural FEA simulations, one of which modeled a deflagration explosion while the other modeled the explosion of a condensed material, were compared to the deformed shape of the table following the blast event. By comparison of the deformations predicted by each model, it was concluded that the damage was most likely the result of the explosion of a condensed explosive material present on the table.

These examples document both qualitative and quantitative methods of structural damage characterization that have been applied to post-blast forensic investigations. However, the limited use of structural methods and lack of formal protocols for data collection and analysis are notable. Furthermore, while examples do exist of terror-related structural dam-

age being simulated at a point in time following the event (Tagel-Din and Rahman, 2006; Isobe, 2017), no prior instances demonstrating the use of structural analysis techniques for expedient characterization of the explosive device in a post-blast forensic investigation environment are present in the literature.

2.2.2 Proposed Techniques for Post-Blast Forensic Investigative Methods Incorporating Structural Damage

Several research efforts have identified the oversight of structural damage in formal methods for post-blast forensic investigation as an opportunity for the development of novel techniques based on the collection and analysis of data related to structural damage. The concept of using post-blast structural analysis for reconstruction of a blast event was explored in Ambrosini et al. (2005) through the combined use of a computational fluid dynamics (CFD) hydrocode to simulate pressure and impulse, isodamage curves from experimental literature, and documentation of visual observations of structural damage. The authors proposed that, in the absence of crater data that could identify the properties of the explosive device, the blast pressures across the undamaged face of a structure affected by a blast event could be modeled using a CFD software package, and then structural damage can be predicted in qualitative terms using empirically generated isodamage curves. Such curves provide a relationship between the peak reflected pressure, impulse, and general extent of damage to specific building components. Through hypothesis testing and iteration, the size and location of the charge is determined by identifying the charge properties necessary for the simulation to predict pressure and impulse maps that project the same extent of structural damage to the building components as observed in the post-blast scene. The

authors concluded that use of their method provided acceptable results when applied to a case study of an actual large scale explosive event resulting in damage to several masonry buildings in an urban environment. However, it should also be noted that while structural damage was considered in the analysis, the researchers did not attempt to directly simulate the damage to the structures using computational structural dynamics approaches, noting that such approaches would have been computationally expensive, since multiple buildings were damaged by the explosion. It is notable that this method reflects similarity to the established and previously explained method of correlating blast overpressure to structural damage.

Reconstruction of structural damage as a tool for post-blast analysis was further explored in Sorensen and McGill (2011b). The authors noted that computational modeling of blast events often requires numerically complex, computationally expensive models and instead proposed that post-blast measurements be taken as a tool to be used qualitatively with other observable evidence. Therefore, as was also seen in Ambrosini et al. (2005), the authors concluded that, while structural damage was valuable to a post-blast investigation, certain aspects of high fidelity numerical modeling were too computationally expensive to be practical to an investigation. The same authors explored the topic in Sorensen and McGill (2011a) from the perspective of material damage, noting that different materials, whether steel, concrete, masonry, glass, or timber, reflect differing failure modes under varying circumstances. The study focused on the use of structural and material damage as indicators of the charge properties, but, as has been seen previously, inference of the explosive location and size was reached by observation of the damage rather than the use of numerical models. Both of these cases reflect strong similarity to the previously described correlation between

peak overpressure and the observed level of damage. Similar research was continued in Sorensen and McGill (2012), in which the objective was to evaluate various blast analysis software that the authors described as "off-the-shelf" potential tools for blast characterization. The authors evaluated fifteen different software packages on the basis of usability to a non-engineer investigator in a post-blast forensics environment. Notably, none of these software packages relied on computational fluid dynamics (CFD) techniques or the FEM. The authors noted that such techniques were excluded from the analysis because of the level of modeling experience required for such programs, cost and maintenance of the software, and because the post-blast investigative community already maintained knowledge of the "off-the-shelf" toolkits evaluated in the study. Although the authors stated that they were unauthorized to give full detail of their analyses, they concluded that the evaluated software solutions showed potential as tools to back-calculate the properties of an explosive device. However, because the software was often limited in its capabilities and sometimes required structural knowledge that would potentially be beyond the scope of knowledge of many forensic investigators, the authors ultimately concluded that instead of investing in software development to better meet the needs of non-engineer investigators, emphasis should be redirected to furthering investigator knowledge of damage types and causes to better equip investigators to use existing software.

The predominant use of explosive residues over structural data was again identified and served as motivation for research conducted in Van der Voort et al. (2015), in which the authors introduced a methodology for inverse determination of the charge mass and point of origin through examination of post-blast data. The authors developed a tool that coupled street mapping data with observable damage inputs and a damage model that was

originally developed through mapping of damage caused by German air raids of England during World War 2. The original damage model estimated the distance to the charge, described as the average circle radius, as a function of the equivalent TNT charge mass. The authors manipulated this model to derive an inverse model for calculation of the charge mass as a function of the observed damages and corresponding distances. Use of this model required comparison to damage level tables and determination of ratios descriptive of the observed damage. Following introduction of the building damage-based model, the authors presented a methodology for inverse calculation of charge properties based on window breakage. The window breakage model was developed as a function of charge mass, range, facade orientation, and window properties. Based on the pressures and impulses required to break windows, the authors derived a model to determine the probability of window breakage for a facade and inversely determine the probable ranges of distance and charge mass by comparison to pressure, impulse, and load curves. The authors applied the tool to several case studies of past explosive events and found it to be effective in relatively open and urban environments. However, the authors also noted that the tool was unable to account for more specific circumstances, such as blast shielding of structures. The authors advised that more advanced problems should be simulated using CFD methods instead of the relatively simple inverse calculation tool. This case study therefore serves as an example of the development of a structural damage-based post-blast forensics tool for calculation of charge properties. However, as has been seen in other case studies, the authors did not attempt to include high-level numerical models in the analysis tool, as indicated by the acknowledgment that application of the inverse tool to blast shielding problems led to under-prediction of the charge properties and should therefore be simulated using CFD

models.

This approach was extended in Verolme et al. (2018) to include a quantitative model for calculation of explosion strength based on debris throw. The authors observed that methods for inversely calculating charge properties have been based on structural damage, as seen in Van der Voort et al. (2015). Therefore, their proposed methodology attempted to similarly estimate charge properties through characterization of the debris field. Characterization of the debris field by the proposed methodology required determination of a list, referred to by the authors as the "checklist", of field measurements, such as point of origin and debris location. Collection of such data allowed for calculation of the debris launch velocity and subsequently the strength of the explosion through application of dynamic equations of motion and empirical formulas for debris launch velocity developed by prior researchers. Through application to two case studies of explosive events with debris throw, the authors concluded that the model produced results that corresponded well to actual events. It should be noted that as was seen in the case of Van der Voort et al. (2015), the authors did not attempt to incorporate CFD or FEM simulations into the model, instead attempting to develop a relatively expedient and practical tool for forensic investigation. It is further noteworthy that, while the strength of the explosive is inversely calculated, the method requires prior knowledge of the epicenter of the blast and is dependent on the quality of the measurements prescribed in the "checklist".

It has therefore been seen in the literature that methods of implementing structural damage in post-blast forensics investigations have been introduced in multiple studies. Many of these research efforts have noted that it is often the case that structural damage, even while acknowledged as having value to a post-blast investigation, is overlooked in favor of

evidence offering a more expedient means of characterizing the explosive charge. Notably, many of the proposed methods for characterizing an explosive charge recommend comparison of peak overpressure or pressure-impulse models to observed structural damage. A similarity can be seen between these proposed methodologies and the established method of comparing structural damage levels to a known overpressure and its estimated TNT equivalence detailed in Beveridge (2011). While the strategy behind the methods exhibit similarity, the proposed methods are dissimilar in that they often involve implementation of relatively more in-depth methods into the analysis. Examples of this include the use of CFD for blast overpressure predictions and the use of kinematic formulas for analysis of debris throw. The similarity is nonetheless noteworthy in that the methods all indicate the relationship between blast overpressure and structural damage.

It should further be noted that while the use of the FEM was sometimes recommended for specific purposes, the observed studies did not propose the use of high-level numerical simulations to model the post-blast damage, typically due to the potentially time-consuming, computationally expensive, and difficult nature of the models required to achieve an accurate representation of the event. It can be reasonably speculated that such modeling difficulties are less than ideal when conducting a potentially time-sensitive forensics investigation, thereby typically resulting in the use of chemical analysis, crater analysis, or sometimes relatively simple comparisons of structural damage to established guidelines for estimating the overpressure corresponding to the observed damage levels.

2.3 Numerical Modeling of Structural Blast Loading

As has been demonstrated in the literature, research has been conducted to examine the use of post-blast structural measurements as a tool for post-blast investigations, and in the cases examined, high fidelity numerical modeling was often considered impractical or used sparingly due to time and computational constraints. Therefore, to better understand the challenges associated with numerical modeling of blast events, relevant research regarding structural blast modeling, particularly using the FEM, will be examined. The FEM is an established method of analysis that has been successfully applied to many applications across numerous fields, notably including structural engineering. The FEM has been implemented for structural engineering problems including linear elastic analyses and also highly nonlinear problems such as collapse, fracture, and blast analysis. As the FEM is an established method for blast analysis, several commercially available, FEM based software packages feature built-in blast analysis options, with two examples being the Abaqus and LS-Dyna software packages.

2.3.1 Modeling of Fracture and Element Separation in the Finite Element Method

Since element separation, collision, and debris field formation are aspects of modeling that are of particular interest to this research effort, the applicability of the FEM to these areas of simulation are reviewed in this section. Since the FEM was originally formulated for continuum mechanics, modeling of cracking and element separation presents a challenge for which multiple specialized models have been developed over time to introduce these capabilities. Two of these models, the smeared cracking model and the element deletion method, have been implemented in case studies for blast analysis of glass lites that are pre-

sented later in this chapter. A third method that has gained popularity and widespread use in other applications requiring element separation is the Extended Finite Element Method (XFEM). Alternatives to these methods for crack modeling have also been developed for the FEM. Due to their widespread use and relevance to this research, this review of FEM cracking models will focus on these three methods.

A notable method that predates the XFEM and element deletion is the smeared cracking model (Rashid, 1968), in which the crack behavior is accounted for through modification of the material properties of the affected elements. Using this method, the cracked material remains a continuum, but changes in material properties assigned to elements in the model attempt to account for the effects of the crack development and growth. A simplified illustration of this method is presented in Figure 2.5, where the smeared representation of crack growth in a simple panel model is depicted. In this figure, the crack propagation is represented by corresponding elements with reduced stiffness. While this method has been effectively used in many cases, it is noteworthy that a known challenge is the mesh-dependent nature of the crack growth (Cervera and Chiumenti, 2006). Furthermore, since the model remains a discretized continuum, the accuracy of the smeared crack model is limited to early crack formation, and the technique is not capable of modeling element separation.

While early methods of modeling crack growth using the FEM included nodal relaxation, in which nodal connectivity was removed at the location of cracking, and incremental re-meshing of the assembly was performed to account for the crack growth, a prominent alternative known as the Extended Finite Element Method (XFEM) was introduced in Moës et al. (1999). Developed and implemented for both two-dimensional and three-

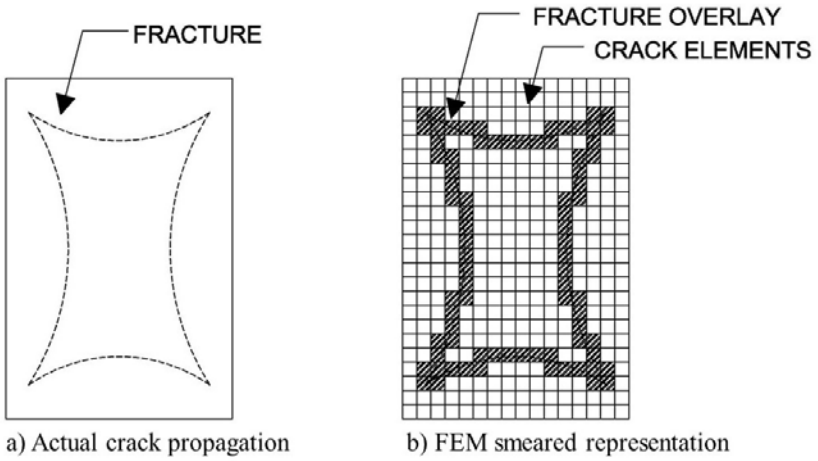

FIGURE 2.5: Illustration demonstrating the smeared method for modeling cracking

dimensional cracking problems, this method offers distinct advantages in that neither re-meshing around the crack growth nor prior knowledge of where the crack will form and propagate is required (Moës et al., 1999; Sukumar et al., 2000; Moës and Belytschko, 2002). Since re-meshing of the problem is not required, the XFEM offers the advantage over earlier methods that the mesh is not forced to conform to the crack (Sukumar et al., 2000). This is accomplished through the use of the mesh in conjunction with a distinct and independent crack representation (Moës et al., 1999). Representation of the distinct crack is achieved through enrichment of the Finite Element approximation using a discontinuous function integrated into the displacement approximation, essentially modeling element separation as the sum of the non-cracking model and the discontinuous enrichment (Moës et al., 1999). While the XFEM has been proven as an effective method for modeling crack formation and propagation, it should be noted that there are several challenges associated with the method, such as issues associated with blending elements, which are constructed between standard and enriched elements (Khoei, 2015). Due to difficulties in accurately modeling the transition between elements, numerous research efforts have been undertaken

to better model the interaction using the XFEM (Khoei, 2015).

A simpler alternative that has gained popularity and offers the advantage of computational simplicity is the element deletion method (Song et al., 2008). This method uses "deleted" elements to represent cracking (Song et al., 2008). Since elements in the mesh are removed, the stress at the interface to these cracked elements is reduced to zero, and nodes may become disconnected, allowing for element separation. This method can be implemented to predict initial failure and propagation through the model when the location of cracking is unknown, as this failure model predicts cracking based on the calculated principal stress in relation to the material failure strength. As is the case with the XFEM, this method is featured in several commercially available Finite Element Method software packages and has furthermore been implemented in several research efforts to model fracture of brittle materials under blast loading. As will be seen through examination of the case studies, accurate representation of cracking using this method has been noted to be dependent upon the mesh refinement of the model. This dependency is attributed to the crack representation through the removal of elements, as the elements must be sufficiently small to accurately follow the crack propagation and account for the effects of the crack without significant error. This is demonstrated through the simple illustration presented in Figure 2.6. It was noted in Song et al. (2008) that, while not always the case, the mass of the deleted elements is set to zero in certain commercially available software packages, particularly LS-Dyna, to negate the associated inertia effects. Removal of element mass was further noted in Pelfrene et al. (2016b) as an often cited criticism of the method. However, it was also noted that the mass of the elements is often retained, and Song et al. (2008) observed that, for certain problems, deletion of the mass did not significantly affect the

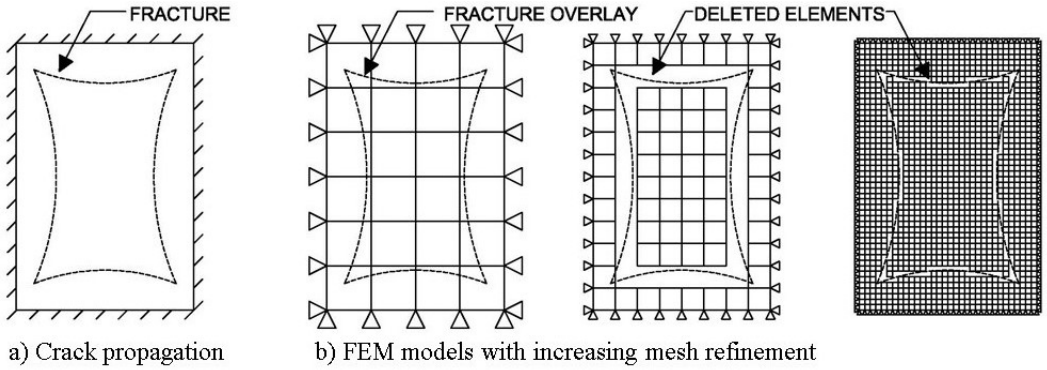

FIGURE 2.6: Illustration of the importance of mesh refinement with the element deletion method

results.

2.3.2 Simulation of Collision and Debris Field Formation in the Finite Element Method

Similar to the simulation of fracture, modeling of collision is inherently a nonlinear problem. However, a further and independent step is required in the form of contact detection. When modeling a problem in which contact may occur at an unknown location, contact simulation requires both an initial means of detecting the presence of any elements in contact and the subsequent step of modeling the interaction between the contacting element nodes. Contact interaction in the FEM requires that the surfaces in contact be defined as "master" and "slave" surfaces, with a search algorithm required to detect both surfaces. While this can be accomplished through the computationally expensive method of individually checking the distances between elements and nodes, multiple contact detection algorithms have been developed to more efficiently accomplish this task (Heinstein et al., 1993).

Following detection of contact between elements, implementation of a contact model is necessary. Due to the development of contact forces resulting from the contact between

elements, specifically in the case of impact collision problems, enforcement of a kinematic contact constraint becomes necessary to properly model the interaction (Zhong and Mackerle, 1994). Two methods that can be used to accomplish this are the penalty method, in which some amount of penetration is allowed between the contacting points, and the Lagrange multiplier method, in which the contact constraint is enforced exactly and penetration is not permitted (Zhong and Mackerle, 1994). Furthermore, a mixed method of kinematic contact, the Eulerian-Lagrangian contact method, was introduced in Haber (1984). Through use of these numerical models along with contact detection algorithms, simulation of collision has been successfully implemented into the FEM.

Despite the successful application of the FEM to blast problems, one area of research in which case studies or methods of analysis were not found was the predictive simulation of debris field formation using the FEM. While critical components required for simulation of debris field formation, specifically fracture and collision, have been successfully incorporated into the FEM using specialized models, simulation of debris field formation presents the challenge of modeling numerous cases of particle dynamics as the elements fragment. Modeling such failure becomes a difficulty because of the continuum assumed in the FEM (Meguro and Tagel-Din, 2002). Although specialized models for fracture have been developed to address this challenge, a discontinuous approach, such as the Discrete Element Method (DEM), is better suited for simulations involving particle phenomena (Munjiza et al., 1995), and debris field problems inherently have the potential for extensive particle phenomena. Similarly, the relatively recently developed combined DEM/FEM has been implemented for discontinuous modeling of fracture problems, including failure of glass under impact loading (Chen, 2013; Gao and Zang, 2014; Chen et al., 2016) and brittle

failure of geologic formations (Morris et al., 2006). However, it has been noted that DEM-based approaches are relatively computationally expensive (Meguro and Tagel-Din, 2002), and literature regarding simulation of glass failure under blast loading using the combined DEM/FEM was not identified.

2.3.3 Case Studies on Blast Modeling of Glass with the Finite Element and Applied Element Methods

As shown in the literature, the FEM is capable of simulating many aspects of blast analysis, including dynamic behavior under loading and element separation. Because of these capabilities, coupled with the fact that external blast loading can be applied either as a dynamic load or using built-in applications featured in multiple commercial Finite Element software packages, the method has been implemented in multiple case studies of blast loading simulation. The literature regarding blast load simulation using the FEM is exceedingly numerous and in many cases beyond the scope of research encompassed in this dissertation. Therefore, certain case studies of particular relevance to this research initiative are examined in this section.

Of particular relevance to this dissertation is the modeling of tempered glass. Tempered glass, in contrast to annealed glass, is created through a quenching process, in which the glass is rapidly quenched after being brought to a critical temperature (Uhlmann, 1980). The rapid quenching process creates a residual stress distribution across the thickness of the glass, and this results in compressive pre-stressing of the glass surfaces. The residual stress distribution takes on a profile that is approximately parabolic, as illustrated in Figure 2.7, where σ_m denotes the mid-plane residual stress, occurring at half the magnitude of the

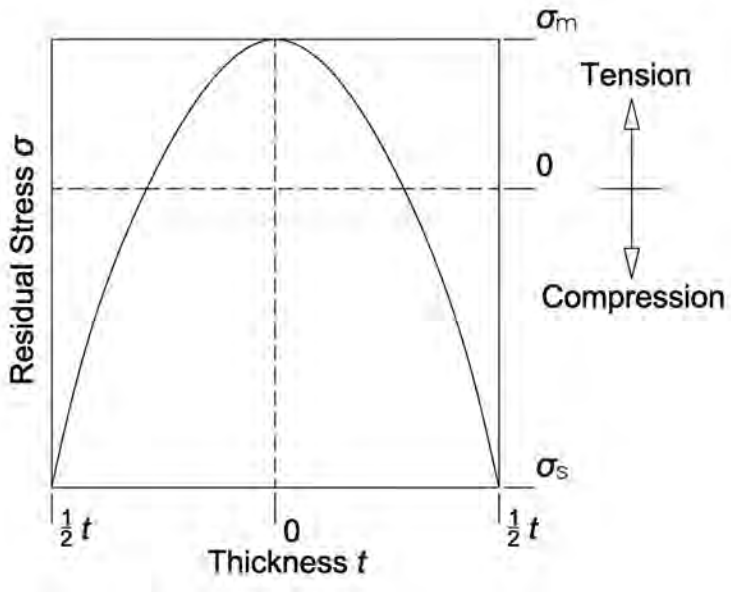

FIGURE 2.7: Simplified illustration of the residual stress distribution across tempered glass

residual surface stress, σ_s. The magnitude of the residual stress varies depending on the level of temper attained, with higher magnitude surface compression corresponding to a higher degree of temper. The value of the surface compression is therefore used to categorize the level of temper, where the minimum surface compression required for classification as fully tempered is specified in ASTM C1048-18 as 69 MPa (10,000 psi) (ASTM, 2018).

The tempering process significantly affects the material properties of glass, notably altering its strength and fracture behavior. Since any external loading must counteract the residual compressive stress acting on the surface, the tensile failure strength of the glass is increased proportional to the surface compression. Further, the fragmentation behavior is influenced by the presence of higher levels of strain energy created by the residual stress. Once fracture of the glass is initiated, the presence of the strain energy typically results in spontaneous fragmentation into numerous, small particles, as opposed to the larger shards generated by fragmentation of annealed glass. It has been noted that although even mild

degrees of temper produce increases in the failure strength, a more full temper is required to achieve reduction in the size of the fragments (Uhlmann, 1980).

The relationship between tempering and fragment size was notably examined in Pourmoghaddam and Schneider (2018) through experimental fracture testing of glass specimens having varying degrees of temper and corresponding residual stress. Experimental fracture testing by impact was conducted in accordance with EN 12150-1 (DIN, 2015) to observe the difference in fragmentation behavior. Specifically, the fragment density, which is defined by the test standard as the number of fragments developed in the 50 mm x 50 mm (1.97 in x 1.97 in) observation field with greatest extent of fracture, was measured for each specimen using an optical scanning system. It was observed that increases in the residual stress corresponded to increases in the fineness of the fracture pattern and fragment density. The authors noted that the fragmentation behavior is dependent on the elastic strain energy (Barsom, 1968), which can be derived assuming linear elastic behavior using continuum mechanics as:

$$U = \frac{1 - v}{E} \int_V \sigma(z)^2 dV \tag{2.3}$$

where E is the modulus of elasticity, v is the Poisson's ratio, $\sigma(z)$ is the residual stress distribution, and V is the volume of the lite. The parabolic residual stress distribution through the thickness, t, as a function of the distance, z, from the midpoint of the thickness is normally approximated for heat tempered glass as:

$$\sigma(z) = \sigma_m \left(1 - 12\frac{z^2}{t^2}\right) \tag{2.4}$$

where σ_m is the magnitude of the residual stress at the midpoint of the cross section. Since

the elastic strain energy is related to the residual stress at the midpoint, the authors noted that an increase in the elastic strain energy corresponds to a greater fragment density. Further, the authors examined the minimum elastic strain energy required for cracks to experience branching, which leads to the extensive fragmentation indicative of tempered glass. It was noted in Fineberg (2006) that crack branching occurs at a minimum elastic strain energy of 35 J/m^2 (2.40 ft-lb$_f$/ft^2). However, for the experimental specimens tested in Pourmoghaddam and Schneider (2018), crack branching was observed to correspond to an elastic strain energy of approximately 50 J/m^2 (3.43 ft-lb$_f$/ft^2). Further, it was observed that for plates of varying thicknesses, the thinner specimen will experience a greater extent of fragmentation for the same magnitude of midplane residual stress. This corresponds to the increasing magnitude of midplane residual stress required to achieve the same magnitude of elastic strain energy as the glass thickness increases.

A further challenge in modeling glass fragmentation is the accurate prediction of the material failure strength. Although the theoretical strength of glass has been noted to reach 16 GPa (2,320 ksi), the experimentally measured strength is significantly lower (Uhlmann, 1980; Bourhis, 2014). The significant discrepancy between the actual and theoretical strength has been attributed to local stress concentrations around surface flaws (Griffith, 1921), which are inevitably present in glass as a product of the manufacturing process and in-service weathering (Uhlmann, 1980; Beason and Morgan, 1984). It was noted in Uhlmann (1980) that the concentration of stress about a surface flaw can result in up to a 100 GPa (14,500 ksi) increase in the stress at the crack tip. Therefore, since fracture of a glass specimen initiates about a flaw, which can occur anywhere across the surface of the glass, both the strength of the specimen and the location of fracture initiation are dependent

upon the presence, distribution, and geometry of surface flaws (Griffith, 1921). Notably, this can result in fracture initiation that does not necessarily correspond to the location of the maximum theoretical stress (Beason and Morgan, 1984).

Because of the variability in the distribution and size of the flaws, prediction of glass failure is often approached using a probabilistic model, in which the probability of failure, as proposed in Weibull (1939), is determined by:

$$P_f = 1 - e^{-B} \tag{2.5}$$

where P_f is the probability of failure, and B is a function representative of the failure risk of the specimen (Beason and Morgan, 1984). A methodology for implementing Equation 2.5 to determine the failure probability of rectangular glass plates under uniform loading was presented in Beason and Morgan (1984), where the failure risk function, B, was determined by:

$$B = k \int_0^w \int_0^h [C(x,y)\hat{\sigma}_{max}(x,y)]^m \, dxdy \tag{2.6}$$

where k and m are parameters used to characterize the distribution of flaws across the surface, w and h are the glass lite dimensions, $\hat{\sigma}_{max}(x,y)$ is the 60 second equivalent maximum principal stress at the coordinates x and y, and C is the biaxial stress correction factor at x and y (Beason and Morgan, 1984). The 60 second equivalent maximum principal stress allows for consideration of the effects of load duration on the failure probability and is determined by transformation of the principal stress by:

$$\hat{\sigma}_{max}(x,y) = \sigma_{max}(x,y)\left(\frac{t_d}{60}\right)^{\frac{1}{16}} \tag{2.7}$$

where $\sigma_{max}(x,y)$ is the maximum principal stress at coordinates x and y, and t_d is the du-

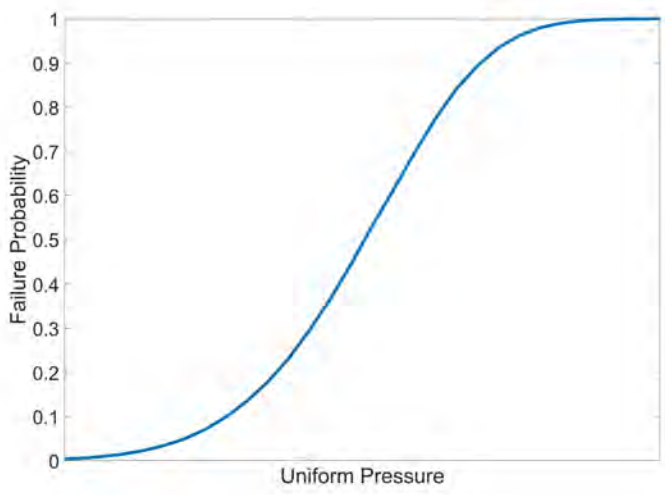

FIGURE 2.8: Typical Weibull failure probability curve for a glass plate specimen subjected to uniform loading

ration of loading. Determination of the 60 second equivalent minimum principal stress, $\hat{\sigma}_{min}(x, y)$, is similarly accomplished using the minimum principal stress in Equation 2.7. The biaxial stress correction factor, C, is determined by

$$C = \left[\frac{2}{\pi} \int_0^{\psi} \left(\cos^2 \theta + r \sin^2 \theta \right)^m d\theta \right]^{\frac{1}{m}} \tag{2.8}$$

where r is the ratio of the minimum to maximum 60 second equivalent principal stresses. The variable ψ is taken as $\pi/2$ if both the maximum and minimum principal stresses are tensile (Beason and Morgan, 1984). However, for the case of a compressive minimum stress, ψ is determined by:

$$\psi = \tan^{-1} \left(\left| \frac{1}{\sqrt{r}} \right| \right) \tag{2.9}$$

Implementation of the described Weibull probabilistic model results in a failure probability curve similar to the one depicted in Figure 2.8, where an increasing uniform pressure corresponds to an increasing probability of failure.

The described probabilistic approach for prediction of window breakage was adapted for design use in ASTM E1300, which prescribes a methodology for determining the probability of window failure (ASTM, 2016). ASTM E1300 recommends the use of Equation 2.5 for prediction of the failure probability with the failure risk function determined over N principal stress values by:

$$B = k \sum_{i=1}^{N} \left(\left(C_i \left(\frac{t_d}{60} \right)^{\frac{1}{n}} (\sigma_{max_i} - \sigma_s) \right)^m A_i \right) \tag{2.10}$$

where n is specified as 16, σ_{max_i} is the maximum principal stress at location i, σ_s is the surface residual stress, and A_i is the area at i. C_i is the i^{th} value of the biaxial stress correction factor, which instead of being determined through integration is approximated by the polynomial function:

$$C_i = -0.005r_i^6 + 0.022r_i^5 + 0.055r_i^4 + 0.039r_i^3 + 0.031r_i^2 + 0.06r_i + 0.8 \tag{2.11}$$

Furthermore, it is specified in ASTM E1300 that the surface residual stress should be included when calculating the ratio r_i, which is determined by:

$$r_i = \frac{\sigma_{min_i} - \sigma_s}{\sigma_{max_i} - \sigma_s} \tag{2.12}$$

Accurate determination of the failure probability using the described methodologies requires reasonable estimates of the surface flaw parameters k and m, which are used to characterize the surface flaw distribution (Beason and Morgan, 1984). Since the flaw distribution varies widely, it was noted in Beason and Morgan (1984) that k and m can only be determined experimentally for a given set of glass plates. In accordance with the procedures detailed in Beason and Morgan (1984), experimental failure testing under static loading is

conventionally conducted over a relatively large sample size, and the failure risk factor is calculated using each measured failure load in conjunction with a range of assumed values of m. The coefficient of variation across the calculated risk factors is subsequently computed, and the optimal value of m is determined as the value corresponding to a coefficient of variation of 1.0. This facilitates determination of the parameter k by:

$$k = \frac{(wh)^{m-1}}{(Eh^2)^m \, B_{mean}} \tag{2.13}$$

where B_{mean} is the mean risk factor determined using the optimal value of m.

However, for design purposes, ASTM E1300 recommends values of 7.0 and 2.86 x 10^{-53} $N^{-7}m^{12}$ (1.365 x 10^{-29} in^{12} lb^{-7}) for parameters m and k, respectively (ASTM, 2016). These values were experimentally determined to represent the typical flaw distribution resulting from 20 years of in-service exposure. It was therefore noted in Beason et al. (1998) that the use of these surface flaw parameters will typically result in under-prediction of the strength of newly manufactured windows.

Although ASTM E1300 accommodates the inclusion of residual stress in the glass failure probability model, the reliability of this approach and the surface flaw parameters has been questioned and, consequently, the failure probability of tempered glass lites has been further examined in several studies. Notably, Oakes (1991) sought to further the failure probability model described in Beason and Morgan (1984) for design use with heat strengthened and tempered glass lites. Since the objective of the study was to develop the model for design use, the author sought to develop a design factor to account for residual stresses. In order to develop design factors for various glass specimens, the author determined the stresses experienced by various annealed glass lite specimens under design loads. Similar

to ASTM E1300, the author determined a new principal stress by subtracting the residual surface compressive stress from the computed principal stress. Subsequently, logarithmic interpolation was performed to determine a new design load corresponding to the new principal stress. The tempered glass design factor used to account for the increased strength by tempering was then computed as the new design load divided by the design load of the annealed glass. The author performed this analysis for numerous scenarios of tempering and specimen aspect ratios and notably determined that the design factor was dependent upon both the level of temper and the geometry of the specimen.

A further effort to extend the failure probability model described in Beason and Morgan (1984) was conducted in Bove (1995) for prediction of the failure probability of heat treated window glass. This author also recommended superposition of the residual surface compressive stress onto the calculated maximum principal stress. Through experimental failure testing of two fully tempered glass samples, the author implemented the adapted failure probability model to estimate the surface flaw parameters of the tempered glass specimens. Notably, the author observed that, although the specimens were nominally identical, significant variation was observed in the flaw parameters estimated for each sample. The author further examined the effects of the surface flaw parameters by computing the failure probability of heat strengthened glass specimens using flaw parameters developed for annealed glass. By comparison with experimental failure testing of the heat strengthened specimens, the author concluded that use the of flaw parameters developed for annealed glass resulted in overprediction of the strength of the heat strengthened glass.

The importance of a probabilistic model, specifically for prediction of window failure under blast loading, was notably detailed in Netherton and Stewart (2009). The authors, al-

though acknowledging the common use of deterministic models in which a boundary value is specified as the failure threshold for prediction of structural failure under blast loading, described the inability of deterministic models to fully account for the many uncertainties associated with a blast event. Because of these uncertainties, the authors introduced a computation based, probabilistic approach for prediction of facade damage under blast loading. The authors modeled window behavior under blast loading using a single degree of freedom model, and a probabilistic approach was adapted through implementation of a Monte Carlo analysis based simulation. The single degree of freedom model was used to predict the peak tensile stress developed under blast loading for a large number of scenarios that were sampled using the Monte Carlo simulation. Uncertainties associated with blast analyses were accounted for using random variation of assigned variables, which were constrained within a specified coefficient of variation. The probability of window failure was then computed based on the number of scenarios in which the calculated tensile stresses exceeded the specified failure strength of the windows. Although use of the single degree of freedom model in conjunction with the probabilistic simulation was successfully demonstrated for prediction of failure probabilities, the authors noted that existing deterministic models for structural behavior under blast loading should be refined, since the described probabilistic approach complimented the deterministic, single degree of freedom model.

The use of Finite Element analysis for probabilistic prediction of laminated glazing failure under blast loading was addressed in Wei et al. (2006). The authors implemented the Weibull probability model and adapted the methodology described in Beason and Morgan (1984), used to account for the random surface flaws and load duration, to be applicable to dynamic analysis. The surface principal stresses required by the probabilistic model were

determined using a Finite Element model developed in the commercially available LS-DYNA3D software package, and the authors examined the effect of various combinations of the surface flaw parameters, k and m, on the predicted failure probability. Various flaw parameters that had been experimentally developed in past studies were implemented, and the authors concluded that the surface flaw parameters used for weathered glass exhibited notably decreased resistance to blast loading.

Similarly, implementation of a probabilistic model for prediction of window failure under blast loading was further recommended in Spiller et al. (2016). The authors conducted open-arena blast tests of annealed, monolithic window panels for evaluation of the predictive capabilities of several software packages, which were used to develop two single degree of freedom models and one explicit Finite Element model. While the results of the single degree of freedom models were found to correlate reasonably well with experimental results, the authors concluded that implementation of the Weibull probability model, as described in Beason and Morgan (1984), in conjunction with the Finite Element model provided accurate predictions of window failure. Further, the authors noted the dependence of the results on the accuracy of the surface flaw parameters, and found that results generated using experimentally estimated surface flaw parameters correlated similarly well with results attained using the flaw parameters recommended in ASTM E1300.

The described studies indicate the importance of implementing a probabilistic approach in conjunction with an accurate, deterministic model for prediction of structural response, as recommended in Netherton and Stewart (2009). Further, successful application of the Weibull probabilistic model, implemented in conjunction with advanced numerical models, for prediction of window failure under blast loading was demonstrated in Wei et al. (2006)

and Spiller et al. (2016).

Research efforts to characterize the behavior of monolithic glass window panels under static loading were notably conducted in Seaman (1967); Iverson (1968); Moore (1980); Meyers (1984). An early effort to experimentally characterize the behavior of monolithic glass window panels was conducted in Iverson (1968) for the purpose of evaluating the resistance of existing structures to nuclear weapons. The author treated the response of the glass window panel as a single degree of freedom system and implemented a differential equation of motion given as:

$$\frac{d^2x}{dt^2} = \frac{1}{m}\left[F(t) - R(x)\right] \tag{2.14}$$

where m is the mass of the panel, $F(t)$ is a time dependent forcing function, and $R(x)$ is a resistance displacement function. The deflection at the center of the simply supported, square window panel under static loading, as predicted by several analytical load deflection relationships, was compared to experimental results compiled in identified literature. The author determined that the best correlation to experimental data was achieved using the load deflection relationship presented in Seaman (1967) and given as:

$$\frac{p}{E}\left(\frac{a}{t}\right)^4 = 21.7\left(\frac{w_0}{t}\right) + 2.80\left(\frac{w_0}{t}\right)^3 \tag{2.15}$$

where p is the pressure across the surface of the panel, E is the modulus of elasticity, a is the unsupported length of the panel, t is the thickness of the panel, and w_0 is the centroidal deflection. It should be noted that Equation 2.15 was derived for square panels with a Poisson's ratio of 0.23. The static deflection behavior of rectangular glass panels of varying dimensions was investigated in Moore (1980) using the Finite Element Method.

The author developed load deflection curves for rectangular plates of various length to width ratios and, through comparison to experimental databases, concluded that the models showed generally good correlation.

The response of rectangular glass window panels under dynamic loading was investigated in Iverson (1968), where the Newmark-Beta method was implemented for approximation of the dynamic loading across the panel. The failure pressure of the glass panel was estimated using an equation derived empirically in Clark (1954) and determined by:

$$P = \frac{kRt^2}{A} \tag{2.16}$$

where R is the ratio of the width to the length of the panel, A is the area of panel, and k is an approximated constant, recommended as 50,000 for tempered glass.

Iverson (1968) further provided equations for estimating the fragment size and spatial density of annealed glass fragments following failure under blast loading and outlined a methodology for estimating glass fragment velocity following failure under blast loading. The described model for estimation of fragment velocity required estimation of five blast wave parameters to be used in conjunction with charts, subsequent equations, and tables.

A single degree of freedom approach was further implemented in Meyers (1984) to develop guidelines for estimating the static failure pressure of simply supported, tempered, monolithic glass panels of various dimensions. Relevant to this dissertation, Meyers (1984) estimated the static failure pressure of 121.9 cm x 81.3 cm (48.0 in x 32.0 in), 4.8 mm (3/16 in) thick, tempered, monolithic glass panels to be 20.4 kPa (2.96 psi). The author further implemented this approach for analytical derivation of curves indicating the blast failure pressure of rectangular, tempered glass panels as a function of the panel dimensions and

the duration of the blast.

More recent efforts to characterize the behavior of both annealed and tempered monolithic window panels were conducted in Zhang et al. (2014, 2015); Zhang and Hao (2016). While these studies were experimental in nature and did not attempt to analytically model the response of the glass panels, they are relevant to this dissertation in that the failure pattern and debris field formation of tempered glass panels were extensively documented. Furthermore, an analytical model for prediction of the fragment size and ejection velocity of brittle materials was presented in Zhang et al. (2004) through relation of the fragment velocity to strain rate and damage.

It has been seen that the discussed research efforts provide guidance on estimating the failure behavior of annealed and tempered monolithic glass panels under blast loading. However, these studies did not attempt to model failure under blast loading using the FEM. It was found that the majority of identified case studies detailing the use of the FEM for blast analysis of glass panels focused on modeling the behavior of laminated glass, which consists of a polymer interlayer, often constructed of polvinyl butyrel (PVB), interwoven between multiple sheets of glass (Gooch, 2007). Because of the lamination between the glass sheets and the interlayer, the multiple layers behave as one membrane. Due to this membrane behavior, a laminated glass panel can remain intact even after fracture has initiated and propagated, depending upon the stiffness of the interlayer (Pelfrene et al., 2016a). As will be demonstrated through the review of relevant literature, case studies are plentiful regarding numerical simulation of the performance of laminated glass under blast loading, while literature pertaining to the behavior of monolithic glass is relatively limited. Many of these studies offer specific detail pertaining to the modeling of the interlayer, while mod-

eling of characteristics exclusive to tempered glass was not addressed. Although it should be noted that it is possible for laminated glass to be constructed using sheets of either annealed or tempered glass, the identified case studies did not model the effects of tempering. However, several case studies of particular relevance to this research initiative have investigated the behavior of laminated glass under blast loading using the FEM for numerical simulation.

A Finite Element model representative of laminated glass as part of a glazing system subjected to blast loading was developed and evaluated in Hooper et al. (2012). The researchers examined the experimental response of the laminated glass specimens through completion of four open-air blast tests. The behavior of the laminated glass specimens under blast loading was captured using high-speed 3D digital image correlation in conjunction with image correlation software to experimentally measure the deflection and strain in the panel. Three of the four experimental tests resulted in failure of the glass windows at the silicone-sealed edge joints, while the remaining test did not result in failure. The pre-cracking and post-cracking behaviors of the glass panels were examined numerically through FEM analyses using the Abaqus software package in conjunction with the Air3D software package for simulation of the blast overpressure. The authors facilitated crack modeling throughout the failure process through the use of two separate models. An initial model was used prior to cracking to simulate the response of the panel prior to the development of the failure stress. Once the failure stress was attained, the strain, position, and velocity output variables from the model were input as initial values into a secondary model for simulation of the behavior after cracking. The authors modeled the pre-cracking problem using both shell elements and solid elements capable of modeling the PVB interlayer present in laminated glass. The

stated purpose of this model comparison was to demonstrate the adequacy of the results obtained using the relatively simpler shell element model compared to the more complex model developed with solid elements. Determination of the fracture pattern at failure was facilitated through examination of the stress pattern across the model, since the pattern of elements attaining failure stress correlated with the fracture pattern. The behavior of the shell element model after cracking was simulated through adjustment of the material properties of the elements using a material plasticity model to represent the cracked laminate. The authors did not implement element deletion. The authors concluded that the model, while exhibiting some differences, correlated well to the experimental tests and showed potential as a useful design tool for blast mitigation.

Laminated glass panels subjected to blast loading were modeled using the commercially available FEM software package LS-Dyna in Hidallana-Gamage et al. (2014). The authors implemented 3D, constant stress, solid elements with separate material models representative of both the laminated glass and the PVB and structural sealant joints. The authors implemented the Johnson-Holmquist failure model (Johnson and Holmquist, 1994) for modeling of the glass elements, while the interlayer and sealant joints were modeled using different material models. The authors explained that implementation of the Johnson-Holmquist failure model resulted in reduction of strength of the elements dependent upon the level of damage, and the first principal stress was used as the failure criteria for the brittle glass elements. The predictive capability of the model was evaluated through comparison to experimental shock tube testing of laminated glass windows, and it was found that the model correlated reasonably well to the experimental results. The authors concluded that the tensile strength of the glass significantly influenced the failure behavior of

the glass and further emphasized the importance of proper representation of the interlayer and sealant joints for the case of laminated glass.

Laminated glass under air blast loading was further examined in Larcher et al. (2012) through comparison of FEM simulations performed using the EUROPLEXUS explicit code to experimental shock-tube tests carried out for the purpose of the study, as well as experimental results obtained from literature. The authors implemented a linear elastic material model with brittle failure for representation of the glass behavior. Three different models were employed for simulation of the post-fracture behavior of the laminated glass panels. The problem was first modeled using layered elements with a failure criteria in which the post-failure stresses were set to zero where any tensile strain developed. While this model effectively restricted the presence of post-failure tensile forces between elements, compressive forces were still allowed. The authors also implemented this failure model in conjunction with 3D solid elements, where it was concluded that such an approach requires an extremely fine mesh. In addition to these two models, a smeared cracking model was implemented with shell elements of differing material properties coincidently placed on shared nodes. The authors explained that the material properties of the shell elements were assigned such that their superimposed behavior exhibited the response of the glass prior to failure, while the post-failure behavior was represented by only one of the two coincident elements. The authors concluded that the smeared cracking model was relatively simple to implement but incapable of modeling the interlayer, due to the linear elastic nature of the model. Therefore, the smeared model was recommended only for small displacement simulations. The study concluded that the solid element models produced the most accurate results at the cost of the greatest computational expense. It should further be noted

that tempered glass was subjected to experimental blast loading in the study. However, the authors specified that numerical representation of the residual stresses in tempered glass was not addressed.

Explicit Finite Element Analysis implemented in the LS-Dyna software package was employed to simulate laminated glass subjected to blast loading in Pelfrene et al. (2016a). To validate the numerical models, the authors experimentally evaluated the fracture behavior of laminated glass panels subjected to air blast loading using a shock tube. The fracture patterns of the panels were observed using high-speed video, and characterization of the panel behavior through fracture included experimental measurement of centroidal displacements and strain across the panels. The authors implemented the Rankine criterion-based element deletion method to model the brittle fracture behavior of the glass and, similar to other case studies in which laminated glass was modeled, included the PVB interlayer in the FE model. The authors found that the immediate deletion of an element upon attaining failure stress often resulted in numerical instability in the simulation. This was attributed to stress wave propagation induced by the release of tension upon element removal. To attenuate the magnitude of the stress wave, the authors introduced a short plastic phase into the simulation. However, it was noted that this resulted in the fracture being governed by von Mises instead of Rankine criteria. Despite generally strong correlation between the numerical simulation and the experimental results, the authors concluded that the element deletion method suffered from serious limitations when applied to the simulation of laminated glass with a PVB interlayer.

Simulation of glass fracture using the element deletion method was further evaluated in Pelfrene et al. (2016b). Although the subject of this study was impact loading rather

than air blast loading, the case study is nonetheless of particular interest to this dissertation because of the implementation of the brittle failure model for glass fracture in the Abaqus software package. The case study is of further relevance in that failure of monolithic glass, as opposed to laminated glass, was investigated. The authors experimentally subjected monolithic glass to drop weight impact tests for comparison with explicit FEM simulations using shell elements and an element deletion failure model. Through comparison of the experimental and analytical results, the authors identified several computational difficulties related to the implementation of the element deletion method on monolithic glass. First, size of the elements could not exceed a critical length or the instantaneous loss in strain energy upon deletion of an element would exceed the physical fracture energy. Second, in the absence of a short plastic phase as recommended in Pelfrene et al. (2016a), spurious element deletion would result due to stress wave propagation induced during the removal of the other elements in the model. Lastly, the authors determined that the directionality of cracking needed to be specified in order to properly reproduce the radial, concentric cracks produced during impact testing. The authors therefore concluded that the element deletion method is highly mesh dependent when modeling local cracking behavior. However, despite the computational challenges, the element deletion method was found to typically result in agreeable results for the behavior of the monolithic glass at the macro scale.

Lastly, a case study detailing the modeling of glass subjected to blast loading using the Applied Element Method (AEM) was presented by Johns (2016). AEM is a relatively new method bearing similarities to both the FEM and DEM that provides computational advantages for simulating nonlinear analyses featuring crack initiation and propagation, element separation, and projectile motion of fragmentation (Meguro and Tagel-Din, 1999). The

AEM is the central numerical tool utilized in this dissertation and is extensively detailed in the following chapter. In Johns (2016), the only commercially available AEM software package, Extreme Loading for Structures (ELS), was used to simulate failure and fragmentation of annealed glazing panels under blast loading. The author performed experimental, open-arena blast testing of annealed glazing panels of varying thickness for benchmarking the predictive accuracy of deflection, failure, and fragmentation behavior within the AEM simulations. Modeling and discretization of the glazing models was performed in ELS using Voronoi polygon shaped elements, which served to better simulate the shard-like failure behavior of annealed glass. Similar to a previously reviewed case study, the author used the CFD software Air3D to simulate the blast wave loading. The authors concluded that the AEM simulations produced reasonable agreement for breakage time, impulse required for fracture, and fragment velocity. The fracture patterns produced in the simulations also correlated reasonably well with observations of panel fracture obtained with high-speed videography of panel failure. Notably, use of the AEM allowed the author to examine the accuracy of ELS for predicting debris field formation by comparing the mass distribution predicted using the simulation to experimentally obtained distributions of debris field mass. The author concluded that the predicted debris field formation correlated reasonably well with the experimental measurements. The author extended benchmarking of the ELS simulations to long-duration blast testing, which was conducted using an air blast tunnel. Although debris field distributions were not compared for the long-duration blast tests, the author determined that the AEM simulations correlated well with measured peak deflections, breakage times, and breakage impulses. Furthermore, it was qualitatively concluded in similar research led by the same author in Johns and Clubley (2016) that panel edge

support had a significant role in the breakage pattern of glazing panels. Examining the experimental failure of glazing panels subjected to long duration blast loading in an air-blast tunnel, the authors found that rigidly clamped edge supports resulted in greater panel breakup, while increased elasticity in the edge supports resulted in the formation of larger shards during breakage. The authors used ELS to replicate this behavior, concluding that the simulation results demonstrated reasonable qualitative agreement. Similar research using the AEM for simulation of brittle failure of masonry panels under blast loading was conducted in Keys and Clubley (2013) and Keys and Clubley (2017). These case studies, which examine the effectiveness of the AEM for prediction of debris field distribution, are reviewed in a following chapter detailing the AEM.

2.4 Concluding Remarks and Identified Knowledge Gaps

Introductions to blast pressure wave behavior, structures subjected to blast loading, and the use of post-blast structural forensics have been presented. An overview of the commonly used FEM and its applicability to blast analysis problems was given, including methodology and relevant case studies pertaining to the modeling of glass failure under blast loading. One case study on the use of the AEM to simulate failure of glazing panels under blast loading was detailed. A brief introduction to the properties of tempered glass relevant to this research effort was also presented. It was notably observed that the use of structural damage in a post-blast forensics investigation is often relegated to a qualitative role, largely due to the time and computational expense required to create accurate simulations and the required modeling experience associated with such models. However, multiple authors have noted the inconsistencies resulting from the qualitative approach and have

attributed this to the many different factors affecting damage levels. In light of this, several case studies have introduced methods of integrating some level of quantitative structural forensics into the analysis. It has further been seen that the FEM has been used to replicate real-world structural phenomena under blast loading with a high level of predictive fidelity. This includes the modeling of glass fracture under blast loading, which is of specific relevance to this research effort. However, certain aspects of structural behavior under blast, specifically debris field formation, have been noted to be beyond the feasible application of the method, and one case study in which the AEM was implemented to model the glass debris field problem was identified. Furthermore, the examined case studies simulated the failure of either annealed or laminated glass. While the case studies simulating failure of laminated glass did detail the methods used to model the interlayer, case studies attempting to simulate the residual stresses present in tempered glass were not identified.

CHAPTER 3: APPLIED ELEMENT METHOD

3.1 The Applied Element Method

While the FEM has been applied as the predominant numerical method for high fidelity simulation of structural response under blast loading, a relatively new method of structural analysis known as the Applied Element Method (AEM), has recently been demonstrated to show promise as an accurate and efficient method for simulating and predicting large deformation, fracture, and fragmentation behavior of structural components (Meguro and Tagel-Din, 2000), (Tagel-Din, 2009). The AEM shares commonality with the FEM and other numerical analysis methods in that it requires the discretization of a continuum into elements and subsequent numerical representation using stiffness and mass matrices. However, the AEM possesses distinct differences and advantages that distinguish it from other current methods and provide capabilities that further its appeal for certain applications, specifically those involving element separation. The development, underlying methodology, and verification of the AEM are discussed in this chapter.

3.1.1 Element Connectivity and Degrees of Freedom in the AEM

The AEM was developed and introduced in Tagel-Din (1998) and Tagel-Din and Meguro (2000a) as an alternative to the Finite Element Method offering the predictive capabilities of the FEM for linear elastic analysis coupled with the post-failure predictive capabilities of the Discrete Element Method (DEM) (Meguro and Tagel-Din, 2000). The AEM is sim-

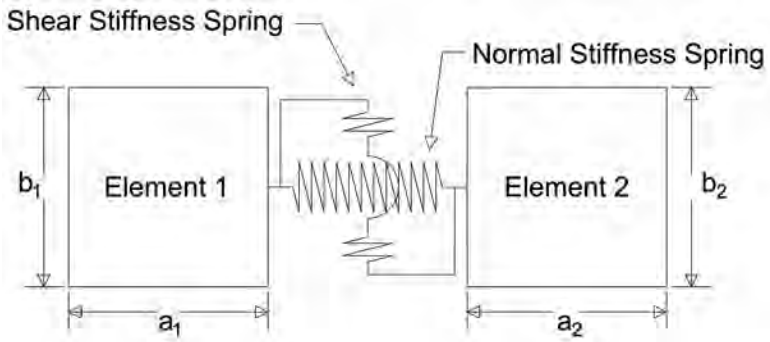

FIGURE 3.1: Simple representation of the spring interaction between a pair of two-dimensional Applied Elements

ilar to the FEM in that a continuum is discretized into a mesh of elements, but distinctly different in that connectivity between elements is not achieved through nodal connectivity. Instead, element connectivity in the AEM is achieved through introduction of interface springs providing stiffness in the normal and tangential directions between element faces (Tagel-Din, 1998). Connectivity of elements using these normal and shear springs is depicted for a simple, two-dimensional case in Figure 3.1, where the two elements are shown connected through one normal and one shear interface spring. The element face is typically subdivided such that an array of springs is located across the surface of the face to improve the discretized representation of the stress distribution and so that bending moments can also transfer across elements. Subdivision of element faces for multiple spring connectivity between elements is depicted in Figure 3.2 for an array of three-dimensional elements.

A notable aspect of this method of connectivity is the ease of meshing when compared to the nodal connectivity implemented in the FEM. Whereas connectivity amongst elements in the FEM requires interaction between the element nodal points, connectivity in the AEM only requires interface contact, since springs can be generated anywhere along the element

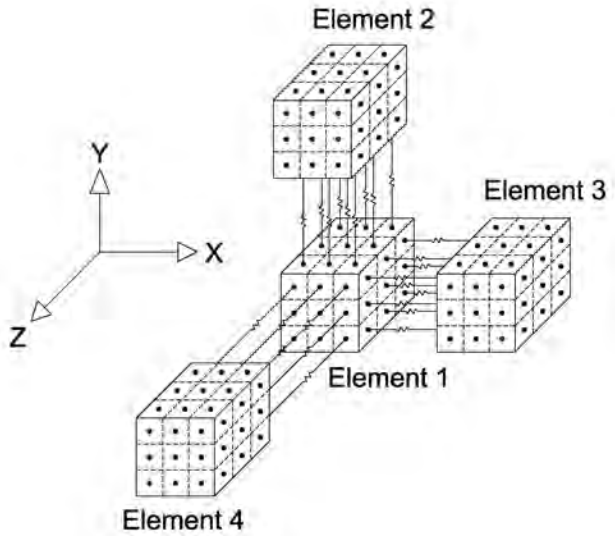

FIGURE 3.2: Representation of the interface spring connectivity in an array of three-dimensional elements in the AEM

faces. This is highly advantageous for problems benefiting from differing element mesh sizes, where transition elements would normally be required in the FEM to maintain nodal connectivity. An example of such a scenario would be modeling of a plate in which a finer mesh is desired in a certain location of the model. Due to the constraints associated with changing mesh sizes in the FEM, implementation of such a mesh in the FEM would require non-quadrangular shaped transition elements between the coarse and fine meshes and typically require increased modeling time to account for implementation of the transition mesh. In contrast, the AEM allows for elements to simply be progressively adjusted in size to meet the mesh refinement requirements (Tagel-Din and Rahman, 2006). This scenario is depicted in Figure 3.3, where the finer mesh is developed in the central region of the body.

The degree of freedom assignments for elements is a further distinction that differentiates the AEM from the FEM. In contrast to the FEM, where degrees of freedom are associated with the nodes, the AEM assigns degrees of freedom only to the centroid of each element.

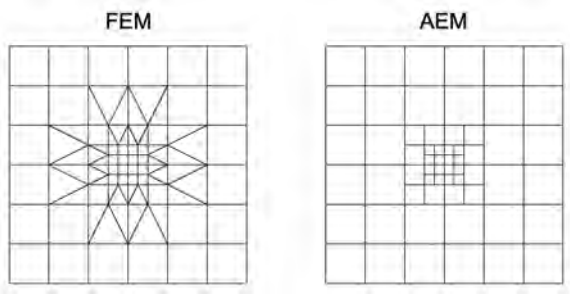

FIGURE 3.3: Comparison of the transition from a coarse to fine mesh within the FEM and AEM

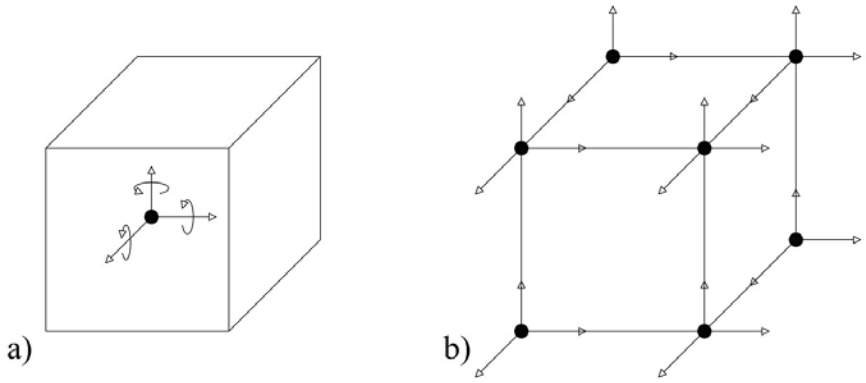

FIGURE 3.4: Comparison of the degrees of freedom for a cuboid element in a) AEM and b) FEM

This is depicted in Figure 3.4, where the degrees of freedom of one three-dimensional AEM element are contrasted with the degrees of freedom of a linear, eight node brick element commonly used in the FEM. The significant reduction in the degrees of freedom per element offers the potential to decrease computational time when performing AEM simulations featuring similar mesh discretization as solid models in the FEM.

3.1.2 Stiffness Matrix Formulation in the AEM

Implementation of the interface spring method of connectivity requires numerical representation of the stiffness of each normal and shear interface spring, where each spring

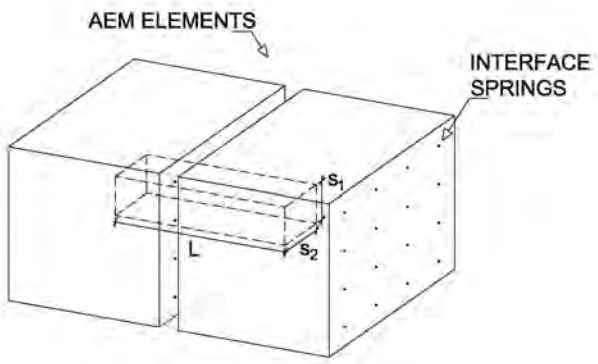

FIGURE 3.5: Element volume corresponding to one interface spring

represents a volumetric slice of an element. This is depicted in Figure 3.5. For an isotropic, linear elastic material, the stiffness of one linear elastic normal interface spring is determined by:

$$k_n = \frac{E s_1 s_2}{L} \tag{3.1}$$

where k_n is the normal spring stiffness, E is the modulus of elasticity of the material, s_1 and s_2 indicate the dimensions of the area of the element face associated with the interface spring, and L is the length of the spring, which corresponds to the distance between the centroids of two elements. Likewise, the stiffness of one shear interface spring is determined by:

$$k_s = \frac{G s_1 s_2}{L} = \frac{E}{2(1+\nu)} \frac{s_1 s_2}{L} \tag{3.2}$$

where G is the shear modulus of the material, and ν is the Poisson's ratio (Meguro and Tagel-Din, 2000).

Due to the definition of degrees of freedom at the element centroid within the AEM, a 6x6 local stiffness matrix is generated for each pair of elements in contact for two-dimensional problems, while a 12x12 local stiffness matrix is generated for each pair of

elements in contact for three-dimensional problems. Derivation of the local stiffness matrix for one pair of elements is facilitated by calculating the restoring forces in each degree of freedom generated when a unit displacement or unit rotation is applied individually to each degree of freedom (Meguro and Tagel-Din, 2000). Examples of this methodology are illustrated in Figures 3.6 and 3.7, depicting the application of unit displacements with the corresponding forces in each degree of freedom for one pair of three-dimensional elements connected at the local $+x$ face of the first element in the pair. The resultant local stiffness matrix for element connectivity on the local $+x$ face is presented in Table 3.1 and was derived following the given dimensions and nomenclature. Since there are three possible scenarios of interface connectivity for cuboid elements, local stiffness matrices associated with element connectivity at the $+y$ and $+z$ faces are derived following the same process and are presented in the Appendix in Table A.1 and Table A.2.

For small deformations, the local load-displacement behavior at one element pair is derived following Hooke's Law and given as:

$$\{f_e\} = [k_e]\{d_e\} \tag{3.3}$$

where $\{f_e\}$ is the vector of local forces acting on the centroids of each element, $[k_e]$ is the stiffness matrix for the interface springs of the element pair in the local coordinate frame, and $\{d_e\}$ is the local displacement vector for the degrees of freedom of each element.

For elements not aligned with the Cartesian axes, which occurs during incremental analysis when elements are displaced relative to their initial orientations, a means of transforming the displacement vectors, force vectors, and stiffness matrices between local coordinates and global coordinates is necessary to facilitate assembly of a global stiffness matrix

TABLE 3.1: The local stiffness matrix for one pair of elements connected at the $+x$ face of element 1

d_1	d_2	d_3	d_4	d_5	d_6	d_7	d_8	d_9	d_{10}	d_{11}	d_{12}
k_n	0	0	0	$k_n c_{n1}$	$-k_n b_{n1}$	$-k_n$	0	0	0	$-k_n c_{n2}$	$k_n b_{n2}$
0	k_{sy}	0	$-k_{sy} c_{n1}$	0	$\frac{a_1}{2} k_{sy}$	0	$-k_{sy}$	0	$k_{sy} c_{n2}$	0	$\frac{a_2}{2} k_{sy}$
0	0	k_{sz}	$k_{sz} b_{n1}$	$-\frac{a_1}{2} k_{sz}$	0	0	0	$-k_{sz}$	$-k_{sz} b_{n2}$	$-\frac{a_2}{2} k_{sz}$	0
0	$-k_{sy} c_{n1}$	$k_{sz} b_{n1}$	$k_{sz} b_{n1}^2 + k_{sy} c_{n1}^2$	$-\frac{a_1}{2} k_{sz} b_{n1}$	$-\frac{a_1}{2} k_{sy} c_{n1}$	0	$-k_n c_{n1}$	$-k_{sz} b_{n1}$	$-k_{sy} c_{n1} c_{n2} - k_{sz} b_{n1} b_{n2}$	$-\frac{a_2}{2} k_{sz} b_{n1}$	$-\frac{a_2}{2} k_{sy} c_{n1}$
$k_n c_{n1}$	0	$-\frac{a_1}{2} k_{sz}$	$-\frac{a_1}{2} k_{sz} b_{n1}$	$\frac{a_1^2}{4} k_{sz} + k_n c_{n1}^2$	$-k_n b_{n1} c_{n1}$	0	0	$\frac{a_1}{2} k_{sz}$	$\frac{a_1}{2} k_{sz} b_{n2}$	$\frac{a_1}{2} \frac{a_2}{2} k_{sz} - k_n c_{n1} c_{n2}$	$k_n b_{n1} c_{n2}$
$-k_n b_{n1}$	$\frac{a_1}{2} k_{sy}$	0	$-\frac{a_1}{2} k_{sy} c_{n1}$	$-k_n c_{n1} b_{n1}$	$\frac{a_1^2}{4} k_{sy} + k_n b_{n1}^2$	$k_n b_{n1}$	$-\frac{a_1}{2} k_{sy}$	0	$\frac{a_1}{2} k_{sy} c_{n2}$	$k_n c_{n2} b_{n1}$	$\frac{a_1}{2} \frac{a_2}{2} k_{sy} - k_n b_{n1} b_{n2}$
$-k_n$	0	0	0	$-k_n c_{n_1}$	$k_n b_{n1}$	k_n	0	0	0	$k_n c_{n2}$	$-k_n b_{n2}$
0	$-k_{sy}$	0	$k_{sy} c_{n1}$	0	$-\frac{a_1}{2} k_{sy}$	0	k_{sy}	0	$-k_{sy} c_{n2}$	0	$-\frac{a_2}{2} k_{sy}$
0	0	$-k_{sz}$	$-k_{sz} b_{n1}$	$k_{sz} \frac{a_1}{2}$	0	0	0	k_{sz}	$k_{sz} b_{n2}$	$\frac{a_2}{2} k_{sz}$	0
0	$k_{sy} c_{n2}$	$-k_{sz} b_{n2}$	$-k_{sy} c_{n1} c_{n2} - k_{sz} b_{n1} b_{n2}$	$\frac{a_1}{2} k_{sz} b_{n1}$	$\frac{a_1}{2} k_{sy} c_{n2}$	0	$-k_{sy} c_{n2}$	$k_{sz} b_{n2}$	$k_{sy} c_{n2}^2 + k_{sz} b_{n2}^2$	$\frac{a_2}{2} k_{sz} b_{n2}$	$\frac{a_2}{2} k_{sy} c_{n2}$
$-k_n c_{n2}$	0	$-\frac{a_2}{2} k_{sz}$	$-\frac{a_2}{2} k_{sz} b_{n1}$	$-k_n c_{n1} b_{n1}$	$k_n b_{n1} c_{n2}$	$k_n c_{n2}$	0	$\frac{a_2}{2} k_{sz}$	$\frac{a_2}{2} k_{sz} b_{n2}$	$\frac{a_2^2}{4} k_{sz} + k_n c_{n2}^2$	$-k_n b_{n2} c_{n2}$
$k_n b_{n2}$	$\frac{a_2}{2} k_{sy}$	0	$-\frac{a_2}{2} k_{sy} c_{n1}$	$\frac{a_1}{2} \frac{a_2}{2} k_{sz} - k_n c_{n1} c_{n2}$	$\frac{a_1}{2} \frac{a_2}{2} k_{sy} - k_n b_{n1} b_{n2}$	$-k_n b_{n2}$	$-\frac{a_2}{2} k_{sy}$	0	$\frac{a_2}{2} k_{sy} c_{n2}$	$-k_n c_{n2} b_{n2}$	$\frac{a_2^2}{4} k_{sy} + k_n b_{n2}^2$

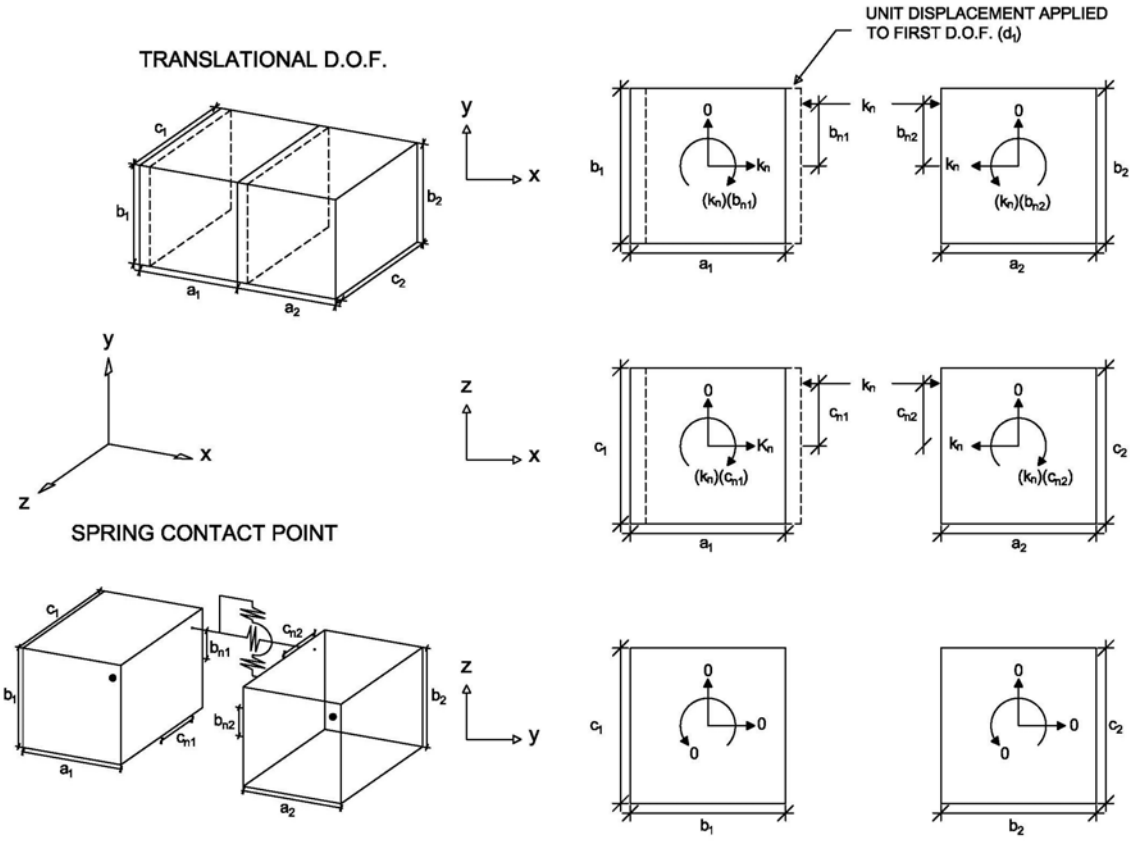

FIGURE 3.6: Determination of the stiffness matrix entries by calculating forces corresponding to unit displacements

as well as to determine incremental spring stresses and strains. As in the Finite Element Method, the transformation between local and global coordinates is accomplished using a transformation matrix developed from Cartesian rotation matrices:

$$[T_{xyz}(\theta)] = [T_x][T_y][T_z] \tag{3.4}$$

where $[T_x]$, $[T_y]$, and $[T_z]$ take the forms presented in Equations 3.5 through 3.7.

$$[T_x] = \begin{bmatrix} 1 & 0 & 0 \\ 0 & cos(\theta_x) & -sin(\theta_x) \\ 0 & sin(\theta_x) & cos(\theta_x) \end{bmatrix} \tag{3.5}$$

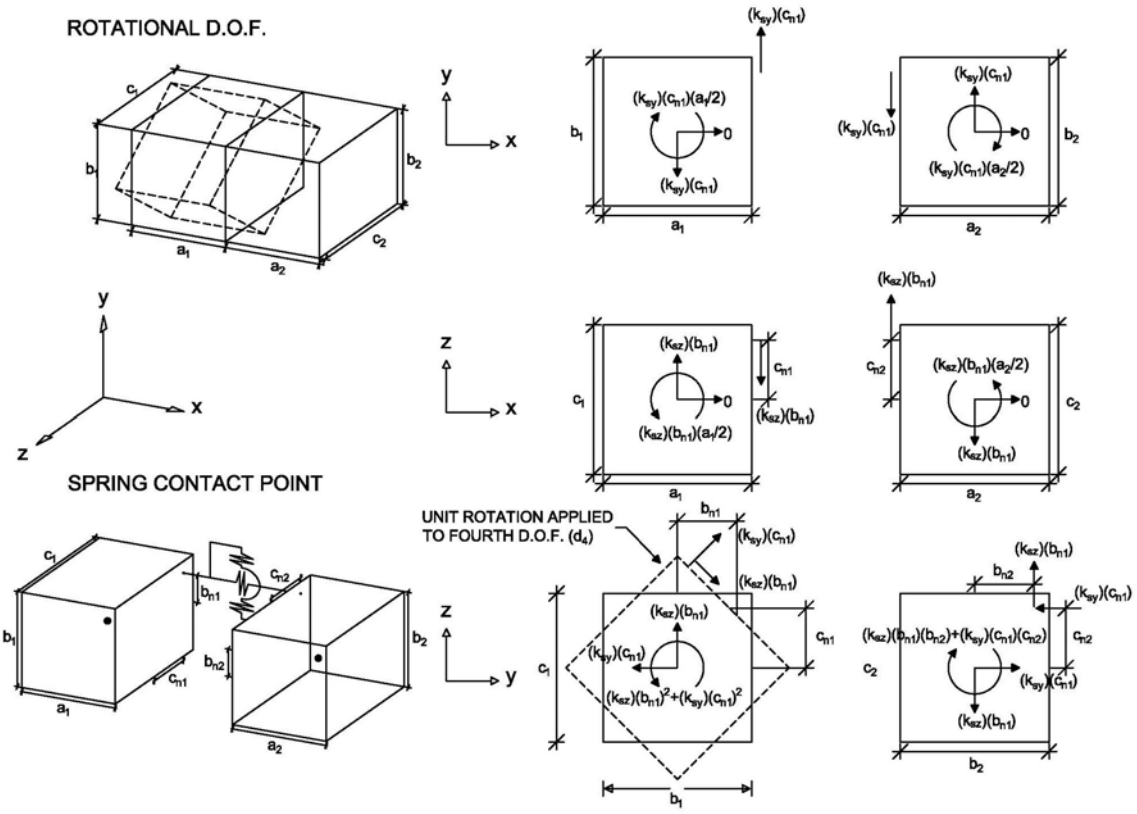

FIGURE 3.7: Determination of the stiffness matrix entries by calculating forces corresponding to unit rotations

$$[T_y] = \begin{bmatrix} cos(\theta_y) & 0 & sin(\theta_y) \\ 0 & 1 & 0 \\ -sin(\theta_y) & 0 & cos(\theta_y) \end{bmatrix} \tag{3.6}$$

$$[T_z] = \begin{bmatrix} cos(\theta_z) & -sin(\theta_z) & 0 \\ sin(\theta_z) & cos(\theta_z) & 0 \\ 0 & 0 & 1 \end{bmatrix} \tag{3.7}$$

Variables θ_x, θ_y, and θ_z are the relative rotation angles following the right hand rule convention. However, since the local stiffness matrix incorporates a pair of elements, the

transformation matrix is expanded to:

$$[T] = \begin{bmatrix} [T_{xyz}(\theta)] & [0_{3x3}] & [0_{3x3}] & [0_{3x3}] \\ [0_{3x3}] & [T_{xyz}(\theta)] & [0_{3x3}] & [0_{3x3}] \\ [0_{3x3}] & [0_{3x3}] & [T_{xyz}(\theta)] & [0_{3x3}] \\ [0_{3x3}] & [0_{3x3}] & [0_{3x3}] & [T_{xyz}(\theta)] \end{bmatrix} \tag{3.8}$$

where θ is the vector of the averaged rotation angles of the first and second elements in the pair. Similarly, the rotation matrix associated with the vector of relative angles between a pair of elements is defined as:

$$[R_{xyz}(\theta)] = [R_x][R_y][R_z] \tag{3.9}$$

where $[R_x]$, $[R_y]$, $[R_z]$ are formulated similarly to Equations 3.5, 3.6, and 3.7 but with implementation of the averaged relative angles between the elements in their respective degrees of freedom.

For the case of an incremental analysis, the relative rotation matrix can be implemented in conjunction with the deformation-displacement relationship $[B]$ to reconstruct the stiffness matrix contribution of one pair of elements as:

$$[k_e] = [B'][R][k_{edge}][B] \tag{3.10}$$

The variable k_{edge} is the spring constitutive relationship defined in Worakanchana and Me-

guro (2006) as:

$$[k_{edge}] = \begin{bmatrix} k_1 & 0 & 0 \\ 0 & k_2 & 0 \\ 0 & 0 & k_3 \end{bmatrix} \tag{3.11}$$

where k_1, k_2, and k_3 are the normal and shear spring stiffness contributions in each of the three planar directions. The element deformation-displacement relationship matrix $[B]$ for a pair of elements represents the spring deformations as the elongations in the x, y, and z planar directions between spring contact points during displacement. Use of this relationship facilitates determination of the resultant forces acting on the centroid of an element resulting from forces in each of the interface springs. For one pair of elements following the formulation described in Worakanchana and Meguro (2006), this results in a 3x12 matrix derived as:

$$[B]_{[1-6]} = \begin{bmatrix} -1 & 0 & 0 & 0 & (z-z_1) & -(y-y_1) \\ 0 & -1 & 0 & -(z-z_1) & 0 & (x-x_1) \\ 0 & 0 & -1 & (y-y_1) & -(x-x_1) & 0 \end{bmatrix} \tag{3.12}$$

$$[B]_{[7-12]} = \begin{bmatrix} 1 & 0 & 0 & 0 & -(z-z_2) & (y-y_2) \\ 0 & 1 & 0 & (z-z_2) & 0 & -(x-x_2) \\ 0 & 0 & 1 & -(y-y_2) & (x-x_2) & 0 \end{bmatrix} \tag{3.13}$$

where x, y, and z are the coordinates at the point of interest, and x_1, y_1, z_1, x_2, y_2, and z_2 are the centroid coordinates for the two elements in the pair. As was the case for the derivation of the element local stiffness matrix, a deformation-displacement matrix exists

TABLE 3.2: Deformation-displacement relationship for one pair of elements connected at the local $+x$ face of element 1

-1	0	0	0	$-c_{n1}$	b_{n1}	1	0	0	0	c_{n2}	$-b_{n2}$
0	-1	0	c_{n1}	0	$\frac{-a_1}{2}$	0	1	0	$-c_{n2}$	0	$\frac{-a_1}{2}$
0	0	-1	$-b_{n1}$	$\frac{a_1}{2}$	0	0	0	1	b_{n2}	$\frac{a_2}{2}$	0

for each of the three possible cases of element connectivity. The element deformation-displacement matrix is presented in Table 3.2 for the local $+x$ face and in Appendix Tables A.3 through A.4 for the local $+y$ and $+z$ faces, respectively. Implementation of the deformation-displacement relationship in an incremental analysis allows for determination of the local forces acting on the element centroid by substitution of Equation 3.10 into Equation 3.3:

$$[f_e] = [B'][R'][k_{edge}][B]\{d_e\} \tag{3.14}$$

The procedure by which Equation 3.14 is formulated for resolution of the interface spring forces into local forces acting on the element centroids is further described with illustrations in Figure A.1.

The displacement vector in local coordinates for an element pair can be obtained by applying the transformation matrix $[T]$ to the displacement vector in global coordinates, $\{D_e\}$:

$$\{d_e\} = [T']\{D_e\} \tag{3.15}$$

Similarly, the vector of local forces acting on a pair of elements can be transformed to global coordinates using:

$$\{F_e\} = [T]\{f_e\} \tag{3.16}$$

where $\{F_e\}$ is the vector of forces in global coordinates for an element pair. By substitution of Equations 3.15 and 3.16 into Equation 3.3, the stiffness matrix for a pair of elements in

global coordinates, $[K_e]$, can be derived as:

$$[K_e] = [T][k_e][T'] \tag{3.17}$$

Following determination of the stiffness contributions of individual pairs of elements in global coordinates, the global stiffness matrix of the array of elements in the complete model can be assembled. The size of the global stiffness matrix prior to applying boundary conditions will be equal to the total number of degrees of freedom in the element array. Boundary conditions are applied by partitioning the global stiffness matrix in the same manner as in the Finite Element Method. With the full global stiffness matrix, $[K]$, the displacement vector for the complete model in global coordinates, $\{D\}$, can be solved for in a static analysis for a given global force vector, $\{F\}$, through:

$$\{D\} = [K]^{-1}\{F\} \tag{3.18}$$

Since the load-deformation response is only accurate for small deformations, an incremental form is used when larger deformations will develop in the static analysis. In the incremental analysis, the incremental global displacements, $\{\Delta D\}$, for each incremental force vector, $\{\Delta F\}$, are produced using a global stiffness matrix updated based on the new orientation of elements and springs at each increment:

$$\{\Delta D\} = [K]^{-1}\{\Delta F\} \tag{3.19}$$

Details on nonlinear analysis and dynamic analysis with the AEM are provided in a later section after preliminaries related to the calculation of stresses and strains are introduced.

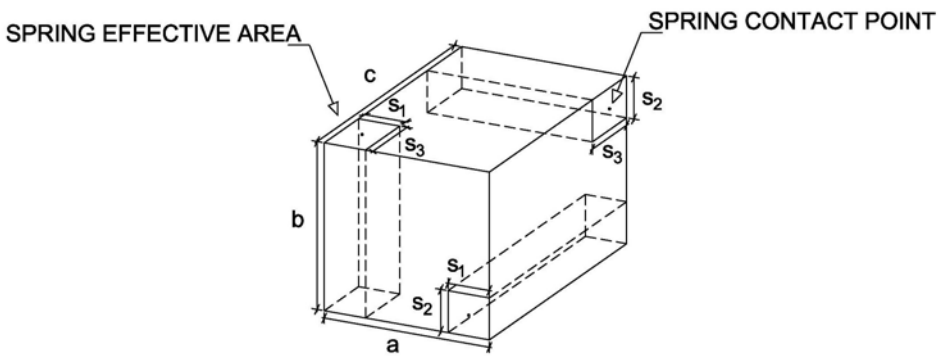

FIGURE 3.8: Effective spring areas on each face of an AEM element

3.1.3 Calculation of Spring Stresses and Strains

Following the calculation of the deformed configuration of the elements in the model in each increment, the stress and strain in each individual interface spring can be calculated. Determination of the spring stress requires that the force in each spring first be determined using the stiffness contribution of each spring in conjunction with the global displacement vector by application of the transformation matrix. This facilitates the calculation of the stress in each spring as the force in the spring divided by the effective area associated with each spring. Since there are only three springs at any spring contact point, only three of the six stress components are determined directly from the forces in the springs. The effective areas associated with individual springs on each element face are illustrated in Figure 3.8. The incremental change in stresses for each individual interface spring is then determined by:

$$\Delta\sigma_i = \frac{\Delta f_i}{s_i s_j} \tag{3.20}$$

$$\Delta\tau_i = \frac{\Delta f_{si}}{s_i s_j} \tag{3.21}$$

$$\Delta\tau_j = \frac{\Delta f_{sj}}{s_i s_j} \tag{3.22}$$

where $\Delta\sigma_i$ is the incremental normal stress in the spring, and $\Delta\tau_i$ and $\Delta\tau_j$ are the incremental shear stress components in the two directions tangent to the element face. The incremental spring force vector, $\{\Delta f_{spring}\}$, can be determined using the relationship:

$$\{\Delta f_{spring}\} = [k_{edge}][B]\{\Delta d_e\} \tag{3.23}$$

For linear elastic materials, normal strains at each spring location, ϵ_n, can be determined using the elastic modulus by:

$$\epsilon_n = \frac{\sigma_n}{E} \tag{3.24}$$

To accommodate nonlinear material constitutive behavior, the incremental strain can be computed from the incremental stress and tangent modulus, E_t, using:

$$\Delta\epsilon_n = \frac{\Delta\sigma_n}{E_t} \tag{3.25}$$

Since springs are only present in the directions normal and tangential to the faces of each element, the complete state of stress is not described by the computed stresses at the spring locations. In order to describe the complete stress state at each spring location and determine principal stresses, it is necessary to interpolate the missing internal stress components from the stresses computed on other faces of the element. An example of the need for the interpolation of internal stress components at a spring location for the case of a two-dimensional element is illustrated in Figure 3.9. For the depicted example, σ_y and τ_{xy} of the top-hand spring can be directly calculated from the spring forces using Equations 3.20 through 3.22. The remaining stress component, σ_x, can then be linearly interpolated from the normal stress components, σ_{x1} and σ_{x2}, associated with springs on the two faces

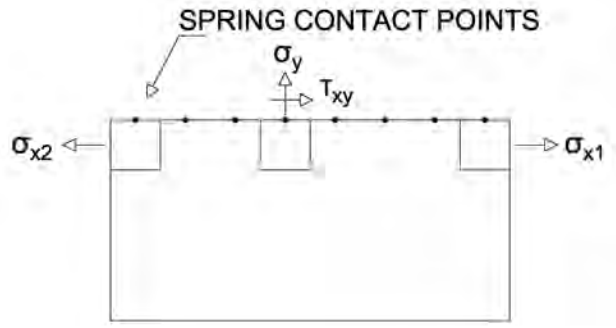

FIGURE 3.9: Interpolation of internal stress components for a two-dimensional element

perpendicular to σ_y through:

$$\sigma_x = \sigma_{x1} + \frac{i - 0.5}{k}(\sigma_{x2} - \sigma_{x1}) \tag{3.26}$$

where σ_{x1} and σ_{x2} are the normal stress components in the springs of the elements on the perpendicular faces, k is the number of springs across the element face parallel to the interpolated stress, and i is the number of the spring at the location where the interpolation is being made. This approach for interpolating missing stress components was detailed in Tagel-Din (1998) and Tagel-Din and Meguro (2000b). The same linear interpolation can be similarly applied to three-dimensional AEM elements with extension to additional stress components, as illustrated in Figure 3.10. In this illustration, σ_x, τ_{xy}, and τ_{xz} are the directly-calculated stress components from the springs at the location of interest, and the remaining stress components, σ_z, σ_y, and τ_{yz}, are determined through linear interpolation of the stresses along the perpendicular faces. After determination of the complete state of stress at each spring location, the principal stresses, σ_p, at each spring location can be determined using principles from continuum mechanics by solving the characteristic

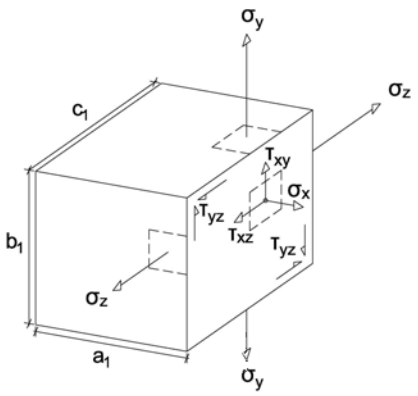

FIGURE 3.10: Interpolation of internal stress components for a three-dimensional element

equation of the stress tensor (Mase et al., 2009):

$$\sigma_p^3 - I\sigma_p^2 + II\sigma_p - III = 0 \tag{3.27}$$

The three stress invariants, I, II, and III, can be computed using the calculated stress components and are defined as (Mase et al., 2009):

$$I = \sigma_x + \sigma_y + \sigma_z \tag{3.28}$$

$$II = \sigma_x\sigma_y + \sigma_y\sigma_z + \sigma_z\sigma_x - \tau_{xy}^2 - \tau_{yz}^2 - \tau_{zx}^2 \tag{3.29}$$

$$III = \sigma_x\sigma_y\sigma_z + 2\tau_{xy}\tau_{yz}\tau_{zx} + \sigma_x\tau_{yz}^2 - \sigma_y\tau_{zx}^2 - \sigma_z\tau_{xy}^2 \tag{3.30}$$

3.2 General Methodology for Nonlinear and Dynamic Analysis

As is typical when predicting deformations beyond small deformation behavior or material behavior beyond the linear elastic range, a nonlinear approach is required when solving nonlinear problems using the AEM (Tagel-Din and Meguro, 2000a). Application of the AEM for nonlinear problems, inclusive of large-deformation analysis and nonlinear material constitutive behavior, was described in Tagel-Din and Meguro (1999) and further demonstrated in Tagel-Din and Meguro (2000a), Tagel-Din and Meguro (2000b), Meguro

and Tagel-Din (2001), and Meguro and Tagel-Din (2002).

The basic formulation of the AEM spring model assumes small, incremental displacements. Consequently, the solution of nonlinear AEM problems necessitates the use of an incremental, dynamic time history analysis. In the incremental approach, the stiffness matrix and the direction of the spring force vectors for the system are reformulated at each increment to capture the nonlinear behavior of the system (Tagel-Din and Meguro, 2000a). The incremental analysis approach to nonlinear problems with the AEM was demonstrated in Tagel-Din and Meguro (2000a) for dynamic, small and large deformation problems, and the effectiveness of the method was verified theoretically through comparison to eigenvalue analysis. The method was verified experimentally in Meguro and Tagel-Din (2001) through comparison of simulations to the results of cyclic load testing of a reinforced concrete structure. Following Tagel-Din and Meguro (1999), the incremental formulation of the dynamic equation of motion for the AEM is:

$$[M]\{\Delta a\} + [C]\{\Delta v\} + [K]\{\Delta u\} = \Delta\{f_{ext}(t)\} + \{R_g\} + \{R_m\} \tag{3.31}$$

where $[M]$ is the mass matrix, $[C]$ is the damping matrix, $\{\Delta f_{ext}(t)\}$ is the incremental, external load vector as a function of time, and Δa, Δv, and Δu are the incremental changes in the acceleration, velocity, and displacement, respectively. $\{R_g\}$ is the residual force vector resulting from geometric changes and can be implemented to simulate the specialized case of large deformation behavior. Likewise, $\{R_m\}$ is the residual force vector resulting from spring removal and can be implemented to simulate nonlinear constitutive behavior. The calculation of the residual force vectors used to simulate nonlinear geometric effects and cracking will be discussed in a later section.

Implementation of Equation 3.31 for solving nonlinear problems requires formulation of the stiffness, mass, and damping matrices. The initial stiffness matrix can be formulated following the methodology described in the previous section. The mass matrix is formulated with the assumption that element mass and moment of inertia are lumped at the element centroids (Tagel-Din and Meguro, 2000a). For cuboid shaped Applied Elements, the lumped mass matrix contribution from each element corresponding to the six degrees of freedom is:

$$[M_{element}] = diag\left(\left[V\rho \quad V\rho \quad V\rho \quad \frac{b^2+c^2}{12}V\rho \quad \frac{a^2+c^2}{12}V\rho \quad \frac{a^2+b^2}{12}\right]\right) \tag{3.32}$$

where V is the volume of the element and ρ is the material density. The damping matrix can be calculated using the Rayleigh method of proportional damping where:

$$[C] = \alpha[M] + \beta[K] \tag{3.33}$$

where α and β are proportionality constants (Tedesco et al., 1999). The mass proportional term introduces damping that is inversely proportional to frequency, while the stiffness proportional term introduces damping that is linearly proportional with frequency. Application of Rayleigh damping with only the mass proportional term was implemented in Tagel-Din and Meguro (2000a), wherein the damping matrix was determined by:

$$[C] = 2\zeta\omega_1[M] \tag{3.34}$$

where ζ is the prescribed damping ratio for the fundamental mode and ω_1 is the first natural frequency of the structure.

It should be noted that for a static nonlinear analysis, the mass and stiffness matrices

are simply set to zero, and the incremental displacement can be solved from the equation of motion (Equation 3.31). For dynamic analyses, it was recommended in Tagel-Din and Meguro (2000a) that Equation 3.31 be solved using the Newmark Beta technique, which facilitates calculation of the incremental acceleration and velocity by:

$$\{\Delta a\} = \frac{1}{\lambda \Delta t^2}\{\Delta d\} - \frac{1}{\lambda \Delta t} v_i - \frac{1}{2\lambda} a_i \tag{3.35}$$

and:

$$\{\Delta v\} = \frac{\gamma}{\lambda \Delta t}\{\Delta d\} - \frac{\gamma}{\lambda} v_i + \Delta t \left(1 - \frac{\gamma}{2\lambda}\right) a_i \tag{3.36}$$

where a_i and v_i are the acceleration and velocity at the beginning of the increment, respectively, Δt is the time increment, and γ and λ are integration parameters that define the assumed variation in acceleration over the timestep (Tedesco et al., 1999). For all analyses conducted in this dissertation, γ and λ were set to $1/2$ and $1/4$, respectively, which yields an unconditionally stable, implicit, and second-order accurate implementation of the Newmark-Beta method.

Substitution of Equation 3.35 and Equation 3.36 into Equation 3.31 yields:

$$\begin{aligned}\left[\frac{1}{\lambda \Delta t^2}[M] + \frac{\gamma}{\lambda \Delta t}[C] + [K]\right]\{\Delta d\} = \Delta\{f_{ext}(t)\} + \{R_m\} + \{R_g\} \\ + \left[\frac{1}{2\lambda}[\mathrm{M}] - \Delta \mathrm{t}\left(1 - \frac{\gamma}{2\lambda}\right)[\mathrm{C}]\right]\{\Delta \mathrm{a}\} \\ + \left[\frac{1}{\lambda \Delta \mathrm{t}}[\mathrm{M}] + \frac{\gamma}{\lambda}[\mathrm{C}]\right]\{\Delta \mathrm{v}\}\end{aligned} \tag{3.37}$$

by which the incremental displacement, $\{\Delta d\}$, can be determined. The incremental spring forces, stresses, and strains can then be solved for using the respective, previously presented Equations 3.20 through 3.26. The stiffness matrix of the system can then be reassembled to account for the calculated orientation of elements, states of stress, and residual force

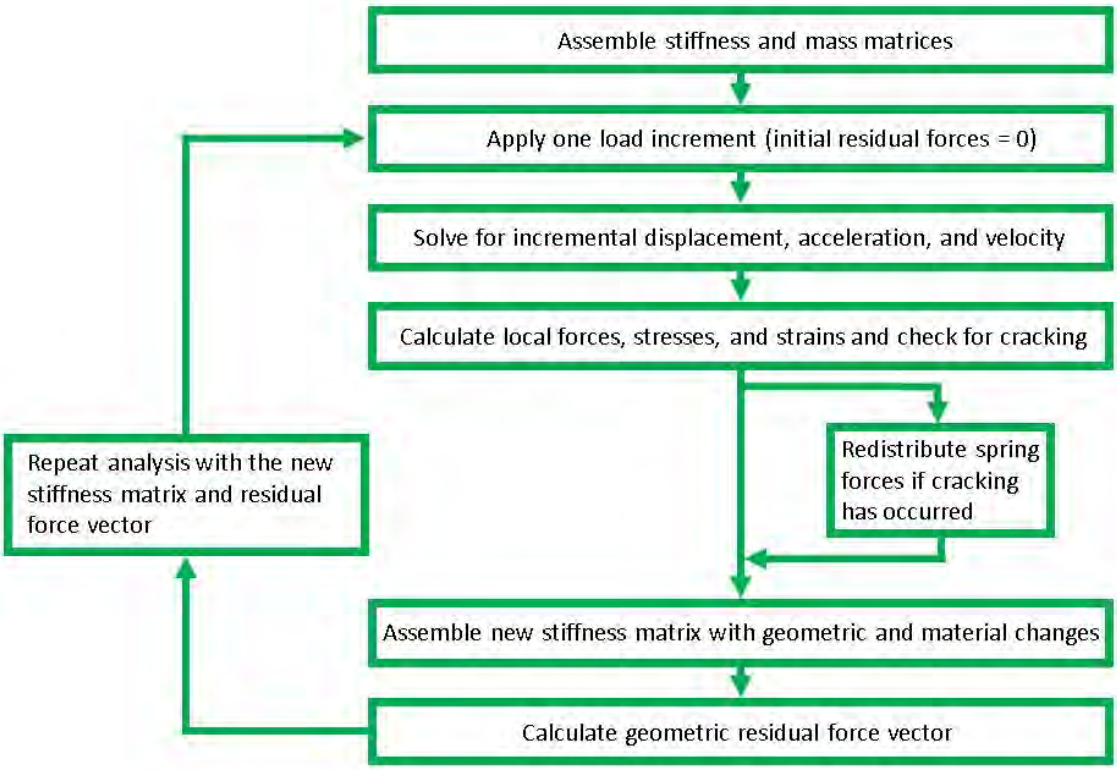

FIGURE 3.11: Summary of the procedure for nonlinear analysis in the AEM

imbalances. As detailed in the following sections, the stiffness matrix assembled in this step is modified to account for specialized cases of nonlinear behavior. After the new stiffness matrix has been assembled, the process can be repeated with application of the subsequent load increment. A flowchart of the process is presented in Figure 3.11.

3.2.1 Nonlinear Geometric Effects

Analysis of large deformation behavior including geometric effects using the AEM was described in Meguro and Tagel-Din (1999) and Tagel-Din and Meguro (2000a). Since large deformation analysis is a specialized case of nonlinear analysis, the previously described procedure is followed with the inclusion of residual forces resulting from imbalance between the force equilibrium on each element in the deformed configuration after each in-

crement. This geometric force residual vector, denoted $\{R_g\}$ in the governing equation of motion, is calculated as the difference between the external force vector and the vectors of internal forces resulting from the applied load increment. Mathematically, the geometric residual force vector is determined by:

$$\{R_g\} = \{f_{ext}\} - \{F_q\} - [M]a - [C]v \tag{3.38}$$

and is calculated after formulation of the stiffness matrix accounting for the incremental displacements (Meguro and Tagel-Din, 1999). The vector of internal forces for each interface spring is calculated by transforming the incremental, global displacements into local coordinates and subsequently substituting the incremental local displacements into the previously introduced Equation 3.19. The interface spring forces are summed over the element for all of the interface springs. Then, the transformation matrix is applied to this vector of local forces to formulate $\{F_q\}$ in global coordinates for each element. The complete $\{F_q\}$ vector incorporates the residual geometric forces over all of the elements in the model.

3.2.2 Nonlinear Constitutive Models

Nonlinear constitutive behavior can be accommodated in the AEM by adjusting the stiffness of individual interface springs during the incremental analysis. Calculation of the stresses and strains at each increment of the analysis facilitates simulation of nonlinear stress-strain response through adjustment of the stiffness of a spring according to the state of strain (Tagel-Din and Meguro, 2000b). Since the stiffness of the spring can be adjusted for the next increment using the state of strain, this method facilitates implementation of various material constitutive laws and can be used to simulate ductile behavior, such as

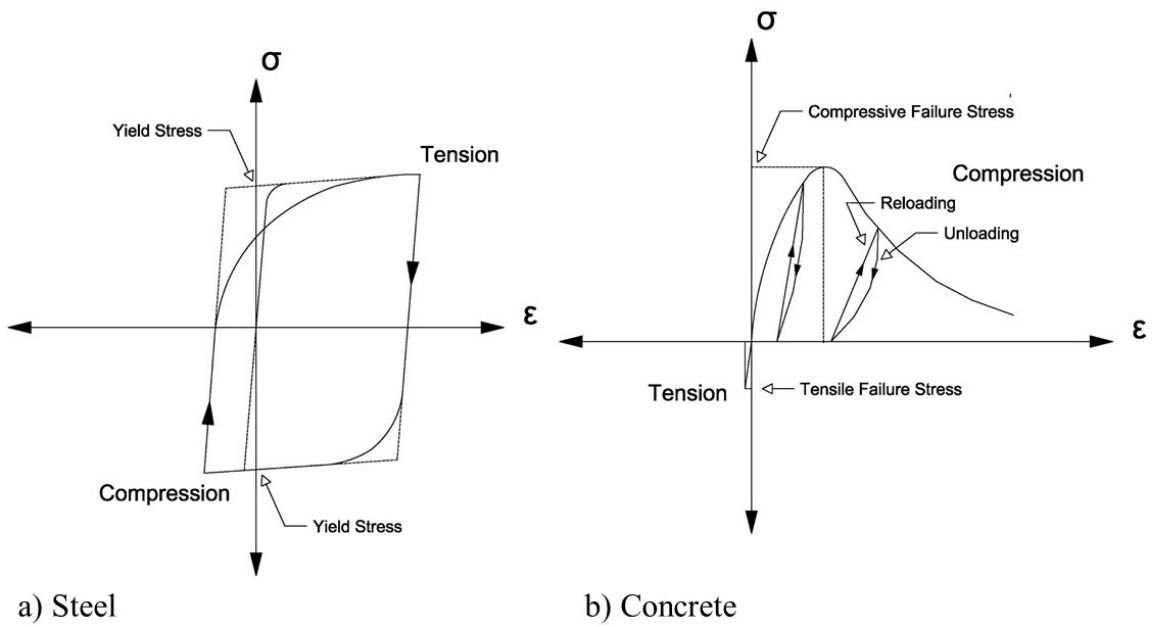

FIGURE 3.12: Material models presented in Meguro and Tagel-Din (2001) by Ristic et al. (1986) and Okamura and Maekawa (1991), respectively

yielding. Models representative of the material constitutive behavior of steel and concrete were adapted from the models presented in Ristic et al. (1986) and Okamura and Maekawa (1991), respectively, in Meguro and Tagel-Din (2001) and are illustrated in Figure 3.12.

Similarly, simulation of brittle failure can be simulated through removal of springs, facilitated through equating the interface spring stiffness to zero when the calculated, tensile principal stresses are found to be in excess of the material failure strength (Tagel-Din and Meguro, 2000b). Meguro and Tagel-Din (2001) implemented a brittle failure model for representation of the shear stress behavior in concrete at failure. This model has been adapted for representation of brittle material failure in this dissertation research and is illustrated in Figure 3.13. The process of modifying the stiffness of the interface spring follows a similar general procedure for brittle failure as detailed for simulation of yielding. However, removal of an interface spring requires redistributing the associated stresses of the removed

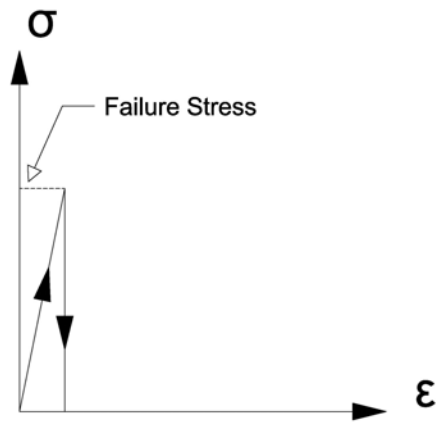

FIGURE 3.13: Stress-strain relationship in an AEM interface spring at failure of a brittle material

interface spring as forces on the elements that were connected by the springs (Tagel-Din and Meguro, 2000b). Redistribution of the interface spring stresses requires calculation of the resultant forces acting on the centroids of the pair of connected elements for each of the twelve degrees of freedom. This is accommodated using the previously introduced Equation 3.14, which implements the deformation-displacement relationship to convert the force at each interface spring to a force at the centroid of the element. Material non-linearities resulting from cracking can therefore be calculated during formulation of the global force matrix, which in turn is implemented into the governing equation of motion.

3.2.3 Element Contact

While fracture is simulated through the removal of interface stiffness springs, collision between elements is simulated through the addition of interface springs at the locations of contact (Tagel-Din and Meguro, 1999). The addition of collision springs at the contact points requires the application of a multi-step process beginning with contact detection between elements and leading into contact modeling to predict the interaction during contact.

Methods of contact detection commonly used with the DEM or FEM can be implemented within the AEM. These methods include the relatively simplistic yet computationally expensive method of individually checking each element for contact with every other element using what is known as a "brute force" algorithm approach (Rojek et al., 2005). One simplified approach for contact detection between Applied Elements was addressed in Tagel-Din and Meguro (1999), wherein the authors applied a geometric coordinates technique to detect element collision. The technique prescribes that the space coordinate of every element be compared in relation to the set model space, which is divided into grids. Contact can then be checked between the element and its neighbor in a manner that is similar to a method commonly used with the DEM (Williams and O'Connor, 1995). It should be noted that when checking for contact, only the distance to element centers was considered, meaning that the authors effectively treated the square or cuboid elements as round or spherical elements with a diameter equal to the element length. It was determined that this method produced accurate results if the element size was minimized (Tagel-Din and Meguro, 1999). An overview of this methodology, including the addition of collision springs, is presented in Figure 3.14.

Following contact detection between elements, the implementation of a contact model is required to accurately model the collision springs. Tagel-Din and Meguro (1999) modeled the normal force in the collision springs using the original normal spring stiffness for the discretized continuum, as determined through Equation 3.1. This methodology parallels a relatively simple method of contact modeling implemented in the DEM. This method predicts contact forces through application of Hooke's Law, originally proposed for use within DEM in Cundall and Strack (1979) through use of the linear force equations given

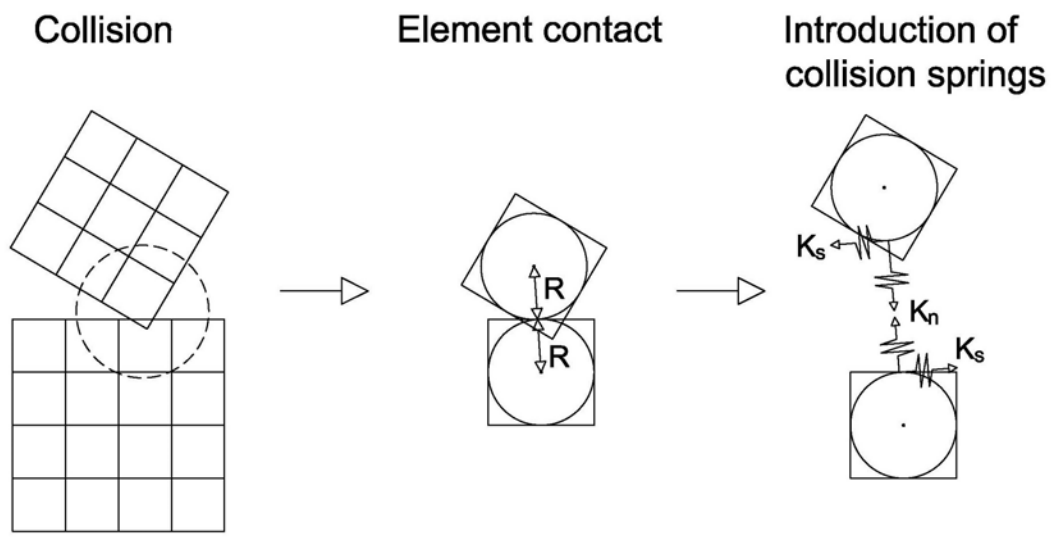

FIGURE 3.14: Representation of the element interaction during collision and subsequent introduction of collision springs following Tagel-Din and Meguro (1999) approach

as:

$$\Delta F_n = K_n \Delta n \tag{3.39}$$

$$\Delta F_s = K_s \Delta s \tag{3.40}$$

where ΔF_n and ΔF_s represent the incremental normal and shear forces, respectively, K_n and K_s are the normal and shear stiffness of the contact spring, respectively, and Δn and Δs are the normal and shear displacements, respectively. In the developed contact model, the stiffness of the contact spring normal to the element centroid was calculated using the previously presented Equation 3.1 for interface spring stiffness. The shear stiffness of the shear collision spring was assumed to be one percent of the calculated stiffness of the normal collision spring (Tagel-Din and Meguro, 1999). It was further assumed that the collision springs were incapable of failing in compression, while being unable to transfer tensile forces. Consequently, the development of any tensile force in the collision spring results in its removal and subsequent element separation during the following time increment. Al-

though compressive failure of the collision spring was not permitted, compressive failure of any existing, continuum, interface springs was allowed.

Energy dissipation during element collision was also addressed in Tagel-Din and Meguro (1999) through modifying the unloading stiffness of collision springs to produce a net energy loss over a contact event. This form of energy dissipation was implemented using a rebound factor, determined as:

$$r = \frac{1}{\sqrt{n}} \tag{3.41}$$

where r represents the rebound factor, and n is the ratio between the loading and unloading stiffness of the collision spring. The difference between the element velocity prior to and after collision is proportional to the rebound factor. As explained in Tagel-Din and Meguro (1999), energy dissipation does not occur if n is equal to one, while all energy is dissipated as n approaches infinity. Using this approach, the necessary unloading stiffness can be determined to accommodate any desired coefficient of restitution.

The methodology proposed in Tagel-Din and Meguro (1999) can be implemented to determine the forces resulting from contact between an element and a fixed plane. This is accomplished using the known displacements and the computed stiffness contribution of the collision spring. The normal stiffness associated with the interface spring is determined by Equation 3.1, while the shear stiffness components are determined by:

$$k_s = \mu k_n \tag{3.42}$$

where μ is the coefficient of friction. This facilitates computation of the stiffness matrix resulting from surface contact in each of the three planar directions. Since the collision

TABLE 3.3: Stiffness matrix of a collision spring contacting an element in the $+x$ direction

k_n	0	0	0	0	0
0	k_{sy}	0	0	0	$\frac{a}{2}k_{sy}$
0	0	k_{sz}	0	$-\frac{a}{2}k_{sz}$	0
0	0	0	0	0	0
0	0	$-\frac{a}{2}k_{sz}$	0	$\frac{a^2}{4}k_{sz}$	0
0	$\frac{a}{2}k_{sx}$	0	0	0	$\frac{a^2}{4}k_{sy}$

TABLE 3.4: Stiffness matrix of a collision spring contacting an element in the $+y$ direction

k_{sx}	0	0	0	0	$\frac{b}{2}k_{sx}$
0	k_n	0	0	0	0
0	0	k_{sz}	$-\frac{b}{2}k_{sz}$	0	0
0	0	$-\frac{b}{2}k_{sz}$	$\frac{b^2}{4}k_{sz}$	0	0
0	0	0	0	0	0
$\frac{b}{2}k_{sx}$	0	0	0	0	$\frac{b^2}{4}k_{sx}$

spring between a fixed plane and an element acts at only one element centroid, this results in a 6x6 stiffness matrix. The element stiffness matrix for collision with a fixed plane in the $+x$ direction is presented in Table 3.3, and the stiffness matrix indicative of collision in the $+y$ direction is presented in Table 3.4. While the same methodology can similarly be implemented to determine the forces resulting from collision with a fixed plane in the $+z$ and $-z$ directions, contact forces in the z direction were not a possibility for the scenarios modeled in this research. This will be discussed further in a later chapter. The computed contact stiffness matrices are implemented for determination of the resultant forces, which are included in the simulation through addition into the residual geometric force vector, $\{F_q\}$. It should be noted that although the full contact stiffness matrix is implemented for determination of the resultant forces, only the stiffness contributions in the normal and shear translational degrees of freedom are added to the global stiffness matrix in their respective degrees of freedom.

It should be noted that more complex, yet often regarded as more effective, methods

of contact modeling in the DEM have been developed using the nonlinear contact theory introduced in Hertz (1882). One such method is the commonly used Hertz-Mindlin contact model developed in Mindlin (1953). It has been postulated that Hertz-based contact models are more theoretically sound at the cost of computational efficiency (Vu-Quoc and Zhang, 1999). Although implementation of such models in the AEM has not been found within the existing literature, the structure of the AEM is such that these methods could be applied if a contact model differing from that implemented in Tagel-Din and Meguro (1999) is desired.

3.3 Implementation of the Applied Element Method

The AEM formulations described in the previous sections have been directly implemented in the MATLAB computing environment to carry out all numerical simulations presented within this dissertation. MATLAB was selected due to its ability to handle relatively large matrix manipulations, high-level programming language, and ability to compile functions and scripts into fast running machine-language instructions. For visualization of the output of simulations, MATLAB subroutines were also developed to translate geometries and results to VTK files that can be read by the popular, open-source Paraview software. The simulation has been developed such that a primary program file, in which the structural geometry, loading, and material properties associated with the simulation are defined, is modified for each different scenario of loading. The primary routine in turn calls multiple generalized subroutines that do not require modification for individual scenarios. The subroutines do not require modification because the values specified for the inputs to the simulation are assigned to named variables, which the AEM routine can subsequently implement across the subroutines. If the value of an input variable has been modified in the

primary routine file, the new variable value will be reflected throughout the subroutines. The general computation procedure followed in the MATLAB routine and supporting subroutines will be discussed in the following sections.

3.3.1 Initialization of the AEM Model

For each simulation performed using the developed MATLAB routine, the structural geometry and mesh discretization must be defined through specification of the cubic dimensions of the model and the number of elements in each of the three planar directions to produce a rectangular prism. The number of interface springs in each direction between element faces must also be specified. Geometry and discretization inputs facilitate construction of an array of uniquely numbered elements and supporting arrays defining the element coordinates in each of the three planar directions. Unique numbering of the elements allows for specifying individual elements or element sets and is critical during subsequent steps, such as assignment of external loading and boundary conditions. If a non-rectangular shaped model, such as a frame, is desired, modification of the geometry is facilitated through specification of the elements to be removed from the element array. Reassignment of the element numbering is automatically performed to reflect the new number of elements and geometric structure. Element numbering further serves as a descriptor of the size of the full stiffness matrix, since the global stiffness matrix prior to partitioning of boundary conditions is equal in size to the total number of degrees of freedom, with six degrees of freedom associated with every element.

Following definition of the model geometry, the connectivity of elements is automatically determined across all surfaces shared by neighboring elements. Specification of the

geometry and number of springs in each element further provides the input required to compile mapping matrices indicating the spatial location of the interface springs throughout the model. Reference to mapping matrices becomes necessary in subsequent calculation of spring stresses and in producing visualization output files for the results. Material properties are defined through specification of the mass density, modulus of elasticity, failure strength, and Poisson's ratio of the material being modeled. Specialized material models, including assignment of a residual stress distribution, can be integrated into the simulation and will be discussed in a later section. It should be noted that the user inputs, such as the material properties, are generalized with respect to units and assume use of consistent units across all properties, as is the case in many commercially available FEM based software packages. The user must therefore keep track of the desired units for each of the input variables.

External loading is prescribed through specification of the element or elements to which the load is to be applied, the degree of freedom in which the load is to act, and the magnitude and direction of the load. Since an external load vector equal in size to the total number of degrees of freedom of the model will be constructed during the simulation, these inputs are simply added into the external load vector in their respective degrees of freedom. Similarly, this allows for specification of any combination of loading acting on the elements, since the loads can simply be superimposed onto one another during construction of the external load vector.

Assignment of boundary conditions is accomplished through specification of the numbered element or elements associated with the degrees of freedom to be constrained. The corresponding degrees of freedom will subsequently be partitioned out of the stiffness,

mass, load, and accompanying matrices after assembly.

3.3.2 Construction of the Stiffness and Mass Matrices

Construction of the stiffness matrix is a relatively computationally expensive component of the simulation and has been developed as a subroutine, since the process follows a uniform procedure using the provided inputs. The subroutine uses the inputs for geometry, mesh discretization, material properties, and element connectivity to calculate the element stiffness matrices of every element pair, which is later used to populate the global stiffness matrix. Assembly of the local stiffness matrices is therefore iterative in that it must be completed for every case of element connectivity in each respective, local face using the formulations specified in Tables 3.1, A.1, and A.2. Because the local stiffness matrix is computed from the contribution of every interface spring, it becomes necessary to construct the contribution to the local stiffness matrix for every spring in the element pair. Computation of the deformation-displacement matrix $[B]$ using Equations 3.12 and 3.13 for each element is also completed during this step. After assembly, the local stiffness matrices can be transformed to global coordinates using the previously introduced Equation 3.17 and subsequently compiled into the global stiffness matrix.

The mass matrix associated with the model is assembled following Equation 3.32, where the element mass, which is calculated using the element volume and mass density, is lumped at the element centroid. This results in a mass matrix of equal dimensions to the global stiffness matrix. Assembly of the mass matrix is completed only once, including for the case of a nonlinear, incremental analysis, since the mass associated with each element does not change. Likewise, the global damping matrix is assembled only once following

Equation 3.33.

3.3.3 AEM Simulation Procedure

Following assembly of the global stiffness, mass, and force matrices, the global displacement vector can be solved. The AEM routine has been written such that displacements are solved incrementally using the Newmark-Beta Method as presented in Equation 3.37. However, for the case of a linear elastic static analysis, the displacement vector is solved in a single step, since nonlinear geometric effects are not considered. Similarly, within static analysis, dynamic effects can be eliminated by nulling the mass and damping matrices. Once the global displacements have been determined, the local displacements at each element can be calculated by application of Equation 3.15. This facilitates determination of element local forces using Equation 3.14. However, as demonstrated in Figure A.1, implementation of this approach further requires assembly of the element stiffness matrix. Reconstruction of the element stiffness matrices with consideration of displacements is therefore performed for all element pairs using Equation 3.10. Calculation of the local stiffness and force matrices facilitates determination of the stress components in each interface spring. Because of the shared variables across these calculations, determination of the element stiffness matrices, local forces, and interface spring stresses are performed in the same subroutine.

If a dynamic or geometrically nonlinear analysis is required, the simulation follows the same general procedure but must be performed incrementally with a user-specified time increment over a specified number of load increments. In the incremental analysis, the first load increment is applied to the external load vector, which can then be used in conjunction

with the initial stiffness matrix to solve for the incremental global displacements. As is the case for a linear elastic static analysis, the global displacements are transformed to local coordinates to determine the local displacements, element forces, and stresses in the interface springs. The element local forces are transformed back to global coordinates using Equation 3.16, and the geometric residual force vector is solved using Equation 3.38. Furthermore, determination of the local displacements facilitates reconstruction of the new global stiffness matrix with inclusion of the new structural geometry through application of the transformation matrix, which is calculated for the new geometry using Equation 3.8. Simulation of material constitutive behavior is also performed during this process, since removal of an individual spring can be performed by omitting the spring from the assembly of the local stiffness matrices. Analysis of the subsequent iteration can then be performed using the new global stiffness matrix, the subsequent load increment, and the calculated geometric residual force vector. The procedure is repeated until the full duration of external loading has been applied or the specified simulation time has been reached.

3.3.4 Output and Visualization of Results

Following calculation of the displacements and stresses across the model, the simulation results are written to an output file that can be imported into the Paraview software package, which is an open source product of Sandia National Laboratories. Paraview offers the benefits of a dedicated visualization program, including fast manipulations of large simulation output for post-processing of results and the ability to apply various, built-in filters to output data. Since displacements are solved at every iteration of the Applied Element simulation, visualization of incremental results is facilitated by writing an output file for

any specified iteration. The output file includes the displaced coordinate of every element corner, which is calculated from the displacement of the element centroid and the element dimensions, and the average magnitude of each stress component at that location, which is computed from the magnitudes of the calculated stress components across the element interface springs. This facilitates mapping of the stress distribution over the corresponding deformed model in Paraview. Since an output file can be written for any iteration, the model can be visualized from its initial state through maximum loading, with a finer time increment corresponding to an increased number of output frames. Because Paraview simply requires the planar coordinates of each element corner, any of the specialized cases of nonlinear behavior, such as large deformation or separation of elements, can be visualized.

3.4 Verification of the Library & Interface

Following development and implementation of the Applied Element Method framework in the MATLAB computing environment, verification of the predictive behavior of the simulator was performed through simulation of several scenarios of structural loading. Scenarios chosen for verification included problems featuring linear elastic behavior, nonlinear geometric and large deformation behavior, brittle failure with material constitutive behavior, and contact. These scenarios were chosen both for their relative ease of comparison to analytical results and because documentation detailing the application of the AEM to these specific problems has been identified in the existing literature. Simulation of problems that had been previously solved using the AEM in the existing literature facilitated further verification of the simulation results through comparison to the literature.

3.4.1 Verification of the AEM Simulator for a Linear Elastic Beam Problem

The first verification was performed to verify the predictive capability of the simulator for small deformation static analysis and stress analysis when applied to exclusively linear elastic problems. The scenario of structural loading was modeled after a problem presented in Meguro and Tagel-Din (2000), wherein a cantilever beam subjected to a point load was modeled to verify the predicted tip deflection and stress distribution. Similar to the identified case study, this problem was simulated using a two-dimensional beam model with a fixed base boundary condition applied to one end. To facilitate comparison of results, dimensions and material properties were kept similar to those used in Meguro and Tagel-Din (2000). The beam was therefore modeled as having a length of 6.0 m (236.22 in), a height of 1.0 m (39.37 in), a thickness of 0.25 m (9.84 in), modulus of elasticity of 840 MPa (121,831.70 psi), and a point load of 10 kN (224.68 lb) acting on the free end parallel to the height of the cross-section. In order to accurately represent the free length of the beam as 6.0 m, the fixed base boundary condition was maintained by restricting the degrees of freedom of an additional row of elements beyond the 6.0 m length. Furthermore, because the degrees of freedom of an AEM element act about the centroid of the element, the modulus of elasticity of the boundary elements was significantly increased relative to the modulus of elasticity of the remaining elements. This simulated the boundary condition occurring at the edge of the element, as opposed to the element centroid, to more faithfully represent the 6.0 m length of the beam. Similar to the identified case study, several different scenarios of square mesh sizes, ranging from a coarse element width of 1.0 m to a fine element width of 0.083 m (39.37 in to 3.28 in), were implemented to examine the effects of mesh discretiza-

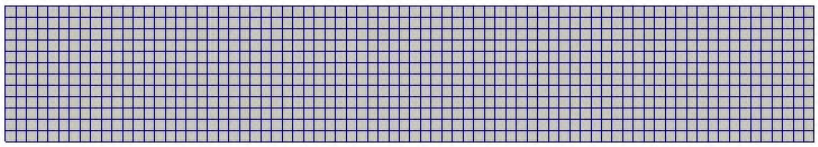

FIGURE 3.15: Paraview rendering of the fine mesh cantilever beam model used for verification of small deformation behavior

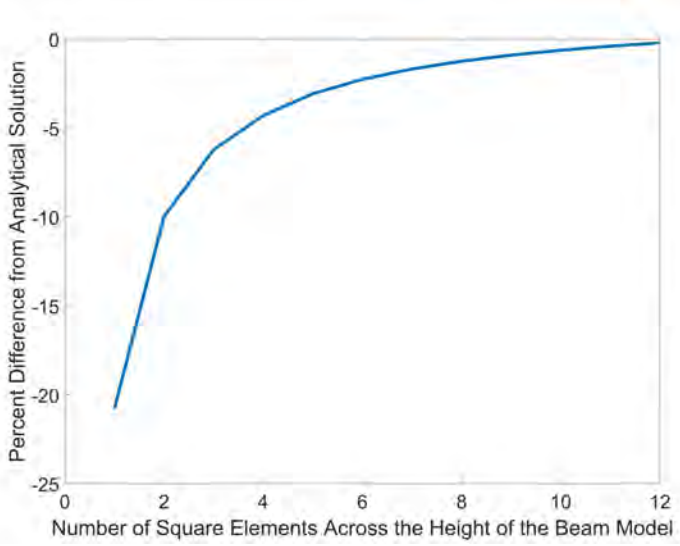

FIGURE 3.16: Percent difference between the analytical and AEM predicted deflection of a cantilever beam over varying mesh sizes

tion on the accuracy of the solution. In all cases, ten interface springs were implemented in each local direction between elements. A Paraview rendering of the cantilever beam model featuring the smallest mesh size (0.083 m) is presented in Figure 3.15.

The predicted end deflections of the beam using the varying mesh sizes were compared to the deflection predicted analytically by Euler-Bernoulli beam theory. The percent difference calculated for each mesh size is plotted in Figure 3.16 to illustrate the convergence of the solution. It can be seen that the relatively coarse mesh sizes significantly underpredicted the deflection, while convergence of the solution with the decreasing mesh size is apparent.

The magnitude of the normal and shear stresses through the thickness of the beam were

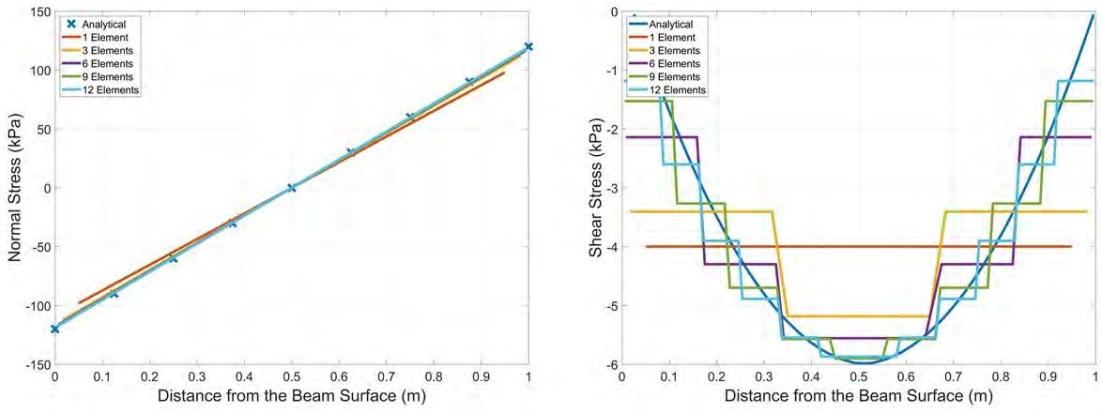

a) Normal stress b) Shear stress

FIGURE 3.17: Predicted normal and shear stresses through the thickness of the cantilever beam

also evaluated at a distance of 1.0 m from the fixed boundary by inspecting the stress in each spring through the beam thickness. Comparison of the normal and shear stresses reveals strong correlation to the analytical solution when an adequately fine mesh size is implemented. This is demonstrated in Figure 3.17, wherein the AEM predicted normal and shear stresses through the thickness of the beam are plotted over varying mesh sizes in comparison to the Euler-Bernoulli analytical solutions. It can be seen that, for both normal and shear stress, the predicted stress converges toward the analytical solution relatively quickly. However, it should be noted that a finer mesh is required for accurate prediction of shear stresses, due to the parabolic nature of the shear stress distribution. Lastly, the predicted distributions of the stress components across the beam for the finest mesh case are plotted in Figure 3.18. For the given loading scenario, the stress components are predicted according to expectations.

Comparison of the AEM predicted results to the analytical solutions indicate that the AEM has been successfully implemented for small deformation, linear elastic analyses.

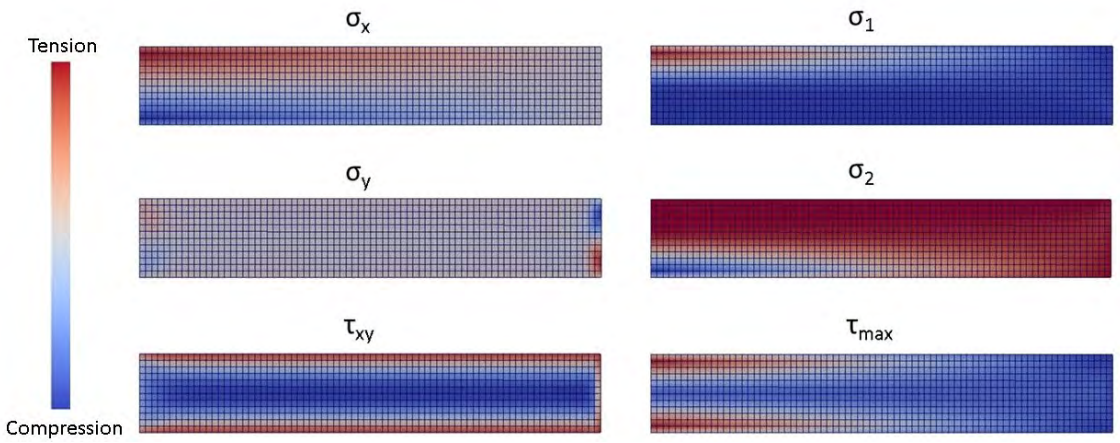

FIGURE 3.18: AEM predicted stress distribution through a cantilever beam subjected to a point load

Accurate prediction of normal and shear stress distribution has been demonstrated. Furthermore, the importance of mesh discretization has been examined through convergence of the predicted displacement at the free end of the beam.

3.4.2 Verification of the AEM Simulator for Dynamic, Large Deformation Analysis of Rigid Body Structures

The second problem implemented for verification of the AEM simulator was modeled after a dynamic simulation presented in Tagel-Din and Meguro (2000a) for verification of the AEM for problems featuring rigid body motion of structural members. The problem was modeled to predict the harmonic motion of an L-shaped structure, as depicted in the Paraview rendering in Figure 3.19, supported by a hinge at one end. The L-shape was modeled with a length and height of 12.0 m (472.44 in) and uniformly sized 1.0 m x 1.0 m (39.37 in x 39.37 in) square elements. The boundary conditions of the problem were applied as a hinge, which restrained only the translational degrees of freedom, to the uppermost element of the L-shape to allow rotation about the hinge. A density of 7,849.0

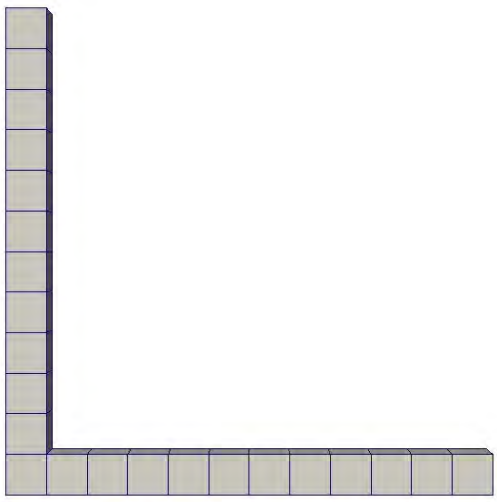

FIGURE 3.19: Paraview rendering of the L-bar model used for verification of the rigid body dynamic behavior of the AEM simulator

kg/m^3 (490 lb/ft^3), structural damping ratio of 0.04, and constant gravity of 9.81 m/s (32.2 ft/s^2) were applied to the L-shape, which was allowed to rotate from its starting position and oscillate about the boundary condition element until reaching its equilibrium position. Progressive renderings in Paraview of the L-shape starting at rest and oscillating about the hinge element are presented in Figure 3.20. An analytical solution for the displacement of the L-bar with respect to time was developed by implementing the equation for harmonic, single degree of freedom displacement, $x(t)$, determined by:

$$x(t) = [A_{Lbar} cos(w_d t) + B_{Lbar} sin(w_d t)]\, e^{-\zeta w_n t} \tag{3.43}$$

where w_n and w_d are the undamped and damped natural frequencies of the fundamental mode, respectively, ζ is the damping ratio, and t is the time increment (Tedesco et al., 1999). A_{Lbar} and B_{Lbar} are determined by the initial conditions, where A_{Lbar} is taken as the

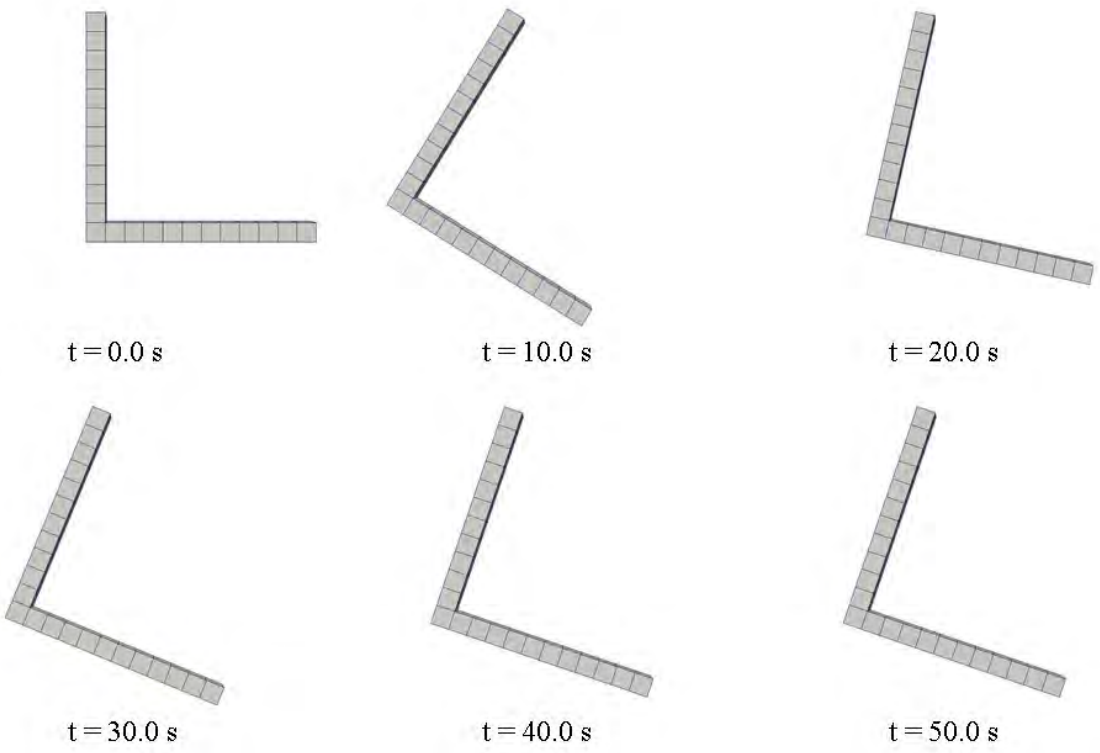

FIGURE 3.20: Paraview rendering of the oscillating L-bar

initial displacement, x_0, and B_{Lar} is determined by:

$$B_{Lbar} = \frac{v_0 + x_0 \zeta w_n}{w_d} \tag{3.44}$$

where v_0 is the initial velocity of zero.

A comparison between the predicted harmonic motion of the L-shape and the analytical solution of the problem is presented in Figure 3.21, depicting the time history of the predicted and analytical rotations of the boundary condition element over time. Strong correlation between the AEM predicted results and the analytical solution were observed, indicating that large displacement dynamic analysis has been successfully implemented in the incremental analysis.

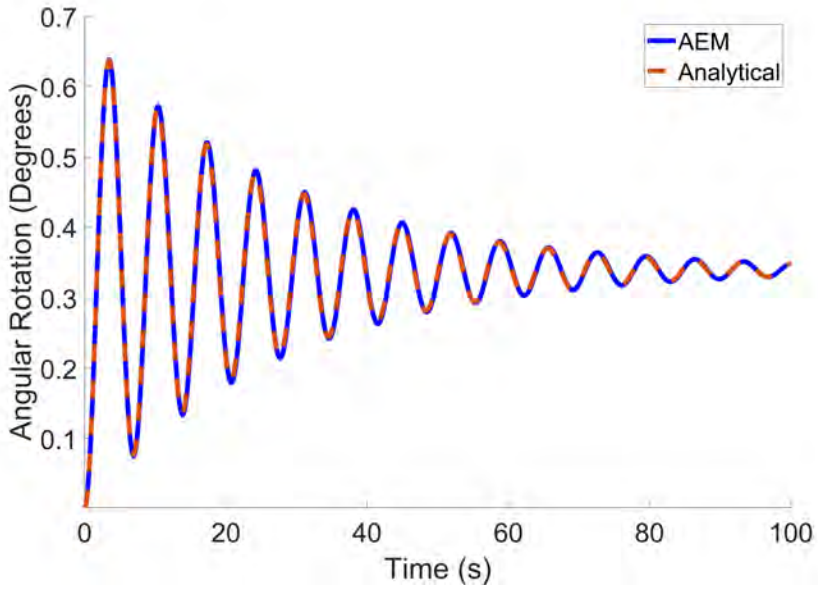

FIGURE 3.21: Comparison between the AEM predicted rotation of the L-bar and the analytical solution

3.4.3 Verification of the AEM Simulator for Large Deformation Static Analysis

The problem serving as the third analytical verification of the AEM simulator was modeled similarly to a large deformation static analysis problem presented in Meguro and Tagel-Din (2002). The two dimensional problem simulated the large deformation of a simply supported beam subjected to a point load at its midspan and was used to verify the predictive accuracy of the AEM simulator for determining displacements and stress distributions following the development of large deformations. The beam was modeled with a total length of 12.0 m (472.44 in) and a 1.0 m (39.37 in) square cross-section. The beam was discretized using 0.2 m x 0.2 m (7.87 in x 7.87 in) elements. The boundary conditions of the model were applied to the exterior elements along the bottom row of the element array, with one element being fixed in translation and free in rotation, while the opposing element was fixed in only the vertical, translational degree of freedom to represent a pin

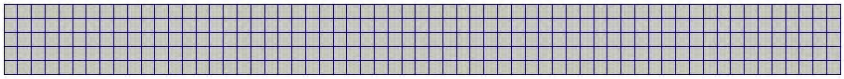

FIGURE 3.22: Paraview rendering of the simply supported beam used for verification of the large deformation behavior of the AEM simulator

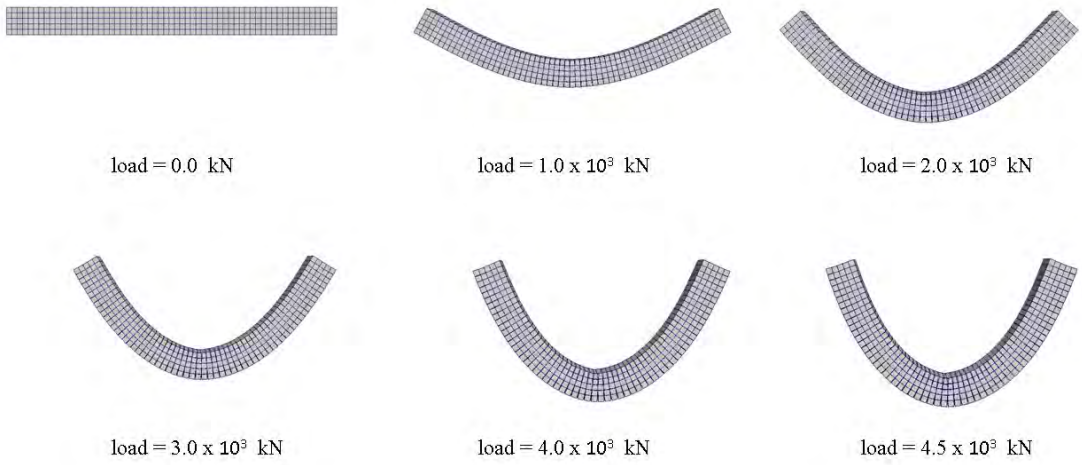

FIGURE 3.23: Paraview rendering of the AEM predicted large deformation behavior of the simply supported beam

and a roller restraint, respectively. A Paraview rendering of the undeformed model is presented in Figure 3.22. The material properties were assigned similar to those presented in Meguro and Tagel-Din (2002) to facilitate comparison between the AEM predicted results and the results presented in the case study. The model was assigned an elastic modulus of 210 MPa (30,457.9 psi), and an incrementally increasing point load was applied at the midspan of the beam. Renderings in Paraview of the predicted deformation of the beam under the increasing load are presented in Figure 3.23. The large deformation behavior of the model is clearly visible as the beam deforms in an arched shape, and the end of the

beam featuring the roller boundary condition moves inward toward the load, while the end featuring the hinged boundary remains fixed in the lateral direction. The arched shape of the deformed beam is indicative of the increasing stiffness of the beam under loading and shows strong correlation to the deformed shape presented in Meguro and Tagel-Din (2002).

For further verification of the predicted load-displacement behavior and for comparison of the stress distribution in the AEM simulation, the same problem was modeled using the FEM in the commercially available Abaqus software package. The beam was modeled in Abaqus using solid C3D8 brick elements with a uniform mesh size of 10.0 cm (3.93 in), while the geometry and material properties assigned to the model were consistent with the those implemented in the AEM model. It should be noted that, because of the difference in how boundary conditions are assigned in the FEM when compared to the AEM, the mesh discretization implemented in the FE model was significantly finer than in the AEM model. Because boundary conditions are applied about the centroid of Applied Elements and about the nodes of Finite Elements, accurate comparison of displacement results required meshing of the FE model in such a way that the boundary nodes were located in the same spatial location as the centroids of the boundary elements in the AEM model. This was similarly true for application of the point load, which was applied to the central Applied Element. The point load in the FE model was distributed over the nodes of the uppermost central elements, resulting in two rows of point loading across the element nodes at midspan. Progressive renderings of the discretized FE model under the increasing point load at midspan are presented in Figure 3.24, and it is evident that the predicted large deformation behavior of the beam correlates with the large displacement behavior predicted by the AEM model.

The AEM and FEM predicted behavior of the simply supported beam under loading was

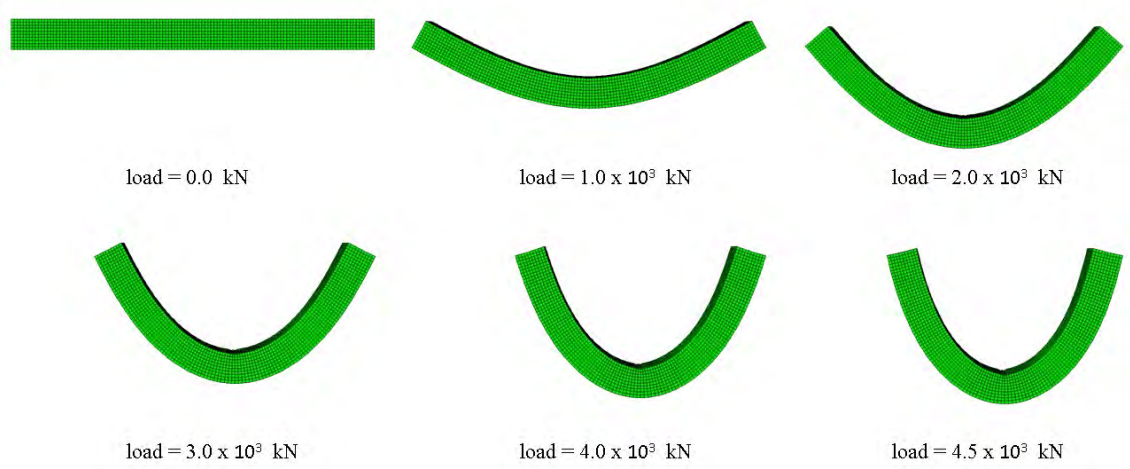

FIGURE 3.24: Progressive renderings of the FEM predicted large deformation of the simply supported beam

further examined through comparison of the load-displacement behavior of the models in the vertical and horizontal degrees of freedom. The vertical displacement at the midspan of the beam, corresponding to the peak vertical displacement, and the horizontal displacement at the roller boundary condition, corresponding to the element centroid in the AEM and the element node in the FEM, were plotted in relation to the applied load at each increment to form load-displacement curves for both translational degrees of freedom. The predicted load-displacement curves of both the AEM and FE models are presented in Figure 3.25 and again indicate the increasing stiffness of the models as the point load increases. Although some variation is evident between the AEM and FEM predicted load-displacement curves, specifically under higher magnitude loading, both models predicted similarly shaped load-displacement curves. Furthermore, the AEM predicted load-displacement curves show strong correlation with the load-displacement curves presented for the similar problem in

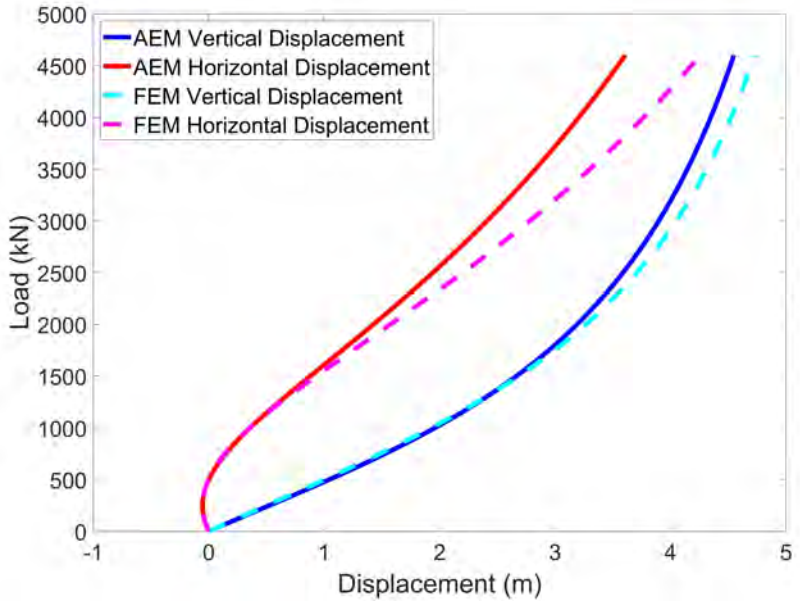

FIGURE 3.25: AEM predicted vertical and lateral displacement of the simply supported beam

Meguro and Tagel-Din (2002). It should be noted that, although distortion control was implemented in Abaqus, some level of local element deformation did occur in the FE simulation, while inclusion of local deformation effects was not considered in the AEM model. This could potentially result in discrepancies in the load-displacement behavior of the two models, especially at extreme levels of large displacement nonlinearity.

The results of the AEM simulation were further verified through comparison of the predicted stress distribution across the model during large deformation to the stress distribution predicted by the FE model. For this comparison, the principal stress corresponding to the longitudinal axis was evaluated. The principal stress distribution across the deformed shape of each model corresponding to a point load magnitude of 4,500 kN (1,012,000 lb) is plotted in Figure 3.26. Comparison of the AEM and FEM renderings indicate strong correlation between the predicted principal stress distributions. Furthermore, the magnitude of

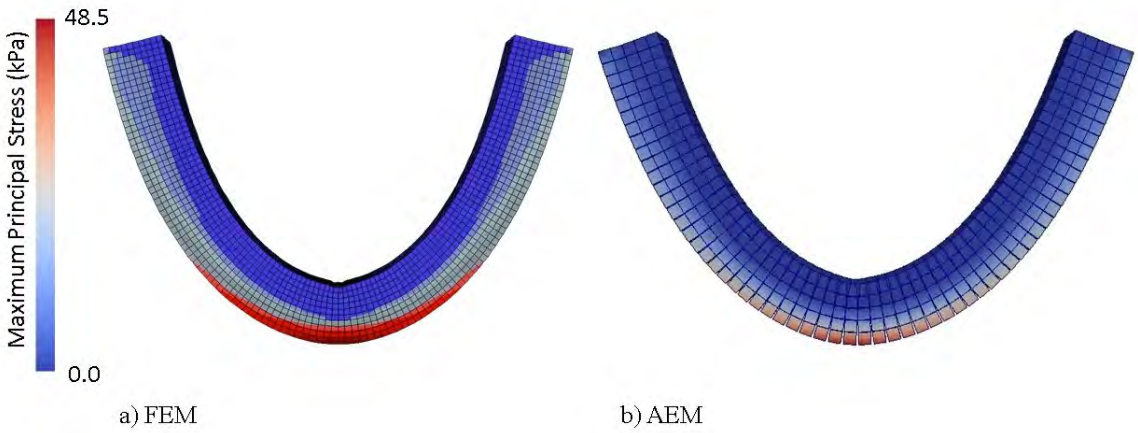

FIGURE 3.26: Predicted principal stress distributions across the FEM and AEM simply supported beam models

the peak principal stress in the bottom extreme fiber of the beam at 4500 kN point loading was predicted to be 48.5 Mpa (7,035.3 psi) and 48.2 Mpa (6,995.0 psi) by the AEM and FE models, respectively, reflecting a 0.6% difference in the AEM predicted peak principal stress when compared to the FE model prediction.

Comparison of the AEM generated results to those found in the literature and to the similar FE model indicate that prediction of large deformation geometric behavior has been successfully implemented in the AEM simulation. Strong correlation between AEM and FEM models has been demonstrated for vertical and horizontal deflected shapes, load-displacement responses, principal stress distribution, and principal stress magnitude.

3.4.4 Verification of Spring Removal and Force Redistribution in the AEM Simulator for Prediction of Brittle Failure

The purpose of the fourth verification was to verify the behavior of the AEM simulator when applied to problems involving element separation through implementation of a brittle failure model. The problem for this verification was modeled similarly to a simulation

presented in Tagel-Din and Meguro (2000a) of a two dimensional beam subjected to a point load at its midspan for the purpose of verifying the element separation and post failure behavior of the model. The beam was modeled as having a square cross section of 1.0 m (39.37 in), a total length of 10.0 m (393.71 in), and a uniform mesh of 0.2 m x 0.2 m (7.87 in x 7.87 in) sized elements. The boundary conditions of the model were assigned to the bottommost element at each end of the beam and assigned the restraints of roller boundaries, which restrained the elements from vertical translation, while allowing rotation and lateral translation.

Assignment of identical roller boundaries to both ends of the beam ensured symmetry of the model about the point load, which was applied to the uppermost, central element. This discretization and application of the central point load was similar to the methodology presented in Tagel-Din and Meguro (2000a), wherein the beam was discretized into an odd number of elements to maintain symmetry about the central column of elements subjected to loading. As in Tagel-Din and Meguro (2000a), material properties representative of concrete, specifically a modulus of elasticity of 2,100 kN/cm^2 (3,045.8 ksi) and tensile failure stress of 0.2 kN/cm^2 (290.1 psi) were assigned to the model. A density of 2,402.8 kg/m^3 (150 pcf) was assigned to the elements, and constant gravity was applied at 9.81 m/s^2 (32.2 ft/s^2) to simulate dynamic motion of the beam after failure. Progressive renderings in Paraview depicting the incremental failure of the brittle beam model, beginning at the time of initial failure and progressing through complete separation into independent segments of elements, are presented in Figure 3.27.

It is demonstrated that the AEM simulation predicts separation on both sides of the central column of elements subjected to loading. This results in symmetric rotation of the

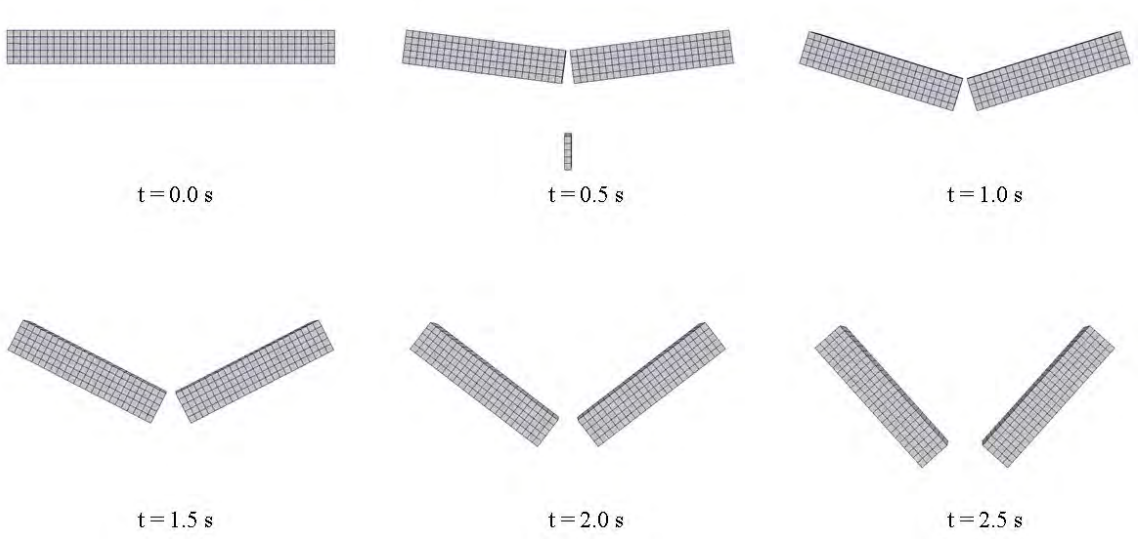

FIGURE 3.27: Progressive renderings of the AEM brittle beam model through failure and element separation under point loading

remaining elements about their respective boundaries as the central column of elements displaces vertically. Symmetry is maintained through failure of the beam and post-failure dynamic behavior, indicating that spring removal and force redistribution is being modeled symmetrically. This predicted failure behavior, in which the beam separates into three independent segments of elements, shows strong correlation to the results presented in Tagel-Din and Meguro (2000a) and indicates that spring removal and force redistribution have been successfully implemented in the AEM simulation.

3.4.5 Verification of the Surface Contact Model in the AEM

The final verification was performed to verify the surface contact behavior and coefficient of restitution model for prediction of contact forces between an element and a fixed planar surface. The problem was modeled to predict the displacement and velocity over time of a single, falling element as it impacts and rebounds from a planar surface. The element for this problem was assigned 4.6 mm (0.1875 in) cubic dimensions, a mass density

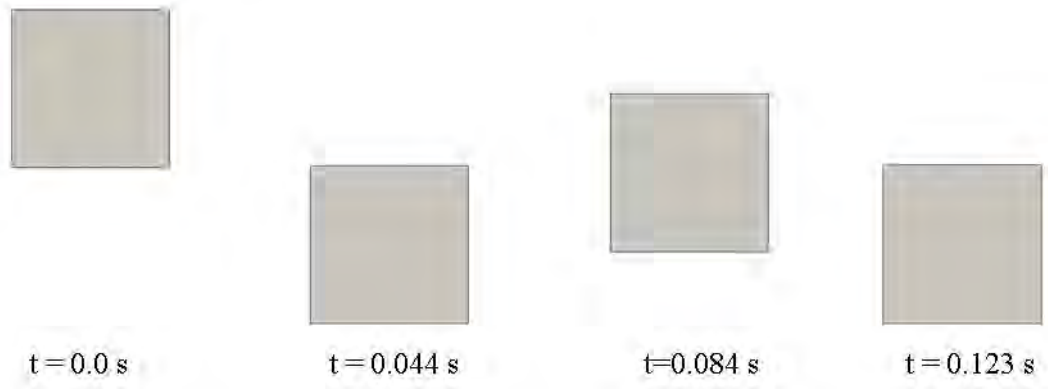

FIGURE 3.28: Paraview rendering of a single AEM element falling under gravity and rebounding with a coefficient of restitution of 0.9

of 7,857.24 kg/m^3 (490 lb/ft^3), a modulus of elasticity of 200 GPa (29,000 ksi), and a coefficient of restitution of 0.9. The element was assigned an initial height over the fixed plane of twice the element size, an initial velocity of zero, and constant gravity of 9.81 m/s^2 (32.2 ft/s^2). The rebounding behavior of the single element is demonstrated through progressive renderings in Paraview as the element falls and rises with respect to time. This behavior is further demonstrated in Figure 3.29 through plotting of the displacement and velocity of the element in the vertical direction, which demonstrates the diminishing magnitude of the rebound displacement. Examination of the peak velocity of the element as it falls and rebounds indicates that the magnitude of each peak occurs at 90% of the velocity of the preceding peak, which corresponds to the assigned coefficient of restitution.

It is therefore demonstrated that the method of energy dissipation proposed in Tagel-Din and Meguro (1999) has been successfully implemented. It should further be noted that Tagel-Din and Meguro (1999) stated that the energy dissipation can also be simulated through implementation of a rebound factor that relates the relative velocity of the element before and after collision. However, although this method was noted as being simple to

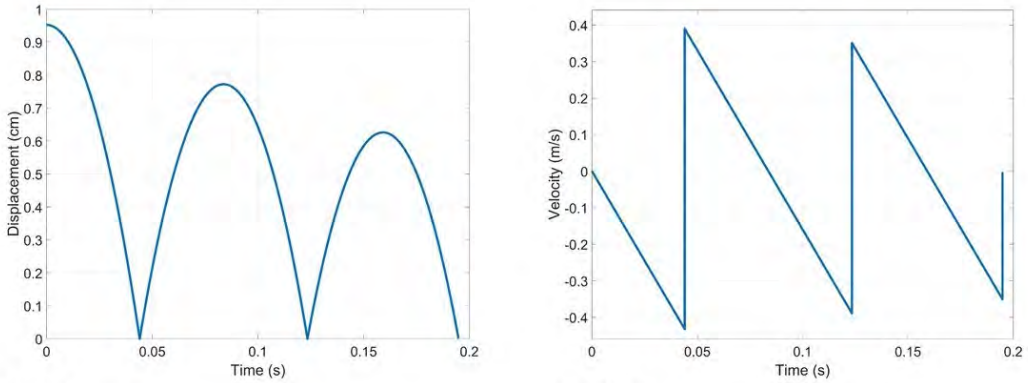

a) Displacement b) Velocity

FIGURE 3.29: Displacement and velocity of the falling and rebounding AEM element

implement, it was also determined to require a smaller timestep throughout the simulation, while the method proposed in Tagel-Din and Meguro (1999) only requires implementation of a small timestep during contact. Use of the element relative velocity reflects similarity to the methodology described for use with the DEM in Cundall and Strack (1979), which recommends application of a damping force determined by the element relative velocity. However, a further motivation for using the described method, as opposed to the damping force method regularly employed in the DEM, is the challenge of relating the damping force to the coefficient of restitution. As demonstrated, this has been accomplished without requiring determination of a proportional damping force.

3.5 Case Studies of Blast Simulation using the AEM

It has been demonstrated that the AEM is capable of modeling linear elastic problems while also being able to replicate complex nonlinearities such as material yielding and failure, element separation, and element collision (Meguro and Tagel-Din, 2000), (Meguro and Tagel-Din, 2001), (Tagel-Din and Meguro, 1999). As will be shown through examination of several case studies, these characteristics underscore the suitability of the AEM for blast

analysis problems.

The effectiveness of the AEM for prediction of both blast analysis and progressive collapse behavior was evaluated in Tagel-Din (2009) through comparison to case studies and simulations completed using the commercially available FEM software LS-Dyna. Using the only commercially available AEM software package, Extreme Loading for Structures (ELS), the author completed AEM analyses of 22 tests, including nine walls and two columns subjected to blast loading and 11 case studies of progressive collapse scenarios. It is noteworthy that in all cases the author followed a blind numerical test approach to provide an unbiased evaluation of the predictive fidelity of the AEM. The author determined that the AEM produced reliable results for all blast and collapse scenarios, finding that the AEM compared favorably with results predicted using LS-Dyna for the blast analyses. It was further noted that the AEM and FEM predicted similar behavior for nonlinear problems in which collapse did not occur. The author concluded that the report demonstrated and validated the reliability of the AEM for prediction of structural behavior under blast loading and during collapse, while also highlighting the efficiency of the AEM when compared to FEM simulations of the same problem.

The AEM had previously been implemented by the same author in Tagel-Din and Rahman (2006) to simulate the collapse of the Alfred P. Murrah Federal Building following the April 1995 bombing. Blast pressures and the subsequent progressive collapse were simulated in the commercial ELS software, where the authors initially simulated the actual event, modeling the problem using 10,000 three-dimensional elements. Following verification of the initial simulation results, the authors performed two “what if” analyses. One “what if” analysis was for the case of a different blast epicenter, while the second “what if”

analysis simulated reinforcement of the transfer girder, which was a critical component that experienced failure and has been considered responsible for the catastrophic collapse. The authors concluded that the simulation of the actual event accurately predicted the collapse shape, elapsed time required for the transfer girder to reach the ground following failure, and the total time required for full collapse.

The AEM was utilized in Asprone et al. (2010) to examine the behavior of a glass fiber reinforced polymer (GFRP) barrier, consisting of GFRP pipes mounted vertically in a reinforced concrete base, subjected to blast loading. The objective of the research was to examine the effectiveness of GFRP barriers for withstanding blast loading. The study involved experimental tests supported by numerical simulations conducted using the AEM. The authors performed the experimental testing using three separate barrier specimens subjected to 5 kg of quarry-grade TNT at variable standoff distances. Instrumentation during the tests included strain gauges, accelerometers, and pressure gauges. The AEM simulations of the events were performed using the commercial ELS software and exhibited good predictive fidelity relative to the experimental blast tests. The authors determined that the analytical model predicted similar accelerations and wall strains. However, comparison of the accelerations indicated a more damped response in the experimental testing when compared to models using an assumed damping ratio that was considered to be reasonable. The authors speculated that this was due to the sensitivity of the lightweight GFRP pipes to air friction following the main shock. It is noteworthy that the mode of structural failure observed in the experiments was correctly predicted by the simulation.

Steel framing systems under blast loading were evaluated by Coffield and Adeli (2014) using the commercial ELS implementation of the AEM. The authors noted that the local

behavior of structural components under blast loading is evaluated more frequently than the behavior of an entire structure. Therefore, the motivation for the research was accurate numerical modeling of a complete, 10 story, five bay, steel structure designed according to conventional design guidance and standards. Three different designs of the same structure were considered and subjected to numerical blast loading, with each design featuring a different means of resisting lateral forces, including a moment resisting frame, a concentrically braced frame, and an eccentrically braced frame. By examining the formation of plastic hinges in the models during blast loading, the authors determined that the braced framing systems most effectively mitigated the blast loads. Likely due to the scale of simulations, the case study did not feature a comparison to experimental results.

The AEM was applied to simulate the nonlinear response of a masonry infill wall subjected to blast loading in Kernicky et al. (2014). Although structural identification and damage characterization were the main focuses of the research, the authors simulated the blast event using ELS to support the plausibility of their conclusions. The experimentally tested wall was modeled using three dimensional Applied Elements representative of the mortar, grout, and steel present in the wall system, while the blast parameters for the simulated blast wave were calibrated to optimally agree with experimentally recorded blast pressures. Although strong agreement was observed in the experimental and predicted reflected pressure across the majority of the sensor locations, the authors did note discrepancies in the reflected pressures across two sensor locations. This was attributed to a difference in elevation of these sensors and to the limitation in ELS that the charge be modeled as spherical, as opposed to the cylindrical charge used for experimental testing. It was notably determined that the ELS software identified a location for the onset of cracking

in the mortar and further damage resulting from impact between a masonry block and steel angle that were consistent with the results obtained from the nondestructive evaluation. The authors also noted a reasonably strong correlation between the experimentally measured, post-blast modal characteristics of the structure and those predicted analytically through the AEM.

Largely because of the difficulties associated with the FEM when modeling collapse and element separation, the AEM was investigated by Keys and Clubley (2013) as a means for predicting debris field formation of masonry panels subjected to blast loading. The authors conducted two experimental blast tests of masonry wall panels. The testing included five identical panels subjected to blast loading from a hemispherical, high-explosive charge as well as testing of a single panel using an air blast tunnel to apply equivalent blast overpressures. Free field pressure transducers, a free field pressure gage, and high-speed cameras were employed to record experimental data during testing, while post-blast data collection included debris field measurements to provide a basis for comparison with analytical results from numerical simulations. The computational modeling was completed using ELS for the structural analysis in conjunction with the computational fluid dynamics software Air3D for predicting overpressure time histories corresponding to the experimental charges. The authors found that, following refinements of the modeling routine, the simulation was capable of predicting debris field formation showing strong correlation to the experimental tests. The research focused on the failure pattern and debris field distribution, and although some discrepancies were identified, it was concluded that accurate results were predicted for both phenomena. The authors extended this research in Keys and Clubley (2017) with AEM simulations of additional masonry wall panel tests. Over the course of two experi-

mental, high-explosive blast tests, the authors subjected a total of nine masonry wall panels to blast loading. The panels were organized spatially to simulate the typical orientation and distribution of the walls in a conventional building. Blast pressures and debris field distribution were measured for both tests. The authors determined that the reflected pressures predicted using the built-in blast wave modeling feature of the ELS software overestimated the experimentally observed overpressures for this problem. To correct this discrepancy, the authors again used the Air3D software to externally generate reflected pressure time histories that were prescribed in the ELS model. The authors concluded that the numerical models produced generally good agreement with the experimental results, yielding accurate predictions for both crack formation and debris field distribution. It was further noted that in one case the AEM correctly predicted initial breakage, temporary equilibrium, and subsequent, slow collapse of a panel, thereby demonstrating the success of the AEM for simulation of problems involving temporary but unstable equilibrium.

Collectively, case studies from the published literature demonstrate successful implementation of the AEM for simulation of structural response to blast loading, notably predicting element separation and progressive collapse. Of particular interest to this research effort, case studies demonstrating the effectiveness of the AEM for modeling debris field formation and the failure behavior of glass have also been performed and have demonstrated the capability of the AEM for simulating pre-failure, failure, and post-failure behavior involving element separation in the same analysis. Examination of these case studies, coupled with the developmental history and function of the AEM, serve to demonstrate the suitability of the method to motivation and objectives of the dissertation research.

CHAPTER 4: EXPERIMENTAL TESTING

Validation of the AEM based blast simulation tool required extensive experimental testing to build databases for comparison and validation of simulation results. The primary experimental database consists of six open-arena blast tests conducted with a facade wall containing glass lite specimens and a debris containment enclosure. This field experimentation includes dynamic characterization of each glass lite specimen, measurement of blast overpressures, observation of lite fracture, and documentation of the debris field formation. Static uniform load characterization of a nominally identical glass lite specimen was also performed in the laboratory to complement the field data and provide a means for calibrating the numerical models and assessing their ability to predict the fracture behavior under static loading conditions. Lastly, laboratory testing was performed to characterize the behavior of rubber gaskets used in the lite supporting framework to support the assignment of boundary conditions to numerical models of the glass lites.

4.1 Open-Arena Blast Testing Program

A key objective of open-arena blast testing was to create an experiment representative of an actual, non-accidental blast event that could affect a conventional structure featuring a typical facade front. Replication of such a scenario was achieved by constructing a small, single story structure outfitted with a fenestration system consisting of six nominally identical glass lite specimens. A series of six open-arena blast tests was conducted with

varying explosive charge weight, composition, and epicenter, and extensive field measurements were collected to characterize the dynamic properties of the lite specimens, record the explosive yield of the test charges, and collect post-blast data on glass fragmentation and debris fields. The design of the experimental test program, testing protocols, instrumentation, and results are detailed in this section.

4.1.1 Test Structure and Specimens

The development of an experimental database for validating the Applied Element modeling and assessing experimental techniques for post-blast forensic investigation supported by computational simulation was performed through open-arena blast testing conducted on a fenestration system designed to replicate a frontal facade often found on commercial structures. This required the design and fabrication of a full-scale test structure featuring a glass lite specimen supporting framework capable of being subjected to repeated blast loading. The resulting test structure, developed specifically for this research, is displayed in Figure 4.1. As detailed in this section, the structure was purpose-built for experimental blast testing with unique features incorporated to facilitate data collection, while retaining many of the features of a conventional fenestration system.

The test structure featured a conventional glazing system with glass lite specimens supported by aluminum mullions. The facade system used for this experimentation featured two rows of three openings for a total of six glass lite specimens. Each set of six tempered glass lites subjected to blast testing featured conventional monolithic, tempered glass measuring 80.0 cm by 121.9 cm (31.5 in by 48.0 in) with a thickness of 4.8 mm (0.1875 in). The rear surface of the glass lites were supported by the aluminum mullions to which

a) Frontal view b) Oblique view

FIGURE 4.1: Photographs of the test structure featuring a facade front outfitted with glass lite specimens

aluminum pressure plates were joined by number 10 screws with 3.5 cm (1.375 in) thread length spaced 7.62 cm (3 inches) on center. All screws in this assembly were torqued to 9.6 N-m (85 in-lbs) using a calibrated torque wrench prior to each test. Typical of a conventional facade system, both the mullions supporting the rear surface of the glass lite specimens and the pressure plates supporting the frontal surface of the specimens featured rubber gaskets for prevention of glass-metal contact and assurance of the seal between the components of the system. A cross-section view of the connectivity of the glass lites to the supporting mullions around each edge of the lite is provided in Figure 4.2.

The fenestration system required structural hardening to ensure that the mullions could be repeatedly used over the course of the blast experimentation without replacing costly components. To provide structural resiliency, a steel frame consisting of welded HSS10x2x$\frac{1}{4}$ steel sections was included in the test structure. The steel frame was located directly behind each mullion with the mullions secured to the tubular frame using countersunk screws.

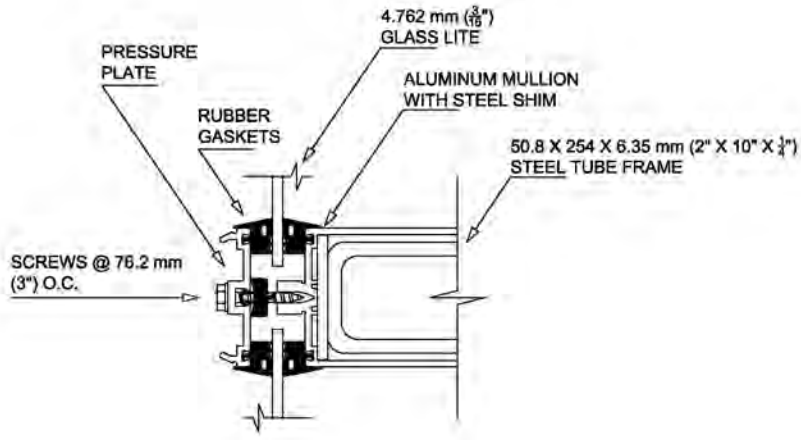

FIGURE 4.2: Side-view of the connected fenestration system components

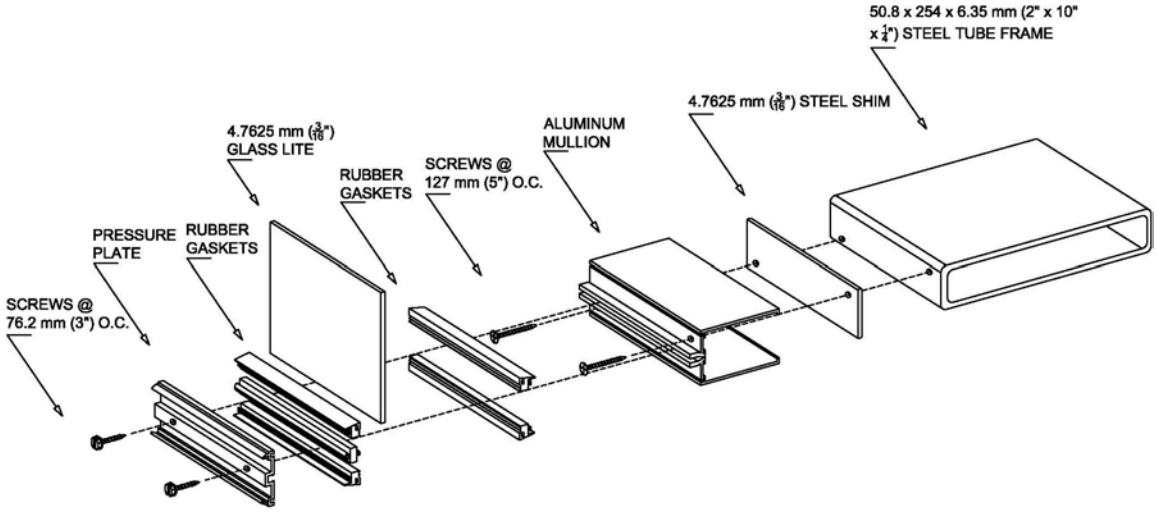

FIGURE 4.3: Method of connectivity for mounting of glass lite specimens

The full assembly supporting each glass lite is depicted in an exploded view in Figure 4.3, which illustrates a volumetric slice of the facade framework from the exterior pressure plate to the steel framing. The assembled facade framework was subsequently bolted to a steel reaction frame comprised of W14x30 columns and 20.32 cm x 20.32 cm x 0.64 cm (8 in x 8 in x 1/4 in) tube strut diagonal braces welded to a strong foundation. The steel reaction frame serves to support the assembled facade framework and fully transfers the blast loads from the facade to a heavily reinforced concrete slab foundation.

Since a critical aspect of this research is evaluating the use of debris field measurements for post-blast forensics, it was further necessary to develop a system for containment of glass fragments generated during the blast test. This was achieved by enclosing a 3.66 meter (12 ft) by 3.05 meter (10 ft) plan area of the concrete slab directly behind the reaction frame using a timber framed structure. The 3 m depth of the room created by the structure was selected to comply with ASTM Standard F1642-12 that is used to evaluate hazards of glazing systems under airblast loadings (ASTM, 2017). An elevation view drawing of the enclosure is presented in Figure 4.4. To ensure that the structure could withstand the full set of blast tests and maintain structural integrity for the entire duration of the test program, the enclosure was constructed using pressure treated 10.2 cm x 10.2 cm (4 in x 4 in) nominal wood studs spaced 40.6 cm (16 in) on center, lateral blocking between studs, and 1.1 cm (7/16 in) plywood sheathing on both interior and exterior wall surfaces, thus exceeding the typical requirements for conventional wood structures. In order to minimize the potential for blast overpressures wrapping around the facade and loading the rear of the lites, high-strength silicone sealant was applied to the seam between the enclosure and the reaction frame, thus minimizing the potential for infiltration of the pressure wave. Access into the timber structure for setup of the tests and post-blast data collection was facilitated by an access door located on one of the two side walls.

4.1.2 Experimental Setup for Debris Field Measurements

Since post-blast measurement of debris fields is a key component of this research, methods were employed to determine the post-blast debris field distribution both within the test enclosure and in the area in front of the glass lites. Notably, with the exception of the first

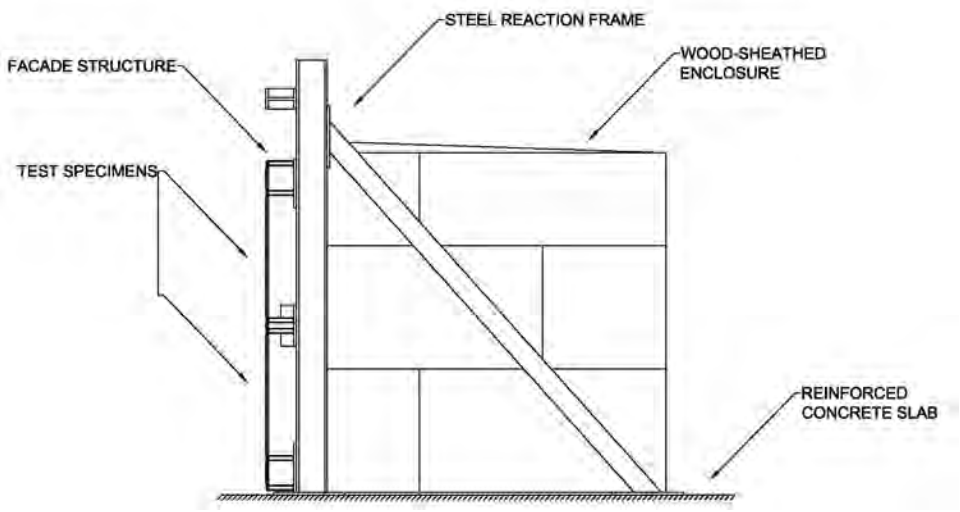

FIGURE 4.4: Elevation view schematic of the facade structure with the attached enclosure

of the six tests, a thin layer of spray paint was applied to the lites. The purpose of the paint was to provide a means of visually differentiating the fragmented lites in the post-blast debris field. No paint was used for the first test to evaluate the performance of 3D scanning technologies on vision glass, while the remaining cases served representative of spandrel glass.

Post-blast characterization of the fragmented glass distribution within the enclosure was facilitated through discretization of the concrete slab directly behind the glass lite specimens into a uniform grid pattern spanning the entirety of the enclosure floor. This allowed for mapping of the distribution of the glass debris through collecting and measuring the mass of the glass fragments within each individual cell of the grid following each blast test. The grid lines were uniformly spaced at 101.6 cm (40 in) lengthwise and 81.3 cm (32 in) across the width to form a 3x3 grid. An adhesive tape was used to demark the grid lines. Glass debris was collected using a wet/dry shop vacuum to carefully acquire debris from the area of each cell. The contents of the vacuum were transferred to plastic buckets, and

the contents were weighed in the laboratory.

A witness panel, located opposite the glass lites, was employed to capture flying debris fragments reaching the rear wall of the enclosure during each blast test. The witness panel was constructed in accordance with ASTM F1642-17 and featured a two layer foam surface backed by 1.1 cm (7/16 in) thick plywood sheathing. The rear layer was constructed of 25 mm (1 in) thick expanded polystrene foam board, while the front layer was constructed of 12.5 mm (0.5 in) thick polyisocyanurate rigid foam insulation with a reflective aluminum facing reinforced with kraft paper and oriented toward the inside of the enclosure. This created a surface into which glass fragments could embed upon impact, allowing for subsequent tracking of the impact location of high-velocity fragments. In accordance with ASTM F1642-17, fragments embedded into the witness panel at a height of 50 cm (20 in) or greater from the floor of the enclosure are classified as "high-hazard" (HH), while those embedded below 50 cm are classified as "moderate-hazard" (MH). Debris on the floor at a distance greater than 1.0 m (40 in) from the rear face of the glazing is classified as "low-hazard" (LH), while glass debris at a distance less than 1.0 m or falling on the suction side of the glazing is classified as "very low-hazard" (VLH). Application of this classification of hazard zones to the test enclosure is illustrated in Figure 4.5. Since each blast test resulted in glass debris being embedded in the witness panel, all witness panels were replaced between tests. This ensured that any embedded debris was a result of the current blast test and not residual debris from the prior test. Photographs of the witness panel and the adhesive tape used to discretize the floor in the enclosure for post blast measurement of debris within the enclosure are shown in Figure 4.6. Discretization of the floor in the enclosure is illustrated in Figure 4.7 with labels assigned to the cells in the grid. Debris

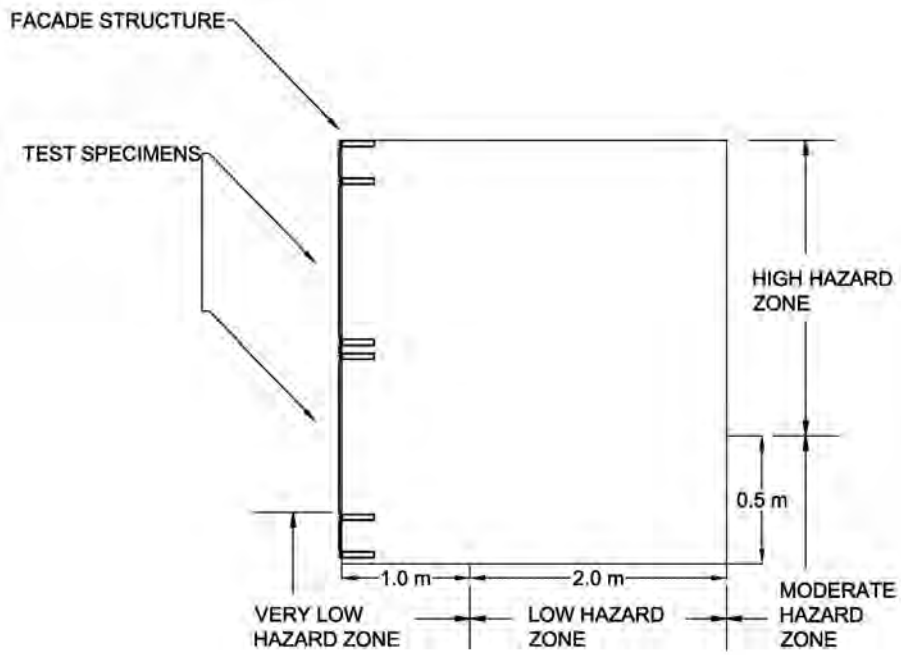

FIGURE 4.5: Classification of debris hazard zones in accordance with ASTM F1642-17

field formation following each blast test was further evaluated volumetrically through the use of a LiDAR scanning system. LiDAR scanning was performed using a Faro Focus 3D x 130 LiDAR Laser Scanner with a camera resolution of 165 megapixels. LiDAR scanning of the interior debris field was performed following each blast test and provided a means of characterizing the debris field beyond mapping the mass of the debris. LiDAR scanning was also performed outside of the enclosure, but the identification of the glass debris outside of the enclosure was generally precluded due to grass and other debris generated from the explosive casing and charge stand. A photograph of the LiDAR scanning system deployed for scanning of the interior of the enclosure is shown in Figure 4.8.

Fragmentation behavior was further evaluated using a regular speed camera located within the enclosure facing the glass lites and a high-speed Phantom V4.3 camera located approximately 73.2 m (240 ft) from the exterior of the glass lites. The regular speed camera

a) Witness panel b) Discretization for debris field mapping

FIGURE 4.6: Witness panel and discretization of the enclosure floor for debris field mapping

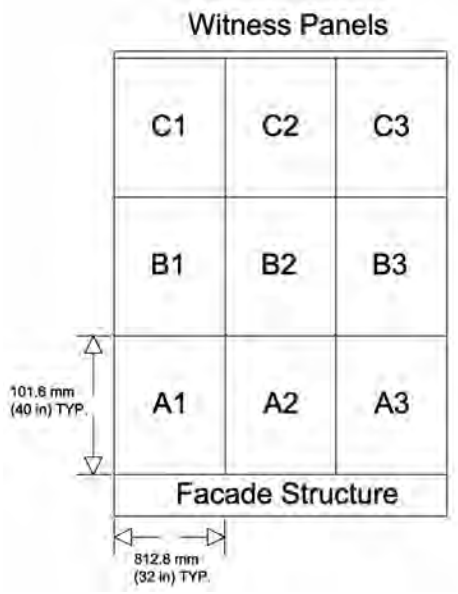

FIGURE 4.7: Discretization and notation of the enclosure floor for debris field mapping

acquired 640 x 480 pixel resolution images at a 30 frame per second (fps) rate. The high speed camera was deployed at a frame rate of between 8,113 and 8,146 fps with a resolution ranging from 128 x 512 to 256 x 256 pixels. The exact camera settings used for each test are presented in Table B.1. The objective of using the regular speed camera was to observe the fragmentation of glass during the tests, while the high-speed camera was used to capture the moment of failure of the glass lites to facilitate determination of the time of failure relative to the time of charge detonation.

FIGURE 4.8: Deployment of the LiDAR scanning system to the interior debris field

4.1.3 Instrumentation for Blast Overpressure Measurements

In order to characterize the explosive yield of each charge used and to provide a measure of the overpressure distribution across the facade, instrumentation for reflected and incident pressure measurements were incorporated into the test setup. Due to the inherent differences between reflected and incident pressure loading, these measurements required the simultaneous use of two different sensor systems. Incident pressure measurements are typically used to experimentally determine the explosive yield, which is necessary in order to establish a TNT equivalent charge weight for each test as an input to the simulations. Reflected pressure time histories serve to validate the distributions of reflected pressures predicted by the numerical codes.

An array of nine flush mount pressure sensors mounted along the face of the facade system was employed to measure the reflected pressures throughout testing. Flush mount pressure sensors were PCB Piezotronics model 102 units, which are piezoelectric trans-

a) Not Mounted b) Mounted – Front c) Mounted – Back

FIGURE 4.9: Typical installation of a flush mount pressure sensor in the facade

ducers with full-scale measurement ranges from 34.5 MPa (5,000 psi) to 69.0 MPa (10,000 psi), depending on the exact model. The specifications for each individual sensor used in the experimental test setup are presented in Appendix B.2. The pressure sensors were mounted in three rows across the bottom, middle, and top of the facade, resulting in the placement of a sensor directly beneath and above each lite specimen. This allowed for measurement of the reflected pressure in locations covering the spatial area around each of the six glass lite specimens. These sensors were mounted in threaded holes prepared in 6.4 mm (0.25 in) thick aluminum plates secured to the facade framework in the same manner as the glass lites. To further ensure similarity between the recorded pressures and those acting upon the glass lite specimens, flush mount pressure sensors were mounted such that the sensor surfaces were even with the glass lite specimens. Photographs of in-field deployment of the reflected pressure transducers are shown in Figure 4.9. A dimensioned schematic of the placement of the reflected pressure transducers in the facade is provided in Figure 4.10 along with shorthand notation used to denote each sensor.

Measurement of the incident blast overpressure was facilitated through the use of two nominally identical, free-air pencil probes positioned at the same elevation as the charge. These pressure transducers were PCB Piezotronics model 137A21 units that feature a full-

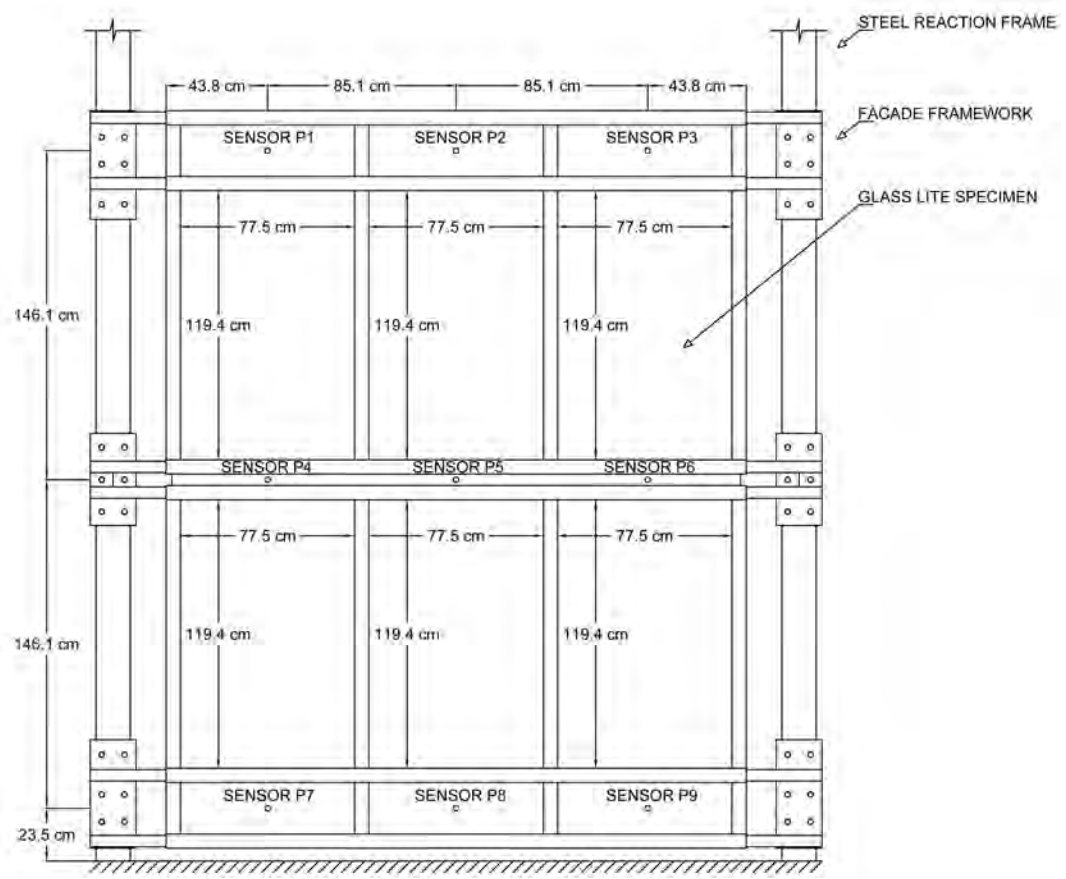

FIGURE 4.10: Locations of reflected pressure transducers

scale range of 34.5 MPa (5,000 psi). The specifications of these pressure transducers are included in Table B.2. Contrary to the flush-mount pressure sensors, which were configured with the active sensing diaphragm either normal to or oblique to the propagation of the blast wave to record the reflected overpressure, each free-air pencil probe features a cylindrical body with a conical tip, such that the pressure wave is minimally disturbed by the pressure of the transducer. The active sensing element is located in the body of the transducer and oriented to measure side-on pressure parallel to the incoming blast wave. A photograph of one of these transducers positioned in the field is provided in Figure 4.11. Each incident pressure transducer was supported by an articulating arm support that permitted the eleva-

FIGURE 4.11: Typical installation of a free-air pencil probe to capture incident overpressures

tion and orientation of the transducer to be adjusted. The standoff distances between each incident pressure transducer and the charge varied based on the charge composition and mass and are documented in the test data sheets provided in Appendix B. A photograph of the complete array of free-air incident pressure and reflected pressure sensors immediately prior to testing is presented in Figure 4.12. All sensors were connected via 304.8 m (1,000 ft) RG-58 coaxial cables to a single data acquisition (DAQ) system located at an approximate 50 m (164 ft) distance from the charge so as to be isolated from effects of the blast wave and ground shock. The DAQ used for all open-arena blast tests was a National Instruments model PXIe-1082 controlled with PXIe-4497 dynamic signal analyzer modules. The PXIe-4497 provides 24-bit resolution simultaneous sampling, 4 mA constant current excitation for the Integrated Electronics piezoelectric transducers, and AC coupling to remove the bias voltage from these transducers. Data collection from all sensors during each test was performed at a sampling rate of 204.8 kHz and was pretriggered by the output from the reflected pressure transducer P5. Use of a pressure-activated trigger removed the potential for premature collection of data that could overrun the data buffers and provided a means for concurrently and automatically pretriggering the high-speed video captures.

FIGURE 4.12: Photograph of typical array of blast overpressure transducers

4.1.4 In-Situ Modal Analysis of Lites

Non-destructive, experimental characterization of the dynamic properties of the glass lite specimens was facilitated through experimental modal analysis conducted prior to each blast test. Due to the likely variance in the stiffness of the rubber gaskets in the facade assembly with changes in ambient temperature, modal analysis of each set of panels was always performed on the same day and immediately prior to blast testing. This ensured that the characterization of boundary conditions for each set of glass lites through the dynamic properties would remain valid for conditions under blast loading. The experimental modal analysis was performed using a roving impulse hammer and stationary array of two reference accelerometers. The reference accelerometers were temporarily adhered to the lite using hot glue and oriented to measure out-of-plane motion in each lite. Both sensors were

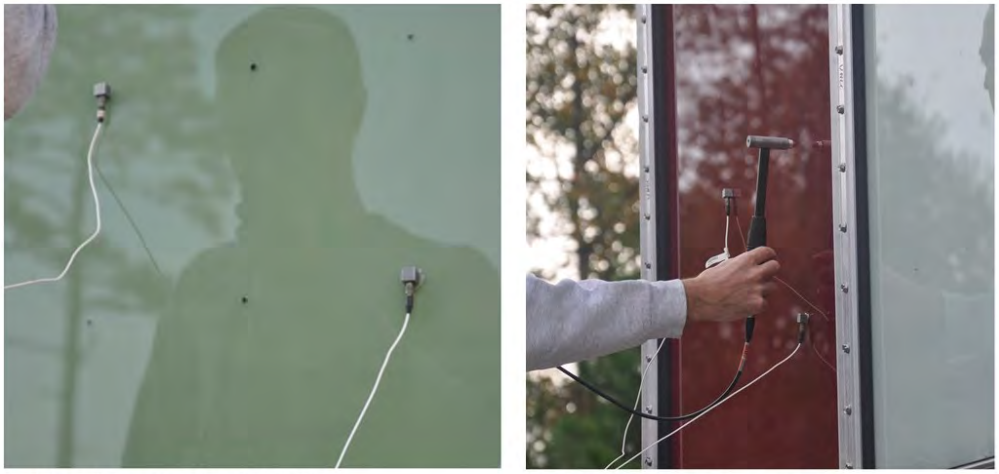

a) Accelerometers bonded to lite b) Roving impulse hammer testing

FIGURE 4.13: In-situ modal analysis of the glass lite specimens

PCB Piezotronics model 333B52 accelerometers that feature a 5 g measurement range and 0.5 to 3,000 Hz frequency range. The impulse hammer used for all modal testing was a PCB Piezotronics model 0860C03 impulse hammer with a measurement range of 2,224 N (500 lbf) and sensitivity of 2.25 mV/N (10 mV/lbf). The accelerometers and impulse hammer were interfaced to the same PXIe-4497 dynamic signal analyzers previously described. Impulse response measurements were obtained with a 5 kHz sampling rate and were pretriggered using the impulse hammer signal. Impulses were applied to each glass lite specimen over a uniformly spaced rectangular grid of 16 locations, configured as four rows of points spaced 23.6 cm (9.3 in) vertically and 15.2 cm (6 in) horizontally. Marking of impulse locations was completed for all tests using a template to ensure uniformity in the modal analysis of all glass lite specimens. Five impulses were applied at each location for averaging of the modal parameter estimates. An example of the vibration testing performed in the field is presented in Figure 4.13. The vibration testing was performed to obtain experimental modal parameter estimates, specifically the natural frequencies, mode shapes, and

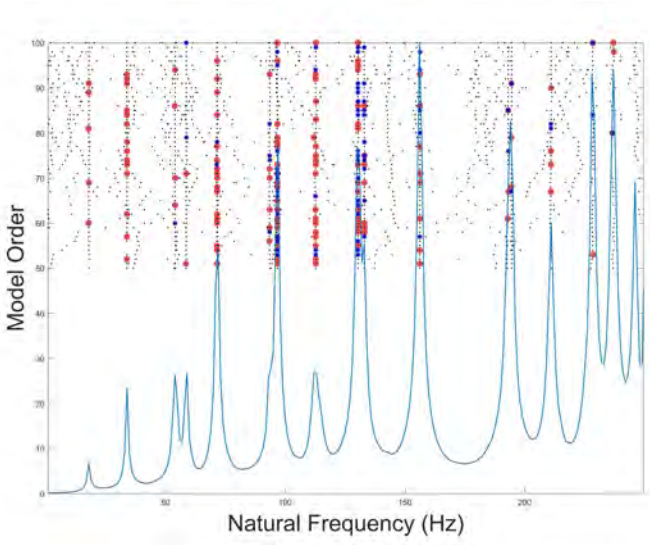

FIGURE 4.14: Typical stabilization diagram with average frequency response function shown in background

damping ratios of each lite. The combined deterministic-stochastic subspace state-space identification algorithm, developed as a robust version of N4SID (numerical algorithms for subspace state space system identification) algorithm, proposed in Van Overschee and De Moor (1996) was applied to the measurement data to obtain these estimates. The system identification algorithm was implemented in the MATLAB computing environment, and experimental modal parameters were obtained by regression over a range of model orders from which a stabilization diagram was used to identify stable poles. A percent variation of 1.0 was used for the stabilization criterion for identification of stable poles for frequency, damping, and mode shape. Figure 4.14 presents a representative stabilization diagram with the frequency response function shown in the background to further aid in the selection of stable poles. Five stable poles from different model orders were averaged to develop the experimental estimate for each natural frequency, damping ratio, and mode shape. Since mode shapes are nondimensional vectors rather than scalar values, the averaging process

required mode matching and scaling prior to averaging to ensure that no single pole biased or corrupted the average. Consistency of the mode shapes used in the averaging process was ensured through application of the modal assurance criterion (MAC), calculated across groups of similar modal parameter estimates. The MAC is calculated as:

$$MAC = \frac{|[\phi_j][\phi_i]^T|^2}{([\phi_j][\phi_j]^T)([\phi_i][\phi_i]^T)} \tag{4.1}$$

where ϕ_j is the reference mode shape, and ϕ_i is the mode shape being compared to the reference (Ewins, 1984). A higher MAC value indicates greater correlation between modes, with the MAC value between two identical modes being 1.0. For all cases of mode averaging, a minimum MAC value of 0.85 was ensured prior to averaging, where modes reflecting a MAC value of less than 0.85 were not considered as estimates of the same mode.

After ensuring consistency in the mode matching process through comparison of MAC values, natural frequencies and relative damping factors could be directly averaged across estimates. However, since mode shapes are nondimensional and of arbitrary scale and phase, it was necessary to normalize the estimates prior to averaging. This was accomplished through application of a Modal Scale Factor, calculated as:

$$MSF = \frac{[\phi_j]^T[\phi_i]}{[\phi_i]^T[\phi_i]} \tag{4.2}$$

where ϕ_j is the reference mode to which the corresponding mode shapes are normalized to, and ϕ_i is the subsequent mode subject to normalization (Allemang, 2003). The product of ϕ_i and the Modal Scale Factor corrects the relative phase and amplitude of the mode shape to be consistent with the reflected mode.

Since two reference accelerometers were implemented during the vibration testing, this

process was completed individually for both sensors and resulted in two sets of modal parameter estimates per lite. The quality of the modal parameter estimates from each reference accelerometer is affected by the proximity of the sensor to nodal lines in each mode, so some of the mode shapes were identified by only one of the two accelerometers. For the remaining cases where estimates for the same mode were identified by both sensors, simple averaging was used to arrive at the final experimental estimates for the modal parameters of each lite. The estimated natural frequencies and damping ratios for each individual lite are presented in Appendix Table B.3 and Table B.4, respectively. In these tables and throughout this dissertation, the numbering of modes corresponds to the number of half wavelengths in the mode shape in the shorter dimension (horizontal) followed by the longer dimension (vertical).

In order to produce a single set of modal parameter estimates representative of the typical dynamic characteristics of one glass lite, averaging of the natural frequencies, relative damping factors, and mode shapes obtained for each of the 36 glass lites used in the field experimentation was performed. However, review of the experimentally measured natural frequencies revealed several outliers, notably all of the glass lites for Test 5 and the first four glass lites for Test 6. The experimentally estimated natural frequencies for these lites are significantly lower than the natural frequencies observed for all other lites. Due to an oversight in the procedural order of operations, the vibration analysis for these lites was performed prior to tightening the pressure plates to the prescribed torque. Consequently, the full stiffness of the boundary was not developed at the time of vibration testing, thereby producing lower natural frequencies in the dynamic response of the lites. The experimental modal parameter estimates obtained from these lites were excluded from the averaging

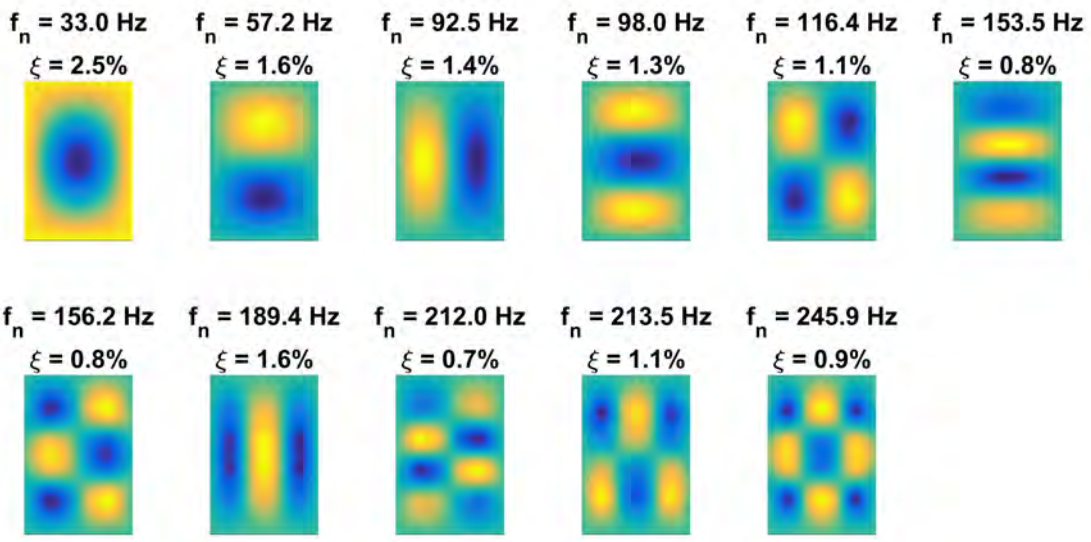

FIGURE 4.15: Average modal parameter estimates for glass lite specimens used in blast tests

TABLE 4.1: Standard deviations of the natural frequency and modal damping estimates across all glass lites

Mode	1,1	1,2	2,1	1,3	2,2	1,4	2,3	3,1	2,4	3,2	3,3
Natural frequency	2.0	2.8	2.4	2.6	2.5	3.9	2.4	3.4	2.4	5.4	2.0
Modal damping	0.3	0.3	0.3	0.3	0.1	0.1	0.6	0.1	0.5	0.2	0.3

process. The final set of modal parameter estimates serving as a representative response of a typical glass lite in the field experimentation is presented in Figure 4.15. Consistent with the averaging process used for individual lites, the Modal Assurance Criteria was used to ensure mode matching, and the Modal Scale Factor was applied to normalize amplitude and phase of the mode shapes prior to averaging.

For all modal parameter estimates subjected to averaging, the variance in the natural frequency and damping ratio estimates of the same modes across all panels was examined by calculation of the standard deviation. The standard deviations of the frequency and damping ratio of each mode is compiled in Table 4.1. The average standard deviation in the natural frequency and damping ratio was determined to be 2.89 and 0.27, respectively.

4.1.5 Explosive Charges

All experimental blast tests were conducted using charge compositions of either high explosive (HE) pentaerythritol tetranitrate (PETN) or lower velocity high explosive ammonium nitrate/fuel oil (ANFO) mixture. PETN is a commonly used component in military explosives and is also commonly employed commercially in detonating cord and blasting caps. ANFO, classified as a blasting agent due to its insensitivity to a No. 8 blasting cap, is a commonly used commercial explosive of relatively low density and detonation rate (Beveridge, 2011). While the actual rate of detonation of the two explosive types varies by exact composition and confinement of the charge, maximum values of the detonation rate of PETN and ANFO have been found to be 8,000 m/s (26,247 ft/s) and 4,500 m/s (14,763 ft/s), respectively (M Dobratz and C Crawford, 1985). Because of the difference in detonation rates, and subsequently the pressure impulses of each charge type, use of the two explosive agents facilitated the collection of data sets representative of both the "sharper" and "softer" pressure impulses of PETN and ANFO, respectively. The prevalence of the two explosive agents, particularly in commercial applications that allow for relative ease of procurement, further made them ideal for open-arena blast testing representative of a real-world scenario. All charges were detonated using a No. 8 detonator. However, because of the insensitivity of ANFO to a No. 8 detonator, detonation of all ANFO charges was facilitated by placement of a booster consisting of approximately 11.3 g (0.4 oz.) of high explosive Composition 2 around the detonator. Photographs of a typical PETN cast booster and an ANFO charge with their respective detonators are presented in Figure 4.16.

Each blast test was conducted with the charge positioned and detonated on a leveled

a) PETN cast booster b) ANFO mixture

FIGURE 4.16: Typical explosive charges used in blast testing

table of relatively negligible mass, as visible in the previously presented photograph in Figure 4.12. The charge table was constructed of a square, plywood surface adhered to a tubular length of cardboard, which was driven into a sand base. This facilitated adjustment of the table as required to achieve the desired height of burst and maintain a level charge table. In all cases, standoff distances were measured from the centroid of the cylindrical charge to the glass lite specimens. The epicenter location of the charge in relation to the set of lite specimens and the size of the charge were varied between the six blast tests to produce different patterns of lite breakage. However, to eliminate one variable from the test matrix, the height of burst, or elevation, of the centroid of the charge was held fixed at 1.0 m (39.75 in) from the bottom elevation of the facade wall throughout the tests. This elevation corresponds to the midheight of the bottom row of lites. The different scenarios of blast loading are summarized graphically in Figure 4.17, which details the charge composition, size in scale weight, and epicenter location relative to the test specimens. The scale weights and charge locations relative to the centerline of the facade wall (ie. the center of the center

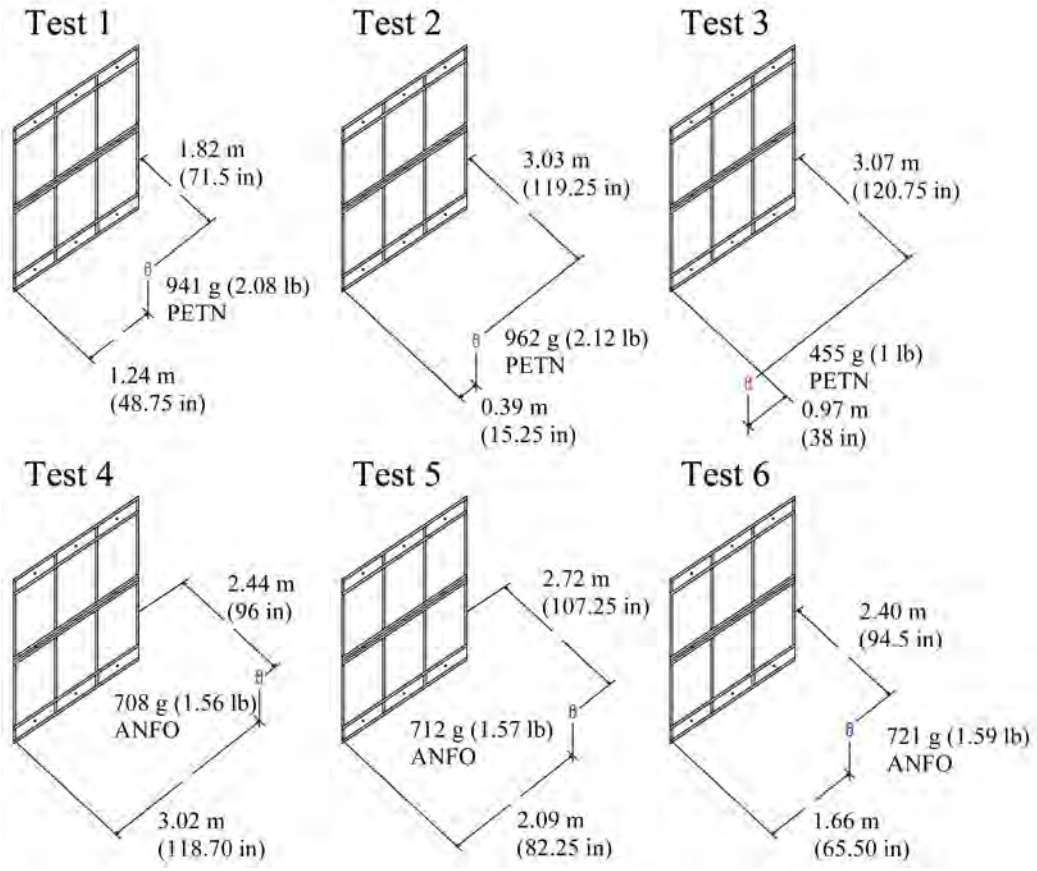

FIGURE 4.17: Summary of charge composition, size, and epicenter for each of the six experimental blast tests

lite), are provided in tabular form in Table 4.2.

4.1.6 Glass Lite Fracture and Debris Fields

Glass lite specimen breakage was observed across all six of the open-arena blast tests. In Test 1 and Test 2 all six of the lites in the facade wall fractured, while only a subset of the six lites fractured in the remaining tests. Photographs of the observed lite failure for each test is presented in Figure 4.18. It can be seen through comparison of Figure 4.18 with the charge locations for each test that, with the notable exception of Test 6, the number and location of lites broken correlated with the size and proximity of the charge. In Tests 3-5, the two lites in closest proximity to the charge experienced failure. However, it was

TABLE 4.2: Scale weight and location of the explosive charges in relation to the centerline of the facade wall

		Weight	Distance From Center Lite	
Test	Composition	g (lb_f)	Parallel, m (in)	Perpendicular, m (in)
1	PETN	941.20 (2.075)	0 (0)	1.82 (71.50)
2	PETN	961.62 (2.12)	-0.85 (-33.50)	3.03 (119.25)
3	PETN	455.86 (1.005)	-2.19 (-86.25)	3.07 (120.75)
4	ANFO	707.60 (1.56)	1.78 (69.95)	2.44 (96.00)
5	ANFO	712.14 (1.57)	0.85 (33.50)	2.72 (107.25)
6	ANFO	721.21 (1.59)	0.43 (16.75)	2.40 (94.50)

observed in Test 6 that Lite 6, which was in the closest proximity to the charge, survived, while Lites 3, 4, and 5 experienced failure. The reason for this asymmetry is not known. It should be noted that Lite 4, which was the most distant of the lites that experienced failure, failed just prior to or during the development of negative overpressures, as indicated by the photograph presented in Figure 4.19. It can be seen that the debris generated by fracture of Lite 4 is located on the exterior of the enclosure as a result of the suction pressures. Since the lite failed at a longer duration than typical of other lites, as indicated by the debris field development, this lite likely reached surface stress that just exceeded the threshold between failure and survival.

The implementation of the high-speed camera to capture the moment of failure of each of the glass lite specimens yielded mixed results over the full series of tests. In most cases, the clear line of sight to the glass lite specimens was ultimately obscured by dust and smoke generated by the explosion. However, the instances of failure for the two lites experiencing fracture in Test 4 were successfully determined from the high-speed video recording. Failure of specimens 3 and 6 occurred at 11.4 milliseconds and 8.2 milliseconds after detonation, respectively. Successful experimental observation of the instance of

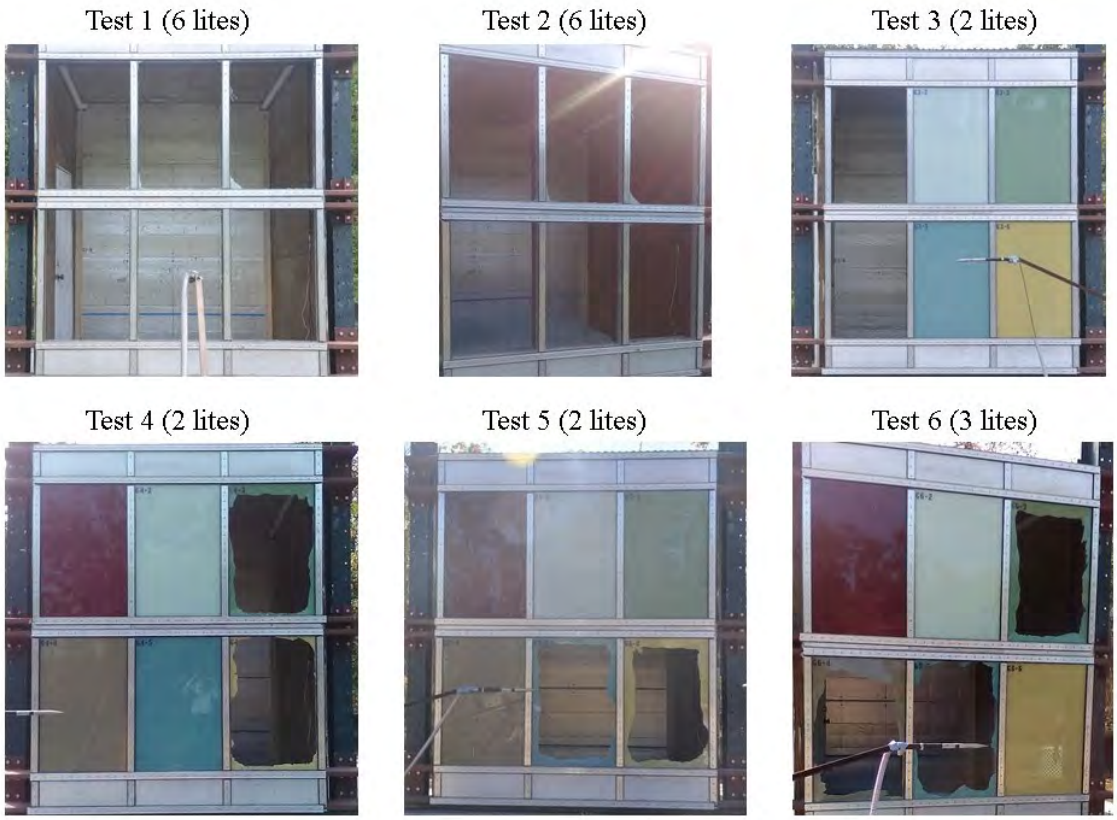

FIGURE 4.18: Observed fracturing of glass lite specimens in each test

failure provides a time of arrival metric for comparison to assess the predictive accuracy of numerical simulations.

Regular speed video located on the interior of the enclosure was successful in capturing the failure of the glass lites, facilitating determination of the overall failure pattern. Progressive, still-frame captures of failure of Lite 5 during Test 5 are presented in Figure 4.20. The corresponding relative time, beginning with the first frame in which failure was observed, is presented beneath each capture. The video indicates that failure initially occurred around the edges of the lite, followed by further fragmentation of the center area of the lite. This failure pattern was typical for lite fracture observed by the camera across the series of tests.

FIGURE 4.19: Exterior debris generated by failure of Lite 4 in suction during Test 6

The post-blast debris field resulting from each test was evaluated visually and subsequently quantitatively through measurement of the mass distribution across the floor of the enclosure. Photographs of the debris field generated within each test are provided in test summary data sheets in Appendix B.

Flying debris was categorized visually through distribution across the floor of the enclosure and through collection by the witness panel. The effectiveness of the witness panel for collecting high and moderate hazard flying debris is demonstrated in Figure 4.21, wherein a photograph of flying debris captured by the witness panel during Test 1 is presented. As evidenced by the fragments of glass embedded in the witness panel, the "high-hazard" threshold, signified by the level line located 0.5 m (20 in) above the floor of the enclosure, was surpassed. During this first test, the greatest quantity of glass fragments embedded in the witness panel. Although the amount of glass debris embedded in the witness panel

FIGURE 4.20: Progressive failure of a glass lite under blast loading

varied significantly across the remaining tests, all tests did result in some flying debris exceeding the "high-hazard" threshold, meaning that all tests resulted in the generation of "high-hazard" flying debris.

Mapping of the debris distribution was facilitated through the described discretization of the enclosure floor into nine grids prior to testing. The distribution of the mass of glass debris for all tests is summarized in Figure 4.22. The mass of glass debris collected from each grid over the full series of testing is also presented tabularly in Table B.5. Through comparison to Figure 4.18, it can be seen that the distribution of glass debris is consistent with the panel breakage pattern. The notable difference in mass distribution between Tests 1 and 2, both of which experienced breakage of all glass lite specimens, is attributed to the difference in charge standoff between the two tests. Whereas the relatively close proximity of the charge to the glass lite specimens during Test 1 resulted in greater debris throw and subsequent concentration of the debris against the witness panel, a more uniform distribution of debris was achieved by using an increased standoff distance during Test 2. While the

FIGURE 4.21: Photograph of the witness panel following Test 1

majority of glass debris landed within the enclosure and was collected for measurement, the mass of any glass debris that was thrown outside of the enclosure was not measured. Mapping of the glass distribution further facilitated quantification of the debris generated during testing by measurement of the debris falling within the "low-hazard" zone as a percentage of the total mass of the failed panels. Since fragment embedment in the witness panel was minimal in Tests 3 through 6, the amount of "very low-hazard" debris, which includes unmeasured fragments landing on the tubular framing or the exterior of the enclosure, is approximately equal to the difference between the total mass of the failed lites and the amount of debris measured in the "low-hazard" zone. Although this methodology was not feasible for the first two tests, which resulted in significant embedment of fragments in the witness panel, the percentages of "low-hazard" and "very low-hazard" debris generated in Test 3 through Test 6 were tabulated and are presented in Table 4.3. It is evident that the majority of debris generated in these four tests can be categorized as "very low-hazard".

Volumetric measurement of the debris field by LiDAR scanning is presented in Figure

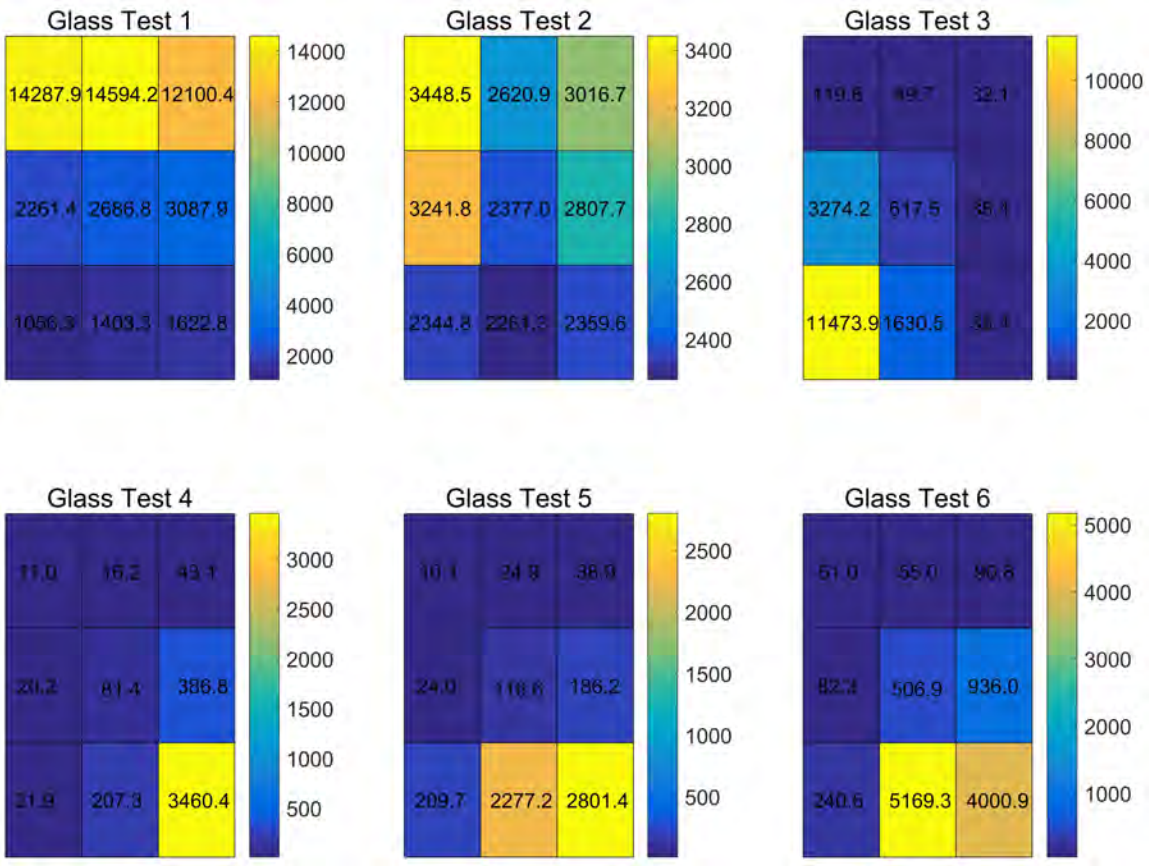

FIGURE 4.22: Mapping of glass debris by mass across the floor of the enclosure

4.23, which depicts aerial perspectives of the interior debris fields generated over the series of tests obtained by the LiDAR scanning and scene reconstruction. As expected, comparison to Figure 4.22 reveals strong correlation between LiDAR scanning and measured distribution of debris mass for each test.

TABLE 4.3: Percent of debris classified as "very low-hazard" and "low-hazard" across Test 3 through Test 6

Test	"VLH" Debris (%)	"LH" Debris (%)
3	81.9	18.1
4	97.6	2.4
5	98.2	1.8
6	95.0	5.0

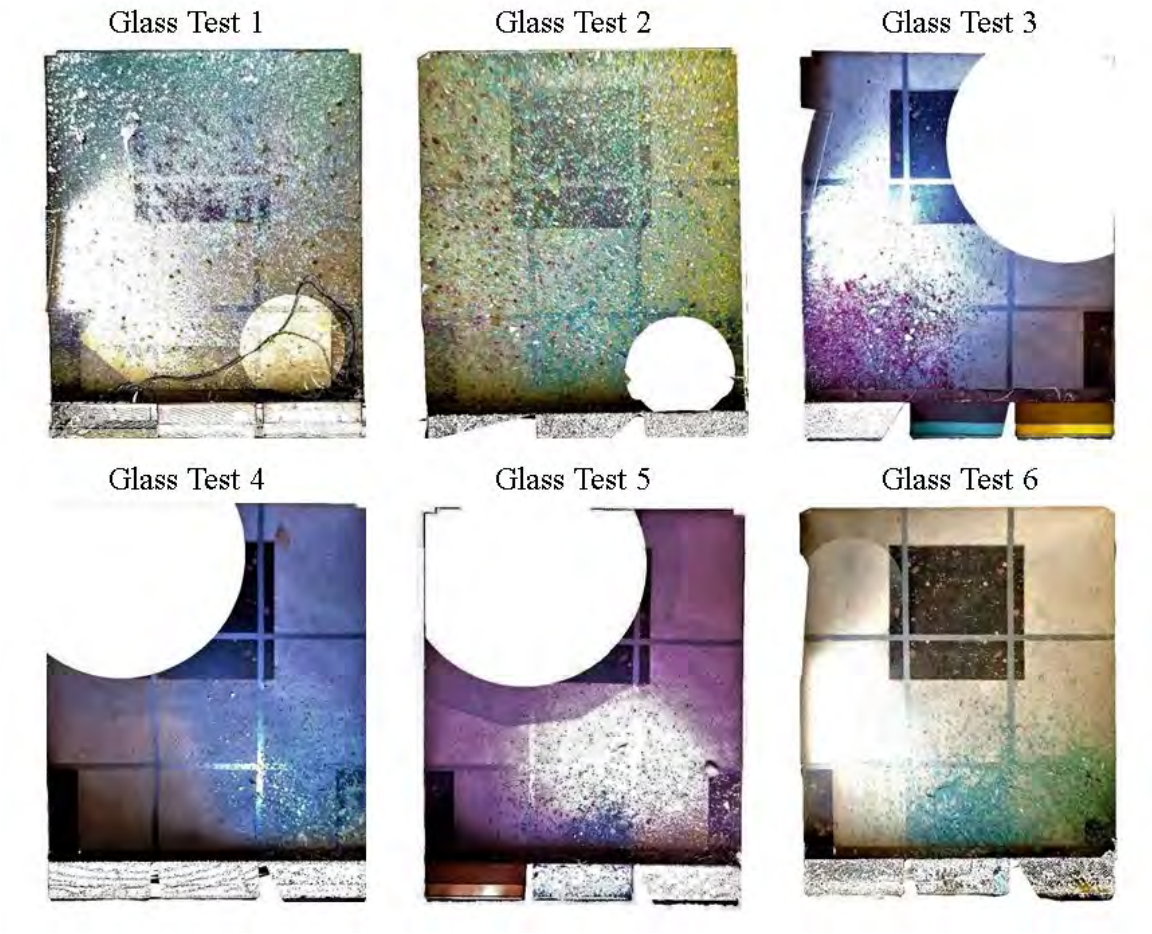

FIGURE 4.23: Plan view of the interior debris field obtained from LiDAR scanning

4.1.7 Measurement of Blast Pressures

The blast loading generated during each test was measured using the previously described instrumentation, which captured the peak reflected and incident blast overpressure and subsequent decay of the pressure wave at each sensor. With the exception of several isolated instances in which the peak overpressure could not be determined due to excessive noise, the peak reflected pressures were measured across the face of the test structure and are reported at each flush mount sensor location in Figure 4.24. Collection of the blast overpressure time histories at each sensor facilitated determination of a TNT equivalence

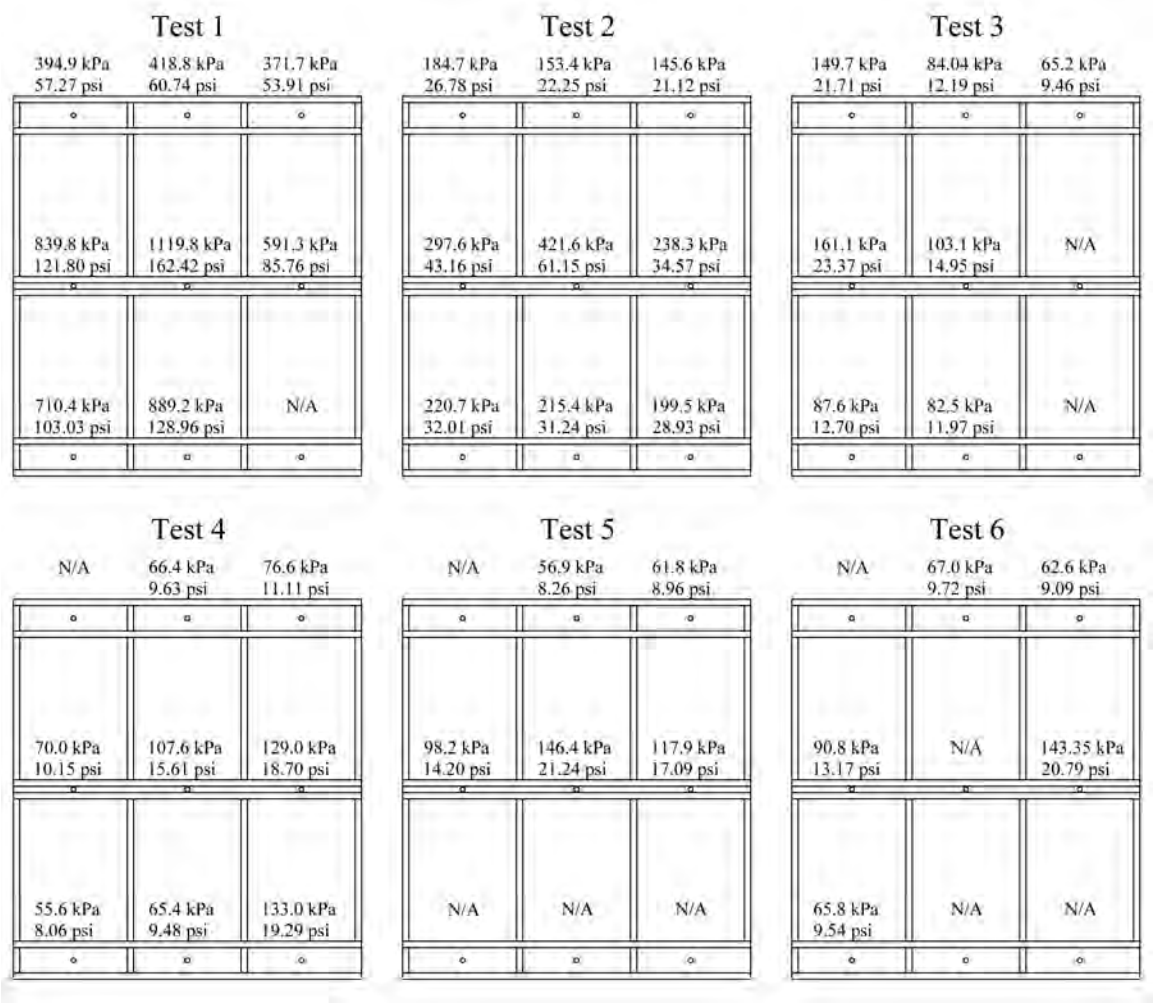

FIGURE 4.24: Peak reflected pressures recorded at each flush-mount pressure sensor location over the full set of blast tests

of each charge. The TNT equivalence is the ratio of the measured charge weight to the weight of a TNT charge that produces loading characteristics equivalent with the pressure measurements. Establishing this TNT equivalence was important to facilitate the use of blast loading models for the numerical simulations of the tests, as established blast loading models are based on TNT explosive yields. To determine the TNT equivalence for each test, an optimization routine was implemented to arrive at the analytical charge weight that most closely replicated all cleanly measured reflected pressure time histories. Kingery-Bulmash

polynomials (Kingery and Pannill, 1964; Kingery et al., 1984) were used to determine modified Friedlander pressure time histories for the analytical TNT charges. The optimization routine was implemented in the MATLAB computing environment using the built-in "fmincon" function and compared the predicted and measured pressure time histories using an objective function consisting of a simple sum of the squares of the residuals:

$$J = \sum_{t=t_a}^{t=t_d} |P_P(t) - P_M(t)|^2 \tag{4.3}$$

where $P_P(t)$ and $P_M(t)$ are the predicted and measured pressures, respectively, at time t over the positive duration of the blast wave. It should be noted that pressure time histories, rather than peak positive impulse, were implemented in the objective function because of the relatively low signal to noise ratio and signal disturbances that frequently appeared in the experimental pressure measurements. Since the impulse is calculated through numerical integration of the pressure time history, these errors would accumulate in the integral, while they were found to have a less significant influence on the objective function developed with the pressure time histories. Since the objective function was summed over multiple sensor locations, implementation of this optimization routine accounted for the various standoff distances and angles of reflection. Data sets indicating excessive noise or unfeasibly high pressure magnitudes were excluded from summation in the objective function. Further, only the measured reflected pressures were included in the optimization, since the reflected pressures across the array of flush mount sensors more closely corresponded to the pressures acting on the glass lite specimens. The incident pressures measured by the free air pencil probes were reserved for validation of the determined TNT equivalences.

The predicted TNT equivalent charge weight for each blast test, as obtained by the opti-

TABLE 4.4: Measured and TNT equivalent charge weight for each experimental blast test

Shot	Composition	Weight, g (lb_f)	TNT Equivalent Weight, g (lb_f)	Equivalence Factor
1	PETN	941.20 (2.075)	742.97 (1.639)	0.790
2	PETN	961.62 (2.12)	771.53 (1.702)	0.803
3	PETN	455.86 (1.005)	375.88 (0.829)	0.827
4	ANFO	707.60 (1.56)	181.68 (0.401)	0.254
5	ANFO	712.14 (1.57)	184.77 (0.408)	0.260
6	ANFO	721.21 (1.59)	116.89 (0.258)	0.162
6**	ANFO	721.21 (1.59)	186.13 (0.411)	0.258

mization routine, is presented in Table 4.4 alongside the measured charge weight. Although the TNT equivalent charge weight was lower than expected across all tests, it is evident that, with the exception of Test 6, the calculated equivalence was strongly consistent across charges of the same composition. Since Tests 4-6 used nearly identical charge weights of the same ANFO composition, the same TNT equivalence is expected across all three tests. Consequently, it is believed that the experimental reflected pressure measurements used for the determination of TNT equivalence for Test 6 did not accurately capture the actual pressure wave. Therefore, the averaged equivalence of the two previous tests conducted with a nominally identical ANFO charge was implemented in simulations of Test 6. This is reflected in the second entry for Test 6, denoted as "6**" in Table 4.4. Plots of the predicted pressure time histories using the TNT equivalent charge weights are presented in Appendix B with comparisons to the measured pressure time histories for each sensor location included in the optimization routine. In addition, plots of the experimentally determined impulse with comparison to the peak positive impulse for the TNT equivalent charge are included in Appendix B. Comparisons between the measured and predicted incident pressure time histories, which were used for validation of the optimization results,

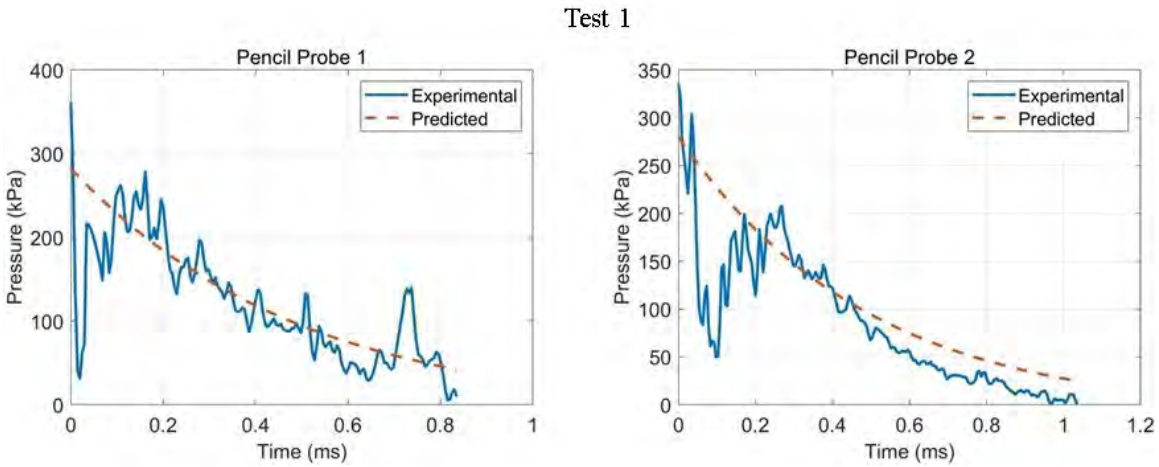

FIGURE 4.25: Comparison of the predicted and measured incident pressure time histories at each of the incident pressure sensor locations for Test 1

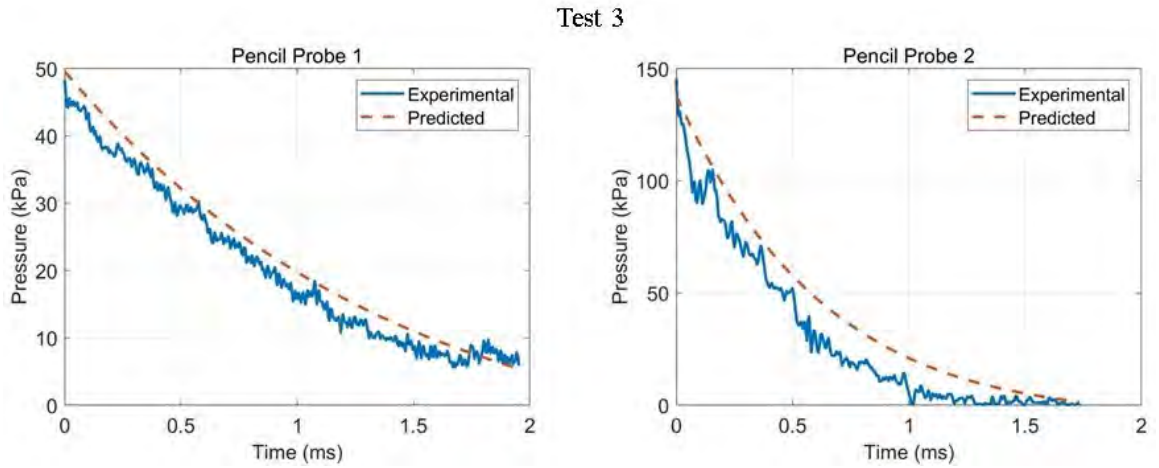

FIGURE 4.26: Comparison of the predicted and measured incident pressure time histories at each of the incident pressure sensor locations for Test 3

are presented in Figures 4.25 through 4.29. Reasonably strong correlation between the TNT equivalent blast loading model and the experimentally measured incident pressures was observed across all tests for which incident pressure measurements were successfully obtained.

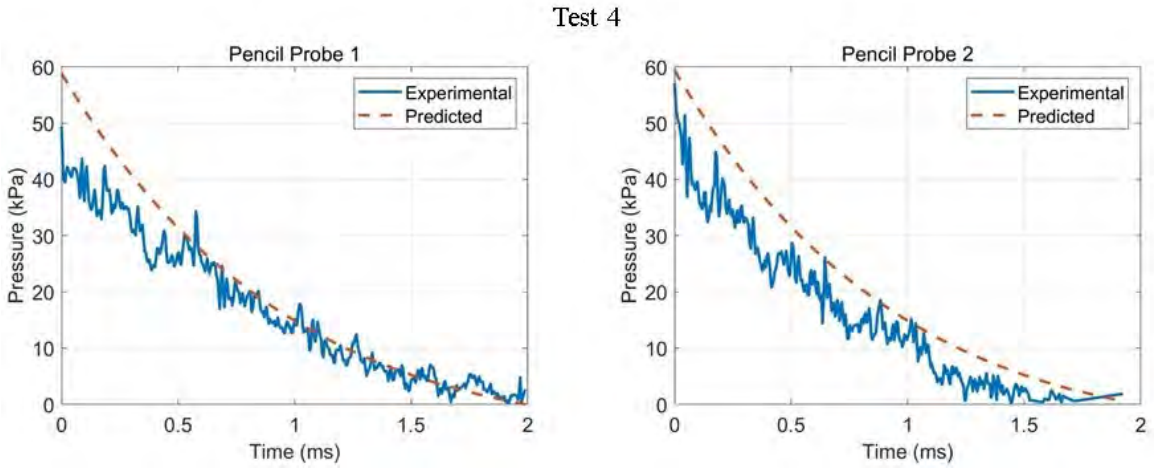

FIGURE 4.27: Comparison of the predicted and measured incident pressure time histories at each of the incident pressure sensor locations for Test 4

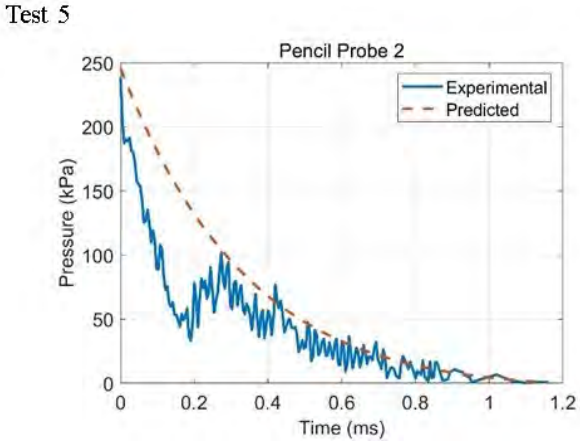

FIGURE 4.28: Comparison of the predicted and measured incident pressure time histories at each of the incident pressure sensor locations for Test 5

4.2 Static Load Testing

Static load testing of a glass lite panel specimen was completed following open-arena blast testing. The objective of experimental static testing was to characterize the load-deformation behavior of a typical lite under static loading as well as physically test the maximum uniform pressure that could be carried by the lite prior to breakage. This experimental data is leveraged in the study for model calibration, specifically with respect to the boundary conditions and fracture strength of the glass. In addition, the static load testing

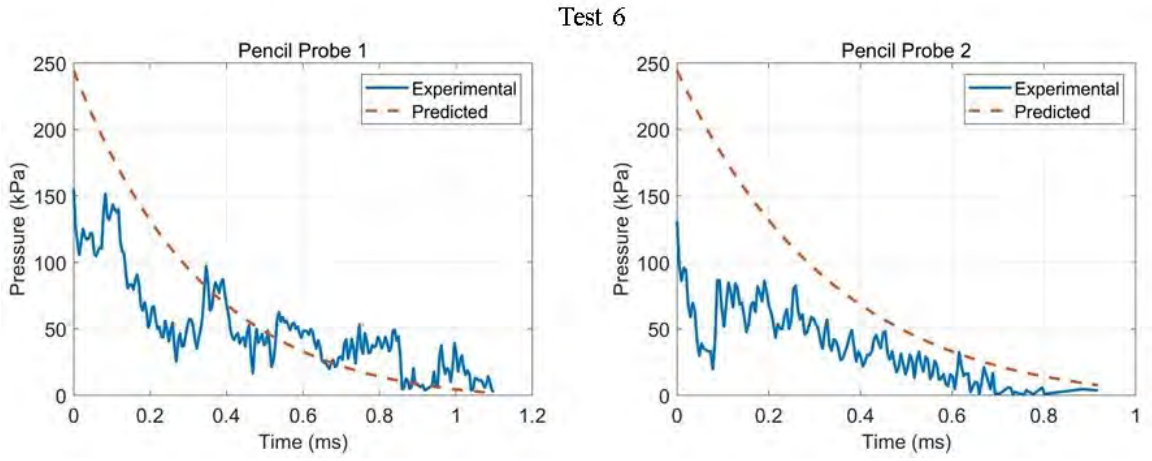

FIGURE 4.29: Comparison of the predicted and measured incident pressure time histories at each of the incident pressure sensor locations for Test 6

data is used in subsequent chapters of this dissertation for experimental validation of the large deformation, nonlinear geometry, and fracture behavior predicted by AEM and FEM models.

4.2.1 Overview of Experimental Setup

Since the measurements collected during static testing would be used for initial calibration of parameters in the AEM and FEM models used to simulate the open-arena blast tests, it was imperative that the boundary conditions of the glass lite specimen during static testing were reproduced as similar as possible to the boundary conditions present during the experimental blast testing. The same facade framework employed in the open-arena blast testing was therefore re-purposed for static experimentation to minimize uncertainties related to the replication of the field boundary conditions and to ensure uniformity between the experiments. Likewise, the installation of the glass lite specimen, including the spacing and torquing of all screws, followed the same procedures as carried out during field testing. Since the pressure plates between glass lites contacted two lites during field testing, repli-

cation of field boundary conditions included placement of additional glass lite specimens neighboring the lite undergoing static testing. Without the presence of the neighboring lites, the pressure plates would contact the static test specimen on an angle that could potentially affect the boundary conditions. Three glass lites were therefore fixed in the frame during experimentation, despite only the middle specimen being subjected to static loading.

Characterization under static loading required a means of applying a controlled, uniform pressure over the glass lite specimen at a rate slow enough to minimize the significance of any dynamic structural response. A uniform pressure was desired for the static testing, because it avoids the challenges of accurately modeling concentrated loads and also since the development of single degree of freedom, nonlinear models for blast analysis of structural components is typically based on uniform loading. The application of a uniform pressure load was achieved through application of vacuum pressure to the rear surface of the glass lite specimen. Vacuum conditions were met by sealing the opening in the facade framework opposite the glass lite specimen to create a pressure chamber to which vacuum pressure could be applied using a laboratory vacuum pump. Control of the magnitude of the vacuum pressure was achieved using a manual vacuum pressure regulator. Continuous measurement of the vacuum pressure acting on the glass lite specimen throughout testing was output by a pressure sensor mounted to the back panel of the vacuum chamber to measure conditions interior to the pressure chamber. The pressure sensor used was a SMC Corporation Model PSE531 with a measurement range of 0 kPa to 101 kPa (14.65 psi) and was directly threaded into the steel panel.

The deflection of the glass lite specimen at the center of the lite was continuously monitored using a dial gage attached to a support on a strong floor foundation. The dial gage

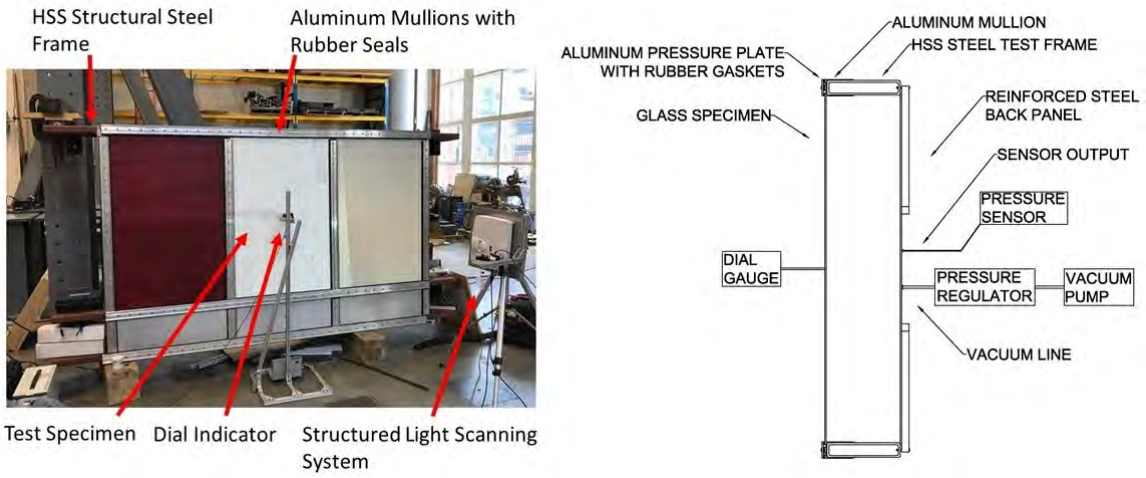

FIGURE 4.30: Experimental setup for static loading of a glass lite specimen

used was a Chicago Dial Indicator Model BG 2720 with a resolution of 0.0025 mm (0.0001 in). In addition to the discrete measurement of deflection at the center of the lite, full-field displacement of the specimen was measured using a structured light scanning system. Due to the time associated with projecting the sequence of structured light patterns and obtaining the digital images necessary for the 3D depth mapping, full-field displacements were only measured at a limited number of discrete increments during the loading. Specifically, full-field displacement was captured in increments of 0.254 cm (0.1 in) of midpoint deflection until 2.54 cm (1.0 in) deflection was attained. Lastly, a Phantom V4.3 high speed camera was employed to capture the fracture pattern of the specimen at failure. A 800 x 600 pixel resolution was used for this testing with a frame rate of 1200.12 fps. The experimental setup for static loading is presented in Figure 4.30, which presents a photograph of the actual test setup alongside a labeled schematic of the cross section of the vacuum chamber.

4.2.2 Modal Analysis of the Glass Lite Specimen Subjected to Static Loading

In accordance with the procedures followed during open-arena blast testing, a vibration analysis was carried out immediately prior to destructive testing. Modal analysis was performed following the same procedure and equipment as previously detailed. System identification of the vibration data was again performed to produce the set of modal parameter estimates presented in Figure 4.31. As expected, the set of modal parameter estimates exhibits strong correlation with those obtained for the glass lites subjected to open-arena blast testing. A comparison between the measured natural frequencies for each case is presented in Table 4.5, which also provides the percentage difference in natural frequencies between the averaged modal parameter estimate from the lites subjected to blast loading and the corresponding mode from the lite used in the static testing. While several of the measured modes indicate less than one percent difference between the modal parameter estimate sets, it should be noted that the fundamental mode of the lite subjected to static loading exhibited a significantly stiffer response than was typically observed during open-arena blast testing. It is speculated that this this difference can possibly be attributed to the presence of sealant around the edge of the panel necessary to maintain a sealed pressure chamber and/or to differences in the ambient temperature and humidity, which could potentially affect the apparent stiffness of the rubber gaskets. With the exception of the fundamental natural frequency, all of the remaining ten experimental natural frequencies agree to within 3.6%. Across the remaining ten natural frequencies, some are higher for the laboratory specimen, but some are lower, and there is no overall bias that would suggest that the dynamic properties of the laboratory specimen were significantly different than that

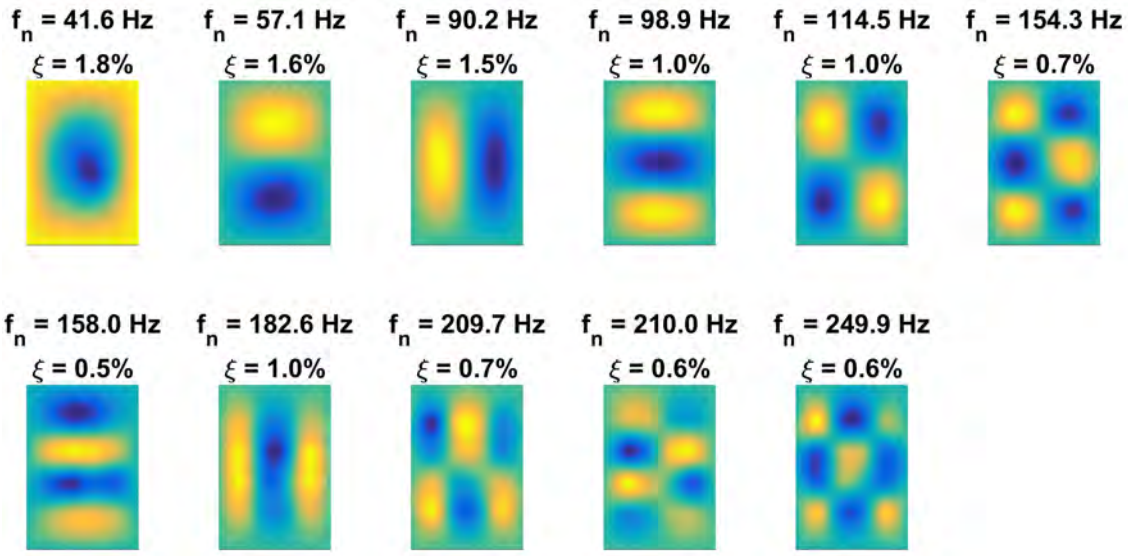

FIGURE 4.31: Modal parameter estimates of the glass lite specimen subjected to static loading

of a typical field specimen.

4.2.3 Load-Deflection Response and Failure

The measured deflection at the center of the glass lite specimen as a function of the applied vacuum pressure is plotted in Figure 4.32. This load-deflection response exhibits moderate nonlinear stiffening, which likely resulted from nonlinear geometric effects occurring due to the deformation of the lite. Nonlinear stiffening of the rubber gaskets under load may have also contributed to the nonlinear stiffening in the response of the lite. The measured full-field deflection of the glass lite is documented in Figure 4.33 through presentation of progressive scans of the full-field deflection. The measured deflection at the center of the lite corresponding to the full-field deflection is specified beneath each rendering. Due of the presence of the dial gage in the field-of-view of the structured light scanner during testing, full-field deflections were only measured unobstructed over half of the glass lite. As indicated by the color mapping, relatively uniform deflections occurred across the

TABLE 4.5: Comparison of natural frequencies for lites subjected to blast testing and the lite subjected to uniform load testing

	Field Specimens	Laboratory Specimen	Difference
Mode	$f_n(Hz)$	$f_n(Hz)$	%
1,1	33.0	41.6	+26.1
1,2	57.2	57.1	-0.2
2,1	92.5	90.2	-2.5
1,3	98.0	98.9	+0.9
2,2	116.4	114.6	-1.6
1,4	153.5	158.0	+2.9
2,3	156.2	154.3	-1.2
3,1	189.4	182.6	-3.6
2,4	212.0	210.0	-0.9
3,2	213.5	209.7	-1.8
3,3	245.9	249.9	+1.6

central area of the lite, with lower magnitude deflections occurring near the boundaries as the rubber gaskets deformed under loading.

Fracture of the specimen occurred at approximately 32.13 kPa (4.66 psi) of uniform vacuum pressure with a corresponding deflection at the center of the glass lite specimen of 32.2 mm (1.26 in). Progressive, high-speed captures of the fracture pattern of the specimen during failure are presented in Figure 4.34. As expected, fracture initiated near the corners of the lite corresponding to the regions experiencing the greatest magnitude of stress. However, it can be seen that fracture did not occur symmetrically, as the upper right corner failed first before the remaining corners experienced failure. The reason for this asymmetry is unknown but could possibly be attributed to a visibly undetectable imperfection present in the lite specimen or an unknown asymmetry in the boundary conditions.

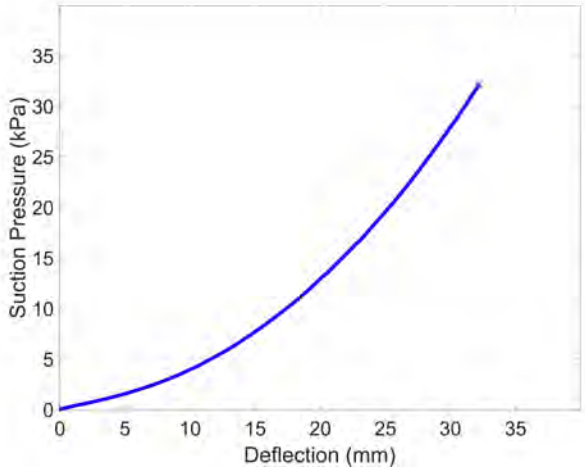

FIGURE 4.32: Load-deflection response of the glass lite specimen under uniform loading

4.2.4 Characterization of Rubber Gaskets

The rubber gaskets contacting each side of the glass lite specimens within the fenestration system were also characterized through static load testing to provide a means of estimating the stiffness of this boundary condition component. The nonlinear material properties of rubber and the complex cross sectional geometry of the rubber gaskets specifically motivated this laboratory characterization of the load-deflection response of the gaskets under compressive loading.

4.2.4.1 Experimental Setup

The rubber gaskets were subjected to compressive loading using the experimental setup photographed in Figure 4.35. As pictured, a 10.2 cm (4 in) section of the exterior pressure plate, complete with the rubber gaskets, was subjected to compression loading between two steel loading plates. The compressive load was increased incrementally using a Chatillon UTSM uniaxial loading frame with a capacity of 2 kN (500 lbs). An incremental increase in the compressive load was achieved by raising the loading plates using the manual controls

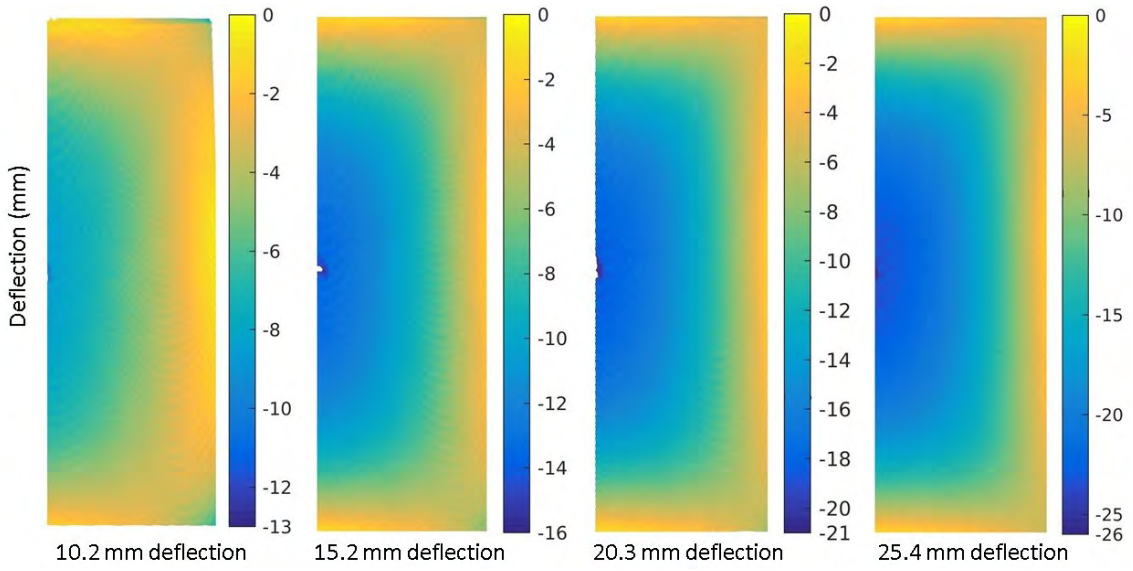

FIGURE 4.33: Full-field out-of-plane deflection of the glass lite specimen under static loading

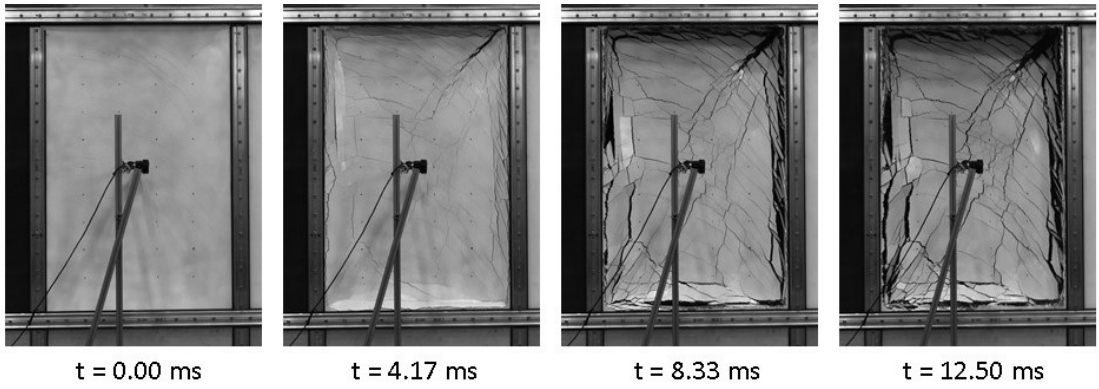

FIGURE 4.34: High-speed imagery of failure of the glass lite specimen under static loading

integral to the loading frame. To minimize dynamic effects and simulate static loading, the loading plate was raised for a timespan of approximately one second between 60 second intervals of no motion. The compressive load throughout testing was measured using a 2 kN (500 lb) capacity load cell with a measurement range of 0 to 2 kN (500 lbs) positioned between the loading frame and the loading plates. A roller bearing was positioned between the load cell and upper loading plate to minimize unintended transfer of moment between the load cell and pressure plate. Displacement throughout testing was measured

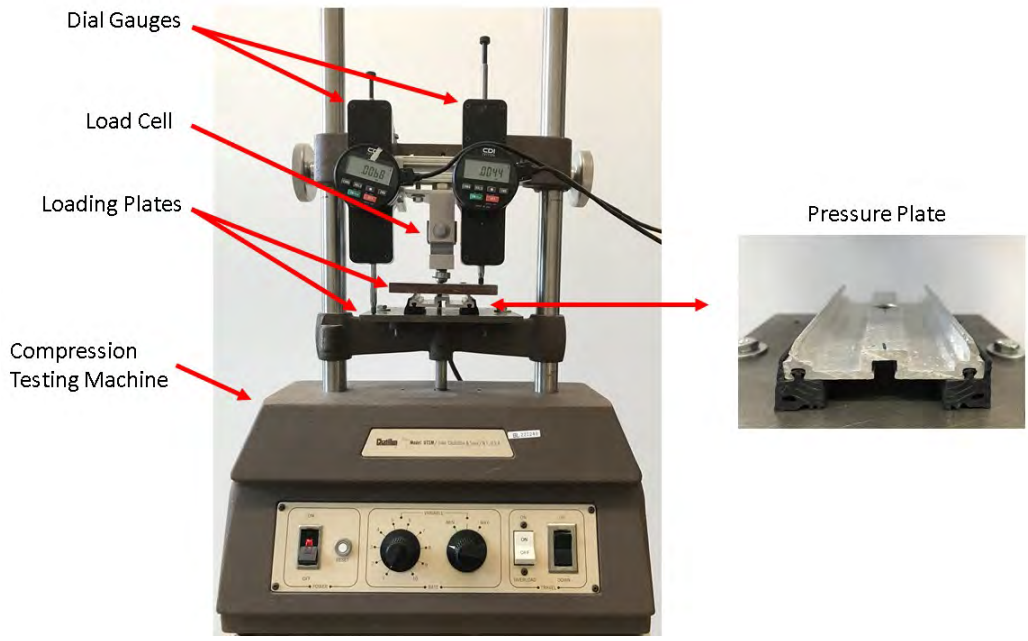

FIGURE 4.35: Experimental compression testing of rubber gaskets

by two Chicago Dial Indicator BG2720 dial gauges with 0.0025 mm (0.0001 in) resolution mounted to fixed points on the load frame. Measurement of the compressive displacement of the rubber gaskets was facilitated by measurement of the displacements of the two loading plates in relation to the fixed mounting points, yielding the total compressive displacement of the rubber gaskets as the relative displacement between the two loading plates.

4.2.5 Load-Displacement Behavior of the Rubber Gaskets

The described static loading test yielded the compressive displacement of the rubber gaskets as a function of the load per unit length presented in Figure 4.36, which represents the compressive load per unit length in each of the two, individual rubber gaskets connected to the pressure plate. The nonlinear stiffening behavior of the rubber gasket is clearly demonstrated by the increasing slope of the response with load.

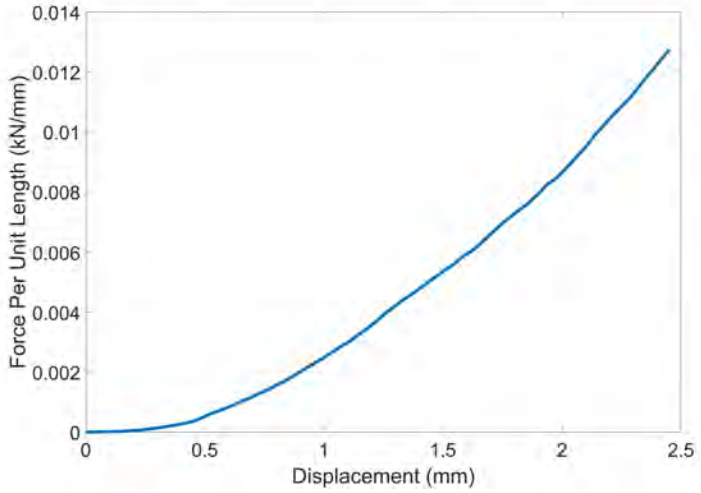

FIGURE 4.36: Experimental compressive load versus displacement curve for one rubber gasket

4.3 Concluding Remarks

Experimental testing necessary for development of databases for comparison to subsequent AEM and FEM simulations has been described. Two major components of experimental testing were open-arena blast testing and static testing of glass lites. As both of these methods involved destruction of the test specimens, modal analyses were carried out to characterize the dynamic properties of the specimens, which are sensitive to the boundary conditions. Strong correlation between the natural frequencies of the set of lites in the field and the lite used in the static testing program confirm consistency in the boundary conditions and general dynamic properties for all lites included in the experimentation. Further subareas of open-arena blast testing included measurement of blast pressures and post-blast collection of debris field data. Lastly, static loading was performed for an individual pressure plate to evaluate the nonlinear compressive stiffness behavior of the rubber gaskets within the fenestration system. The static load testing components of the test program serve to build the experimental database from which numerical models will be calibrated

and subsequently compared to field observations to remove uncertainties that have the potential to produce erroneous conclusions during performance evaluation of the numerical simulations. Following calibration of the numerical models, the field measurements will serve as a real world case study for comparing the simulation capabilities and predictive fidelity of the numerical modeling techniques.

CHAPTER 5: DEVELOPMENT AND VERIFICATION OF AEM MODELS OF GLASS LITES

The development of an accurate model for simulating the structural response of the glass lite specimens was required prior to addressing the ultimate objective of simulating debris field formation under blast loading using the Applied Element Method. Beyond implementation and verification of the Applied Element Method as described in Chapter 3, critical challenges toward development of the model included accurate representation of the in-situ boundary conditions for prediction of the load-deflection response, verification of dynamic behavior, inclusion of residual stress effects into the simulation, and development of a macro-scale failure model appropriate for tempered glass.

As will be described in detail, the boundary condition assignments are calibrated to the behavior measured in the static loading experiment described in Chapter 4 and successfully verified through comparison to a FEM model. Further, a viscoelastic material model based on the Kelvin-Voigt model is successfully implemented for simulation of the rubber gaskets present around the edges of the glass lite specimen. The dynamic behavior of the lites predicted using the viscoelastic material model is successfully validated against the experimentally estimated modal parameter estimates. A method for assignment of residual stresses in the AEM simulation is developed and verified through analysis of the relationship between residual stress and the predicted strain energy, as described in Chapter 2. Further, a failure model is developed for macro-scale modeling of fracture and fragmenta-

tion in tempered glass. The implementation of the residual stresses and failure model are demonstrated with nonlinear simulations of fracture and fragmentation of glass lites with different degrees of tempering.

5.1 Description of the Applied Element Model of a Single Glass Lite Specimen and Verification with a Comparable Finite Element Model

Prior to development of Applied Element models of the glass lite specimen featuring in-situ boundary conditions, an initial Applied Element model of a glass lite was developed for verification by comparison to nonlinear stress analysis conducted with a similar Finite Element model. The objective of the initial model was to verify the predictive fidelity of the Applied Element simulation for prediction of load-deflection behavior and stress distribution in a plate-like model under uniform, static loading.

A single glass lite specimen was modeled as being geometrically identical to the experimental specimens by adopting the full 80.0 cm x 121.9 cm x 4.8 mm (31.5 in x 48 in x 0.1875 in) outside dimensions of an individual lite. The model was discretized using a mesh size of 9.525 mm (0.375 in) in the plane of the lite, which yielded a discretization of 84 elements across the width, 128 elements across the height, and 1 element through the thickness. This mesh size was implemented because, as will be later demonstrated, it is fine enough to accurately predict the behavior of the lite without incurring the computational expense associated with a finer mesh. A uniform distribution of 10 interface springs was implemented in each planar direction between elements, resulting in assignment of 100 interface springs between each element pair. In total, the model of the glass lite consisted of 10,752 elements and 2,129,200 total springs. Since six degrees of freedom are assigned about the centroid of each Applied Element, the implemented mesh resulted in 64,512 de-

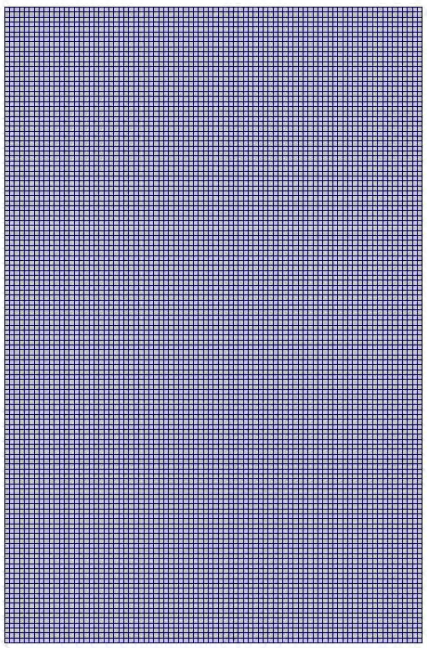

FIGURE 5.1: Rendering of the meshed Applied Element model of a single lite

grees of freedom. A rendering of the Epplied Element model in the Paraview software package is presented in Figure 5.1.

Material properties typical of glass, including a modulus of elasticity of 68.9 GPa (10,000 ksi) and a Poisson's ratio of 0.22 were assigned to the elements. The mass density was assigned as 2,533.56 kg/m^3 (158 lb/ft^3) based on the measured weight and calculated volume of the lites. As observed in the literature, the boundary conditions of glass lites mounted in conventional fenestration systems are typically modeled using roller boundary assignments, which prevent out-of-plane translation while allowing rotation and in-plane translation (Iverson, 1968). The initial AEM model for verification with the comparable FEM model therefore featured roller edge conditions, which were implemented by constraining the out-of-plane translational degrees of freedom of the outermost edge elements.

A comparable Finite Element model was developed using the Abaqus software package,

and in order to maintain uniformity between the AEM and FEM models, the Finite Element model was developed using the previously described material properties and the full geometry of the glass lite. The Finite Element model was discretized using a mesh of 4.76 mm (0.1875 in) square S4R elements, which are reduced integration quadrilateral shell elements, featuring four nodes per element. Roller boundary conditions were implemented in the model by constraining the out-of-plane translational degree of freedom of the outermost nodes along each edge of the model. The mesh and boundary condition assignments resulted in 43,008 elements, 43,433 nodes, and 260,598 degrees of freedom.

Static loading was applied to both the AEM and FEM models as a uniformly distributed force acting in the out-of-plane degree of freedom of all element centroids or nodal points, respectively. To allow for development of nonlinear behavior, loading was applied incrementally over 100 increments until a peak, uniform pressure of 32.13 kPa (4.66 psi) was attained. This peak value of uniform pressure was selected, since it corresponded to the peak pressure applied during experimental static testing and would later be implemented for verification of the boundary condition assignments. Application of incremental loading facilitated comparison of the midpoint deflection of both models developed under uniform loading. The resulting load-deflection curves of both models are presented for comparison in Figure 5.2. Although some deviation in the predicted deflection is evident between the models, both models reflect similar nonlinear behavior, as the response of both models exhibits increased stiffness with load due to nonlinear geometric effects. The peak deflections of the FEM and AEM models under the maximum load are 34.0 mm (1.34 in) and 32.8 mm (1.29 in), respectively, which corresponds to a percent difference of 3.5%.

The behavior of the Applied Element simulation was further verified through comparison

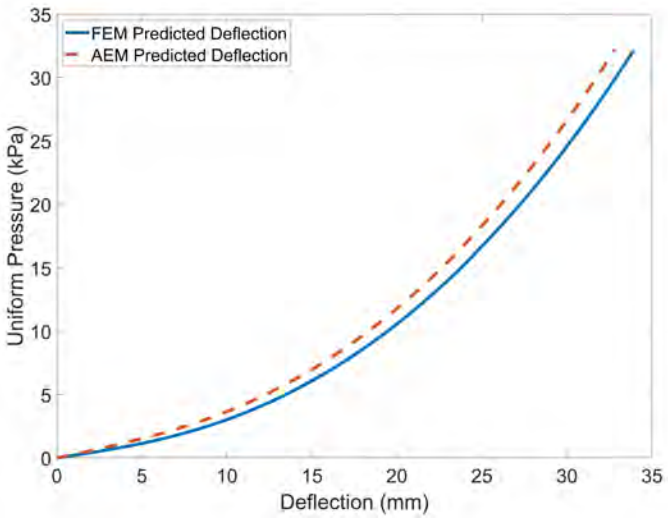

FIGURE 5.2: Load-displacement predicted by the AEM and FEM glass lite models featuring roller boundary conditions

of the predicted principal stress distribution with the principal stress distribution predicted using the commercial Finite Element software. The maximum principal stresses of both models at peak deflection are plotted in Figure 5.3. It is evident that similar distributions are predicted by both models. The peak stresses occur in the FEM model at the Gaussian integration points nearest the tensile surface of the model, while the stresses in the AEM model are plotted across the interface springs nearest the tensile surface. Consequently, the FEM analysis is expected to predict principal stresses that are slightly higher in magnitude than those obtained from the AEM. Further, the peak magnitudes of principal stress predicted by the FEM and AEM models are 180.7 MPa (26,208.1 psi) and 167.2 MPa (24,244.5 psi), respectively. This corresponds to a percent difference of 8.1%.

5.2 Modeling of the In-Situ Boundary Conditions

Following verification of the static behavior of the AEM model featuring roller boundary conditions, a significant challenge toward development of models for static and open-arena

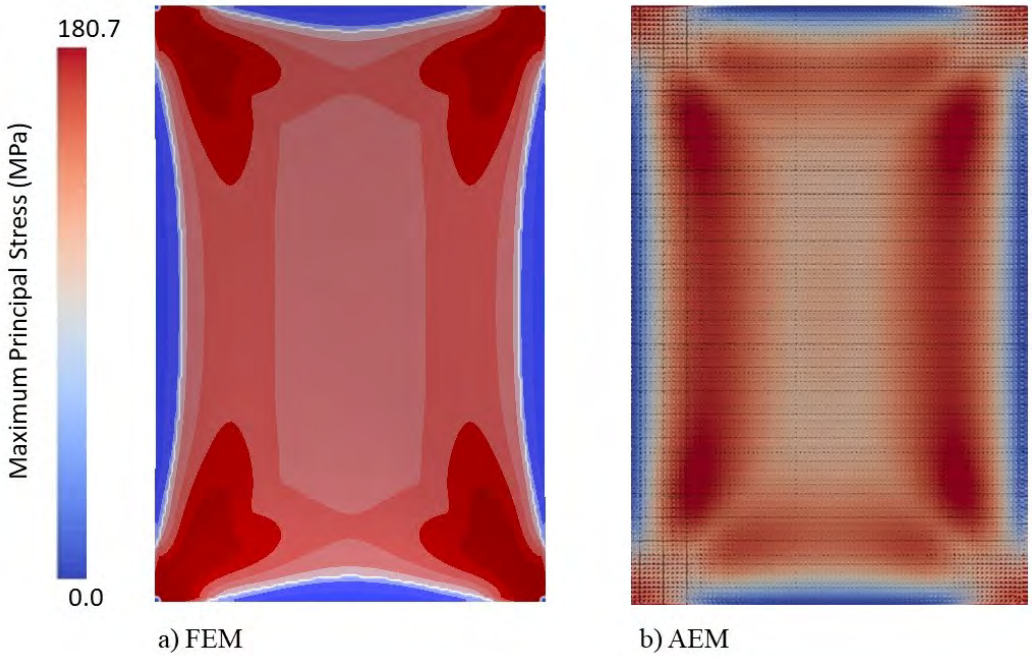

FIGURE 5.3: Maximum principal stress distribution predicted by the AEM and FEM glass lite models featuring roller boundary conditions

blast loading was accurately representing the in-situ boundary conditions of the glass lite specimens mounted in the fenestration system. As described and depicted in Chapter 4, the connectivity of each glass lite specimen in the fenestration system featured multiple components, including aluminum pressure plates, zinc screws, and rubber gaskets. As evidenced by the experimental load-deflection curve developed from static testing and from visual observation of the connection, a simple, idealized boundary constraint, such as the previously modeled case of roller boundary conditions, could not be reasonably assumed. This is demonstrated in Figure 5.4, which presents a comparison between the experimentally measured load-deflection curve and the load-deflection curves predicted with implementation of various, fixed boundary constraints, which were applied to the outermost elements along the edges of the Applied Element model. Although the measured response of the glass lite was most similar to the simulation with the roller boundary conditions, it is evident that

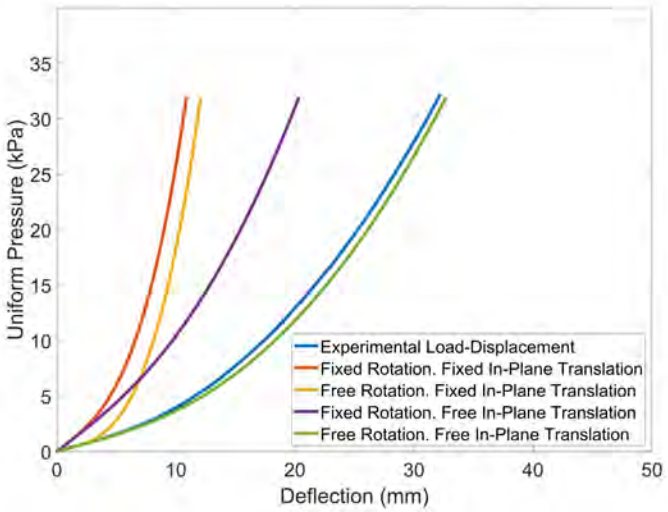

FIGURE 5.4: Comparison of the experimental load-displacement to the load-displacement predicted with simple boundary constraints

assumption of fully constrained or pinned boundary conditions overpredicts the stiffness of the model, while assumption of roller boundary conditions underpredicts the stiffness.

Since the material properties of each individual component in the actual connection were not known, and because of the challenges associated with modeling interconnected components of differing properties, the boundaries were modeled by introduction of linear elastic springs to the elements along the edges of the model. Introduction of boundary springs facilitated a means to reasonably simulate the partially restrained boundary condition presented by the fenestration system, while avoiding the complexities of modeling each component in the system. As detailed in the following section, the suitability of the stiffness assigned to the boundary springs was assured through model calibration of the spring stiffness assignments performed to optimize the similarity of the response of the model under uniform loading to the measured response obtained from the static load test. Translational springs were applied to the in-plane and out-of-plane translational degrees of freedom of

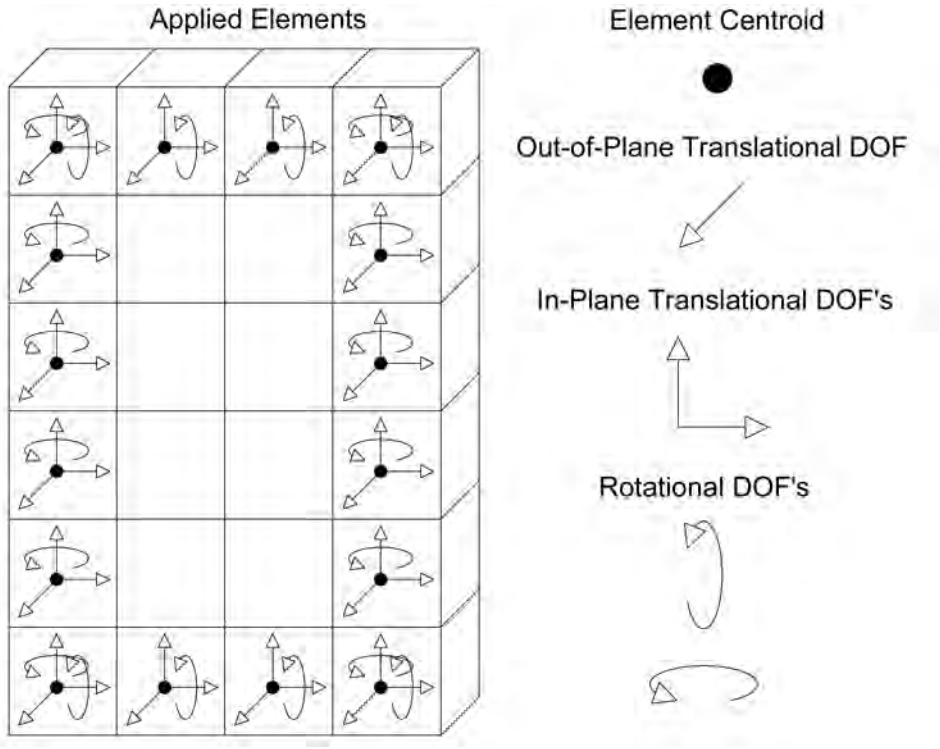

FIGURE 5.5: Illustration of the degrees of freedom to which boundary springs were assigned

the elements located along each outer edge of the model and rotational stiffness was applied in the degree of freedom acting about the respective model edge associated with each boundary element. These degrees of freedom to which the boundary stiffnesses were assigned are illustrated for a reduced-scale model in Figure 5.5.

As will be demonstrated, assignment of linear elastic boundary springs successfully accounted for the unknown stiffness at the supporting edges. However, a further challenge was presented by the significant thickness of the rubber gaskets on either side of the specimens and its effect on the dynamic response of the lites. Rubber is a viscoelastic material, so its behavior under dynamic loading differs from its behavior under static loads. The nonlinear behavior of the gaskets was therefore addressed through introduction of a frequency dependent viscoelastic material model, which models dynamic effects using a complex

modulus of elasticity defined as:

$$E^* = E' \left[1 + i\eta\right] \tag{5.1}$$

where E' is the storage modulus, defined as the real part of the complex modulus, and η is the loss factor, defined as the tangent of the angle between the complex modulus and the real axis (Baz, 2018). The viscoelastic material model was implemented in the simulation using the Kelvin-Voigt approach, which simulates dynamic, viscoelastic behavior using a spring and damper in parallel (Baz, 2018). Following the Kelvin-Voigt approach, the loss factor is linearly proportional to frequency, ω, and computed as:

$$\eta = \frac{c_d}{E}\omega \tag{5.2}$$

where E is the modulus of elasticity, and c_d is the damping coefficient of the material (Baz, 2018). Tuning of the viscoelastic model was facilitated by adjustment of the damping coefficient, which was implemented in the simulation by assignment to dashpots. The dashpots were introduced at each boundary element and acted in parallel with the existing out-of-plane translational and rotational edge springs. A simplified depiction of a Kelvin-Voigt model as implemented in the model is illustrated in Figure 5.6. As will be later demonstrated, addition of the dashpot can significantly affect the dynamic properties of the model, specifically at higher frequency response. However, because the complex modulus of elasticity is proportional to the frequency, the static behavior of the model is unaffected.

5.3 Calibration of Boundary Conditions in the Model

For calibration of the Applied Element model, the static load test was simulated as previously described by applying uniform loading, introduced as equally distributed forces, in

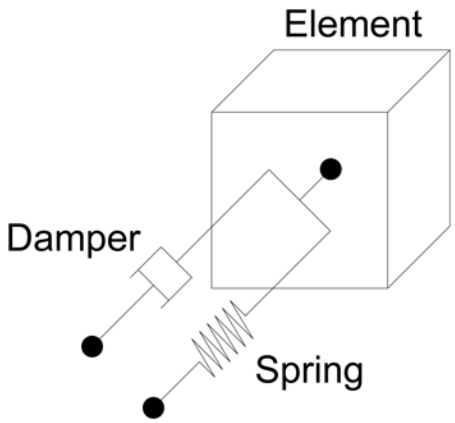

FIGURE 5.6: Simple illustration of the Kelvin-Voigt model for viscoelastic behavior

the out-of-plane degree of freedom of each element in the AEM model. Static loading was again applied incrementally to adequately represent the nonlinear geometric behavior observed during experimental testing. The AEM simulation was compared to the experimental results by examining the predicted midpoint deflection and the experimental midpoint deflection, as measured by the dial gage. Quantifying the fit between the predicted and measured load-deflection curves provided a metric for calibration of the model boundary conditions.

Optimal assignments for the stiffness of the boundary springs were determined through manual tuning of the spring stiffness assignments to arrive at the stiffness values resulting in the best fit to the experimental load-deflection curve. During this manual calibration process, all in-plane translational springs, regardless of edge direction, were assigned the same stiffness. Likewise, all rotational springs and all out-of-plane translational springs were grouped and assigned the same stiffness. Consequently, the model calibration was restricted to only three stiffness assignments. During the manual tuning process, it was observed that each of the three stiffness assignments independently affected the character-

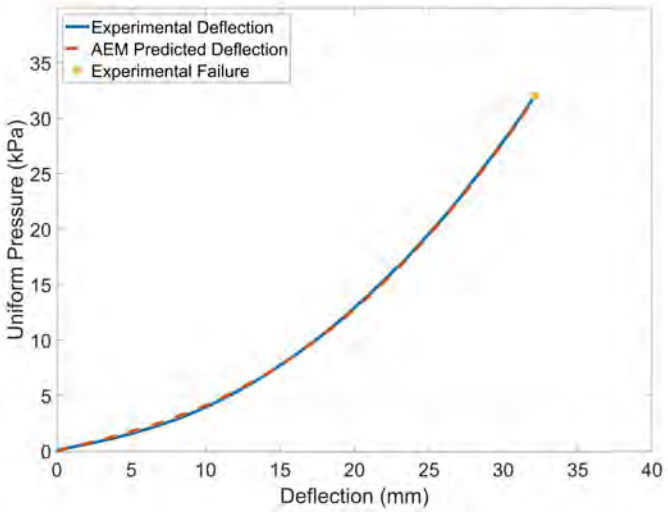

FIGURE 5.7: Comparison of the experimental static deflection to the deflection predicted using the tuned AEM model

istics of the load-displacement curve. This is observable in Figure 5.4. While an increase in the rotational stiffness corresponds to an almost immediate increase in the tangent stiffness throughout the full span of the load-displacement curve, an increase in the in-plane translational stiffness is insignificant at lower magnitude loading and only results in increased stiffness after membrane action is developed following significant geometric nonlinearity. Similar to the rotational stiffness, the out-of-plane translational stiffness was found to affect the tangent stiffness throughout the full range of the load-displacement curve. However, as previously evidenced by Figure 5.4, the out-of-plane stiffness alone was not capable of accurately predicting the response of the lite.

Strong correlation to the experimental load-deflection curve was achieved following this approach, as demonstrated in Figure 5.7, which depicts the experimental load-deflection curve in comparison to the load-deflection curve predicted with implementation of the calibrated stiffness values presented in Table 5.1. Validation of the boundary assignments was

TABLE 5.1: Calibrated AEM boundary spring parameters

In-Plane Translational Stiffness	577.9 N/cm (330 lb/in)
Out-of-Plane Translational Stiffness	490.4 N/cm (280 lb/in)
Rotational Stiffness	1186.2 N-cm/rad (105 lb-in/rad)

provided through comparison of the measured and predicted full-field deflections, which are plotted in Figure 5.8. As described in Chapter 4, full-field deflections were measured at specified increments of midpoint deflection. Comparison of the predicted full-field deflections at the corresponding load increments indicates strong correlation between the measured and predicted deflection patterns. The predicted load-deflection curve and full-field deflections demonstrate that the boundary stiffnesses have been successfully calibrated to predict a similar response to the experimental results.

As an additional means of validation, the calibrated stiffness of the out-of-plane boundary springs is compared to the experimentally measured load-displacement response of the rubber gaskets. As described in Chapter 4, the rubber gaskets were subjected to static loading to develop a load-displacement curve, which is plotted in comparison to the calibrated, linear elastic stiffness parameter assignment in the out-of-plane degree of freedom in Figure 5.9. Although the linear elastic boundary spring is not able to replicate the mildly nonlinear response of the rubber gaskets, the similar magnitudes of resistance provided across the range of displacements expected near the boundary of the lite supports the plausibility of the out-of-plane stiffness assigned to the boundary springs in the model.

Calibration of the viscoelastic material model was accomplished through manual tuning of the material damping coefficient implemented in the Kelvin-Voigt model. The damping coefficient was determined through optimizing the correlation between the predicted and

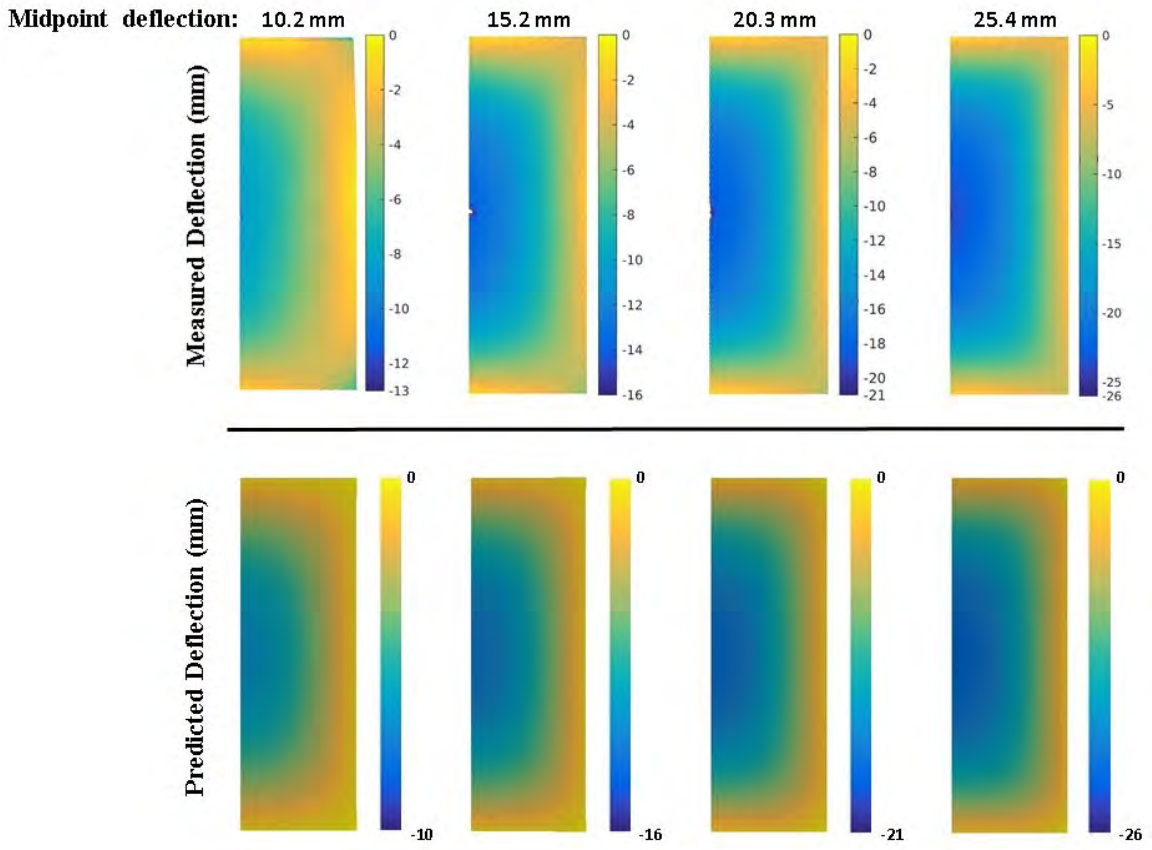

FIGURE 5.8: Comparison of the measured full-field deflections to the full-field deflections predicted by the calibrated Applied Element model

measured natural frequencies, which, as described in Chapter 4, were measured across the full set of experimental tests. Determination of the non-proportionally damped modal response of the Applied Element model was facilitated by assembling the state matrix of the system. The state matrix of the system, $[A]$, is developed from a state-space representation of the multiple degree of freedom model and is constructed with the global stiffness, mass, and damping matrices, denoted $[K]$, $[M]$, and $[C]$, respectively.

$$[A] = \begin{bmatrix} [0] & [I] \\ -\left[M^{-1}K\right] & -\left[M^{-1}C\right] \end{bmatrix} \tag{5.3}$$

In Equation 5.3, $[0]$ is a matrix of zeros and $[I]$ is an identity matrix, both of which are

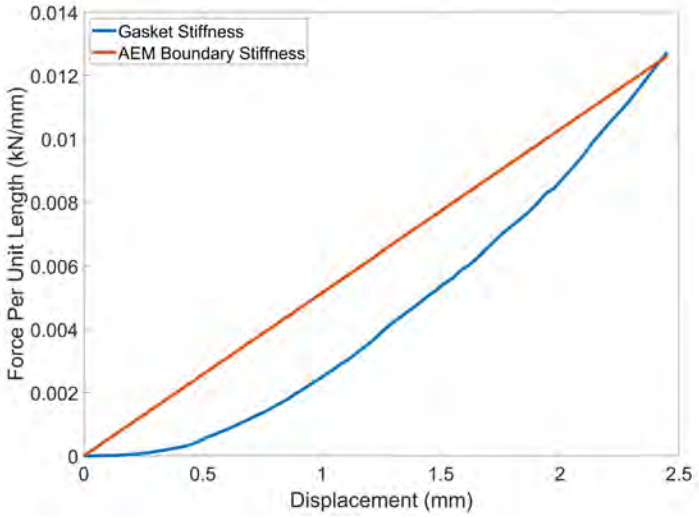

FIGURE 5.9: Comparison of the stiffness of the out-of-plane boundary springs in the AEM model to the experimentally measured stiffness of the rubber gasket

dimensionally similar to the stiffness, mass, and damping matrices (Roemer and Mook, 1992). A set of predicted natural frequencies and corresponding mode shapes for the damped AEM model could then be determined by eigenanalysis of matrix $[A]$. It should be noted that since the global damping matrix is required for compilation of matrix $[A]$, the results determined following this methodology are affected by the structural damping assigned to the glass lite, which was implemented with mass proportional damping. Equation 3.34 was used to determine the mass proportional damping coefficient as the product of the assigned damping ratio of the fundamental mode, the mass matrix, and the fundamental natural frequency, ω_1. For computation of the global damping matrix of the model, ω_1 was taken to be 33.0 Hz, which corresponds to the experimentally measured fundamental frequency of the glass lites subjected to open-arena blast testing. As described in Chapter 4, the average, experimentally estimated damping ratio of the fundamental mode was 0.025, or 2.5%. However, since this experimental measurement accounts for damping in

the entire assembly, including the viscoelastic response of the rubber gaskets, which were simulated using the Kelvin-Voigt model, a damping ratio typical of glass was selected for computation of the structural damping of the lite itself. It was observed in the literature that several past research studies, specifically Ramos et al. (2013) and Bedon et al. (2019), had experimentally estimated the damping ratio of clamped glass plates to range from 0.35% to 0.81% and 0.63% to 1.06%, respectively. The mass proportional damping in the AEM model was therefore established using an assumed damping ratio of 1%, since this value correlated with past studies without being unreasonably low relative to the experimentally estimated damping ratio.

While the experimental measurements compiled during static load testing were previously used for calibration of the boundary spring stiffnesses, the dashpot element in the Kelvin-Voigt model was calibrated using the experimental modal parameters averaged over open-arena blast testing, as presented in Figure 4.15. As noted in Chapter 4, the modal parameter estimate sets from static and open-arena blast testing indicated strong correlation to one another, with the exception of the fundamental mode. However, because damping plays a significant role in the prediction of dynamic behavior, and since the AEM model would be employed to predict the dynamic response of the specimens under blast loading, it was determined that the experimental modal parameter estimate set from open-arena blast testing should be implemented for calibration of the dynamic properties. The optimal damping value determined through manual tuning was evaluated using the objective function:

$$J = \sum \left| \frac{f_{exp} - f_{AEM}}{f_{exp}} \right| \tag{5.4}$$

where f_{exp} and f_{AEM} are the experimentally estimated and predicted natural frequencies, respectively, at corresponding modes. This objective function computes the sum of the percent differences between the experimental and analytical natural frequencies at the corresponding modes, which were paired using the Modal Assurance Criterion, which was implemented as described in Chapter 4. It should be noted that, because of the dissimilarity in the fundamental natural frequency between static and open-arena blast testing, the first mode was excluded from summation in the objective function.

An optimal solution for the Kelvin-Voigt damping coefficient was determined through manual tuning to be 0.001, and the modal parameter estimates predicted using the calibrated boundary assignments are presented in Figure 5.10 with comparison to the experimental modal parameter estimates. It is evident that strong correlation to the experimentally estimated modal parameter estimates was attained across the 11 modes.

The set of natural frequencies predicted using the calibrated boundary assignments is presented in Table 5.2. As demonstrated, the absolute percent difference is less than 5% for the majority of the modes, while the maximum, absolute percent difference is 8.5%. Furthermore, the importance of including the Kelvin-Voigt model is demonstrated by tabulation of the predicted natural frequencies with and without the dashpot. While some of the individual, predicted frequencies deviate slightly more from the experimental estimates when the dashpot is included, the overall fit of the results is improved. Further, the natural frequencies of all but three modes are consistently underpredicted when the dashpot is excluded. Inclusion of the dashpot results in a more uniform distribution of underpredicted and overpredicted natural frequencies, as demonstrated graphically in Figure 5.11. It is demonstrated in the following subsection that the effect of addressing the viscoelastic be-

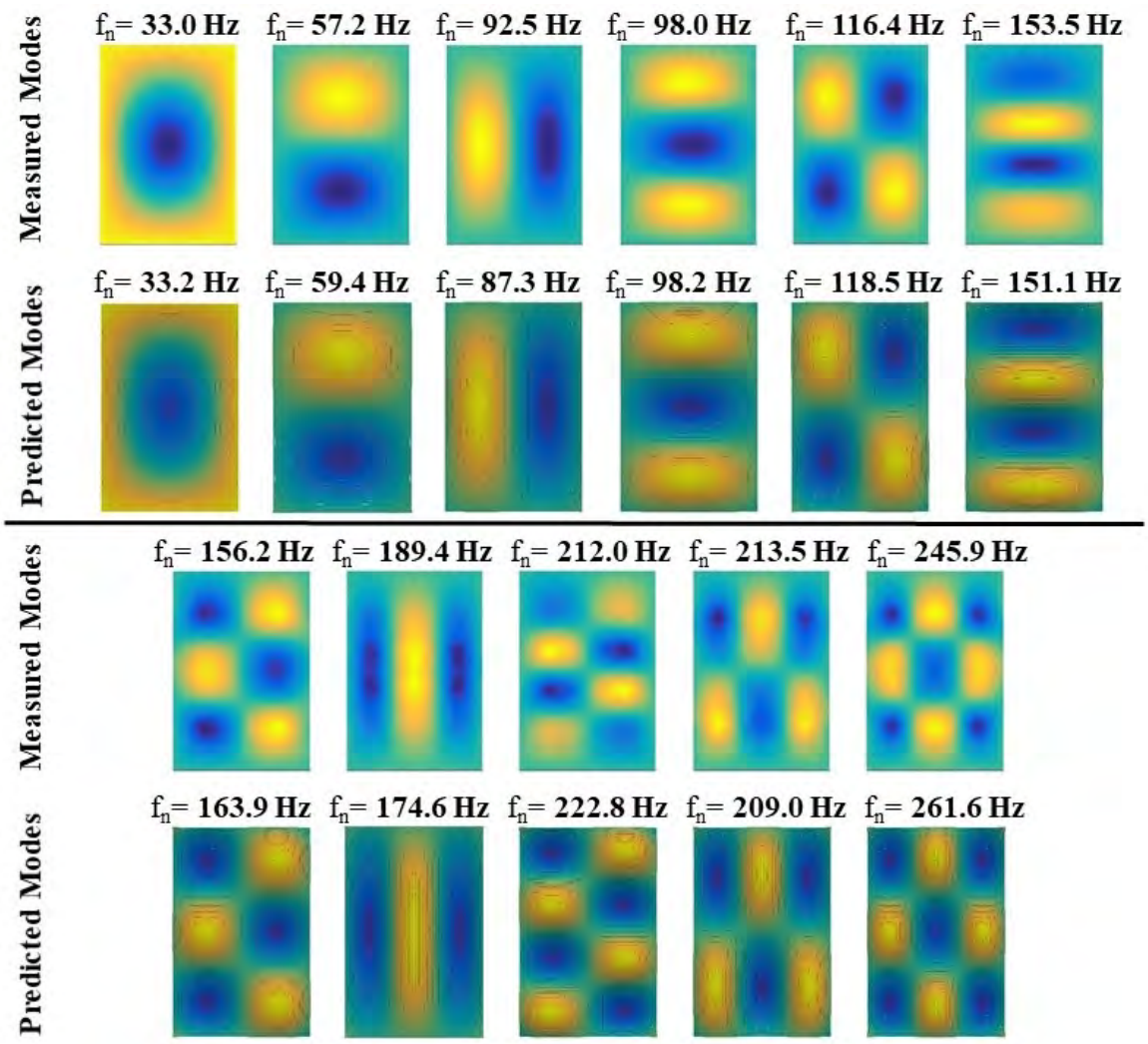

FIGURE 5.10: Comparison of the experimentally measured and AEM predicted modal parameter estimates

havior of the rubber gaskets using the Kelvin-Voigt model becomes more significant with further mesh refinement.

5.4 Effects of Refining the Mesh of the Applied Element Model

An additional Applied Element model was developed using the same material properties as previously described but with a reduced, 4.76 mm (0.1875 in) cubic mesh size, in order to examine the effects of mesh refinement on the boundary parameters and model correlation. In order to maintain uniformity between models with respect to the geometric loca-

TABLE 5.2: Comparison of the AEM predicted natural frequencies to the measured natural frequencies of lites subjected to blast testing

	Field Specimens	AEM Model without Dashpot	Difference	AEM Model with Dashpot	Difference
Mode	$f_n(Hz)$	$f_n(Hz)$	%	$f_n(Hz)$	%
1,1	33.0	33.16	+0.5	33.21	+0.6
1,2	57.2	59.01	+3.1	59.35	+3.6
2,1	92.5	86.45	-7.0	87.29	-6.0
1,3	98.0	96.74	-1.3	98.19	+0.2
2,2	116.4	115.60	-0.7	118.48	+1.8
1,4	153.5	146.63	-4.7	151.08	-1.6
2,3	156.2	156.27	0.0	163.91	+4.7
3,1	189.4	168.43	-12.5	174.56	-8.5
2,4	212.0	206.46	-2.7	222.81	+4.9
3,2	213.5	196.51	-8.6	209.01	-2.1
3,3	245.9	237.78	-3.4	261.63	+6.0

tion of the boundary stiffness assignments, the outer geometry of the model was reduced to 79.06 cm x 118.43 cm (31.125 in x 46.625 in). The geometries representing the free area of the glass lite therefore remained the same in both models. The refined mesh produces 42,164 elements, corresponding to 252,984 degrees of freedom. The boundary conditions were modeled as previously described through introduction of a viscoelastic spring-dashpot model to the edge elements. Since this model featured twice the number of boundary elements as the coarser meshed model, the stiffness assignments for the translational springs should be exactly half of that determined for the coarser mesh model. Consequently, the stiffness of the translational springs in the refined mesh model were established from the previous calibration. However, the rotational stiffness at the boundary was not found to scale proportionally with the mesh refinement. It is believed that this is a result of the small angle assumption used to derive the spring stiffnesses in the AEM formulation. To arrive at a rotational spring assignment for the refined mesh model, the manual calibration

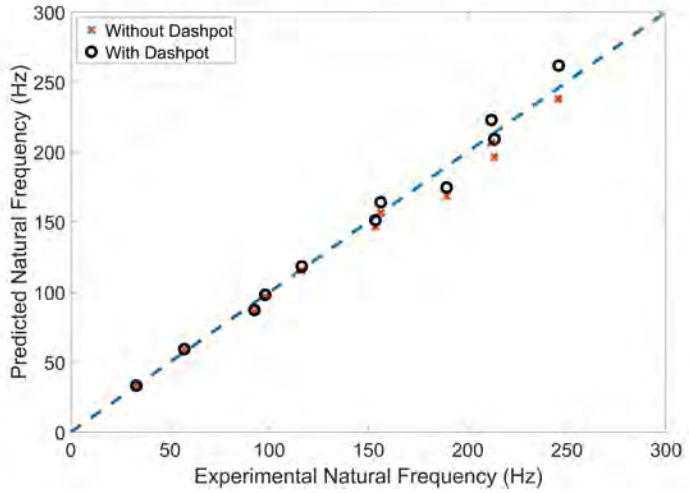

FIGURE 5.11: Comparison of the predicted natural frequencies with and without the dashpot

TABLE 5.3: Identified spring stiffness assignments of the refined meshed Applied Element model

In-Plane Translational Stiffness	83.2 N/cm (165 lb/in)
Out-of-Plane Translational Stiffness	245.2 N/cm (140 lb/in)
Rotational Stiffness	1073.3 N-cm/rad (95 lb-in/rad)

routine previously described was used. The identified values for the spring stiffness assignments are presented in Table 5.3. The predicted load-deflection curve is presented in Figure 5.12 with a comparison to the experimentally measured central deflection of the lite, and full-field deflections are compared in Figure 5.13. It is apparent that, as was the case for the model with the coarser mesh, strong correlation with the experimental deflection was achieved. It is further evident that, with the exception of the rotational stiffness, the magnitudes of the boundary spring stiffness parameters directly scaled with the mesh size.

Following static calibration, manual tuning of the viscoelastic dashpot elements was implemented with the previously described methodology to determine an optimal damping value to produce consistency with the measured dynamic properties of the lites. The damping value found to produce optimal correlation between the dynamic properties of the

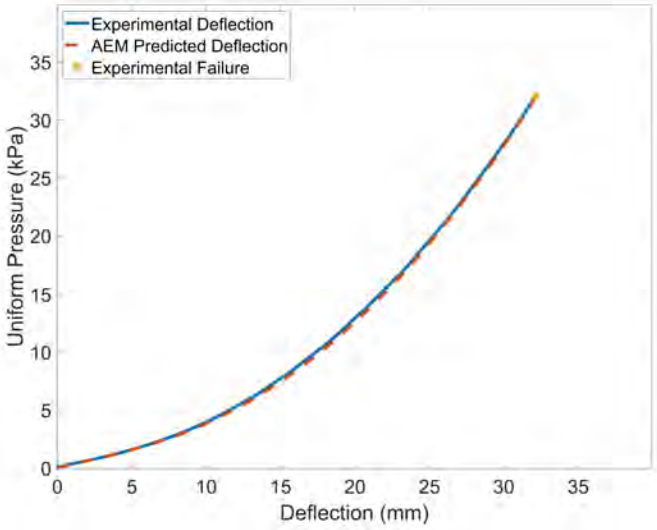

FIGURE 5.12: Comparison of the experimental static deflection to the deflection predicted by the tuned, fine mesh AEM model

model and the experimental modal parameter estimates was 0.004, which is a significant increase over the previously determined damping value for the model featuring a coarser mesh. Further, it was observed that inclusion of the Kelvin-Voigt model more significantly affected the modal parameter estimates of the refined mesh model. This is detailed in Table 5.4, where prediction errors for natural frequencies are presented for the case where the boundary is modeled as purely elastic and for the case where a viscoelastic boundary condition is modeled. While the predicted modal parameter estimates of the AEM model featuring the viscoelastic boundary indicate strong correlation with the experimental data, as further demonstrated visually in Figure 5.14, it is apparent that poor correlation is achieved when the boundary is simply modeled as linear elastic.

The observed difference in the rotational boundary assignments of the coarse and refined mesh models can be attributed to the interface spring stiffness formulation implemented in the AEM. Since the original derivation of the AEM was based on an assumption of

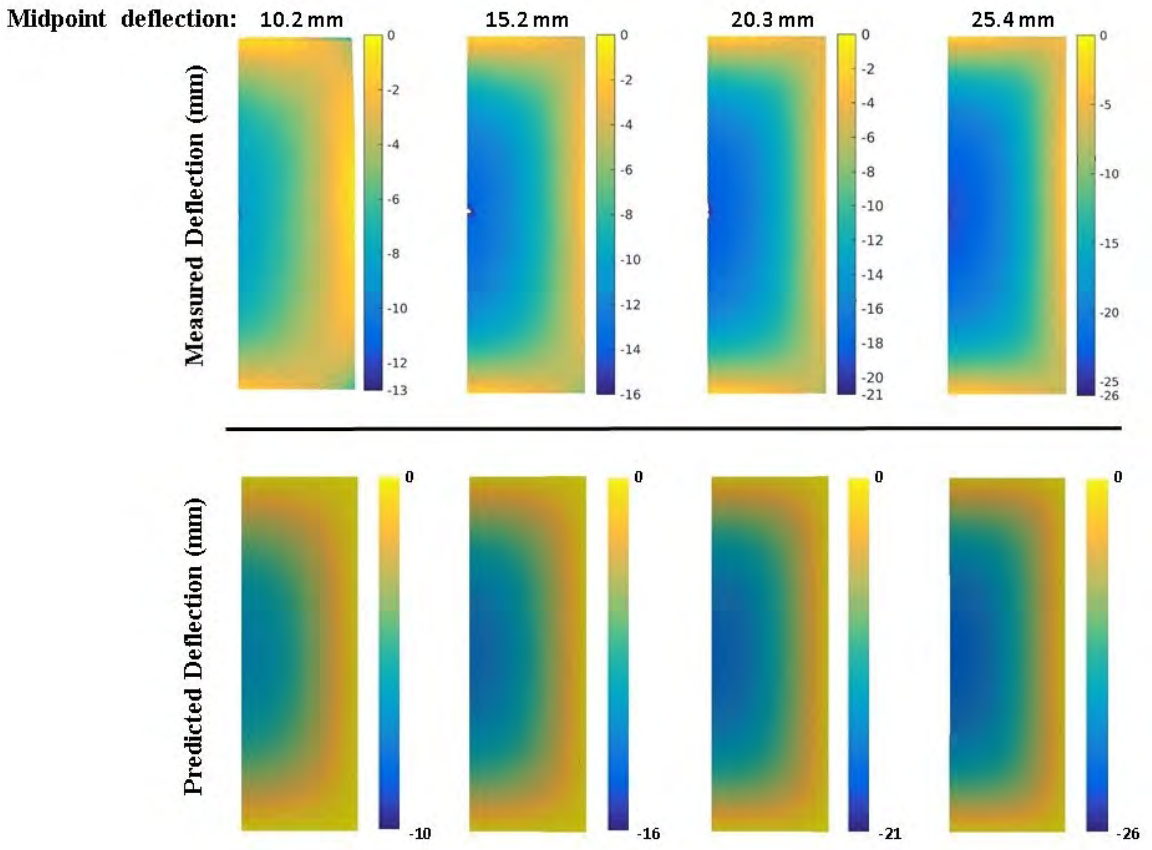

FIGURE 5.13: Comparison of the measured full-field deflection to the full-field deflection predicted by the calibrated, fine mesh Applied Element model

cuboid elements, implementation of non-cuboid, specifically plate-like, elements can result in underprediction of the interface spring shear stiffness in the in-plane translational degree of freedom. Since the in-plane shear stiffness is used for computing the interface spring rotational stiffness contribution, this noticeably affects the bending behavior of the model. The significant difference in the effect of the Kelvin-Voigt model is attributable to the greater sensitivity of the refined mesh model to changes in the rotational degree of freedom. While application of the damping to the rotational stiffness of the edge springs does not significantly affect the coarse mesh model, the modal parameter estimates of the refined mesh model are significantly affected. This difference is not observed for the out-of-plane

TABLE 5.4: Comparison of the refined mesh, AEM predicted natural frequencies to the measured natural frequencies of lites subjected to blast testing

	Field Specimens	AEM Model without Dashpot	Difference	AEM Model with Dashpot	Difference
Mode	$f_n(Hz)$	$f_n(Hz)$	%	$f_n(Hz)$	%
1,1	33.0	31.19	-5.8	32.00	-3.1
1,2	57.2	52.05	-9.9	54.64	-4.7
2,1	92.5	84.40	-9.6	91.86	-0.7
1,3	98.0	88.25	-11.0	95.27	-2.9
2,2	116.4	102.27	-13.8	114.18	-1.9
1,4	153.5	138.66	-10.7	153.88	+0.2
2,3	156.2	134.00	-16.6	153.77	-1.6
3,1	189.4	167.57	-13.0	196.19	+3.5
2,4	212.0	179.84	-17.9	211.13	-0.4
3,2	213.5	182.98	-16.7	218.21	+2.2
3,3	245.9	210.19	-14.5	256.19	+4.0

translational stiffness, which similarly affects both models.

5.5 Verification of the Calibrated AEM Model through Comparison to the FEM

Following calibration of the AEM model, the single glass lite was modeled using the FEM in the Abaqus software package for further verification of the model's behavior. The FEM model featured identical geometric and material properties to the previously developed FEM model featuring pinned boundary constraints. However, the boundary conditions were modeled using built-in connector elements, which featured assignable stiffness values in the translational and rotational degrees of freedom. Implementation of the connector elements facilitated calibration of the boundary stiffness in the in-plane translational, out-of-plane translational, and rotational degrees of freedom using the previously described methodology for calibration of the AEM model. The stiffness assignments of the connector elements were calibrated through manual tuning and produced the load-displacement curve presented in Figure 5.15 with comparison to the experimental measurements. The corre-

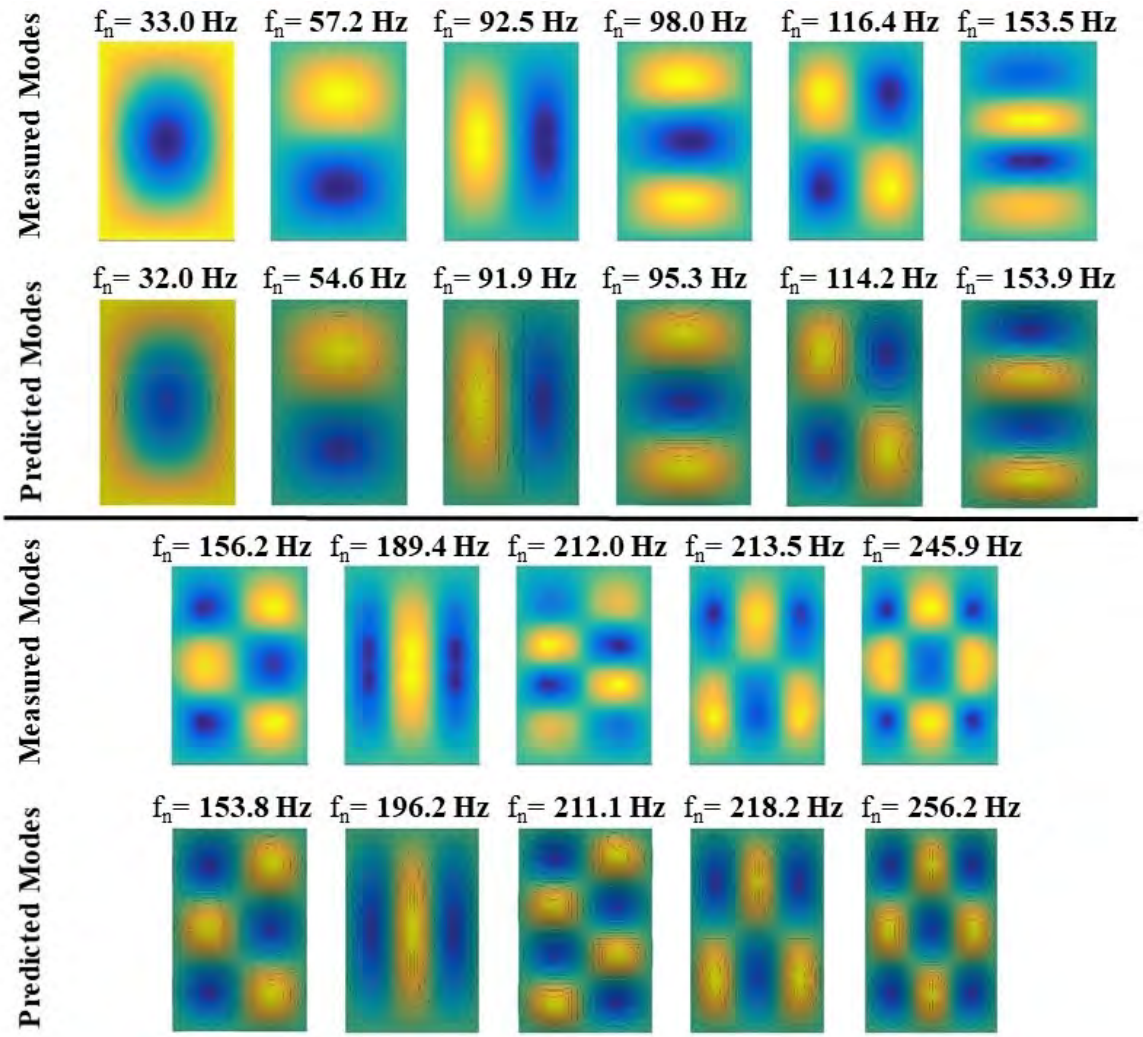

FIGURE 5.14: Comparison of the experimentally measured and predicted modal parameter estimates using the fine mesh Applied Element model

sponding, calibrated stiffness assignments are presented in Table 5.5. It is evident that, as was the case for the previously described AEM simulations, strong correlation with the experimentally measured load-deflection curve was achieved through manual tuning. Although similarity exists between the optimal solutions for the AEM and FEM simulations, some variation is exhibited, specifically in the in-plane stiffness assignment. It is believed that the difference in the boundary assignments between the two methods is related to the difference in the boundary spring elements, which are assigned about the Applied Element

TABLE 5.5: Calibrated FEM connector element stiffnesses

In-Plane Translational Stiffness	43.8 N/cm (25 lb/in)
Out-of-Plane Translational Stiffness	376.5 N/cm (215 lb/in)
Rotational Stiffness	157.6 N/cm/rad (90 lb/in/rad)

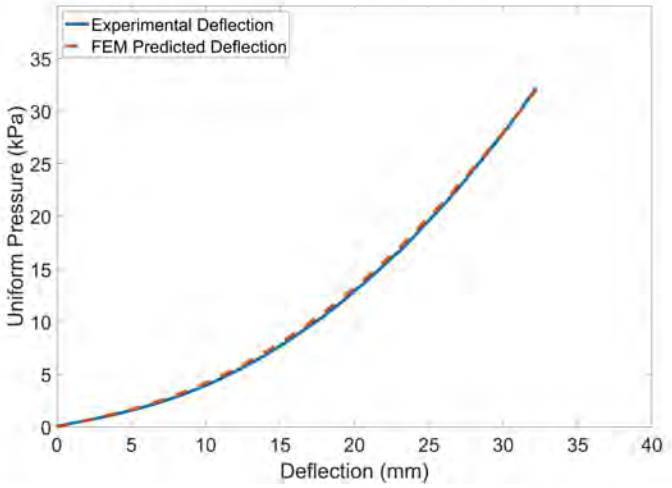

FIGURE 5.15: Comparison of the experimental static deflection to the deflection predicted by the FEM model

centroids, as opposed to the nodes of the Finite Elements.

The behavior of the rubber gaskets was again simulated using the previously described viscoelastic model, which was implemented in the FEM model through introduction of built-in damper elements acting in parallel with the out-of-plane translational and rotational connector elements. These damper elements were calibrated to the experimental modal parameter estimates using the previously described methodology for calibration of the dashpot elements in the AEM model. An optimal damping value of 0.0035 was determined through manual calibration, and the corresponding modal parameter estimates are presented in Table 5.6 with comparison to the modal parameter estimates predicted by the AEM model. In order to maintain uniformity between the modal comparisons, the AEM model featuring the refined mesh is implemented for the comparison, since the FEM

TABLE 5.6: Comparison of the AEM and FEM predicted natural frequencies to the measured natural frequencies of lites subjected to blast testing

	Field Specimens	AEM Model with Dashpot	Difference	FEM Model with Dashpot	Difference
Mode	$f_n(Hz)$	$f_n(Hz)$	%	$f_n(Hz)$	%
1,1	33.0	32.00	-3.1	32.10	-2.8
1,2	57.2	54.64	-4.7	55.56	-3.0
2,1	92.5	91.86	-0.7	90.16	-2.6
1,3	98.0	95.27	-2.9	96.03	-2.0
2,2	116.4	114.18	-1.9	114.36	-1.8
1,4	153.5	153.88	+0.2	153.73	+0.2
2,3	156.2	153.77	-1.6	155.47	-0.5
3,1	189.4	196.19	+3.5	189.39	0.0
2,4	212.0	211.13	-0.4	213.70	+0.8
3,2	213.5	218.21	+2.2	214.33	+0.4
3,3	245.9	256.19	+4.0	256.03	+4.0

model featured elements of the same size. It is evident that both the FEM and AEM models achieve strong, and very similar, correlation with the experimental modal parameter estimates.

5.6 Modeling of Residual Stresses and Tempered Glass Failure

As described in Chapter 2 and illustrated in Figure 2.7, the tempering process imparts a residual stress distribution through the thickness of tempered glass. Since the presence of residual stress significantly affects both the strength and the fragmentation pattern of the glass upon fracture initiation, including the residual stress distribution in the AEM model was necessary for accurate prediction of debris field formation under blast loading. None of the existing literature to date on the Applied Element Method addresses the incorporation of residual stress in the analysis, so a numerical approach needed to be formulated to facilitate the application of the AEM for tempered glass simulations. Likewise, the fracture process in tempered glass is unique in that it is driven by initial fracture at surface flaws, followed by

propagation of fracture through the inner region of the glass that is subject to tensile residual stress. A macro-scale modeling approach for this type of fracture process has also not been addressed with the AEM in the existing literature. The development and implementation of a failure model capable of reasonably predicting the fragmentation of tempered glass at the macro-scale was necessary to provide a plausible path toward simulating with the AEM the debris fields developed by tempered glass.

The AEM provides a natural way of incorporating residual stress distributions, since the state of stress throughout the model is described directly by the stress in the interface springs throughout the model. Since the stresses are described at each interface spring, inclusion of residual stresses in the simulations for this research has been accomplished by superposition of the residual stress assignments onto the calculated interface spring stresses through the thickness of the cross section of the elements. The residual stress assigned at each interface spring was established as the average of the theoretical residual stress distribution over the area associated with the interface spring by integration of Equation 2.4. Since the Applied Element analysis is performed using an incremental form of the equation of motion, the residual stresses are computed at the start of the simulation and stresses resulting from external loading are simply superimposed on the residual stresses.

While assignment of residual stress magnitudes can be incorporated with relative simplicity into the AEM simulations, the number of interface springs required for an accurate approximation of the effects of the residual stress was a further consideration that needed to be addressed prior to implementation. Assigning a residual stress magnitude at each interface spring through the thickness results in a stepwise approximation of the parabolic residual stress. This is demonstrated in Figure 5.16, which depicts the stepwise, approximated

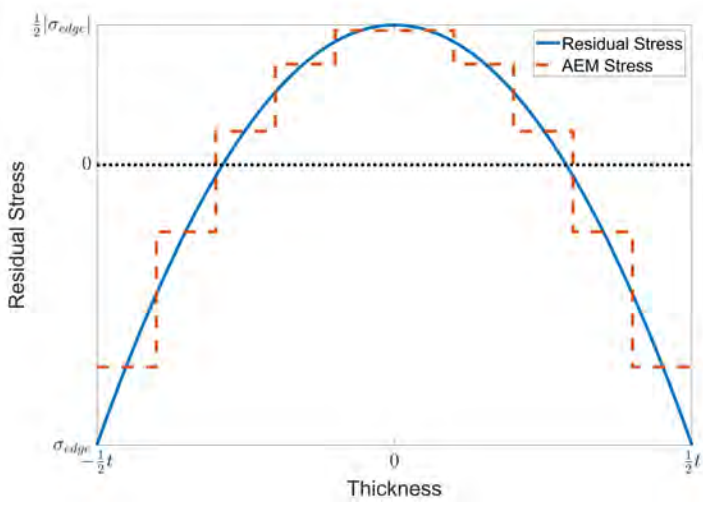

FIGURE 5.16: Comparison of the analytical residual stress distribution to the residual stresses assigned to the Applied Element model

residual stress distribution assigned over the 10 interface springs through the thickness of the Applied Elements compared to the analytical residual stress distribution. It is evident that an increased number of interface springs corresponds to a more accurate approximation of the residual stress distribution. However, because computation time increases with the number of interface springs, it is beneficial to examine the relationship between the number of interface springs and the predicted residual stress to balance the accuracy of the residual stress distribution with the computational expense.

It has been established that the extent of fragmentation in tempered glass depends on the elastic energy stored in the specimen through the residual stress distribution. Consequently, the number of springs through the thickness of the model should be dictated by the accuracy by which the stepwise approximation to the residual stress distribution replicates the true elastic strain energy. Pourmoghaddam and Schneider (2018) noted that integration of

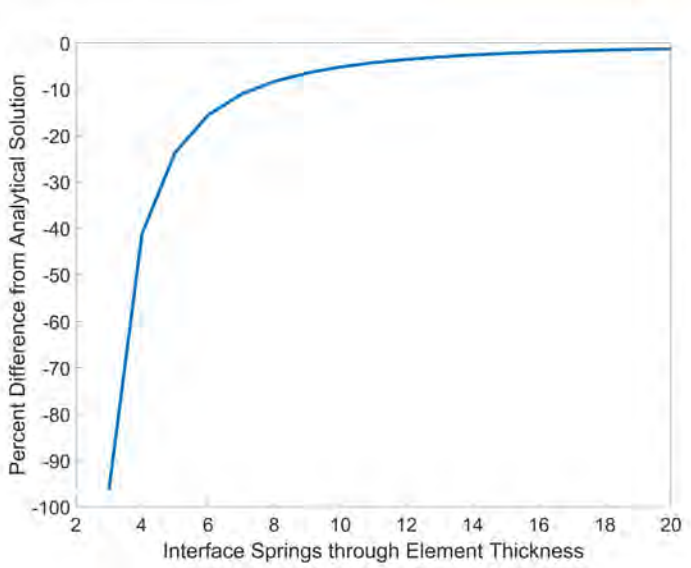

FIGURE 5.17: Convergence of the predicted strain energy with an increase in the number of interface springs

Equation 2.3 over the unit thickness of a specimen yields:

$$U = \frac{4}{5}\left(\frac{1-v}{E}\right)t\sigma_m^2 \tag{5.5}$$

where σ_m is the magnitude of the midpoint residual stress.

Convergence of the predicted strain energy in the Applied Element model with an increasing number of interface springs was examined by computing the elastic strain energy through the thickness of the model. Since the elastic strain energy is calculated as the integral of the residual stress distribution, the elastic strain energy through the Applied Element can be computed as the area under the stepwise residual stress distribution. As the number of interface springs increases, the percent difference between the elastic strain energy in the AEM model and analytical solution decreases exponentially, as shown in Figure 5.17. It is evident that the rate of convergence sharply decreases as more than 6 interface springs are implemented. Implementation of 20 interface springs through the element thickness

reduces the absolute percent difference to 1.3%. Assignment of the residual stress distribution over 10 interface springs, which was selected for implementation in this study to balance the accuracy with the increased computational cost, results in a 5.2% difference between the predicted strain energy and the analytical solution. It should be noted that application of residual stresses through the element thickness is unchanged for the finer, cubic mesh. Since the residual stress distribution is assigned to the interface springs through the element thickness, which remained the same for both models, the previously presented residual stress distribution is again applicable.

The residual stress distribution corresponding to a surface compressive stress of 68.9 MPa (10 ksi) was selected for the simulations developed for this research. As described in the literature, this is the minimum value required for classification as fully tempered, per ASTM C1048-18. Further, as noted in the literature, past studies have observed development of crack branching to correspond to minimum elastic strain energies of 35 J/m^2 (2.40 ft-lb$_f$/ft^2) (Fineberg, 2006) and 50 J/m^2 (3.43 ft-lb$_f$/ft^2) (Pourmoghaddam and Schneider, 2018). For the 4.76 mm (0.1875 in) thickness of the specimens in this research, implementation of a residual stress distribution corresponding to a 68.9 MPa (10 ksi) surface compressive stress results in a theoretical strain energy of 48.7 J/m^2 (3.34 ft-lb$_f$/ft^2), as computed using Equation 2.3.

Simulation of glass lite failure requires implementation of a failure model. As discussed and demonstrated in Chapter 3, element separation can be simulated in the AEM through removal of interface springs and redistribution of the associated forces. However, for the verification of brittle failure presented in Chapter 3, spring failure was determined simply by the Rankine criteria. Although applicable for the purposes of the presented verification

problem, use of the principal stress as the sole failure criteria for the glass lite models is inhibited by the residual stress distribution, which can result in increased tensile stresses in the subsurface interface springs. As described in the literature, tempered glass fails at the surface, even when higher magnitudes of principal stress exist below the surface. Use of the Rankine failure criteria for tempered glass simulations therefore requires restricting the initial spring failure to the layers of interface springs nearest the outermost surfaces of the AEM model. Following failure in the outermost layer of interface springs, spring failure was allowed in the subsequent layer. After failure had occurred in the two outermost spring layers, any spring through the element thickness was allowed to fail based on Rankine criteria.

Following initial failure in the outermost layers of interface springs based on Rankine criteria, a further challenge in development of the failure model was presented by the release of the strain energy associated with the residual stress. Since the extensive fragmentation of the glass lite after initial failure could not be accurately replicated simply by allowing springs to continue failing based on Rankine criteria, a macro-scale failure model for behavior of the glass lite after initial fracture was developed based on the known velocity of the fragmentation front in tempered glass. This velocity has been experimentally determined in past studies to be approximately 1,500 m/s (59,055 in/s) in tempered soda-lime glass (Schardin, 1959; Varner and Wightman, 2012; Quinn, 2019). The macro-scale failure model implemented into the Applied Element simulation uses a radius that propagates outward from the initial spring failure location at this velocity. Any interface springs located within the calculated radius at each timestep are permitted to be removed from the simulation to represent crack propagation if their maximum principal stress exceeds the specified

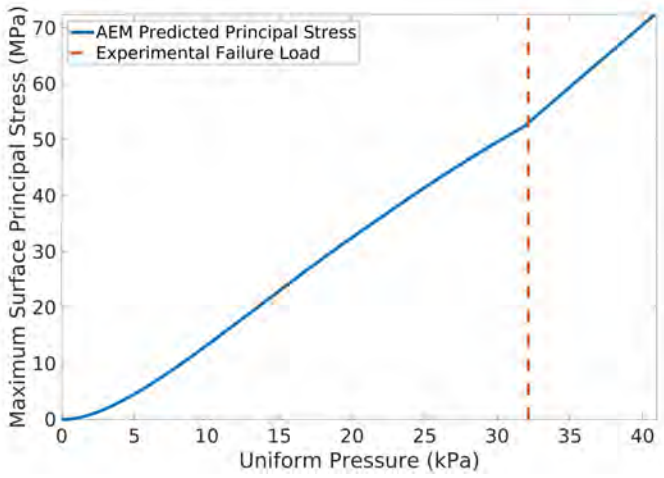

FIGURE 5.18: Maximum surface principal stress predicted by the AEM model under static loading with a surface residual compression of 68.9 MPa (10 ksi)

failure strength.

The developed macro-scale failure model employs a deterministic glass strength, although the assigned deterministic strength can be calculated to correspond with a specific probability of glass lite failure if a probabilistic model is available for the glass strength. When simulating the uniform static load experiment, the deterministic glass strength was established by analyzing the response of the coarser mesh model with the calibrated boundary conditions. The maximum principal stress across the surface layer of interface springs computed at the measured failure load of 32.13 kPa (4.66 psi) was used to establish the glass strength. This is demonstrated in Figure 5.18 for the case of the residual stress distribution corresponding to a 68.9 MPa (10 ksi) compressive residual stress, which, as previously described, was implemented because ASTM C1048 specifies this as the minimum surface compression for fully tempered glass. The experimental failure load of 32.13 kPa (4.66 psi) corresponds to a maximum surface principal stress of 53.0 MPa (7,688.95 psi).

The predicted fragmentation of the glass lite under static loading using the described

macro-scale failure model is presented in Figure 5.19, which presents renderings of the progressive element separation in the model. The corresponding experimental observations of the lite fragmentation under static loading, as captured by high-speed camera, are included for comparison of the predicted and experimental results. It should be noted that the experimental observation suggests that the lite fracture originated in the upper right corner and the fragmentation was consequently asymmetric. This is expected due to the random distribution of surface flaws and a deterministic simulation is not capable of replicating such behavior. It should also be noted that some of the experimentally observed fragmentation may not be visible in the high speed video, since the surface layer of paint used to enable the structured light scanning obscured the view of internal cracking in the glass lite. However, the AEM simulation does predict fragmentation typical of tempered glass and the relative size of the fragments appears consistent with the experimental observations. It should be noted that only complete element separation in the AEM is visible in the rendered image of the AEM simulation, but additional interface springs have failed within regions that appear to be larger contiguous areas, which would represent additional dicing of the glass.

Following development and implementation of the described failure model, a further comparison was conducted to verify that the macro-scale failure model results in plausible predictions for the effect of the residual stress distribution on the predicted failure load and fragmentation density. Five additional scenarios, including the case of annealed glass and four cases of residual stress distributions corresponding to compressive surface stresses of 17.2 MPa (2.5 ksi), 34.5 MPa (5.0 ksi), 51.7 MPa (7.5 ksi), and 86.2 MPa (12.5 ksi), were simulated using the previously described static loading model. Since the presence of resid-

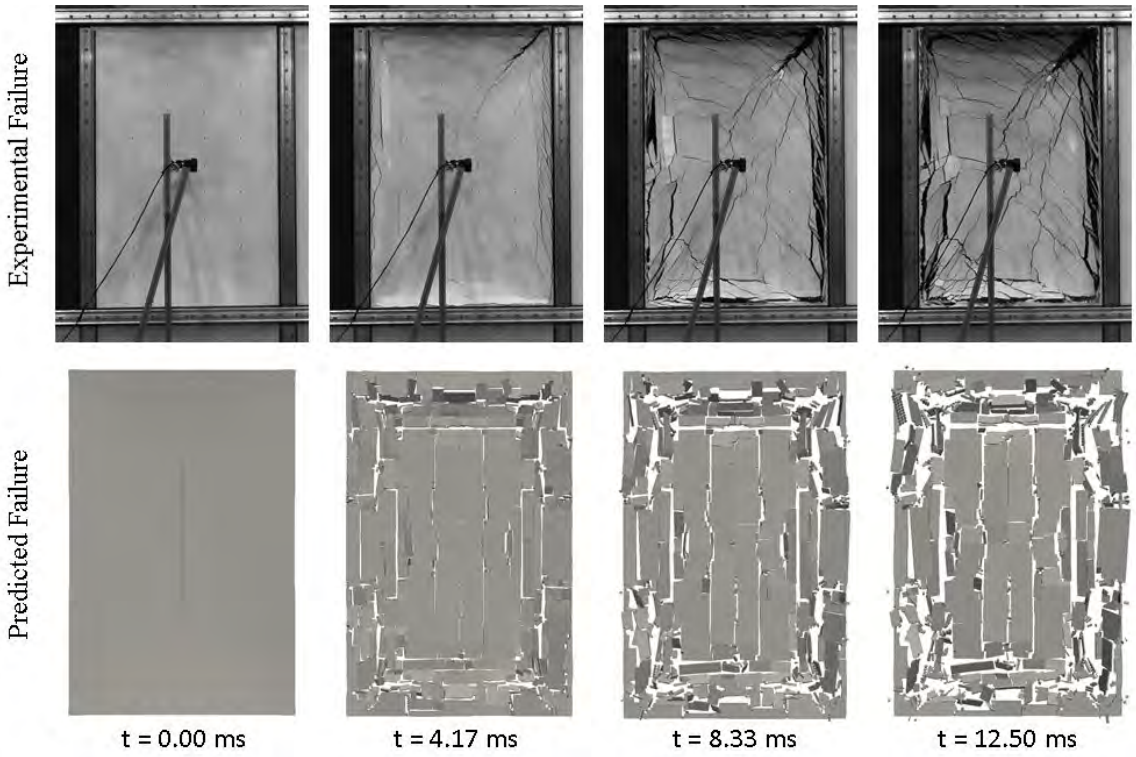

FIGURE 5.19: Predicted fragmentation under static loading with experimental observation for reference

ual stress should not affect the deterministic failure strength at the surface of the glass, the failure stress across all scenarios was assumed to be the previously determined value of 53.0 MPa (7,688.95 psi). The peak principal stress at each simulation increment for each case is plotted against the predicted uniform pressure causing failure in Figure 5.20, and the corresponding, predicted failure pressures are tabulated in Table 5.7. As expected for an identical deterministic failure strength, an increase in the magnitude of the residual stress corresponds to an increase in the capacity of the lite. Renderings of the fragmentation of each model at 12.5 ms after initial fracture are presented in Figure 5.21. It is evident that as the residual stress increases, the increased internal strain energy released upon failure correlates with increased extent of fragmentation and fragmentation density. This is expected and is a well known phenomena for tempered glass fragmentation (Barsom, 1968;

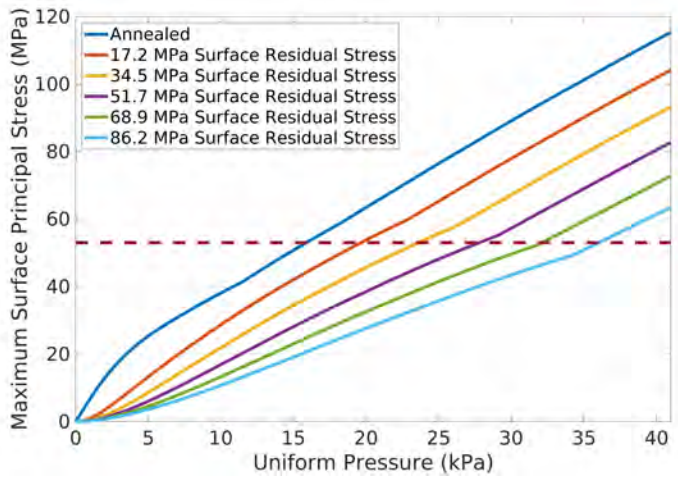

FIGURE 5.20: Maximum surface principal stresses under static loading predicted using the AEM model for varying cases of surface compression stress

TABLE 5.7: AEM predicted failure pressures corresponding to a failure stress of 37.0 MPa (5,363.19 psi) for varying cases of residual surface compression stress

Surface Residual Compression	Predicted Failure Pressure
0 MPa (0 ksi)	15.86 kPa (2.30 psi)
17.2 MPa (2.5 ksi)	19.65 kPa (2.85 psi)
34.5 MPa (5.0 ksi)	23.58 kPa (3.42 psi)
51.7 MPa (7.5 ksi)	27.79 kPa (4.03 psi)
68.9 MPa (10.0 ksi)	32.13 kPa (4.66 psi)
86.2 MPa (12.5 ksi)	35.99 kPa (5.22 psi)

Pourmoghaddam and Schneider, 2018). The importance of including the residual stress distribution is exemplified by the extreme differences in fragmentation observed for the annealed and tempered glass models. The annealed glass model and models with low residual surface compression stresses exhibit fragmentation into larger, shard-like sections of elements, typical of annealed and heat strengthened glass. Strain energies from residual surface compression stresses exceeding 51.7 MPa (7.5 ksi) are observed to be sufficient to produce extensive fragmentation and dicing that are characteristic of the crack branching that occurs in tempered glass fracture.

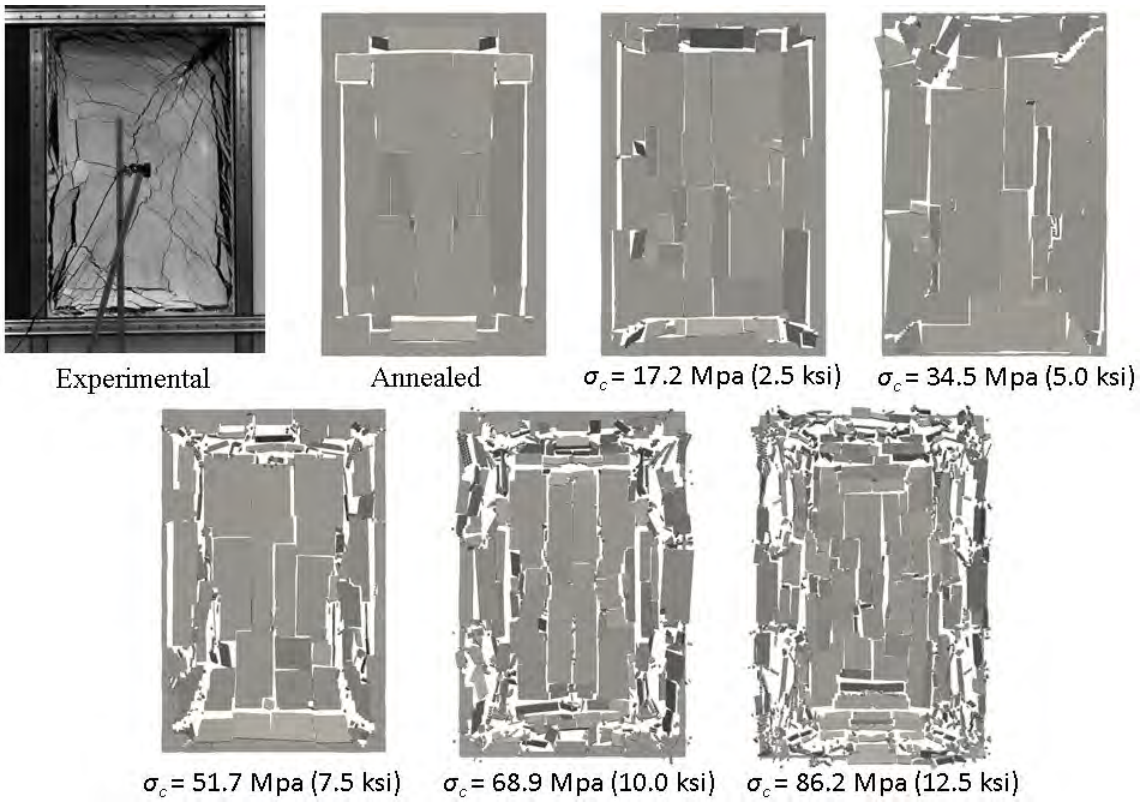

FIGURE 5.21: Experimental fragmentation at 12.5 ms after initial fracture compared to Applied Element simulations generated with different residual surface compression stress

5.7 Development of the Applied Element Model for Blast Loading

The glass lite specimens subjected to open-arena blast testing were modeled as an array of six identical Applied Element models positioned geometrically identical to the experimental setup. Since the results of the coarse mesh Applied Element model indicated strong correlation with experimental results, and because of the increased computational cost associated with the refined mesh model, the coarser of the two meshes was implemented in AEM simulations of the open-arena blast tests. Each individual glass lite model in the array was identical to the coarse meshed model calibrated to the measured static load response and modal parameters. As was the case for calibration of the dynamic properties of the boundary conditions, mass proportional damping was implemented, where the global

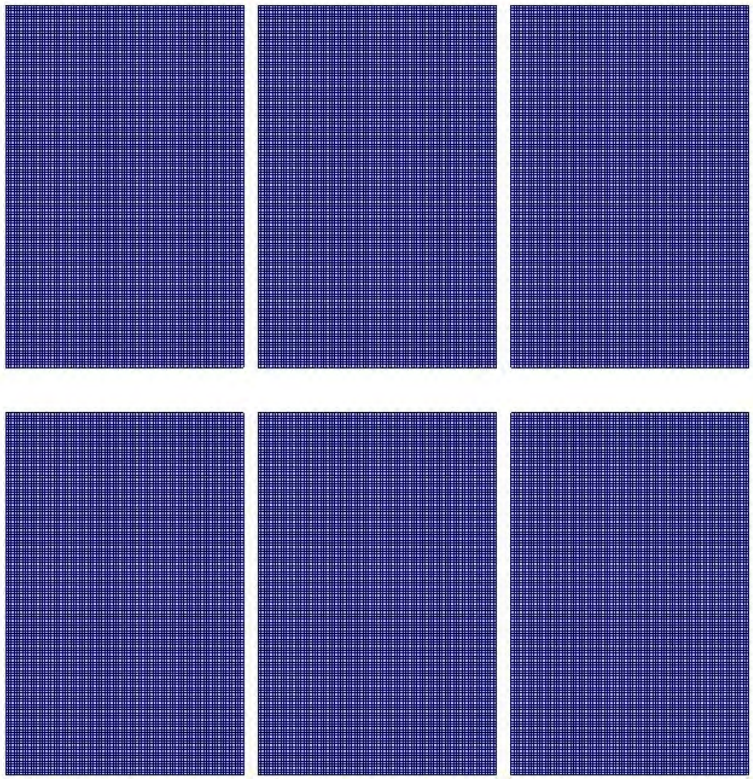

FIGURE 5.22: Rendering of the Applied Element mesh for simulation of the array of six lites in the open-arena blast tests

damping matrix was determined as:

$$[C] = \alpha[M] \tag{5.6}$$

where α is the mass proportional damping constant, which was computed to be 4.15 for a damping ratio of 0.01 and a fundamental frequency of 33.0 Hz. A rendering of the Applied Element model is presented in Figure 5.22.

As described in the literature review, the peak reflected pressure under blast loading and the subsequent decay of the pressure wave are typically represented using the modified Friedlander equation shown in Equation 2.2. It is evident that Equation 2.2 requires the peak reflected overpressure, a dimensionless constant determined by the impulse that establishes the exponential rate of decay of the overpressure, and the duration of positive

phase loading for computing the reflected pressure as a function of time. For the AEM models described in this dissertation, the modified Friedlander equation was implemented over the dynamic, incremental blast analyses as:

$$p_r(t) = P_r\left(1 - \frac{t - t_a}{t_d}\right)e^{\frac{-b_i(t-t_a)}{t_d}} \tag{5.7}$$

where $p_r(t)$ is the reflected pressure as a function of time and therefore the reflected pressure at a specific simulation increment, P_r is the peak reflected pressure, b_i is the dimensionless constant, t is the time, t_a is the time of arrival of the blast pressure wave, and t_d is the duration of the blast pressure wave. The variables P_r, b_i, t_a, and t_d were estimated using Kingery-Bulmash polynomials, as described in the literature review, for the scenarios of charge location and optimal TNT equivalent weight, which are described in Chapter 4. This facilitated determination of the blast pressure time history acting on each element in the out-of-plane degree of freedom for each scenario of blast loading using Equation 5.7. It should be noted that as a result of the relatively short duration of blast waves, and to ensure that the dynamic response of the glass lites was adequately simulated, a timestep of 1e−05 was implemented in all simulations of open-arena blast testing. Since P_r, b_i, t_a, and t_d correlate with the predicted reflected pressure across the model as a function of time, the distributions of these variables across the model are plotted in Figure 5.23 for the scenario of Test 1, in which the charge was centered on the lower middle glass lite specimen, designated Lite 5. The symmetry of the blast loading model is evident, and it is further evident that the Applied Elements nearest the charge are subjected to the highest magnitudes of peak reflected pressures. Inversely, the time of arrival and duration of loading increase with increasing distance from the charge. Similar plots developed using

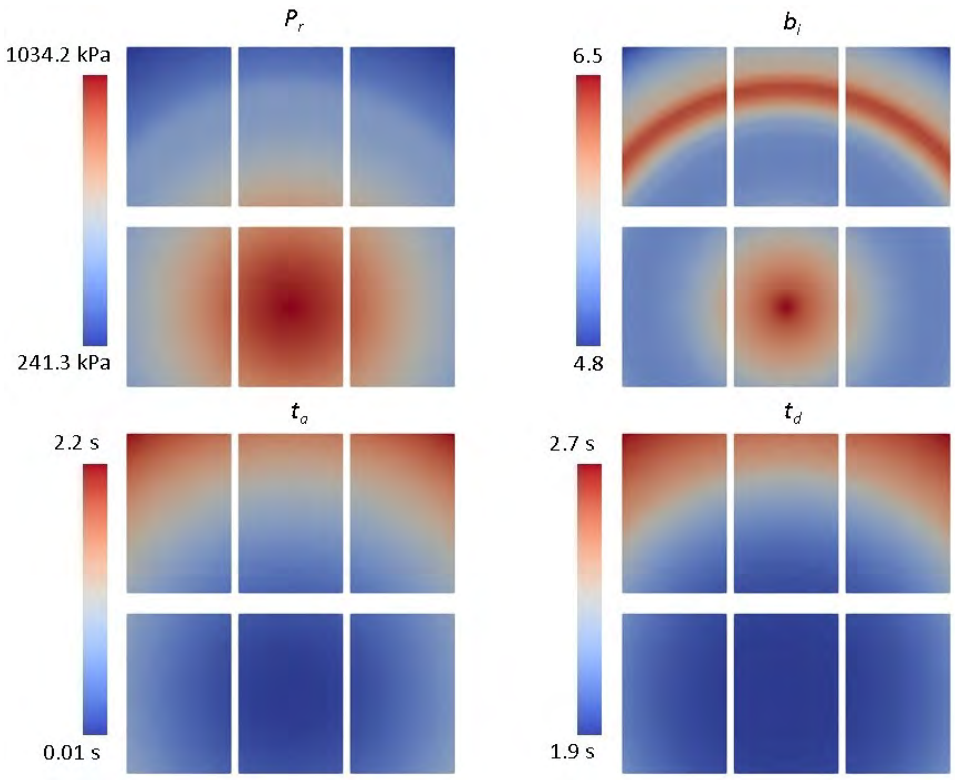

FIGURE 5.23: Predicted distribution of P_r, b_i, t_a, and t_d across the Applied Elements using the charge properties from Test 1

the charge properties of the remaining scenarios of open-arena blast testing are included in the Appendix in Figure C.1 through Figure C.5.

CHAPTER 6: PROBABILISTIC APPROACH TO LITE FRACTURE

As discussed in the literature review, prediction of glass failure is conventionally approached using a probabilistic model to forecast the probability of failure as a function of the computed failure risk factor, which is dependent on the geometry, material properties, external loading, and the condition of the specimen. In this chapter, the Glass Failure Prediction Model and probabilistic methodologies described in the literature are extended to the Applied Element Method to produce the capability of estimating the failure probability of glass lite specimens subjected to static and dynamic loading. Surface flaw parameters for the glass failure prediction model are sourced from the literature, and the static test results are used to assess the plausibility of the cumulative failure probabilities computed using the Applied Element model. The Glass Failure Prediction Model is then applied to dynamic Applied Element analysis and used to simulate individual lite fracture probabilities across the six open-arena blast tests. Lastly, joint probabilities are computed for the different combinations of lite breakage patterns to assess the plausibility of the results relative to the experimental observations.

6.1 Prediction of Failure Probability using the Applied Element Models

As described in Chapter 2, the failure behavior of a glass lite is dependent upon the surface condition of the specimen, because fracture initiates at a surface flaw. Since the surface flaw distribution varies widely across specimens, glass failure is conventionally predicted

using the previously described Glass Failure Prediction Model, which computes the failure probability using Equation 2.5. As described in the literature review, the failure probability is dependent upon a failure risk factor, denoted as B and computed using Equation 2.6, that considers the geometric properties of the specimen, the surface flaw parameters, and internal stresses, which are incorporated into the risk factor through the 60 second equivalent maximum principal stress and the biaxial stress correction factor. Although the geometry and surface condition are physical properties of a specific specimen and must be measured or estimated, the 60 second equivalent maximum principal stress and the biaxial stress correction factor were predicted using the previously described Applied Element models, which were adapted for probabilistic analysis.

6.1.1 Prediction of Failure Probability under Static Loading

As described in Beason and Morgan (1984) and demonstrated in Equation 2.6, the failure risk factor is determined cumulatively over the surface area of the specimen. Since the biaxial stress correction factor and equivalent maximum principal stress are featured in the failure risk factor, application of Equation 2.6 requires computation of the minimum and maximum principal stresses across the surface area of the specimen. As previously described in Chapters 3 and 5, the Applied Element method provides a means for determining the principal stress throughout the entire model, since the state of stress is described by the calculated stress components in each interface spring. This facilitates characterization of the principal stresses throughout the model by computing the minimum and maximum principal stresses, σ_{min} and σ_{max}, respectively, at every interface spring. It should be noted that, although the principal stresses are computed at every interface spring, only the layers

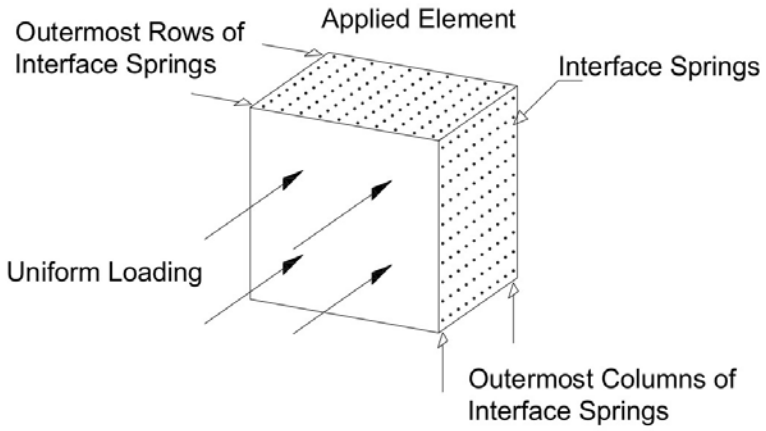

FIGURE 6.1: Identification of the surface layers of interface springs

of interface springs nearest the outermost surfaces were implemented in the probabilistic failure model, since failure of a glass specimen will typically occur at the surface. This is illustrated in Figure 6.1. For the case of annealed glass, σ_{min} and σ_{max} are directly computed as the predicted minimum and maximum principal stresses. This facilitates determination of the 60 second equivalent principal stresses, the equivalent ratio of minimum to maximum 60 second equivalent principal stresses, denoted r_{equiv}, and the biaxial stress correction factor at every surface interface spring. The 60 second equivalent maximum principal stress, $\hat{\sigma}_{max}(x, y)$, is determined by Equation 2.7, which transforms the maximum principal stress using the load duration, t_d. For the static loading simulations, the 60 second equivalent maximum and minimum principal stresses were computed simply as the maximum and minimum principal stresses in the plane of the lite, since the rate of loading was sufficiently slow in the laboratory test. As described in Chapter 4, the uniform pressure load was increased incrementally and held nearly constant for a duration of 60 seconds at each increment, so rate dependent effects are assumed to be negligible for this test.

For the case of tempered glass, the surface compressive residual stresses must be consid-

ered when computing the maximum and minimum 60 second equivalent principal stresses. As prescribed in ASTM E1300, the surface compressive stress should be subtracted from the predicted minimum and maximum principal stresses (ASTM, 2016). This is readily accomplished in the Applied Element simulation since the residual stress distribution is superimposed on the calculated principal stresses. It should be noted that, when determining the maximum and minimum principal stresses for use in the probabilistic failure model, only the principal stresses occurring in the plane of the lite were considered, since the probabilistic failure model is based on plane stress analysis. This corresponds to the assigned residual stress distribution, which was superimposed over only the in-plane stresses.

Following determination of the 60 second equivalent principal stresses for either annealed or tempered glass, the biaxial stress correction factor at each interface spring can be determined using Equation 2.8, and the failure risk factor at each interface spring can subsequently be computed through adaptation of Equation 2.6. Adaptation of Equation 2.6 to determine the individual failure risk of one interface spring in the Applied Element Method yields the risk function:

$$B_{spring} = k\left[C(x,y)\hat{\sigma}_{max}(x,y)\right]^{m} A_s \tag{6.1}$$

where A_s is the surface area attributed to an individual interface spring in the model. Since uniform element sizes and uniform interface spring distributions were implemented for the developed Applied Element simulations, A_s was determined for all cases as the surface area of one Applied Element divided by the number of springs per element considered in the probabilistic model. This resulted in 20 springs per element, since 10 outermost surface springs were associated with each face. Alternatively, this surface area per spring can be

calculated by dividing the total surface area of the lite by the total number of interface springs on that surface. The cumulative failure risk factor of the full glass lite was computed through summation of the failure risk factor of every interface spring throughout the model as:

$$B_{lite} = \sum B_{spring} \tag{6.2}$$

This summation is equivalent to computing the joint probability of failure for any of the surface interface springs in the model. Determination of the lite failure probability was accomplished by substitution of the cumulative failure risk of the lite into Equation 2.5. Implementation of the procedures described in Beason and Morgan (1984) for prediction of failure probability under uniform static pressure is therefore accomplished with relative simplicity using the AEM.

6.1.2 Prediction of Failure Probability under Blast Loading

Implementation of the described probabilistic model requires further modification for prediction of the failure probability under dynamic blast loading. Specifically, the normalization of the load duration through 60 second equivalent principal stresses can not be performed directly using Equation 2.7, since the principal stress is time dependent and not associated with an easily determined reference duration. Likewise, the biaxial stress correction factor is time dependent.

Adaptation of the failure probability model for incremental, dynamic analyses was addressed in Wei et al. (2006), where it was noted that a 60 second equivalent maximum principal stress can be determined using the integral of the time varying principal stress

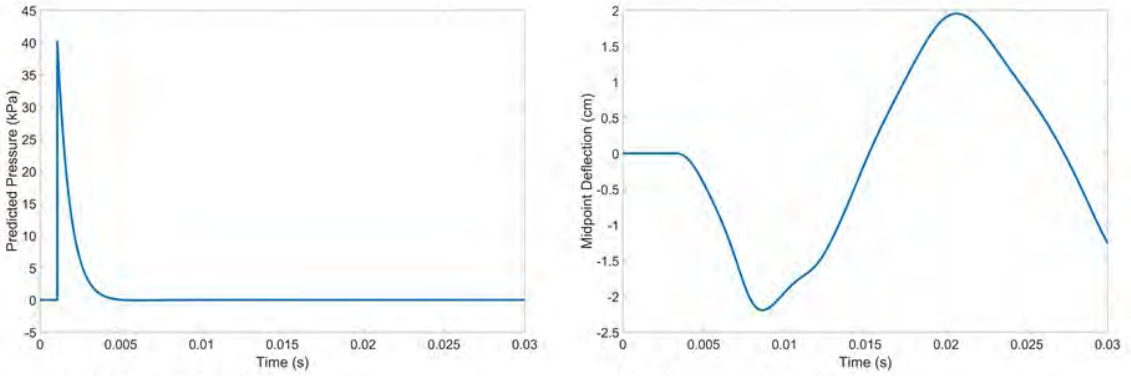

a) Blast overpressure b) Midpoint deflection

FIGURE 6.2: Comparison of the reflected pressure and corresponding midpoint deflection of a glass lite over the same time duration in the AEM simulation

with respect to time, as determined by:

$$\hat{\sigma}_{max}(x,y) = \left[\frac{1}{60}\int_0^{t_d} \sigma_{max}(x,y,t)^n dt\right]^{\frac{1}{n}} \tag{6.3}$$

where $\sigma_{max}(x,y,t)$ is the maximum principal stress at coordinates x and y at time t, and n is a surface flaw parameter taken as 16. Equation 6.3 is similarly implemented using $\sigma_{min}(x,y,t)$ to determine the 60 second equivalent minimum principal stress, $\hat{\sigma}_{min}(x,y)$. For quasi-static and longer duration dynamic loading, such as wind, the duration of the loading is used to establish t_d. However, Wei et al. (2006) acknowledged that in most blast analyses, the dynamic response of the specimen continues for a longer duration than the relatively short duration of the positive phase of the blast overpressure. This is demonstrated in Figure 6.2, which compares the reflected pressure and the deflection predicted at the midpoint of a glass lite in the AEM blast loading model. It is evident that the duration of the reflected pressure wave is significantly shorter than the duration of the response of the lite. Since the stresses in the lite develop over the full duration of the simulation response, the load duration, t_d, is recommended to be taken as the duration of the positive phase response of

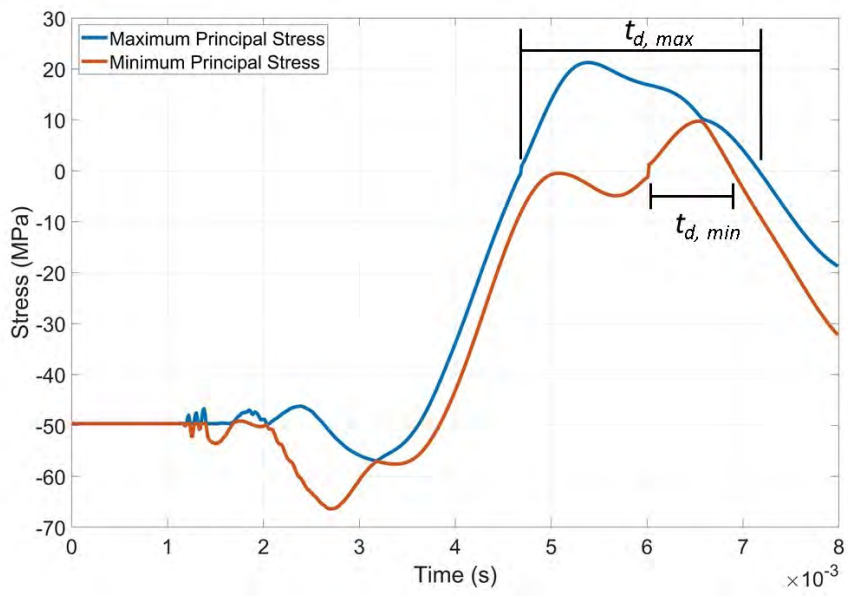

FIGURE 6.3: Comparison of the maximum and minimum principal stress at the same point of the AEM glass lite model during the predicted response to blast loading

the specimen, instead of the duration of the blast wave (Wei et al., 2006). This methodology was adapted for use in the AEM simulations by allowing the integration to occur only when the principal stress is positive. This is demonstrated in Figure 6.3, which plots AEM results for minimum and maximum principal stresses at one location of the glass lite over a portion of its response to blast loading. It is evident that the principal stresses are not uniformly positive for equal durations of the response. The durations of the integration, denoted $t_{d,max}$ and $t_{d,min}$, which are used for computation of $\sigma_{max}(x, y, t)$ and $\sigma_{min}(x, y, t)$, respectively, therefore correspond to the durations when the respective principal stress is positive. Numerical integration of Equation 6.3 at each interface spring during the incremental Applied Element simulation can be accomplished by summation of the product of the principal stress and the simulation timestep raised to the power n at each increment.

This methodology can be applied to cases of annealed glass, or tempered glass can be simulated through superposition of the residual stress distribution onto the computed, in-

plane principal stresses, as described for the static loading case. When applied to tempered glass, the numerical integration of Equation 6.3 should only be performed when the maximum principal stress is tensile, or positive. In this way, the 60 second equivalent maximum principal stress, and likewise the failure risk factor for the individual spring, will be zero at any location where the loading was not sufficient to overcome the large compressive surface residual stress in the lite. In other words, the probability of lite failure remains zero at any locations throughout the lite where the surface stress remains compressive. Following determination of the 60 second equivalent principal stresses at every spring location, the ratio of minimum to maximum 60 second equivalent principal stresses can be computed consistent with the ASTM E1300 approach using:

$$r_{equiv} = \frac{\hat{\sigma}_{min}(x,y)}{\hat{\sigma}_{max}(x,y)} \tag{6.4}$$

Similarly, the dynamic biaxial stress correction factor at each interface spring can then be determined by:

$$C_{dyn}(x,y) = \left[\frac{2}{\pi}\int_0^{\psi}\left(\cos^2\theta + r_{equiv}\sin^2\theta\right)^m d\theta\right]^{\frac{1}{m}} \tag{6.5}$$

It should also be noted that the nature of the equivalent stress calculation in Equation 6.3 requires that the numerical integration for the 60 second minimum principal stress be performed when the minimum principal stress is greater than zero. This is a simplification required by the nature of the stress equivalent calculation, which results in a condition where negative 60 second equivalent minimum principal stresses are approximated as zero. In the Glass Failure Prediction Model, the minimum principal stress is only used to calculate the biaxial stress correction factor. Furthermore, as shown in Figure 6.4, the effect of

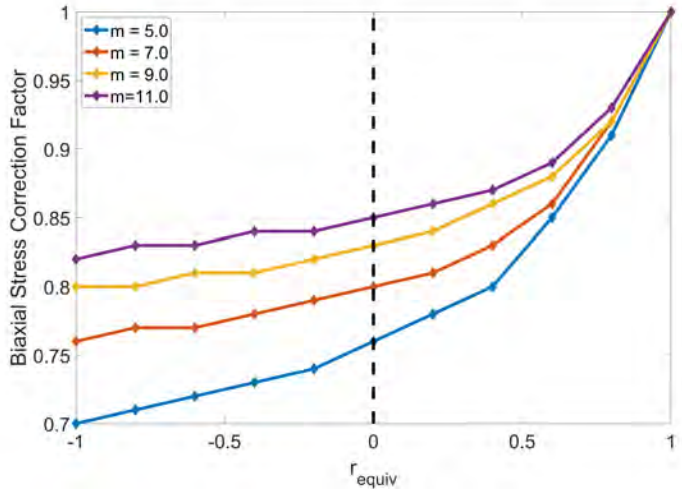

FIGURE 6.4: Relationship between r_{equiv} and the biaxial stress correction factor, as defined in Beason and Morgan (1984)

treating minimum principal stresses as zero, thereby limiting r_{equiv} to the range of 0 to 1, is insignificant, as the biaxial stress correction factor changes very little below 0. Substitution of the adapted biaxial stress correction factor and 60 second equivalent maximum principal stress into the failure risk function presented in Equation 2.6 yields the dynamic failure risk function determined by:

$$B_{dyn}(x,y) = k \int_0^w \int_0^h \left[C_{dyn}(x,y) \hat{\sigma}_{max}(x,y) \right]^m dxdy \tag{6.6}$$

As was the case for static loading, determination of the failure risk factor at each interface spring allows for subsequent numerical computation of the failure risk factor of each glass lite by summation of the interface spring failure risk factors. Similarly, the failure probability is computed by substitution of the failure risk factor into Equation 2.5.

6.1.3 Verification of Surface Flaw Parameters with Static Response

As demonstrated, the stress inputs required for implementation of the Glass Failure Prediction model can be computed using the AEM. However, accurate prediction of the failure

probability requires estimation of the surface flaw parameters, k and m, which describe the surface flaw distribution. The values of these parameters are conventionally obtained for a specimen by subjecting a large set of nominally identical glass specimens to experimental failure testing, which is conducted using an experimental setup similar to the static test described in Chapter 4 (Abiassi, 1981), or by sourcing empirical values from the literature. Since static failure testing of a sample size suitable for estimation of k and m was beyond the scope of this research, reasonable estimates for the flaw parameters were sourced from the literature and evaluated using the AEM model developed for the uniform static load test. Surface flaw parameters were evaluated through implementation in the described Glass Failure Prediction Model to compute the cumulative failure probability distribution corresponding to the glass lite specimen under uniform static loading. By comparing the measured failure load from the single static test described in Chapter 4 to the cumulative failure probability distributions, a surface flaw parameter combination resulting in plausible agreement with the experimental result could be identified.

Following this methodology, the stresses across the surface of the glass lite were computed using the calibrated Applied Element model for uniform static loading, as previously described in Chapter 5, and the predicted failure probability at each load increment was determined using Equations 2.5, 2.6, 2.7, 2.8, and 2.9. The Applied Element model was implemented for nonlinear static analysis as described in Chapter 5, including superposition of the residual stress magnitudes, which, as prescribed in ASTM E1300, should be included for determination of the failure probability (ASTM, 2016). During this nonlinear static analysis, the glass was modeled as linear elastic with infinite tensile strength to eliminate nonlinear material response and spring removal. This is consistent with proba-

bilistic methods for estimating glass failure, as these methods only provide a measure of the probability of lite breakage and do not simulate the post-fracture behavior of the lites. The nonlinear static analysis was performed for uniform static pressures ranging from 0 to 41.4 kPa (6.0 psi) with load incrementation of 0.41 kPa (0.06 psi) per step.

The flaw parameters adopted for use in the AEM model were determined by evaluating and adjusting the flaw parameters recommended in ASTM E1300, since the ASTM flaw parameters are conventional design values. As described in the literature review, ASTM E1300 recommends 7.0 and 2.86 x 10^{-53} $N^{-7}m^{12}$ (1.365 x 10^{-29} in^{12} lb^{-7}) for parameters m and k, respectively, for design use. However, as noted in Beason et al. (1998), these flaw parameters are representative of a 20 year service life. Further, the ASTM flaw parameters were obtained from tests performed on annealed glass and developed using analytical formulas for the glass lite response, which assume idealized roller boundary conditions, in contrast to the calibrated boundary model featured in the AEM simulations. The flaw parameters recommended in ASTM E1300 were therefore evaluated using both the AEM model featuring the calibrated boundary conditions and the AEM model featuring roller boundary conditions. The resulting failure probability curve of each model is plotted in Figure 6.5 with comparison to the experimental failure load under static loading. Each curve indicates the predicted cumulative failure probability as a function of the applied uniform pressure. It is evident that the experimental failure load corresponds to a relatively low predicted probability of failure when the calibrated boundary conditions are implemented, while the roller boundary conditions result in a significantly higher prediction of the failure probability. The surface flaw parameters were therefore manually tuned such that the failure probability computed at the failure load observed in the experimental test

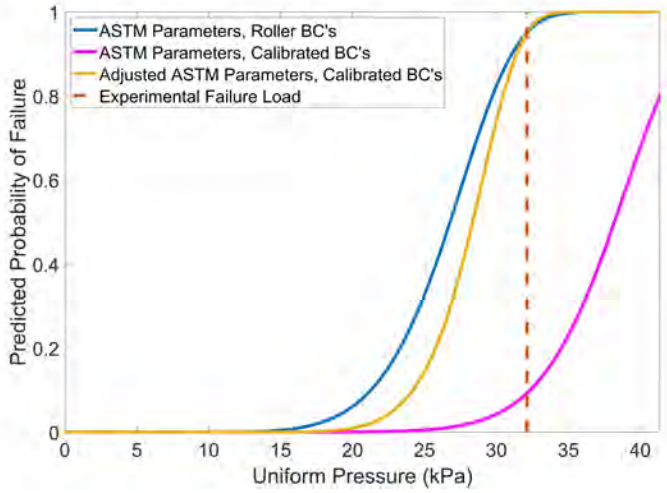

FIGURE 6.5: Cumulative failure probabilities predicted using roller constraints and tuned boundary conditions

was consistent between the AEM model with the calibrated boundary conditions and the model with the roller boundary conditions. This tuning only changed surface flaw parameter k and was done to compensate for the idealized analytical model used to derive the original surface flaw parameters adopted by ASTM E1300. Applying an adjustment factor of 31.0 yielded the third failure probability curve plotted in Figure 6.5 and resulted in flaw parameters of 7.0 and 8.87 x 10^{-52} $N^{-7}m^{12}$ (4.232 x 10^{-28} in^{12} lb^{-7}) for m and k, respectively. The experimental failure load corresponds to a predicted failure probability of 0.95 when the adjusted flaw parameter set is implemented.

6.2 AEM Models for Failure Probability under Blast Loading

The Applied Element model of the array of six glass lite specimens in the test facade, previously described in Chapter 5, was used along with the developed probabilistic failure analysis methodology described in Section 6.1.2 to predict the probability of failure for each glass lite in the open-arena blast tests described in Chapter 4. The AEM model used

for the probabilistic blast analysis featured the calibrated boundary spring assignments and implemented the adjusted flaw parameters, where values of 7.0 and 8.87 x 10^{-52} $N^{-7}m^{12}$ (4.232 x 10^{-28} in^{12} lb^{-7}) were assigned to m and k, respectively. The blast simulations used the known charge epicenters and estimated TNT equivalent charge masses, previously presented in Chapter 4 in Table 4.4. A timestep of 1 x 10^{-5} seconds was used for each simulation. As was the case for the static simulation, the probability of failure was calculated using the principal stresses from the surface layer of springs on the rear face of the lites.

Computation of the principal stresses at each of the spring locations facilitated determination of the equivalent maximum principal stress, $\hat{\sigma}_{max}$, equivalent minimum principal stress, $\hat{\sigma}_{max}$, and the biaxial stress correction factor, C_{dyn}, across the surface of the lite. The distributions of these variables across the rear (tensile) surfaces of the full set of glass lites are depicted for Test 1 in Figure 6.6. The 60 second equivalent maximum and minimum principal stresses, the duration of the integration, and the biaxial stress correction factor predicted using the AEM simulation performed with the calibrated boundary conditions are plotted for Test 1. The symmetry resulting from the centered charge location of Test 1 is apparent. The distribution of principal stresses, while having some similarity to the principal stress distribution under uniform loading, also clearly reflects significant interaction of modes of higher frequency than the fundamental mode. This is expected due to the relatively short standoff distance of the charge and serves to highlight the importance of high fidelity simulation rather than using nonlinear SDOF models, which capture only the behavior of the fundamental mode. Similar plots for the remaining tests are presented in Figures D.1 through Figure D.5 in the Appendix. Determination of these variables fa-

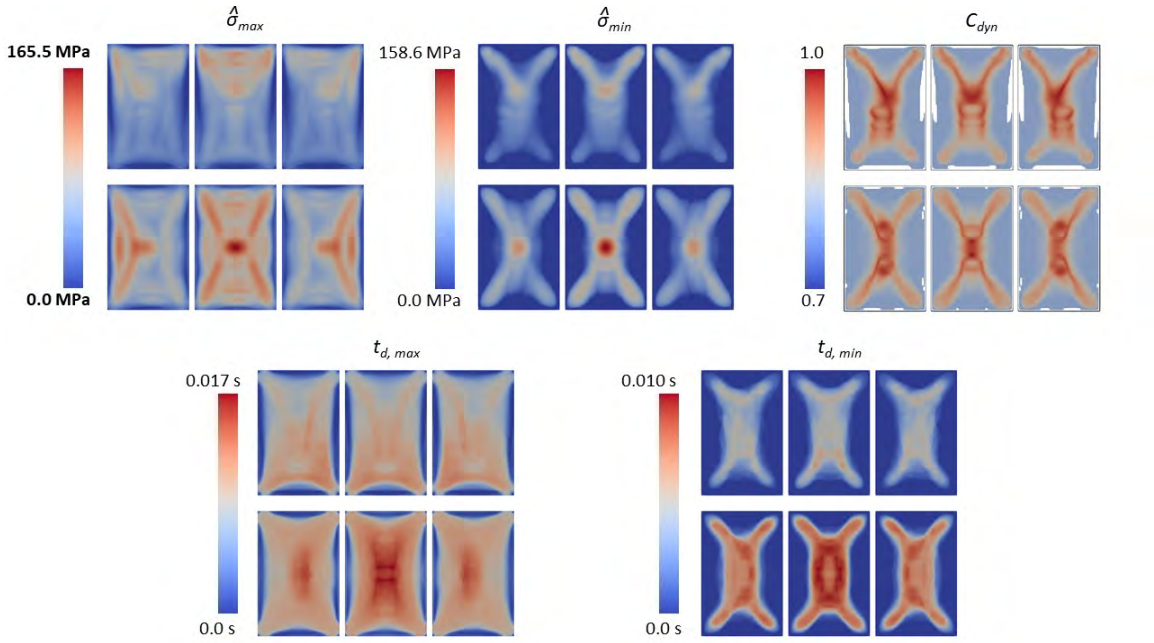

FIGURE 6.6: Predicted $\hat{\sigma}_{max}$, $\hat{\sigma}_{min}$, $t_{d,max}$, $t_{d,min}$, and C_{dyn} across the tensile surface of the glass lite using the calibrated AEM model for Test 1

cilitated subsequent computation of the cumulative failure probability across the tensile surface of the lite.

6.3 Predicted Failure Probabilities under Blast Loading

The failure probabilities for all glass lite specimens predicted using the AEM model are summarized in Figure 6.7 across all six open-arena blast tests. The complete specimen set is illustrated for each test with the corresponding predicted failure probability of each lite. Shading is used to denote specimens that failed during the experimental blast test program. It is notable that for all cases of observed lite failure, a nonzero failure probability is predicted, while a failure probability of less than 1.0 is predicted for all surviving glass lite specimens. However, it is evident that, with the exception of Test 3, in all cases where the blast overpressures were low enough to produce fracture of only a subset of the lites, a low failure probability is developed for many of the lites that did fail during the open-arena

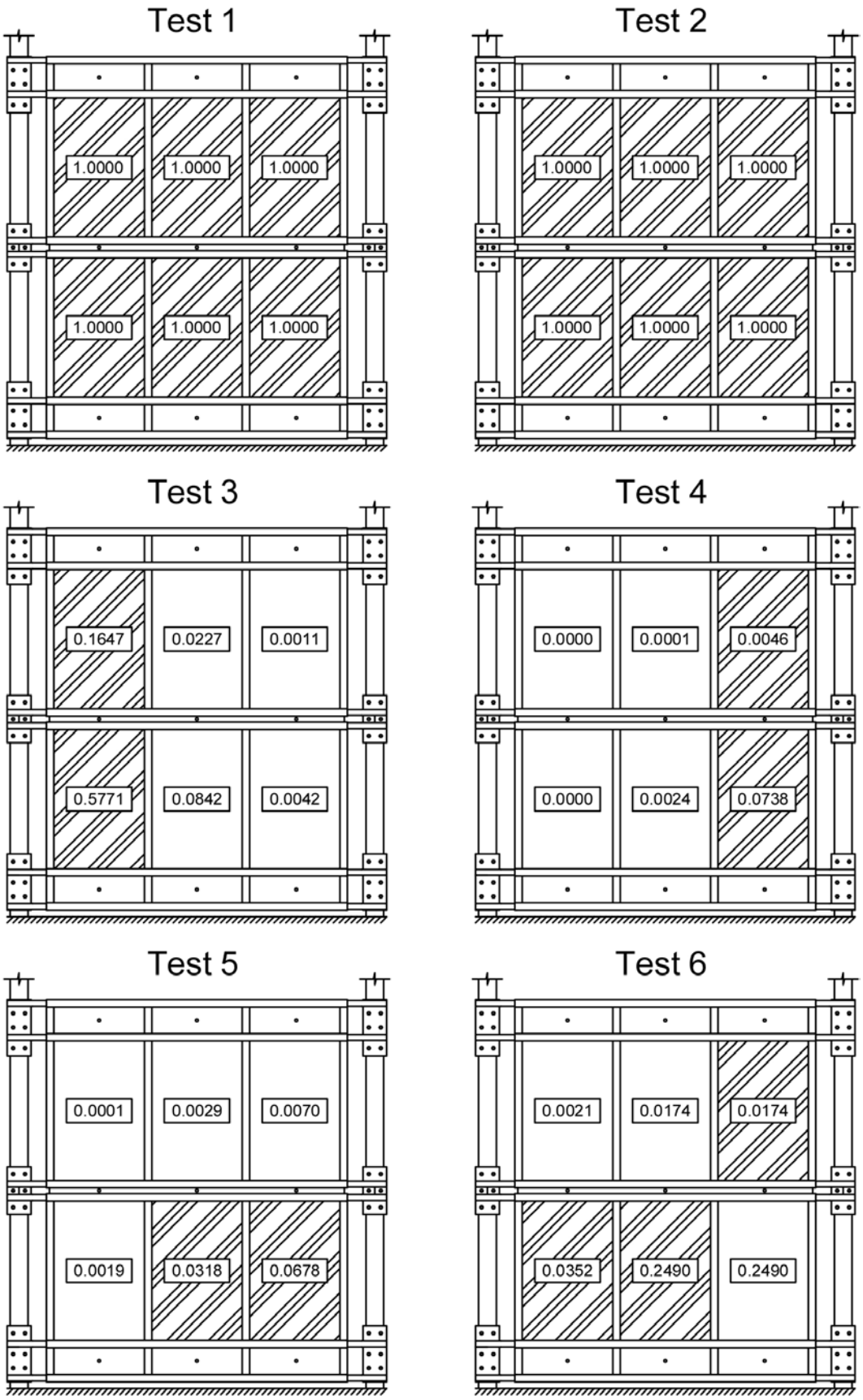

FIGURE 6.7: Failure probability of each glass lite specimen across all blast tests predicted using the AEM model

blast testing. The low failure probabilities are largely attributable to the unknown surface flaw parameters of the glass lite specimens. As previously detailed, the predicted failure probabilities produced by the Glass Failure Prediction Model are sensitive to changes in surface flaw parameters k and m, which can only be determined experimentally. Further, as noted in the literature review, Bove (1995) observed the importance of implementing flaw parameters developed specifically for tempered glass. Unlike annealed glass, the surface flaw parameters for tempered glass are sensitive to specimen geometry and size, which cannot be captured by a single set of k and m values. In addition to uncertainties in the surface flaw parameters, the low failure probabilities may be a result of extending the load duration factors from the glass failure prediction model, which is normally applied to durations on the order of seconds, down to millisecond durations. Due to the nature of blast loading, integration of the principal stress was completed over a load duration that is relatively short in comparison to the load durations conventionally encountered during in-service use. It is possible that the short duration contributed to the unexpectedly low failure probabilities. Further, it should be recognized that the blast simulations used to develop the individual failure probabilities used TNT equivalent charge masses that were based on calibrating Kingery-Bulmash blast parameters to match experimental measurements of reflected and incident pressures. In this process, the TNT equivalent masses were found to be significantly less than those expected based on published TNT equivalence for both PETN and ANFO. It is possible that experimental error lead to inaccurate measurement of the reflected and incident pressures and, consequently, that the AEM blast simulations were performed with blast overpressures that were significantly lower than those developed in the open-arena tests. Lastly, although the implemented probabilistic approach was modified to ad-

dress highly impulsive loading, it was not developed specifically for a blast environment, in which specimens are more susceptible to sustaining damage from debris impact. The AEM simulations do not account for the effects of any impacts from debris potentially projected toward the glass lites by the blast overpressure. Debris impact could have been responsible for producing failure in lites that otherwise would have a low probability of failure under the blast loading alone, such as Lite 3 in Test 4.

6.3.1 Computation of Joint Failure Probabilities

In a real-world scenario of post-blast forensic investigation and analysis, it is likely that information would be available on glass fracture and survival for a relatively large number of lites. Rather than evaluating individual glass lite failure probabilities, in such a scenario it would be more informative to examine the joint probabilities associated with the response of all lites observed in the field investigation. By computing the joint failure probabilities for different combinations, one could identify the most probable observation of lite failure across the set of available lites as well as any other plausible observations with joint probabilities above an established threshold.

Computation of joint failure probabilities was not completed for Tests 1 and 2, since a failure probability of 1.0 was predicted for all specimens. Further, it is evident from Figure 6.7 that although reasonable failure probabilities were predicted for Test 3, the predicted failure probabilities were low for the final three tests producing patterns of partial specimen breakage. Therefore, although joint probabilities were computed for all tests producing patterns of partial specimens breakage, Tests 4, 5, and 6 were specifically included to produce illustrative examples. The previously calculated failure probability for each glass

lite specimen facilitated subsequent determination of the joint probability associated with every possible combination of lite breakages in the facade. If the individual lite failures are treated as independent events, the joint probability corresponding to breakage patterns observed across the complete array of six lites, $P(s)$, is:

$$P_s = P_{Lite1} x P_{Lite2} x P_{Lite3} x P_{Lite4} x P_{Lite5} x P_{Lite6} \tag{6.7}$$

This joint probability was computed for every possible pattern of lite failure using the failure probabilities developed for each individual lite from the AEM simulation. This allowed for determination of the most probable scenarios of lite breakage across the facade with their corresponding probabilities. The predicted probability of the three most probable scenarios of lite breakage for Test 3, Test 4, Test 5, and Test 6 are presented in Figure 6.8, where shading is again used to denote specimen failure. For Test 3, the observed lite failure scenario was associated with a joint probability of more than 8%, while there is a predicted nearly 43% probability that the lower left lite nearest the charge would fail while the other lites survived. A joint probability of nearly 32% was associated with the scenario of survival of the complete specimen set. For the remaining Tests, the joint probabilities amplify the issues associated with the low failure probabilities forecast for the lites that were observed to fail. Since the highest failure probability of any lite in the remaining tests was less than 26%, and since significantly lower failure probabilities were forecast for the remaining lites, the observed lite failure scenario of each test produces a joint probability that is very low and the prediction model suggests that the most probable observation was all lites surviving their respective blast event.

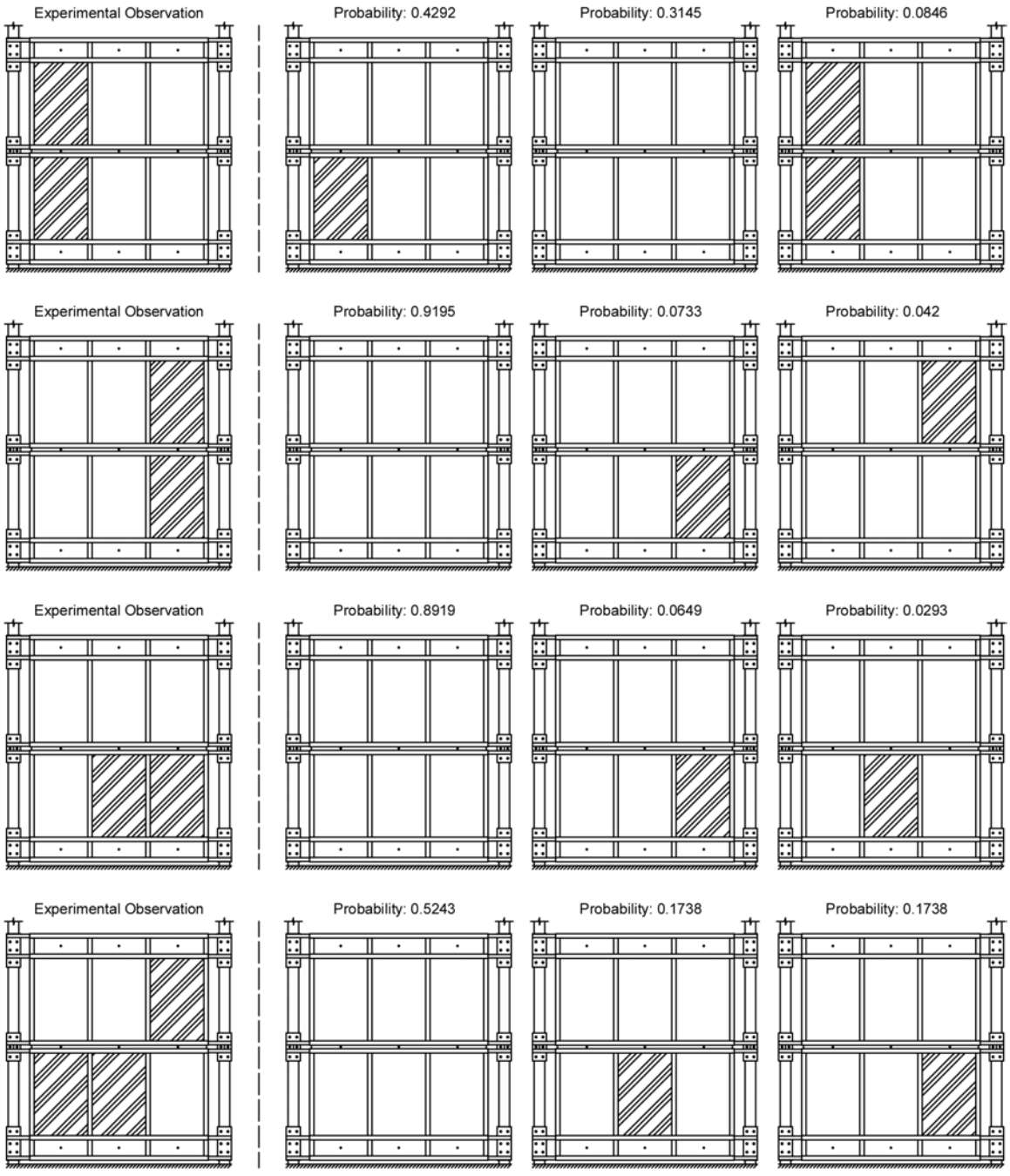

FIGURE 6.8: Three most probable scenarios of lite failure predicted for Test 3 through Test 6 with comparison to the observed failure patterns

6.4 Conclusion

The Glass Failure Prediction Model based on the Weibull probabilistic distribution and described in Chapter 2 was implemented for the first time within the Applied Element Method to predict the failure probability of glass lites subjected to static uniform loading and open-arena blast loading. Surface flaw parameters were sourced from a design standard, evaluated against results from experimental static testing, and adjusted modestly to account for the calibration of the boundary conditions in the model. The selected set of surface flaw parameters was found to produce plausible cumulative failure probability distributions for the uniformly loaded tempered glass lite relative to the measurements obtained during laboratory static testing. The Glass Failure Prediction Model was extended to dynamic analysis using the techniques proposed in Wei et al. (2006) modified for implementation in the Applied Element Method and to incorporate residual stresses in tempered glass. AEM simulations were performed for the six open-arena blast tests and probabilities of lite breakage were computed for each of the individual lites. In all observed instances of lite breakage, the predicted failure probability was nonzero. Likewise, for all instances of lites that did not break, the predicted probability was less than 1.0. However, unexpectedly low failure probabilities were calculated for most scenarios where the blast pressures were low enough that only a subset of the lites failed. The lower than expected failure probabilities are attributed to uncertainties in the surface flaw parameters for the Glass Failure Prediction Model, extension of the load duration correction to exceptionally short durations, potential experimental error in the measurement of reflected and incident pressures that were used to establish the blast loading used in the model, and potential effects of de-

bris blown into the glass lites during the explosion. Lastly, the use of joint probabilities to assess plausible and most probable scenarios of lite breakage across building facades with several glass lites was illustrated. Although a reasonable joint probability was computed for the breakage pattern observed for Test 3, generally low joint probabilities were associated with the observed failure probabilities of Tests 4 through 6.

CHAPTER 7: PREDICTION OF GLASS DEBRIS FIELDS USING THE AEM

7.1 Introduction

As discussed in the literature review and in Chapter 3, the AEM is advantageous for simulating debris field formation because of its ability to predict nonlinear dynamic response, fracture, fragmentation, particle dynamics, and contact behavior all in the same simulation. In this chapter, the AEM methodologies and models described in the previous chapters are adapted and implemented to simulate debris field formation under blast loading. Necessary extensions of the AEM software routines, including modeling of surfaces in the test enclosure, implementation of a contact model, and inclusion of aerodynamic drag forces on projected fragments are described. Fracture, fragmentation, and debris field formation are successfully simulated with the AEM, and the predicted debris field distributions are evaluated through comparison to the debris fields generated during the open-arena blast tests previously described in Chapter 4. Although the AEM moderately over predicts the debris throw in most simulations, the predicted debris fields exhibit generally good correlation with the experimental results. Possible causes of discrepancies between the experimental and predicted results are discussed at the end of this chapter.

7.2 AEM Models for Glass Debris Field Prediction

A primary objective of simulating the formation of glass debris fields following the fracture and fragmentation under blast loading was to predict the debris distributions for the

open-arena blast testing scenarios. In a post-blast forensic investigation, two primary types of observations for glass lites will be available: the presence or absence of glass lite failure, and the glass debris fields generated by lites that were damaged by the blast overpressures. While the probabilistic models in the previous chapter seek to address analysis of the first type of observation, field observations of debris field density and throw need to be complemented by numerical tools to support hypothesis testing of determined explosive charge properties.

Applied Element models for simulating glass failure and debris field formation were developed for all of the open-arena blast tests described in Chapter 4. Since the objective of this chapter is to predict debris field distributions, as opposed to predicting whether a specimen will fail, as addressed in the previous chapter, and since lite failure would be known to a practitioner in a post-blast forensic analysis, only the glass lites that failed during experimental testing were modeled in the AEM simulations. This avoided the computational expense required to simulate the response of all six lites in the facade when only a subset of the lites generated the debris field. Each blast simulation used the known charge epicenter and the corresponding TNT equivalent charge mass that was previously determined in Chapter 4 and presented in Table 4.4. The six simulations performed for prediction of debris field formation are visually summarized, including the number and location of the glass lite specimens with the epicenter and TNT equivalence of the charge, in Figure 7.1. Shading is used to denote the glass lite specimens included in each simulation. Each individual glass lite was modeled as geometrically identical to the AEM model of a single glass lite featuring the mesh size of 9.525 mm (0.375 in), as described in Chapter 5. This corresponded to 10,752 elements with 64,512 degrees of freedom per lite. The number of

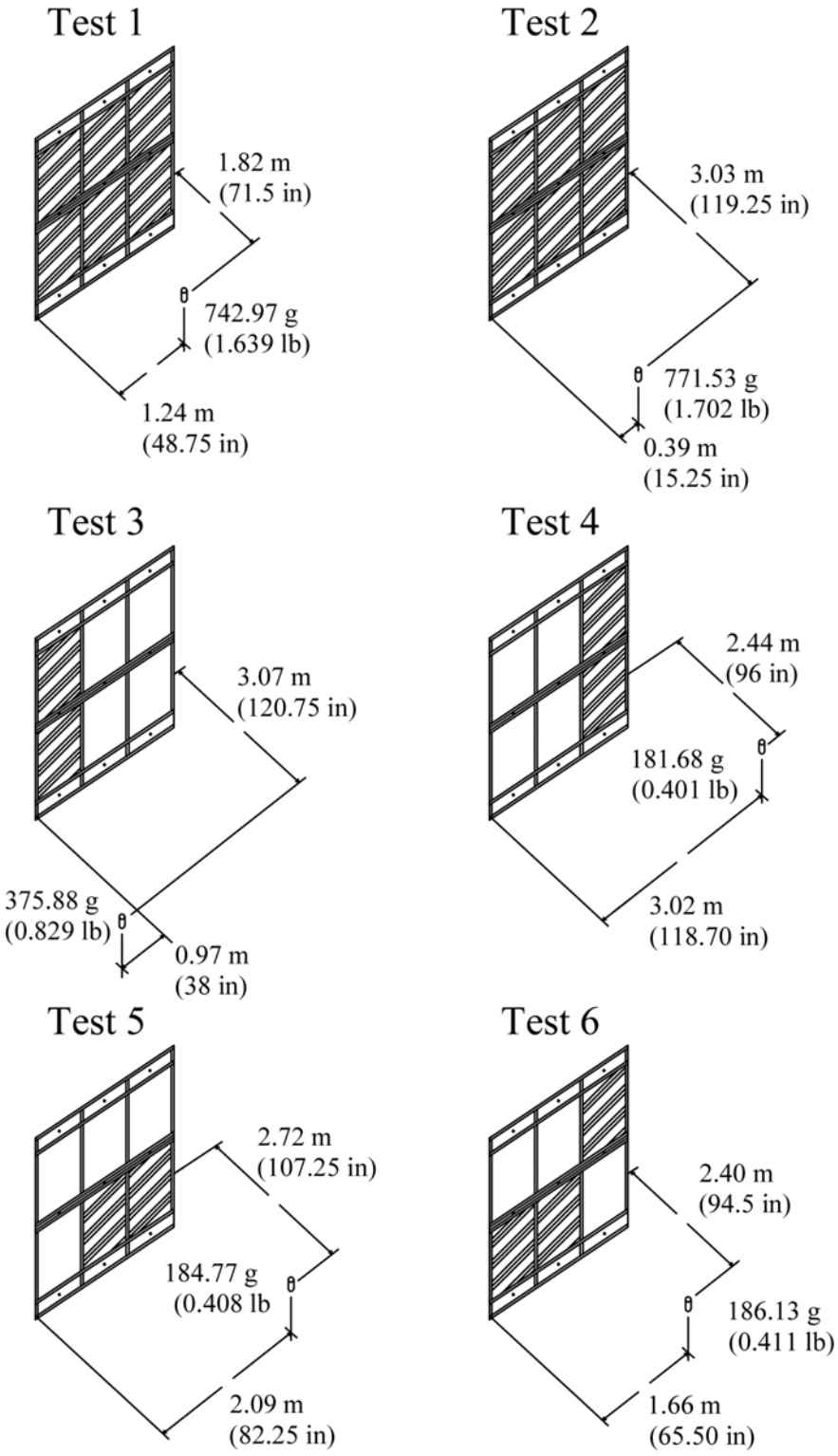

FIGURE 7.1: Scenarios of open-arena blast testing modeled in the AEM simulations for prediction of glass debris fields

TABLE 7.1: Number of elements and degrees of freedom in the AEM models

Test	Number of Lites	Elements	Degrees of Freedom
1	6	64,512	387,072
2	6	64,512	387,072
3	2	21,504	129,024
4	2	21,504	129,024
5	2	21,504	129,024
6	3	32,256	193,536

elements and degrees of freedom featured in each AEM model are summarized in Table 7.1.

Consistent with the AEM models described in the previous chapters, a modulus of elasticity of 68.9 GPa (10,000 ksi) and a Poisson's ratio of 0.22 were assigned to the Applied Elements. The boundary conditions of the lites were represented using the viscoelastic model with stiffness and damping parameters calibrated to the measured static and dynamic response of the lites, as previously described in Chapter 5 and enumerated in Table 5.1. Similar to the simulations used for prediction of the failure probability under blast loading, the AEM simulations again implemented mass proportional damping with a mass proportional damping constant of 4.15 to model the structural damping inherent to the glass lites. To account for the effects of tempering, each glass lite was assigned the parabolic theoretical residual stress distribution through the glass thickness corresponding to a residual surface compression stress of 69 MPa (10 ksi). Residual stresses were applied through superposition of the prescribed stresses onto the computed principal stresses using the methodologies described in Chapter 5. As was the case for prediction of the failure probability under blast loading, blast overpressures were applied to the model by using the Kingery-Bulmash model to estimate the blast overpressure time history across every ele-

ment for each scenario of blast testing. Pressure time histories were determined using the modified Friedlander equation, as previously described in Chapter 5. The simulation, including the duration of the blast wave and the subsequent response of the glass lite models, was performed over a total simulation time of 2.2 seconds. This was significantly longer than the duration of the blast wave and was implemented to provide sufficient time for the Applied Elements to fully come to rest after the projected fragments interacted with the defined surfaces of the test enclosure.

The macro-scale tempered glass failure model developed for the AEM based on initial surface failure and subsequent interior spring failure at the rate of crack propagation previously described in Chapter 5 was again implemented for prediction of the lite fragmentation and element separation. However, the assigned deterministic failure strength of the AEM models for prediction of debris field formation varied from the deterministic failure strength of the models described in Chapter 5. Because of the significant effect of load duration on the failure strength of glass, the static failure strength determined in Chapter 5 could not be reasonably assumed as the dynamic failure strength. Further, accurate prediction of debris field formation required that all of the glass lites featured in the AEM simulations experienced failure, meaning that the assigned failure stress must be attained in every glass lite model. Since the maximum principal stress in the model correlates with the predicted probability of failure, the glass lite that experienced the lowest magnitude principal stress was identified by examination of the predicted failure probabilities under blast loading. It is evident from the predicted failure probabilities presented in Figure 6.7 that glass lite specimen Lite 3 from Test 4 developed the lowest predicted probability of failure across all of the lites that did exhibit failure in the experimental program. Further, the maximum

principal stress experienced by any interface spring in the model under blast loading could be determined as described in Chapter 6. It was found that the maximum principal stress developed in any surface interface spring in Lite 3 from Test 4 was 42.8 MPa (6,208 psi). A deterministic failure strength of 42.8 MPa (6,208 psi), based on Rankine criterion, was therefore assigned in all the AEM simulations for prediction of debris field formation.

One aspect of simulating the projection of glass fragments under blast loading that has not been previously addressed in the literature on AEM is the need to model aerodynamic drag on the elements once they exhibit particle motion. This is potentially a very important phenomena to include when simulating debris formation from blast loading since the particle velocities of the ejecta may be significant. Aerodynamic drag is commonly computed by:

$$F_D = \frac{1}{2}\rho v^2 C_D A \tag{7.1}$$

where ρ is the material density, v is the particle velocity, C_D is the drag coefficient, and A is the surface area subjected to drag force (Hoerner, 1965). Equation 7.1 was implemented in the AEM simulation to compute the drag force acting in each of the translational degrees of freedom during every simulation increment. Drag forces were not considered in the rotational degrees of freedom, since the purpose of introducing drag force was to accurately model the trajectory of the elements, while the angular orientation of the elements was considered of lesser importance. It was assumed that the experimental specimens encountered air resistance inside the test enclosure immediately following fragmentation. For all simulations, ρ was taken as the assigned material density, and the area A was taken as the constant surface area of the element normal to the blast loading at the start of the simula-

tion. The particle velocity, v, in each degree of freedom was taken as the computed velocity of the element in the respective degree of freedom at each simulation increment. While the angular orientation of each element relative to the direction of air flow would be a changing quantity over the duration of the simulation, a constant drag coefficient of 0.925 was assumed for simplicity. This drag coefficient was arrived at as the average of the drag coefficients experienced by a cube normal and oriented at an angle of 45 degrees to the direction of air flow. The drag coefficients for these two cases were sourced from the literature as 1.05 and 0.8, respectively (Hoerner, 1965). These two drag coefficients are indicative of turbulent flow, which was considered reasonable due to the nature of blast loading. Since the AEM assigns degrees of freedom to the centroid of each element, incorporating the aerodynamic drag force into the incremental equation of motion is straightforward, as the drag forces can simply be added to the external body forces acting on each element.

7.2.1 Simulation of Enclosure Surfaces

The walls and floor of the test enclosure described in Chapter 4 were modeled in the AEM simulations through assignment of boundary planes. With the exception of contact between an element and the boundary plane representing the back wall of the test enclosure where the witness panel was installed, contact was modeled using the single spring collision model described in Chapter 3 for contact between an element and a fixed plane. This contact model was not implemented for the rear wall, since the rear wall of the test enclosure featured a foam witness panel that captured any flying debris. Any Applied Elements contacting the boundary plane defined for the witness panel were subsequently constrained for the remainder of the simulation, thereby effectively capturing their spatial location at

the time of impact with the simulated witness panel. Similarly, any elements predicted to fall outside of the test enclosure were subsequently constrained for the remainder of the simulation if they contacted the plane of the ground. The single spring contact model implemented for the side walls of the enclosure, floor of the enclosure, and steel framework of the facade was previously demonstrated in Chapter 3 through verification of the behavior of a single bouncing element. Since both the verification model and the AEM models for debris field formation featured fixed boundary planes, and since contact is modeled on an individual basis for each element and is not dependent on the total number of elements, the contact model was implemented as demonstrated in the verification problem. Following this methodology, the coordinates of all elements were examined at every simulation increment in relation to the assigned boundary planes, and a collision spring was added if contact was detected. This allowed for computation of the resulting forces and stiffnesses in the collision spring, which were then included in the global force and stiffness matrices as described in Chapter 3.

It should be noted that a reduced modulus of elasticity was implemented for computation of the normal and shear stiffness components of the collision springs. The purpose of reducing the modulus of elasticity in relation to the modulus of the glass elements was to maintain a minimum simulation timestep of 1e-05, since the required fineness of the simulation timestep is proportional to the spring stiffness, meaning that a large stiffness value in the contact model will require a significantly reduced timestep. Reduction of the stiffness between colliding particles has been observed in past research studies to effectively increase the permissible simulation timestep for DEM simulations (Yuu et al., 1995; Milburn et al., 2005; Malone and Xu, 2008), and as described in the literature review, the

implemented AEM contact model is similar to the contact models employed in the DEM. Although increasing the timestep to reduce computation time has been employed for DEM simulations, it should be acknowledged that Lommen et al. (2014) advised that caution should be taken when using this method, since reduction of the particle stiffness can potentially affect the results. However, implementation of a simulation timestep finer than 1e-05 was deemed impractical for this research effort because of the required computation time. It was determined that the required timestep could be achieved by assigning the modulus of elasticity of the contact spring to 689.5 MPa (100 ksi).

Implementation of the single spring contact model presented in Chapter 3 required assignment of the rebound factor, r, and the friction coefficient, μ. As described in Chapter 3, the rebound factor is dependent upon the coefficient of restitution, which is determined as the ratio of the post-collision velocity to the pre-collision velocity of the element. Since many different factors, including the material properties, impact velocity, and angle of impact affect the coefficient of restitution during a collision, the actual coefficient of restitution of each glass lite fragment during experimental testing was not known. The coefficient of restitution of impacting particles can be experimentally determined, as demonstrated in multiple studies (Lun and Savage, 1986; Tatara and Moriwaki, 1982; Chau et al., 2002; Imre et al., 2008). However, a similar experimental investigation to characterize the coefficient of restitution of the glass lite fragments impacting the floor of the enclosure was beyond the scope of this dissertation. It was therefore necessary to assume a reasonable estimate of the coefficient of restitution. It was observed in the literature that the coefficient of restitution during the collision of two spherical glass specimens has been experimentally estimated to be between 0.9 and 1.0 (Lun and Savage, 1986; Tatara and Moriwaki,

1982). However, it is believed that this is significantly higher than the coefficient of restitution experienced by the experimental glass fragments during open-arena blast testing, since the referenced studies determined the value for collision between two nominally identical glass spheres. It is believed that the actual coefficient of restitution of the impact between the glass fragments and the concrete floor of the test enclosure was significantly lower, due to the asymmetric, non-spherical shape of the glass fragments, the roughness of the edges of the glass fragments, energy dissipation resulting from further fragmentation upon impact, and the material properties of the concrete. Therefore, a reduced value of 0.5 was implemented in the AEM simulations of debris field formation.

It was similarly determined that an assumed coefficient of friction, μ, between the elements and the contact plane, would need to be sourced from the literature. However, because studies measuring the coefficient of friction for the interaction between glass and concrete surfaces were not identified, a value was selected based on studies characterizing the friction coefficient for interactions between concrete and steel. Notably, Zhang et al. (2008) used a shaker table to experimentally measure the coefficient of friction between concrete and steel specimens. The authors observed an initial friction coefficient of 0.5, which increased to approximately 0.8 as the experiment continued. Further, Fiorio (2005) experimentally measured the coefficient of friction between steel discs and concrete surfaces that had been exposed to varying levels of weathering under sub freezing conditions. For smooth surfaced specimens, Fiorio (2005) observed the friction coefficient to range from 0.46 to 0.73. Based on the results of these past studies, a coefficient of friction of 0.5 is believed to be reasonable for this research and was implemented in the AEM simulations of debris field formation.

7.3 Results

Renderings of the initial geometries of the AEM models developed for the prediction of glass debris fields are presented in Figure 7.2. These renderings depict the initial locations of the specimens that failed under open-arena blast testing. In each simulation, the Applied Elements associated with each glass lite are visualized with the color of the surface paint used in field experimentation. However, it should be noted that the Applied Elements in the simulation of Test 1 are uniform in color, since surface paint was not applied during the first open-arena blast test. In addition, the boundary planes and surfaces that define the contact surfaces for the walls of the test enclosure, the floor, and the steel members of the facade reaction structure are shown in these renderings.

An example of the fracture, fragmentation, and debris field formation in response to the blast loading as predicted by the AEM simulation is demonstrated in Figure 7.3, which presents a series of timesteps from the simulation for Test 2. The simulation time associated with each frame is included beneath each rendering. The example of the progressive failure behavior is presented for Test 2, since this test included the complete set of glass lite specimens and also featured surface paint to visually differentiate the debris. Progressive renderings of the fracture, fragmentation, and debris field formation predicted for all tests are presented in the appendix in Figure E.1 through Figure E.6.

Although the high speed video recorded during the experimental tests was too obscured by smoke from the explosion to provide clear experimental observations of the progression of fragmentation of the glass lites for comparison to the AEM simulations, the experimental tests produced different extents of glass fragments retained in the aluminum mullion fix-

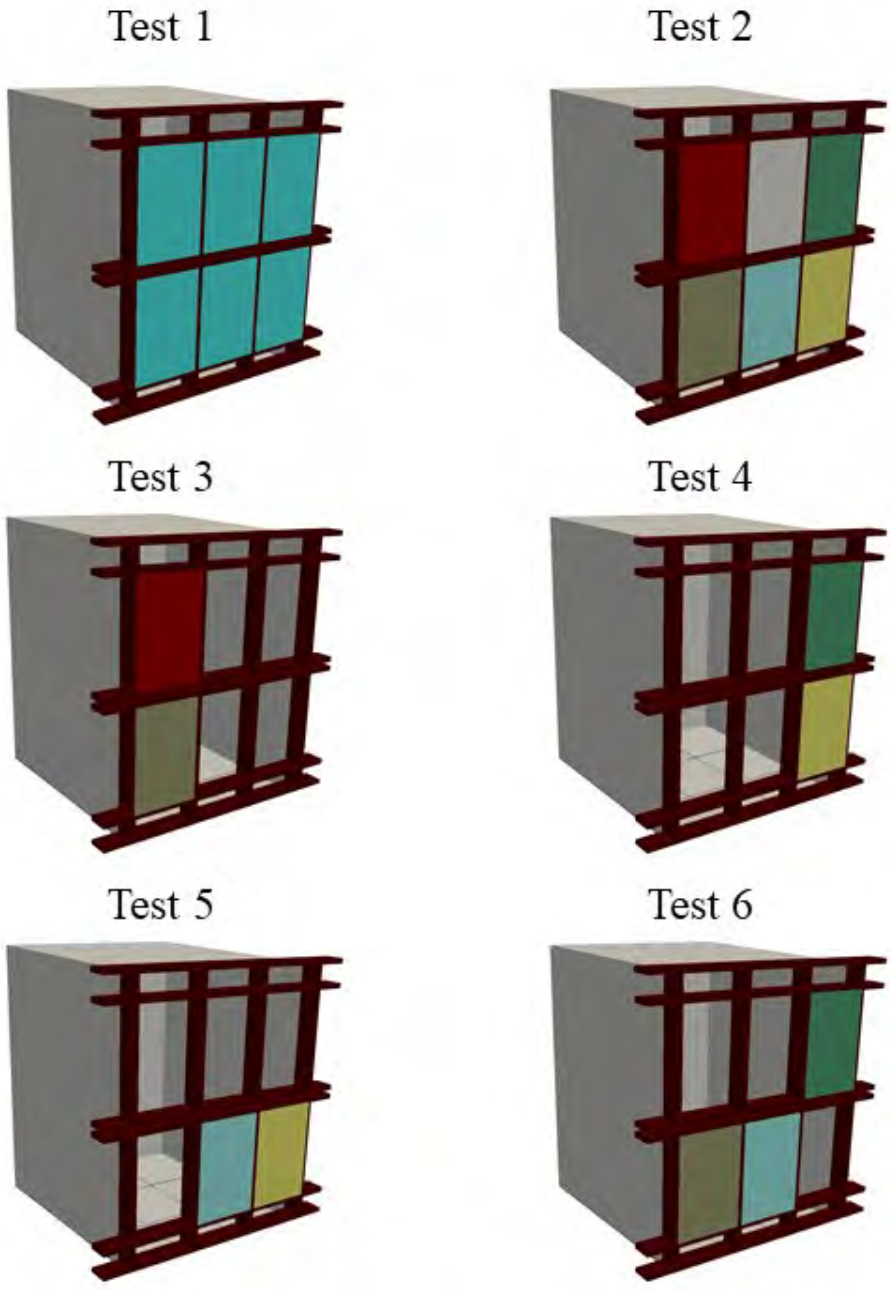

FIGURE 7.2: Oblique view renderings of the AEM models for debris field formation prior to application of blast loading

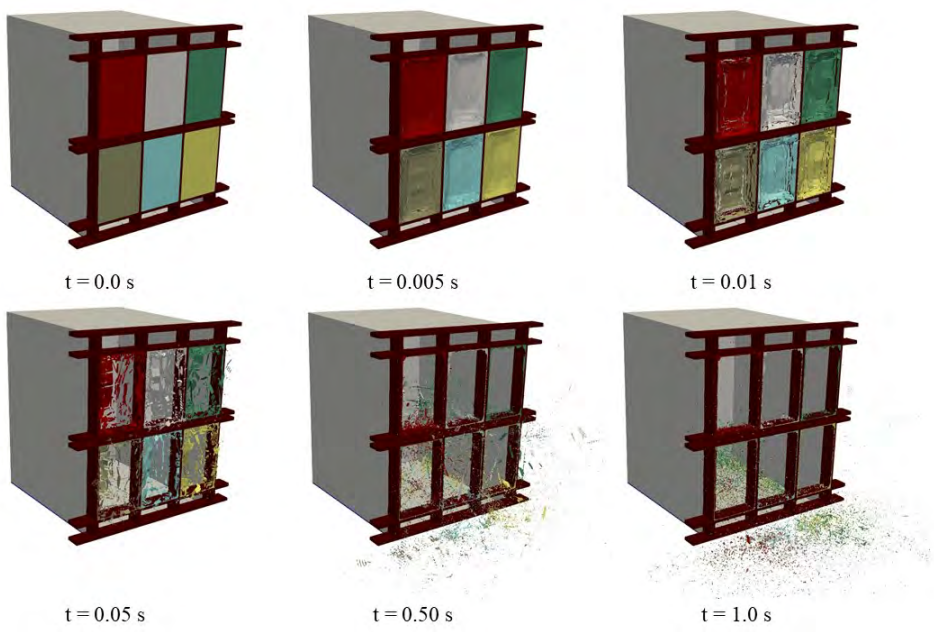

FIGURE 7.3: Progressive renderings of the fracture, fragmentation, and debris field formation predicted for Test 2

tures that could be used qualitatively as a secondary means of assessing the plausibility of the predicted fragmentation behavior in the AEM simulations. A frontal view of the facade following each simulation is presented in Figure 7.4, which illustrates that relatively large glass fragments were predicted to remain held in the supporting mullions for each of the simulations performed with the lower TNT equivalent charge weights associated with the tests conducted with ANFO. In the simulations performed with the higher TNT equivalent charge weights associated with the PETN charges, no large glass fragments were predicted to remain held in the supporting fixtures. These predictions for the large glass fragments retained in the test fixture agree with the experimental observations documented in Chapter 4 in Figure 4.18.

Renderings of the glass debris fields predicted by the AEM analysis are presented in Figure 7.5. It is evident that in all cases, the glass lite model attained the assigned minimum

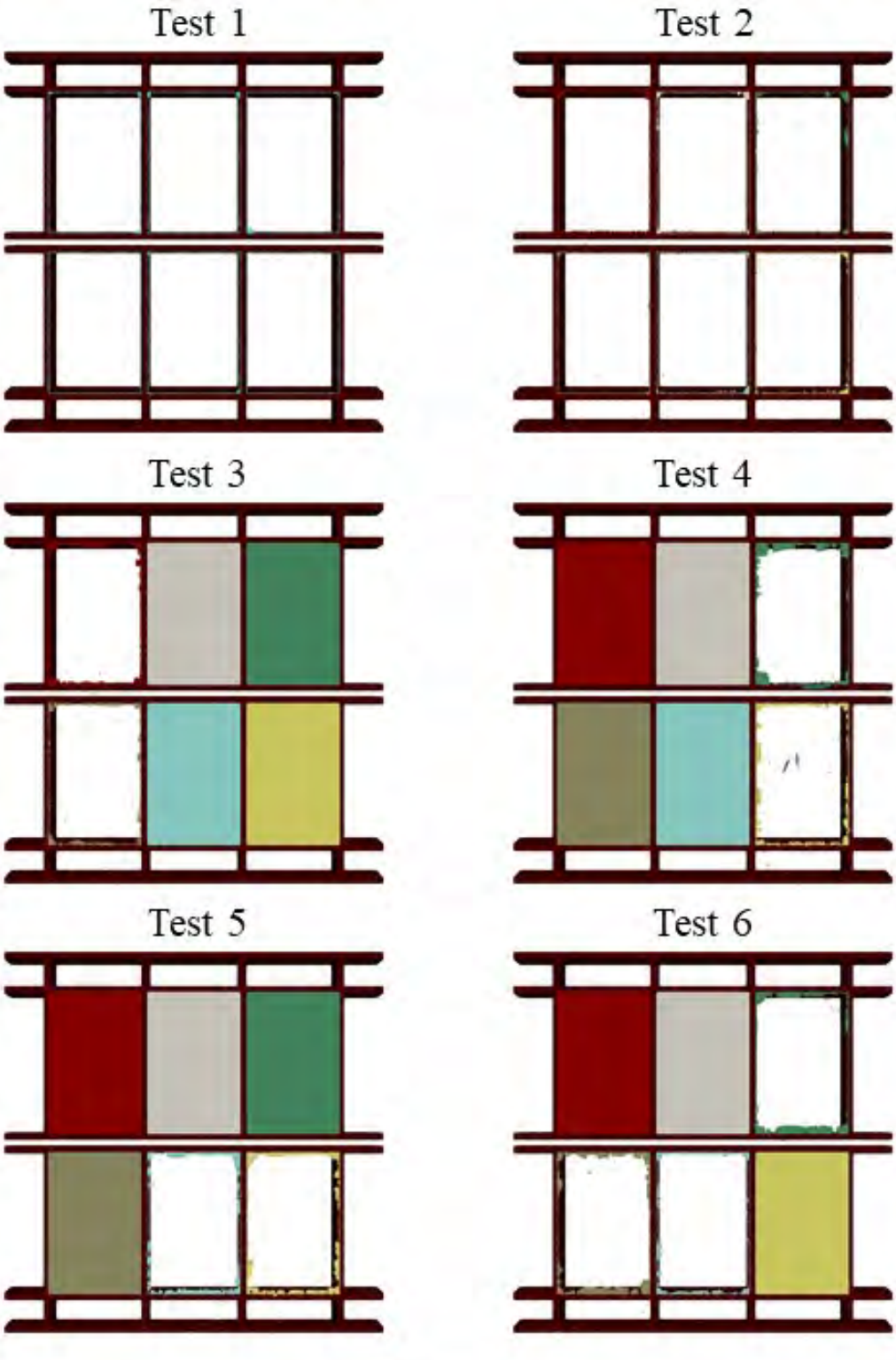

FIGURE 7.4: Frontal view renderings of the AEM glass lite models after simulating fragmentation under blast loading

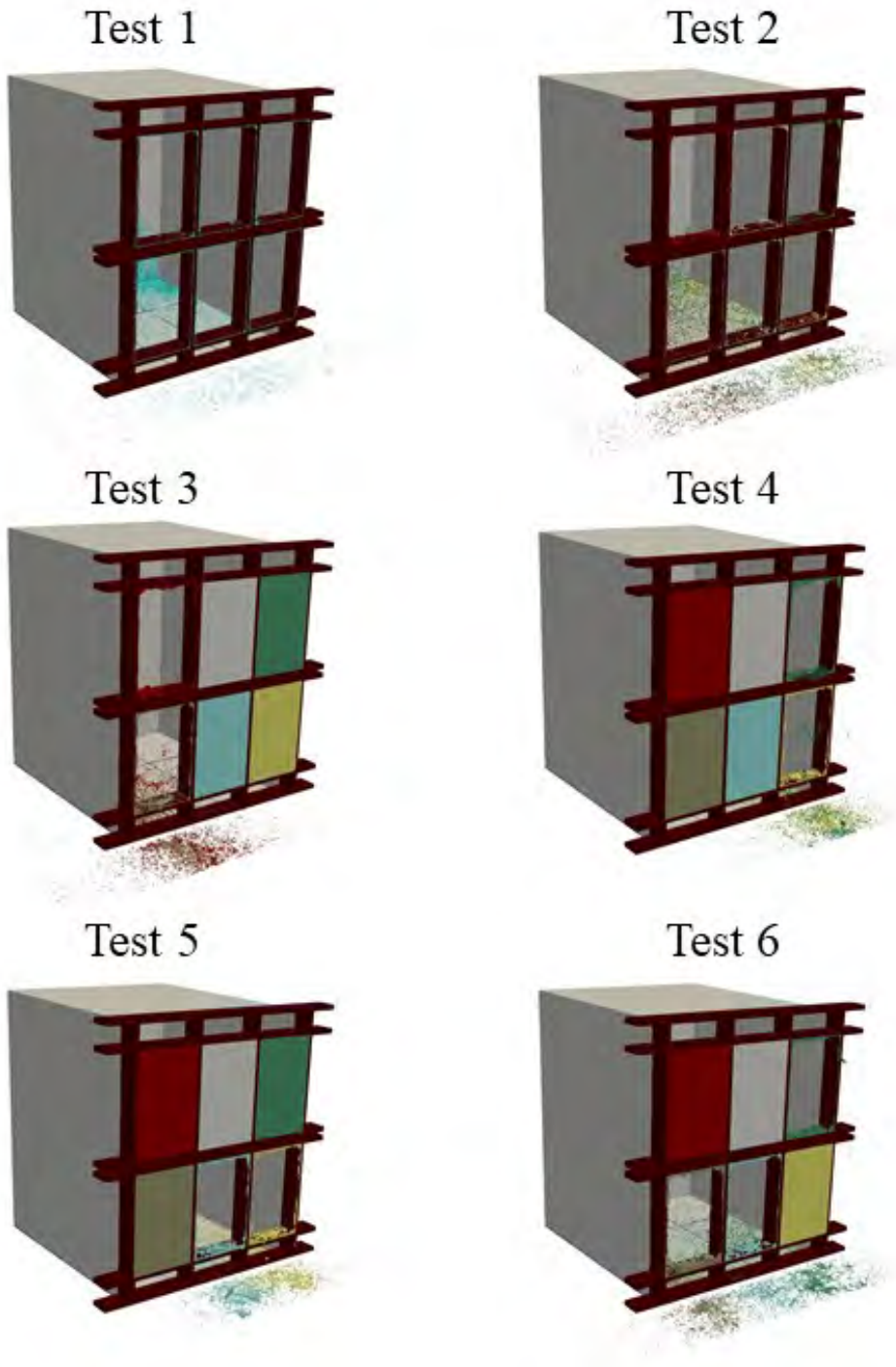

FIGURE 7.5: Oblique view renderings of the AEM glass lite models after simulating fragmentation under blast loading

failure stress, which allowed for fracture, fragmentation, subsequent particle motion, and contact with the boundary planes. It is also evident from Figure 7.5 that a significant portion of the predicted debris is located outside of the enclosure. This is consistent with the experimentally observed debris fields, which were distributed on the interior and exterior of the enclosure.

The debris field distributions predicted by the AEM simulations were evaluated both by visual comparison with the LiDAR scans presented in Figure 4.23 and by comparison of measured distributions of glass debris within the gridded areas of the floor of the enclosure. Qualitative comparisons between the LiDAR scans of the debris fields within the test enclosure and the debris fields predicted by the AEM simulations are presented in Figure 7.6. The similarity between the observed and predicted debris distributions is evident. As expected, the debris generated by each individual lite was largely thrown either directly behind of directly in front of the respective window opening. Figure 7.7 and Figure 7.8 provide additional qualitative comparisons between the AEM simulation results and the experimental observations using test photographs, which further demonstrate the similarity between the measured and predicted results. Figure 7.7 presents a comparison of the debris distributions across the floor of the test enclosure, while Figure 7.8 presents a similar comparison of the exterior debris fields. As described in Chapter 4 and demonstrated in Figure 4.22, the floor of the enclosure was discretized into nine grids for experimental measurement of the debris distribution by mass. Determination of the mass of debris predicted by the AEM simulation within each of the gridded areas was facilitated by analyzing the centroid coordinates of the Applied Elements in the final time step of each simulation. Since all elements were equal size and uniform in mass, the total mass of glass debris in each grid

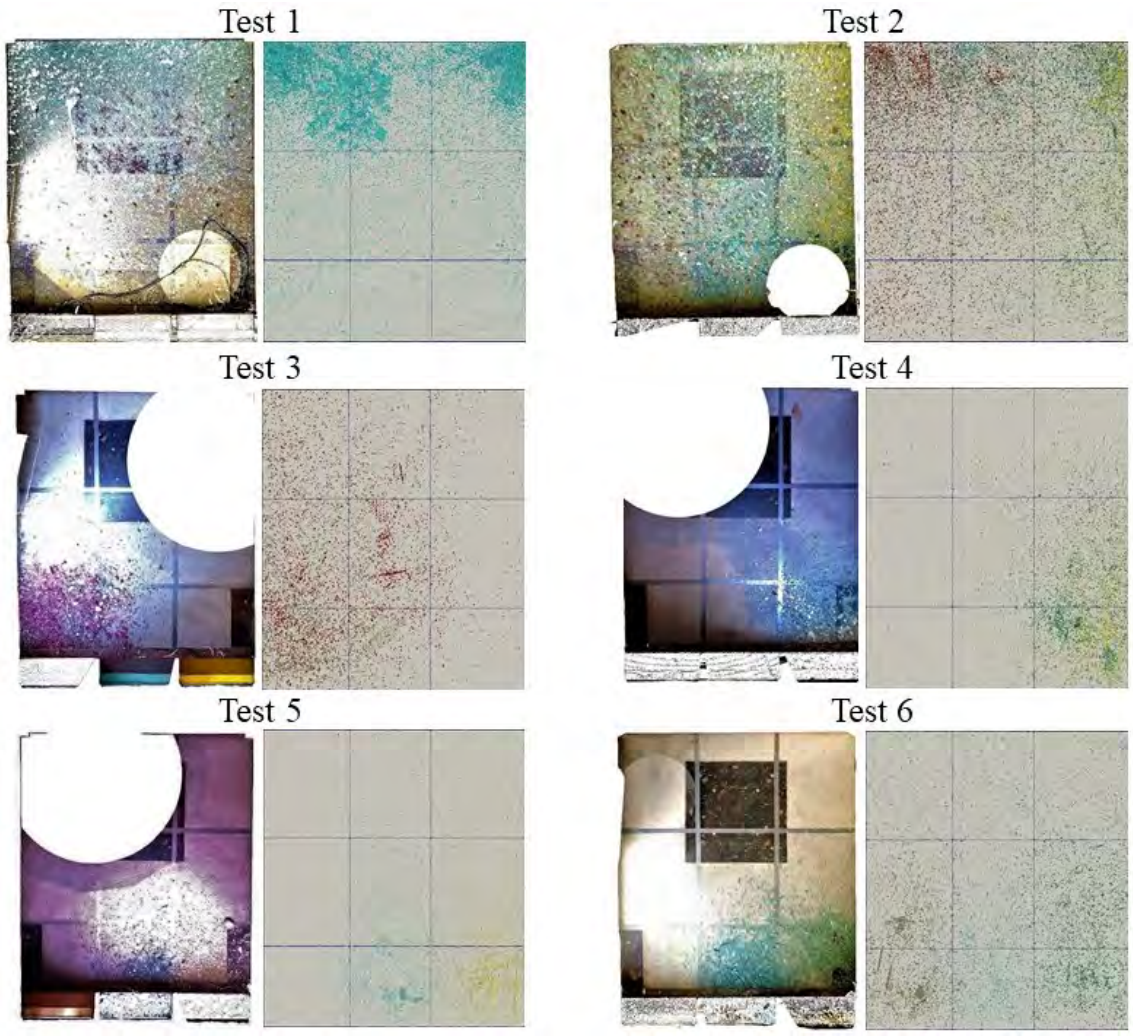

FIGURE 7.6: Visual comparison of the experimentally observed and predicted debris field distributions

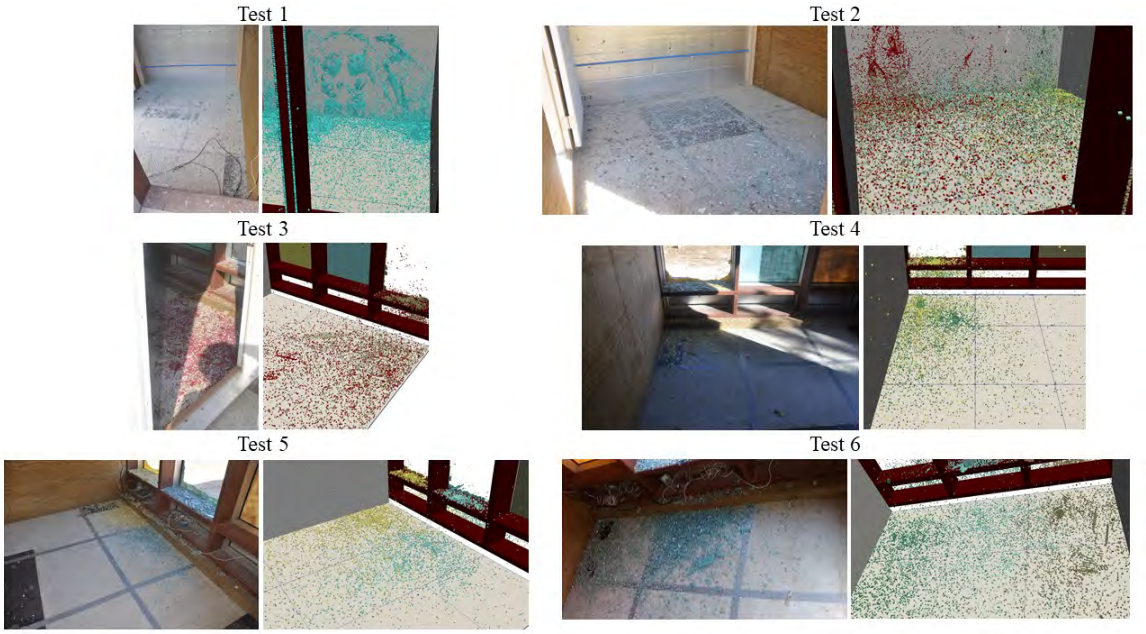

FIGURE 7.7: Visual comparison of the experimentally observed and predicted interior debris field distributions using photographs from experimentation

FIGURE 7.8: Visual comparison of the experimentally observed and predicted exterior debris field distributions using photographs from experimentation

was directly related to the number of elements. The predicted interior debris distribution is plotted in Figure 7.9. It should be noted that an additional, distinct row of gridded areas is included in each of the plots in Figure 7.9. These gridded areas represent the steel tube sections supporting and extending directly behind the glass lites. Significant quantities of glass debris were observed to land on this section of the facade framework during experimental testing. This is demonstrated in Figure 7.10, which presents a photograph of the experimentally observed debris distribution across the steel tubing following Test 5. However, the mass of debris that landed on the steel tube sections was not measured during open-arena blast testing, as evidenced in Figure 7.11, which presents the measured mass distributions for all of the tests. Although a direct comparison of the predicted and measured mass distributions across the steel tube sections cannot be performed, the significant quantity of debris predicted to land on the steel tube sections indicates qualitative agreement with the visual observations of the debris fields. Further, the predicted debris distributions across the floor of the test enclosure achieve generally strong correlation with the experimental measurements, although it is evident that the predicted debris distribution is typically more dispersed relative to the experimental observation. It should be noted that the masses in the gridded areas nearest the glass lite specimens are significantly over predicted for Test 6. This discrepancy is attributed to the unusual failure behavior observed during Test 6. As noted in Chapter 4, Lite 4 from Test 6 appeared to fail outward, resulting in a significant exterior debris field. This behavior was not replicated in the AEM simulation of Test 6, which predicted positive phase failure of Lite 4.

The debris distributions are further evaluated by comparison of the measured and predicted masses of debris in each grid of the enclosure floor across all tests in Figure 7.12.

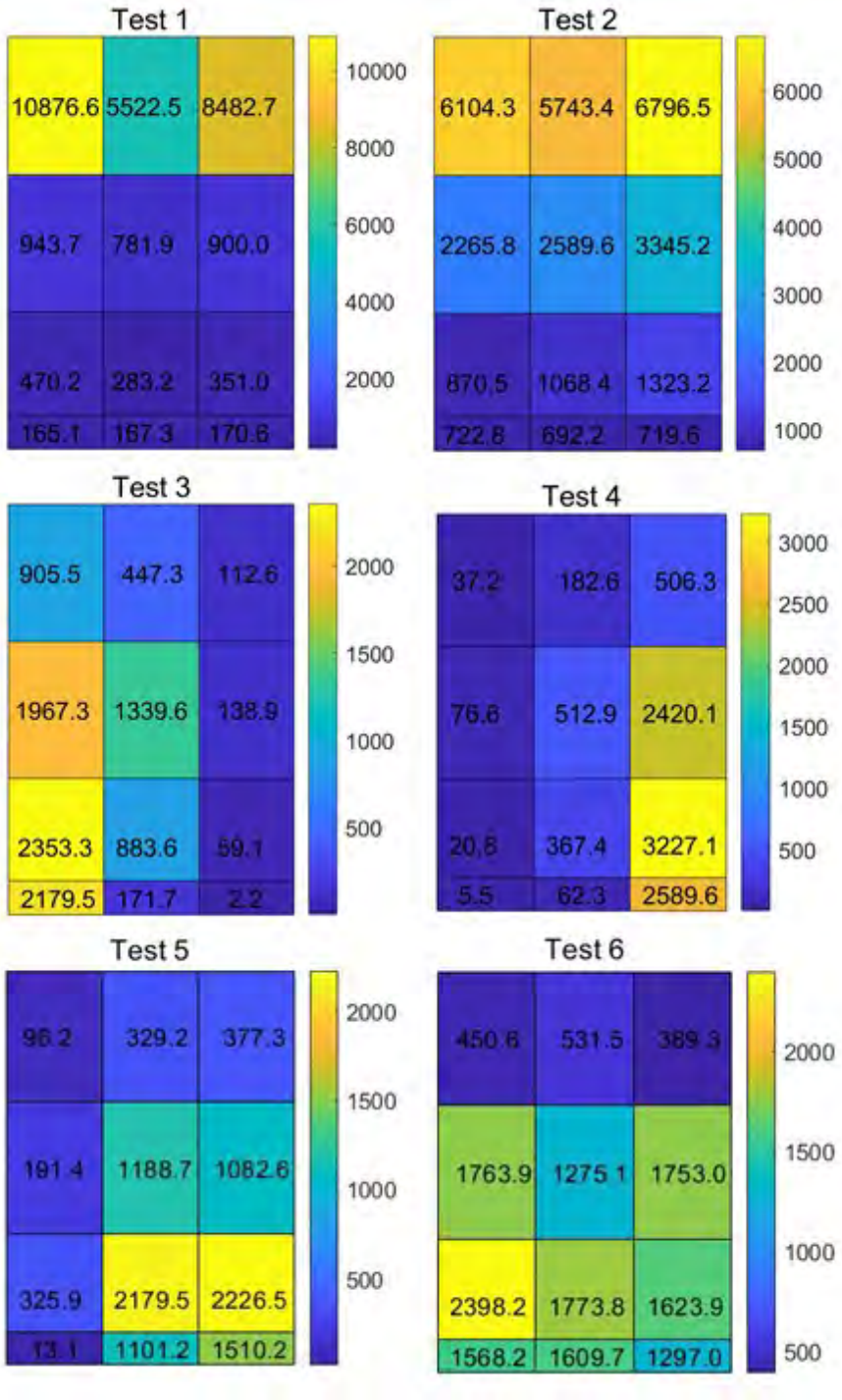

FIGURE 7.9: AEM predicted distributions of debris mass in grams

FIGURE 7.10: Photograph of debris that landed on the facade framework during Test 5

Each data point in Figure 7.12 corresponds to the measured and predicted masses in one grid for one of the tests, and the test associated with each data point is indicated. Although the distribution indicates that small quantities of measured debris typically correspond to moderate overprediction of the mass, the difference between the measured and predicted masses decreases as the quantity of measured debris increases.

The increased predicted dispersion of the debris results in a greater quantity of debris categorized as "low-hazard", as prescribed in ASTM 1642-17. The predicted percentages of debris classified as "very low-hazard" and "low-hazard" were computed for Tests 3 through 6 and are presented in Table 7.2 with comparison to the experimental measurements. Test 1 and Test 2 are not included in the comparison, since those scenarios of experimental testing generated significant quantities of "moderate-hazard" and "high-hazard" debris, which was captured in the witness panel and not measured by mass. Although the amount of "low-hazard" debris is moderately over predicted in all cases, relatively strong correlation is observed between the experimental and predicted results for Test 3. Lastly, the "moderate-hazard" and "high-hazard" debris predicted to be captured by the witness panel for each test is presented qualitatively in Figure 7.13. It is evident that significant

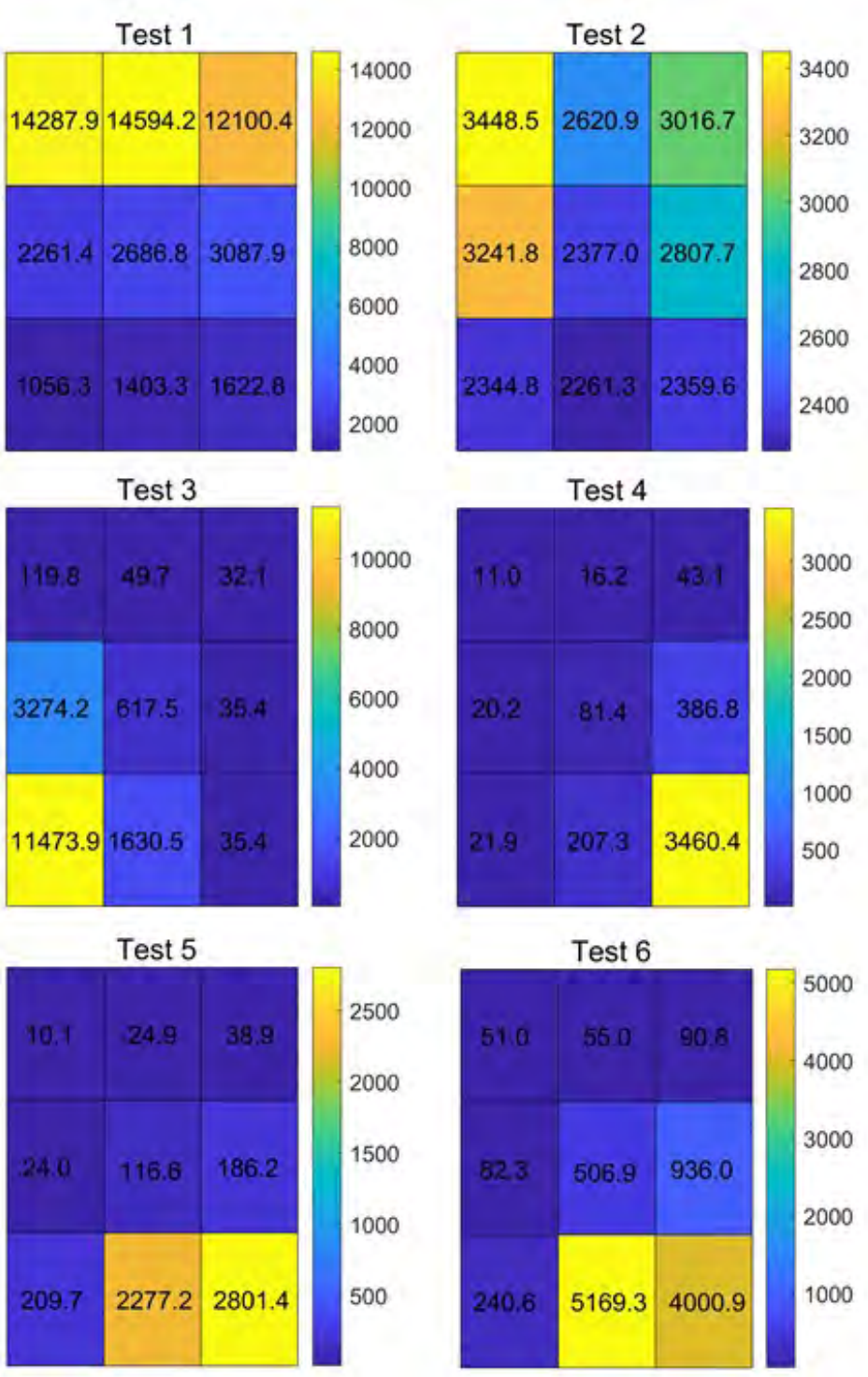

FIGURE 7.11: Measured distributions of debris mass in grams

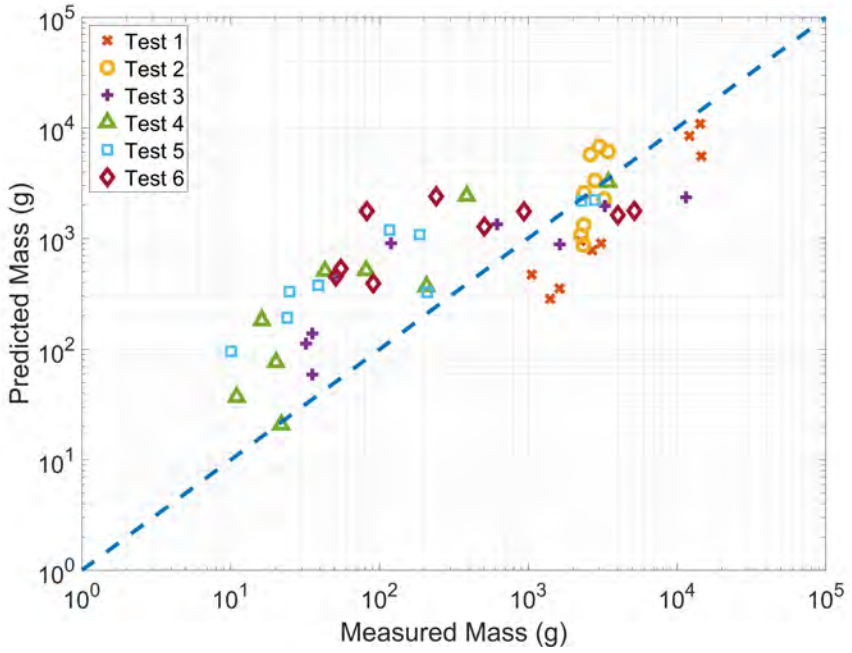

FIGURE 7.12: Comparison between the measured and predicted masses of debris across the floor of the enclosure for all tests

TABLE 7.2: Comparison of the predicted and experimental debris classified as "very low hazard" and "low hazard"

	Measured		Predicted	
Test	"VLH" Debris (%)	"LH" Debris (%)	"VLH" Debris (%)	"LH" Debris (%)
3	81.9	18.1	78.7	21.3
4	97.6	2.4	83.8	16.2
5	98.2	1.8	85.8	14.2
6	95.0	5.0	82.2	17.8

"moderate-hazard" and "high-hazard" debris is predicted for Tests 1 and 2, while minimal "moderate-hazard" and "high-hazard" debris is predicted for the remaining tests. This correlates with the observed debris distributions across the witness panels during experimental testing. The renderings of the predicted debris that is captured by the witness panels in Test 1 and Test 2 may appear to show more glass than observed in the experimental tests because larger fragments of glass were observed to be retained by the witness panels in the experiments, but the hard boundary constraint imposed in the simulation at the witness panel would have caused any larger fragment reaching the witness panel to fracture into individual elements.

It is evident that the AEM models for debris field formation typically over predicted the debris throw following fragmentation. It is likely that internal pressurization of the test enclosure during the blast tests may have occurred that would have affected the projection of debris in the experiments, which was not accounted for in the simulations because this would have required a more complex fluid-structure interaction model than the aerodynamic drag considerations included in the analysis. The test enclosure was fully sealed through the use of construction sealants in any air gaps in order to prevent wrap-around of the blast overpressures during the tests. However, this air sealing of the test enclosure could have caused internal air pressure to significantly increase in the test enclosure when the lites experienced large deformation deflections and subsequent fracture. This speculation is supported by damage developed around the door of the enclosure, which was in some cases forced open during the tests as a result of the positive internal pressure. If there was positive internal pressure that developed resistance to air flow within the test enclosure, the debris flow would have been shorter than if the test enclosure was fully ventilated. In

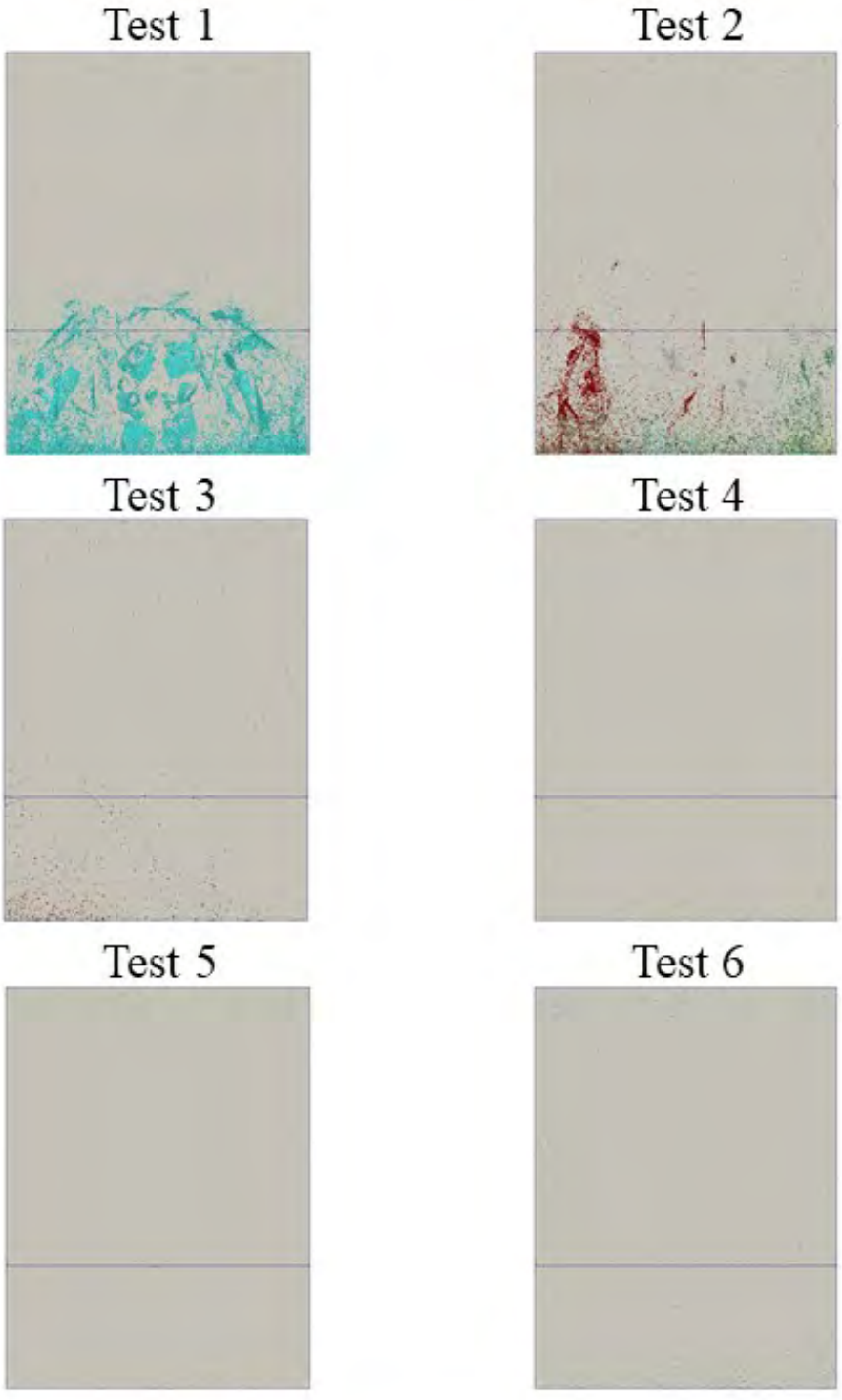

FIGURE 7.13: Predicted debris distribution across the witness panel for all tests

addition, it is possible that the discrepancy in the predicted debris distribution was partially attributable to the implemented blast loading model. As explained in the previous chapter, the blast pressure model was developed using Kingery Bulmash polynomials, which were developed using spherical TNT charges, as opposed to the cylindrical charges composed of either PETN or ANFO used for this research. Finally, the debris field formation is affected by the assigned deterministic failure strength for the glass. As previously explained, a deterministic failure strength was assigned uniformly across all tests and was determined as the minimum failure strength that would allow for failure of all glass lites. As described in the literature review and Chapter 6, the actual failure strength of a glass specimen varies due to variation in surface flaws. Therefore, it is likely that the actual failure strength of the experimental glass lites varied across every specimen and was likely higher for many lites than the value assigned in the simulation.

7.4 Conclusions

The Applied Element Method was implemented to simulate the fracture, fragmentation, and debris field formation of the tempered glass lite specimens subjected to the six scenarios of open-arena blast testing described in Chapter 4. In order to accurately predict the post-fragmentation behavior of the glass particles, the AEM models described in Chapter 5 for simulation of blast loading were extended to incorporate aerodynamic drag forces and contact interactions, which were simulated using two different contact models to represent the surfaces of the test enclosure. A simplified contact model that constrained any contacting element was used to model the foam witness panel and the ground outside the test enclosure, while the single spring collision model described and verified in Chapter 3

was implemented to model contact between the Applied Elements and the walls, floor, and facade framework of the test enclosure.

The predicted glass debris fields demonstrate generally strong qualitative correlation with the experimentally observed debris fields. Notably, the AEM simulations replicated experimental observations, including the general distribution pattern of the debris across all tests, the debris fragments that remained held to the facade during the tests that implemented ANFO charge compositions, and the relatively large quantities of "moderate-hazard" and "high-hazard" debris generated during Test 1 and Test 2. However, comparison of the predicted and experimental debris distributions by mass indicate that the AEM simulations moderately over predict the debris throw, which results in less dense debris distributions when compared to the experimental observations. Since the developed AEM routines have been verified for simulation of theoretical particle dynamics, as described in Chapter 3, it is believed that the increased debris projection is attributable to differences pertaining to the blast loading environment. Specifically, the AEM models implemented a blast loading model developed around a spherical charge, as opposed to a cylindrical charge. Further, it is probable that pressurization of the test enclosure during experimental testing resulted in increased air resistance in comparison to the aerodynamic drag forces simulated in the AEM model. Lastly, the predicted debris distribution of each test could have been affected by assignment of a single, uniform failure strength across all glass lite models, since it is probable that the actual failure strength varied across each experimental glass lite specimen.

CHAPTER 8: CONCLUSION

8.1 Summary and Concluding Remarks

The methodologies described and implemented in this dissertation accomplish the overarching objective of demonstrating the ability to predict fracture, fragmentation, and debris field formation of conventional tempered glass lites subjected to blast loading using the relatively new Applied Element Method. Toward achieving this objective, a brief overview of blast wave overpressure and structural response to blast loading was presented with specific focus on the consideration of structural damage in post-blast forensics analyses. It was observed that, although structural damage is sometimes employed in a qualitative role for characterization of a blast event, numerical simulation of structural damage is typically not considered during post-blast forensic investigations, due to the difficulty of modeling complex phenomena, such as fracture and fragmentation, under blast loading. Challenges associated with simulating glass failure under blast loading were highlighted through discussion of the current state of practice for numerical simulation of glass lites under blast loading and through presentation of a corresponding review of relevant case studies. It was demonstrated that although the Finite Element Method has been employed to predict fracture of glass lites under blast loading through introduction of complex failure models, the Finite Element Method is incapable of predicting debris field formation, unless coupled with a secondary method capable of simulating particle dynamics.

A simulation framework was therefore developed for this dissertation around the relatively new Applied Element Method, which was introduced in Tagel-Din (1998) and, as demonstrated through presentation of relevant case studies, has been successfully implemented in past research efforts to predict highly nonlinear behavior, including progressive collapse, fracture, and debris field formation. The simulation framework was developed progressively through introduction of increasingly advanced extensions to a developed software library for modeling static and dynamic linear elastic behavior, nonlinear geometric effects, nonlinear material constitutive laws, particle dynamics, and element contact. This development of the simulation framework was accompanied by verification and validation of the predictive fidelity of the simulator using comparable analytical and Finite Element models and databases of experimental results, respectively. Experimental results were compiled over an extensive set of experimental tests, which included six open-arena blast tests and one uniform static loading test of conventional tempered glass lite specimens. The open-arena blast tests were conducted on a fully enclosed test structure that featured tempered glass lite specimens mounted in a conventional facade framework. The charge standoff, size, and composition were varied across tests to create different scenarios of blast loading. Collected data included vibration data for characterization of modal properties of individual specimens, reflected and incident blast overpressures for characterization of the blast loading, and post-blast measurement of debris fields. The uniform static loading test was conducted using a test specimen nominally identical to the specimens subjected to open-arena blast testing and was mounted in the same facade framework. Data collected for the uniform static loading test included vibration data for characterization of the modal response, load-deflection measurements, and high speed videography of the specimen fail-

ure.

The experimental scenarios of open-arena blast testing and uniform static loading were simulated using the developed AEM simulation framework. Primary challenges specific to the tempered glass specimens used in this research that were addressed during model development included calibration of boundary conditions, modeling of the fragmentation behavior associated with tempered glass, probabilistic forecasting of the likelihood of glass lite failure within the simulation framework, and simulation of element contact for predicting glass debris fields.

Accurate simulation of the boundary conditions was achieved through introduction of translational and rotational boundary springs coupled with a Kelvin-Voigt model for the viscoelastic response of the rubber gaskets supporting the lites in the mullion system. Assignments for the boundary springs and dampers in the Kelvin-Voigt model were determined through a model updating routine that leveraged the measured static and dynamic properties of a typical glass lite specimen. The accuracy of this boundary model was demonstrated through comparison of the predicted and experimental modal response and the load-deflection behavior under uniform static loading. Strong correlation was achieved with the experimental results, and further verification was completed through development of comparable FEM models using a commercially available FEM software package. Both the AEM and FEM models achieved similarly strong correlation with the experimental modal parameter estimates and the experimentally measured load-deflection curve.

The residual stress distribution associated with tempered glass was successfully introduced into the Applied Element Method by superposition of residual stresses onto the stresses computed in the interface springs of the Applied Elements. In addition, a macro-

scale failure model was introduced to simulate the fracture and fragmentation process in tempered glass. Strong correlation between the predicted fracture pattern under static loading and the observed fracture pattern was achieved and the expected relationship between degree of tempering and fragmentation density was successfully reproduced using the developed failure model.

As a further component of this dissertation, the well known Glass Failure Prediction Model was implemented through the AEM simulation framework to forecast the failure probabilities of the glass lites under static loading and for each of the six scenarios of open-arena blast testing. This probabilistic failure model predicts breakage of a specimen based on the surface flaw distribution, which is characterized by empirical surface flaw parameters. Although the literature typically recommends experimental estimation of surface flaw parameters, flaw parameter values for this research effort were adapted from the flaw parameters prescribed in ASTM E1300 for design use. Adaptation of the Weibull probabilistic model for application to blast loading was described, and prediction of the failure probabilities under blast loading was demonstrated. Although a failure probability of greater than zero for all glass lite specimens that did fail in the experimental tests and less than one for all specimens that did not fail was predicted, it was observed that the predicted failure probabilities for the tests conducted with ANFO charges were generally lower than expected for most of the specimens observed to fail during the open-arena blast tests. It is believed that the low failure probabilities can be attributed to uncertainties in the surface flaw parameters and uncertainties in the blast loading, which was not as well measured for the tests conducted with the ANFO charges.

Lastly, the simulation framework was successfully extended to predict glass debris fields

by introducing a single spring collision model to determine contact forces and stiffnesses developed between designated boundary planes and any contacting elements. The single spring collision model was successfully implemented for prediction of glass debris fields following fragmentation under blast loading. Although the predicted debris fields demonstrated qualitative correlation with the observed debris fields, it was found that, in most cases, the AEM simulations overpredicted the debris throw. The difference in the debris distribution density is attributed to pressurization of the test enclosure during open-arena blast testing, since increased internal pressure in the test enclosure would have increased the flow of air and, consequently, the projectile motion of carried glass debris. A further discrepancy between the predicted and measured debris mass distributions was observed across the section of the enclosure nearest the specimens, where the AEM simulations typically underpredicted the debris mass. This discrepancy is attributed to the mass of unmeasured debris that remained on the facade structure during experimental testing, since only debris that reached the floor of the enclosure was measured experimentally.

Although further refinement of the developed AEM models for predicting glass debris fields under blast loading is recommended, formation of tempered glass debris fields has been successfully simulated. This research effort therefore contributes to the current knowledge base of AEM modeling by demonstrating that the AEM methodologies introduced in Tagel-Din (1998) are capable of simulating the fracture, fragmentation, and debris field formation of tempered glass lites under blast loading. The Applied Element Method has been extended for the first time for simulating the failure of tempered glass and, as a further component of this dissertation, has been adapted and implemented for the first time for predicting the failure probability of glass lites using the Glass Failure Prediction Model.

8.2 Recommendations for Future Work

- *Experimental characterization of the surface flaw parameters for probabilistic prediction of failure* - Although the AEM methodologies were successfully employed to forecast failure probabilities under static and open-arena blast loading using the Glass Failure Prediction Model, it is believed that the correlation between the predicted probabilities and the breakage patterns observed during open-arena blast testing could be improved through implementation of surface flaw parameters better representing the condition of the glass lite specimens. It is recommended that future efforts conduct experimental static failure testing of a specimen set large enough to experimentally estimate the surface flaw parameters of the specimens being modeled, as recommended in Beason and Morgan (1984).

- *Calibration of the parameters in the contact model* - The single spring collision model used to model contact with the boundary planes for predicting debris fields implemented an assumed coefficient of restitution and an assumed friction coefficient, since experimental characterization of these properties was beyond the scope of this dissertation. It is believed that the correlation between the predicted and observed debris fields could potentially be improved through implementation of contact parameters better representing the collision between the elements and the floor of the enclosure. Sensitivity analyses to determine the effects of changing the coefficient of restitution and friction coefficient are therefore recommended for future work.

- *Introduction of an inter-element contact model* - The simulations for prediction of glass debris fields only modeled contact between the elements and boundary planes.

Contact between elements was not considered. As described in the literature, simulation of contact between Applied Elements can be facilitated by introducing an interface spring between the elements. Development of an inter-element contact detection model, development of an inter-element contact model, and analysis of the sensitivity of the predicted debris field distributions to inclusion of inter-element contact modeling are recommended as areas of future research.

- *Sensitivity analysis of the effect of charge size and epicenter on the debris field formation* - One of the primary motivations of this work is to facilitate simulation-based hypothesis testing in post-blast forensic investigations using observations of damage to structural and nonstructural building components. The experimental tests and simulations performed in this dissertation reveal that lite failure and debris fields are sensitive to charge size and location. However, the sensitivity of the lite failure probabilities and predicted debris fields to small changes in charge size and location have not been exhaustively studied. The developed AEM simulation framework could be leveraged to examine this sensitivity in order to bound the degree of certainty that could be expected for hypothesis testing of scenarios.

- *Extension and application of the AEM simulation framework to other structural and nonstructural building components* - Glass failure and debris fields were specifically selected for this dissertation due to the prevalence of glass in commercial and residential structures as well as its vulnerability to fracture during blast loading, which makes it a good "witness" to explosive events. However, as detailed in the literature review, other damage mechanisms in structural and nonstructural building mem-

bers, such as plastic deformation in metal components, lead to additional, valuable post-blast forensic observations. Extending and experimentally validating the AEM simulation framework to such damage mechanisms would lead to a more holistic hypothesis testing tool for post-blast forensic investigation.

REFERENCES

Abiassi, J. J. (1981). *The strength of weathered window glass using surface characteristics*. PhD thesis.

Allemang, R. J. (2003). The modal assurance criterion–twenty years of use and abuse. *Sound and Vibration*, 37(8):14–23.

Ambrosini, D., Luccioni, B., Jacinto, A., and Danesi, R. (2005). Location and mass of explosive from structural damage. *Engineering Structures*, 27(2):167–176.

Ambrosini, R., Luccioni, B., Danesi, R., Riera, J., and Rocha, M. (2002). Size of craters produced by explosive charges on or above the ground surface. *Shock Waves*, 12(1):69–78.

Asprone, D., Nanni, A., Salem, H., and Tagel-Din, H. (2010). Applied element method analysis of porous gfrp barrier subjected to blast. *Advances in Structural Engineering*, 13(1):153–169.

ASTM (2016). Standard practice for determining load resistance of glass in buildings. Standard E1300-16, ASTM International.

ASTM (2017). Bases for design of structures – serviceability of buildings and walkways against vibrations. Standard F1642-17, ASTM International.

ASTM (2018). Standard specification for heat-strengthened and fully tempered flat glass. Standard C1048-18, ASTM International.

Baker, W. E. (1973). *Explosions in Air*. University of Texas press.

Barsom, J. M. (1968). Fracture of tempered glass. *Journal of the American Ceramic Society*, 51(2):75–78.

Baz, A. M. (2018). *Active and Passive Vibration Damping*. John Wiley and Sons Ltd.

Beason, W. L., Kohutek, T. L., and Bracci, J. M. (1998). Basis for astm e 1300 annealed glass thickness selection charts. *Journal of structural engineering*, 124(2):215–221.

Beason, W. L. and Morgan, J. R. (1984). Glass failure prediction model. *Journal of Structural Engineering*, 110(2):197–212.

Bedon, C., Fasan, M., and Amadio, C. (2019). Vibration analysis and dynamic characterization of structural glass elements with different restraints based on operational modal analysis. *Buildings*, 9(1):13.

Beveridge, A. (2011). *Forensic Investigation of Explosions, Second Edition*. International Forensic Science and Investigation. Taylor & Francis.

Bourhis, E. (2014). *Glass: Mechanics and Technology*. Wiley.

Bove, P. M. (1995). *Failure prediction for heat treated window glass*. PhD thesis, Texas Tech University.

Brasie, W. C. and Simpson, D. W. (1968). Guidelines for estimating damage from chemical explosions. In *Proceedings of the Symposium on Loss Prevention in the Process Industries*, pages 91–102. Association of Industrial Chemical Engineers.

Cervera, M. and Chiumenti, M. (2006). Smeared crack approach: Back to the original track. *International Journal for Numerical and Analytical Methods in Geomechanics*, 30(12):1173–1199.

Chau, K., Wong, R., and Wu, J. (2002). Coefficient of restitution and rotational motions of rockfall impacts. *International Journal of Rock Mechanics and Mining Sciences*, 39(1):69–77.

Chen, X. (2013). *Investigation on the impact damage of glass using the combined finite/discrete element method*. PhD thesis, University of Birmingham.

Chen, X., Chan, A. H., and Yang, J. (2016). Simulating the breakage of glass under hard body impact using the combined finite-discrete element method. *Computers & Structures*, 177:56–68.

Clark, W. C. (1954). Window and glass hazards under wartime conditions and recommended protective measures. Technical report, General Services Administration.

Coffield, A. and Adeli, H. (2014). An investigation of the effectiveness of the framing systems in steel structures subjected to blast loading. *Journal of Civil Engineering and Management*, 20(6):767–777.

Cundall, P. A. and Strack, O. D. (1979). A discrete numerical model for granular assemblies. *Geotechnique*, 29(1):47–65.

DIN (2015). Glass in building - thermally toughened soda lime silicate safety glass - part 1: Definition and description. Standard EN 12150-1, DIN.

Ewins, D. J. (1984). *Modal Testing: Theory and Practice*. Research Studies Press, LTD., Taunton, Somerset, England.

FEMA (2003). Fema-426: Reference manual to mitigate potential terrorist attacks against buildings.

Fineberg, J. (2006). The dynamics of rapidly moving tensile cracks in brittle amorphous material. In *Dynamic fracture mechanics*, pages 104–146. World Scientific.

Fiorio, B. (2005). Wear characterisation and degradation mechanisms of a concrete surface under ice friction. *Construction and Building Materials*, 19(5):366–375.

Friedlander, F. G. (1946). The diffraction of sound pulses i. diffraction by a semi-infinite plane. *Proc. R. Soc. Lond. A*, 186(1006):322–344.

Gao, W. and Zang, M. (2014). The simulation of laminated glass beam impact problem by developing fracture model of spherical dem. *Engineering Analysis with Boundary Elements*, 42:2–7.

Garner, D. D., Fultz, M. L., and Byall, E. B. (1986). The atf approach to post-blast explosives detection and identification. *Journal of Energetic Materials*, 4(1-4):133–148.

Gooch, J. W. (2007). *Encyclopedic Dictionary of Polymers*. Springer New York.

Griffith, A. A. (1921). Vi. the phenomena of rupture and flow in solids. *Philosophical transactions of the royal society of london. Series A, containing papers of a mathematical or physical character*, 221(582-593):163–198.

Haber, R. B. (1984). A mixed eulerian-lagrangian displacement model for large-deformation analysis in solid mechanics. *Computer Methods in Applied Mechanics and Engineering*, 43(3):277–292.

Heinstein, M., Attaway, S., Swegle, J., and Mello, F. (1993). A general-purpose contact detection algorithm for nonlinear structural analysis codes. Technical report, Sandia National Labs.

Hertz, H. R. (1882). Uber die beruhrung fester elastischer korper und uber die harte. *Verhandlung des Vereins zur Beforderung des GewerbefleiBes, Berlin*, page 449.

Hetherington, J. and Smith, P. (1994). *Blast and Ballistic Loading of Structures*. Butterworth-Heinemann Ltd.

Hidallana-Gamage, H. D., Thambiratnam, D. P., and Perera, N. J. (2014). Numerical modelling and analysis of the blast performance of laminated glass panels and the influence of material parameters. *Engineering Failure Analysis*, 45:65–84.

Hoerner, S. (1965). *Fluid-dynamic drag: practical information on aerodynamic drag and hydrodynamic resistance*. Hoerner Fluid Dynamics.

Hooper, P., Sukhram, R., Blackman, B., and Dear, J. (2012). On the blast resistance of laminated glass. *International Journal of Solids and Structures*, 49(6):899–918.

Imre, B., Räbsamen, S., and Springman, S. M. (2008). A coefficient of restitution of rock materials. *Computers & Geosciences*, 34(4):339–350.

Isobe, D. (2017). *Progressive Collapse Analysis of Structures: Numerical Codes and Applications*. Elsevier Science.

Iverson, J. H. (1968). Existing structures evaluation. part 2. window glass and applications. Technical report, Stanford Research Institute.

Johns, R. (2016). *Investigating Annealed Glazing Response to Long-Duration Blast*. PhD thesis, University of Southampton.

Johns, R. V. and Clubley, S. K. (2016). The influence of structural arrangement on long-duration blast response of annealed glazing. *International Journal of Solids and Structures*, 97:370–388.

Johnson, G. R. and Holmquist, T. J. (1994). An improved computational constitutive model for brittle materials. In *AIP Conference Proceedings*, volume 309, pages 981–984. AIP.

Kernicky, T. P., Whelan, M. J., Weggel, D. C., and Rice, C. D. (2014). Structural identification and damage characterization of a masonry infill wall in a full-scale building subjected to internal blast load. *Journal of Structural Engineering*, 141(1):D4014013.

Keys, R. and Clubley, S. K. (2013). Modelling debris distribution of masonry panels subject to blast loads using experimental & applied element methods. In *15th International Symposium on Interaction of the Effects of Munitions (ISIEMS 15)*. Infrastructure Group.

Keys, R. A. and Clubley, S. K. (2017). Establishing a predictive method for blast induced masonry debris distribution using experimental and numerical methods. *Engineering Failure Analysis*, 82:82–91.

Khoei, A. (2015). *Extended Finite Element Method: Theory and Applications*. Wiley Series in Computational Mechanics. Wiley.

Kingery, C., Bulmash, G., and Laboratory, U. A. B. R. (1984). *Air Blast Parameters from TNT Spherical Air Burst and Hemispherical Surface Burst*. Technical Report ARBRL. Ballistic Research Laboratories.

Kingery, C. and Pannill, B. (1964). Peak overpressure vs scaled distance for tnt surface bursts (hemispherical charges). Technical Report 1518, U.S. Army Ballistic Research Laboratory.

Larcher, M., Solomos, G., Casadei, F., and Gebbeken, N. (2012). Experimental and numerical investigations of laminated glass subjected to blast loading. *International Journal of Impact Engineering*, 39(1):42–50.

Lommen, S., Schott, D., and Lodewijks, G. (2014). Dem speedup: Stiffness effects on behavior of bulk material. *Particuology*, 12:107–112.

Lun, C. and Savage, S. (1986). The effects of an impact velocity dependent coefficient of restitution on stresses developed by sheared granular materials. *Acta Mechanica*, 63(1-4):15–44.

M Dobratz, B. and C Crawford, P. (1985). *LLNL Explosives Handbook Properties of Chemical Explosives and Explosive Simulants*. Lawrence Livermore National Laboratory, University of California, Livermore, CA.

Malone, K. F. and Xu, B. H. (2008). Determination of contact parameters for discrete element method simulations of granular systems. *Particuology*, 6(6):521–528.

Mase, G., Smelser, R., and Mase, G. (2009). *Continuum Mechanics for Engineers*. Computational Mechanics and Applied Analysis. CRC Press.

Meguro, K. and Tagel-Din, H. (1999). Simulation of buckling and post-buckling behavior of structures using applied element method. *Bulletin of Earthquake Resistant Structure, IIS, University of Tokyo*, 32:125–135.

Meguro, K. and Tagel-Din, H. (2000). Applied element method for structural analysis: Theory and application for linear materials. *Structural Eng./Earthquake Eng.*, 17(1):21–35.

Meguro, K. and Tagel-Din, H. (2001). Applied element simulation of rc structures under cyclic loading. *Journal of Structural Engineering*, 127(11):1295–1305.

Meguro, K. and Tagel-Din, H. S. (2002). Applied element method used for large displacement structural analysis. *Journal of Natural Disaster Science*, 24(1):25–34.

Meyers, G. E. (1984). Design criteria and preliminary acceptance test specifications for blast resistant windows. Technical report, Navel Civil Engineering Lab.

Milburn, R., Naylor, M., Smith, A., Leaper, M. C., Good, K., Swift, M. R., and King, P. (2005). Faraday tilting of water-immersed granular beds. *Physical Review E*, 71(1):011308.

Mindlin, R. D. (1953). Elastic spheres in contact under varying oblique forces. *J. Applied Mech.*, 20:327–344.

Moës, N. and Belytschko, T. (2002). Extended finite element method for cohesive crack growth. *Engineering Fracture Mechanics*, 69(7):813–833.

Moës, N., Dolbow, J., and Belytschko, T. (1999). A finite element method for crack growth without remeshing. *International Journal for Numerical Methods in Engineering*, 46(1):131–150.

Moore, D. M. (1980). Proposed method for determining the thickness of glass in solar collector panels.

Morris, J. P., Rubin, M., Block, G., and Bonner, M. (2006). Simulations of fracture and fragmentation of geologic materials using combined fem/dem analysis. *International Journal of Impact Engineering*, 33(1-12):463–473.

Munjiza, A., Owen, D., and Bicanic, N. (1995). A combined finite-discrete element method in transient dynamics of fracturing solids. *Engineering Computations*, 12(2):145–174.

National Research Council (1995). *Protecting Buildings from Bomb Damage: Transfer of Blast-Effects Mitigation Technologies from Military to Civilian Applications*. National Academies Press.

Netherton, M. D. and Stewart, M. G. (2009). Probabilistic modelling of safety and damage blast risks for window glazing. *Canadian Journal of Civil Engineering*, 36(8):1321–1331.

NIJ (2000). *A guide for explosion and bombing scene investigation*. U.S. Dept. of Justice, Office of Justice Programs, National Institute of Justice, Washington, DC.

Oakes, T. A. (1991). *The development of design factors for heat-strengthened and tempered glass based on the glass failure prediction model*. PhD thesis, Texas A&M University.

Okamura, H. and Maekawa, K. (1991). *Nonlinear Analysis and Constitutive Models of Reinforced Concrete*. Gihodo Co. Ltd.

Pape, R., Mniszewski, K. R., Longinow, A., and Kenner, M. (2010). Explosion phenomena and effects of explosions on structures. iii: Methods of analysis (explosion damage to structures) and example cases. *Practice Periodical on Structural Design and Construction*, 15(2):153–169.

Pelfrene, J., Kuntsche, J., Van Dam, S., Van Paepegem, W., and Schneider, J. (2016a). Critical assessment of the post-breakage performance of blast loaded laminated glazing: Experiments and simulations. *International Journal of Impact Engineering*, 88:61–71.

Pelfrene, J., Van Dam, S., Sevenois, R., Gilabert, F., and Van Paepegem, W. (2016b). Fracture simulation of structural glass by element deletion in explicit fem. In *Challenging Glass Conference Proceedings*, volume 5, pages 439–454.

Pourmoghaddam, N. and Schneider, J. (2018). Experimental investigation into the fragment size of tempered glass. *Glass Structures & Engineering*, 3(2):167–181.

Pritchard, D. (1981). Breakage of glass windows by explosions. *Journal of Occupational accidents*, 3(2):69–85.

Quinn, G. D. (2019). On terminal crack velocities in glasses. *International Journal of Applied Glass Science*, 10(1):7–16.

Ramos, A., Pelayo, F., Lamela, M., Canteli, A. F., Huerta, C., and Acios, A. (2013). Evaluation of damping properties of structural glass panes under impact loading. In *COST Action TU0905 Mid-Term Conference on Structural Glass; Belis, J., Louter, C., Mocibob, D., Eds*.

Rashid, Y. (1968). Ultimate strength analysis of prestressed concrete pressure vessels. *Nuclear Engineering and Design*, 7(4):334–344.

Ristic, D., Yamada, Y., and Iemura, H. (1986). Stress-strain based modeling of hysteric structures under earthquake induced bending and varying axial loads. Technical Report 86-ST-01, School of Civil Engineering, Kyoto University.

Roemer, M. and Mook, D. (1992). Mass, stiffness, and damping matrix identification: an integrated approach. *Journal of Vibrations and Acoustics*, 114(3):359–363.

Rojek, J., Zarate, F., de Saracibar, C. A., Gilbourne, C., and Verdot, P. (2005). Discrete element modelling and simulation of sand mould manufacture for the lost foam process. *International Journal for Numerical Methods in Engineering*, 62(11):1421–1441.

Schardin, H. (1959). Velocity effects in fracture. In *ICF0, Swampscott-MA (USA) 1959*.

Seaman, L. (1967). Response of windows to sonic booms. Technical report, Stanford Research Institute.

Shukla, A., Rajapakse, Y., and Hynes, M. (2013). *Blast Mitigation: Experimental and Numerical Studies*. Springer New York.

Song, J.-H., Wang, H., and Belytschko, T. (2008). A comparative study on finite element methods for dynamic fracture. *Computational Mechanics*, 42(2):239–250.

Sorensen, A. and McGill, W. L. (2011a). What to look for in the aftermath of an explosion? a review of blast scene damage observables. *Engineering Failure Analysis*, 18(3):836–845.

Sorensen, A. and McGill, W. L. (2012). Utilization of existing blast analysis software packages for the back-calculation of blast loads. *Journal of Performance of Constructed Facilities*, 26(4):544–546.

Sorensen, A. D. and McGill, W. (2011b). Toward guidance for identifying and measuring structural damage following a blast event. In *Vulnerability, Uncertainty, and Risk: Analysis, Modeling, and Management*, pages 857–864.

Sozen, M. A., Thornton, C. H., Corley, W. G., and Sr, P. F. M. (1998). The oklahoma city bombing: structure and mechanisms of the murrah building. *Journal of Performance of Constructed Facilities*, 12(3):120–136.

Spiller, K., Packer, J. A., Seica, M. V., and Yankelevsky, D. Z. (2016). Prediction of annealed glass window response to blast loading. *International Journal of Impact Engineering*, 88:189–200.

Sukumar, N., Moës, N., Moran, B., and Belytschko, T. (2000). Extended finite element method for three-dimensional crack modelling. *International Journal for Numerical Methods in Engineering*, 48(11):1549–1570.

Swisdak, M. M. J. (1994). Simplified kingery airblast calculations. Technical report, Naval Surface Warfare Center Indian Head Division.

Tagel-Din, H. (1998). *A New Efficient Method for Nonlinear, Large Deformation and Collapse Analysis of Structures*. PhD thesis, University of Tokyo.

Tagel-Din, H. (2009). High fidelity modeling of building collapse with realistic visualization of resulting damage and debris using the applied element method. *Rep. No. HDTRA1-09-P*, 6.

Tagel-Din, H. and Meguro, K. (1999). Applied element simulation for collapse analysis of structures. *Bull. of Earthquake Resistant Struct. Res. Ctr*, pages 113–123.

Tagel-Din, H. and Meguro, K. (2000a). Applied element method for dynamic large deformation analysis of structures. *Doboku Gakkai Ronbunshu*, 2000(661):1–10.

Tagel-Din, H. and Meguro, K. (2000b). Nonlinear simulation of rc structures using applied element method. *Doboku Gakkai Ronbunshu*, 2000(654):13–24.

Tagel-Din, H. and Rahman, N. A. (2006). Simulation of the alfred p. murrah federal building collapse due to blast loads. In *Building Integration Solutions*, pages 1–15. American Society of Civil Engineers.

Tatara, Y. and Moriwaki, N. (1982). Study on impact of equivalent two bodies: coefficients of restitution of spheres of brass, lead, glass, porcelain and agate, and the material properties. *Bulletin of JSME*, 25(202):631–637.

Tedesco, J. W., McDougal, W. G., and Ross, C. A. (1999). *Structural Dynamics: Theory and Applications*. Addison Wesley Longman, Boston, MA.

Uhlmann, D. R. (1980). *Elasticity and Strength in Glasses*. Academic Press.

US Army Corps of Engineers (2008). *Structures to Resist the Effects of Accidental Explosions*. Naval Facilities Engineering Command.

USBDC (2015). Explosives incident report. Technical report, Bureaus of Alcohol, Tobacco, Firearms, and Explosives.

USBDC (2017). Explosives incident report. Technical report, Bureaus of Alcohol, Tobacco, Firearms, and Explosives.

Van der Voort, M., Van Wees, R., Brouwer, S., Van der Jagt-Deutekom, M., and Verreault, J. (2015). Forensic analysis of explosions: Inverse calculation of the charge mass. *Forensic Science International*, 252:11–21.

Van Overschee, P. and De Moor, B. (1996). *Subspace Identification for Linear Systems: Theory - Implementation - Applications*. Kluwer Academic Publishers, Dordrecht, Netherlands.

Varner, J. and Wightman, M. (2012). *Fractography of Glasses and Ceramics VI*. Ceramic Transactions Series. Wiley.

Verolme, E., Van der Voort, M., Smits, R., Weerheijm, J., Koh, Y., and Kang, K. (2018). A method for backward calculation of debris in a post blast scene. *Journal of Loss Prevention in the Process Industries*, 51:54–64.

Vu-Quoc, L. and Zhang, X. (1999). An accurate and efficient tangential force–displacement model for elastic frictional contact in particle-flow simulations. *Mechanics of Materials*, 31(4):235–269.

Wei, J., Shetty, M. S., and Dharani, L. R. (2006). Failure analysis of architectural glazing subjected to blast loading. *Engineering failure analysis*, 13(7):1029–1043.

Weibull, W. (1939). A statistical theory of strength of materials. *IVB-Handl.*

Wesevich, J. W. and Olson, D. B. (2005). Explosion forensic analysis. In *Structures Congress 2005: Metropolis and Beyond*, pages 1–10.

Williams, J. R. and O'Connor, R. (1995). A linear complexity intersection algorithm for discrete element simulation of arbitrary geometries. *Engineering Computations*, 12(2):185–201.

Worakanchana, K. and Meguro, K. (2006). Voronoi applied element method for structural analysis: Theory and application for linear and non-linear materials. *Bulletin of Earthquake Resistant Structure Research Center*, (39).

Yuu, S., Abe, T., Saitoh, T., and Umekage, T. (1995). Three-dimensional numerical simulation of the motion of particles discharging from a rectangular hopper using distinct element method and comparison with experimental data (effects of time steps and material properties). *Advanced Powder Technology*, 6(4):259–269.

Zhang, P., Nagae, T., McCormick, J., Ikenaga, M., Katsuo, M., and Nakashima, M. (2008). Friction-based sliding between steel and steel, steel and concrete, and wood and stone. In *Proceedings of the 14th World Conference on Earthquake Engineering, Beijing, China*, pages 12–17.

Zhang, X. and Hao, H. (2016). The response of glass window systems to blast loadings: An overview. *International Journal of Protective Structures*, 7(1):123–154.

Zhang, X., Hao, H., and Wang, Z. (2014). Experimental investigation of monolithic tempered glass fragment characteristics subjected to blast loads. *Engineering Structures*, 75:259–275.

Zhang, X., Hao, H., and Wang, Z. (2015). Experimental investigation on monolithic tempered glass window responses to blast loads. *International Journal of Protective Structures*, 6(2):287–309.

Zhang, Y.-Q., Lu, Y., and Hao, H. (2004). Analysis of fragment size and ejection velocity at high strain rate. *International journal of mechanical sciences*, 46(1):27–34.

Zhong, Z.-H. and Mackerle, J. (1994). Contact-impact problems: a review with bibliography. *Applied Mechanics Reviews*, 47(2):55–76.

APPENDIX A: COMPILATION OF STIFFNESS MATRIX DERIVATIONS

A.1 Stiffness Matrix Derivation

A.2 Deformation-Displacement Relationships

A.3 Resolution of Element Local Forces from Interface Spring Forces

TABLE A.1: The local stiffness matrix for one pair of elements connected at the $+y$ face of element 1

d_1	d_2	d_3	d_4	d_5	d_6	d_7	d_8	d_9	d_{10}	d_{11}	d_{12}
k_{sx}	0	0	0	$k_{sx}c_{n1}$	$-\frac{b_1}{2}k_{sx}$	$-k_{sx}$	0	0	0	$-k_{sx}c_{n2}$	$-\frac{b_2}{2}k_{sx}$
0	k_n	0	$-k_n c_{n1}$	0	$-k_n a_{n1}$	0	$-k_n$	0	$k_n c_{n2}$	0	$k_n a_{n2}$
0	0	k_{sz}	$\frac{b_1}{2}k_{sz}$	$-k_{sz}a_{n1}$	0	0	0	$-k_{sz}$	$\frac{b_2}{2}k_{sz}$	$k_{sz}a_{n2}$	0
0	$-k_n c_{n1}$	$\frac{b_1}{2}k_{sz}$	$\frac{b_1^2}{4}k_{sz}$ $+k_n c_{n1}^2$	$-\frac{b_1}{2}k_{sz}a_{n1}$	$k_n a_{n1}c_{n1}$	0	$k_n c_{n1}$	$-\frac{b_1}{2}k_{sz}$	$\frac{b_1}{2}\frac{b_2}{2}k_{sz}$ $-k_n c_{n1}c_{n2}$	$\frac{b_1}{2}k_{sz}a_{n2}$	$-k_n a_{n2}c_{n1}$
$k_{sx}c_{n1}$	0	$-k_{sz}a_{n1}$	$k_n c_{n1}a_{n1}$	$k_{sz}a_{n1}^2$ $+k_{sx}c_{n1}^2$	$-\frac{b_1}{2}k_{sx}c_{n1}$	$-k_{sx}c_{n1}$	0	$k_{sz}a_{n1}$	$-\frac{b_2}{2}k_{sz}a_{n1}$	$-k_{sz}a_{n1}a_{n2}$ $-k_{sx}c_{n1}c_{n2}$	$-\frac{b_2}{2}k_{sx}c_{n1}$
$-\frac{b_1}{2}k_{sx}$	$-k_n a_{n1}$	0	$k_n c_{n1}a_{n1}$	$-\frac{b_1}{2}k_{sx}c_{n1}$	$k_n a_{n1}^2$ $+\frac{b_1^2}{4}k_{sx}$	$\frac{b_1}{2}k_{sx}$	$k_n a_{n1}$	0	$-k_n c_{n2}a_{n1}$	$\frac{b_1}{2}k_{sx}c_{n2}$	$\frac{b_2}{2}\frac{b_1}{2}k_{sx}$ $-k_n a_{n1}a_{n2}$
$-k_{sx}$	0	0	0	$-k_{sx}c_{n1}$	$\frac{b_1}{2}k_{sx}$	k_{sx}	0	0	0	$k_{sx}c_{n2}$	$\frac{b_2}{2}k_{sx}$
0	$-k_n$	0	$k_n c_{n1}$	0	$k_n a_{n1}$	0	k_n	0	$-k_n c_{n2}$	0	$-k_n a_{n2}$
0	0	$-k_{sz}$	$-\frac{b_1}{2}k_{sz}$	$k_{sz}a_{n1}$	0	0	0	k_{sz}	$-\frac{b_2}{2}k_{sz}$	$-k_{sz}a_{n2}$	0
0	$k_n c_{n2}$	$\frac{b_2}{2}k_{sz}$	$-\frac{b_1}{2}\frac{b_2}{2}k_{sz}$ $-k_n c_{n1}c_{n2}$	$-\frac{b_2}{2}k_{sz}a_{n1}$	$-k_n a_{n1}c_{n2}$	0	$-k_n c_{n2}$	$-\frac{b_2}{2}k_{sz}$	$\frac{b_2^2}{4}k_{sz}$ $+k_n c_{n2}^2$	$\frac{b_2}{2}k_{sz}a_{n2}$	$k_n a_{n2}c_{n2}$
$-k_{sx}c_{n2}$	0	$k_{sz}a_{n2}$	$-k_n c_{n1}a_{n2}$	$-k_{sz}a_{n1}a_{n2}$ $-k_{sx}c_{n1}c_{n2}$	$\frac{b_1}{2}k_{sx}c_{n2}$	$k_{sx}c_{n2}$	0	$-k_{sz}a_{n2}$	$\frac{b_2}{2}k_{sz}a_{n2}$	$k_{sz}a_{n2}^2$ $+k_{sx}c_{n2}^2$	$\frac{b_2}{2}k_{sx}c_{n2}$
$\frac{b_2}{2}k_{sx}$	$k_n a_{n2}$	0	$-k_n c_{n1}a_{n2}$	$-\frac{b_2}{2}k_{sx}c_{n1}$	$\frac{b_1}{2}\frac{b_2}{2}k_{sx}$ $-k_n a_{n1}a_{n2}$	$\frac{b_2}{2}k_{sx}$	$-k_n a_{n2}$	0	$k_n c_{n1}a_{n2}$	$\frac{b_2}{2}k_{sx}c_{n2}$	$\frac{b_2^2}{4}k_{sx}$ $+k_n a_{n2}^2$

TABLE A.2: The local stiffness matrix for one pair of elements connected at the $+z$ face of element 1

d_1	d_2	d_3	d_4	d_5	d_6	d_7	d_8	d_9	d_{10}	d_{11}	d_{12}
k_{sx}	0	0	0	$\frac{c_1}{2}k_{sx}$	$-k_{sx}b_{n1}$	$-k_{sx}$	0	0	0	$\frac{c_2}{2}k_{sx}$	$k_{sx}b_{n2}$
0	k_{sy}	0	$-\frac{c_1}{2}k_{sy}$	0	$k_{sy}a_{n1}$	0	$-k_{sy}$	0	$-\frac{c_2}{2}k_{sy}$	0	$-k_{sy}a_{n2}$
0	0	k_n	k_nb_{n1}	$-k_na_{n1}$	0	0	0	$-k_n$	$-k_nb_{n2}$	k_na_{n2}	0
0	$-\frac{c_1}{2}k_{sy}$	k_nb_{n1}	$\frac{c_1^2}{4}k_{sy}+k_nb_{n1}^2$	$-k_na_{n1}b_{n1}$	$-\frac{c_1}{2}k_{sy}a_{n1}$	0	$\frac{c_1}{2}k_{sy}$	$-k_nb_{n1}$	$\frac{c_1}{2}\frac{c_2}{2}k_{sy}-k_nb_{n1}b_{n2}$	$k_na_{n2}b_{n1}$	$\frac{c_1}{2}k_{sy}a_{n2}$
$\frac{c_1}{2}k_{sx}$	0	$-k_na_{n1}$	$-k_nb_{n1}a_{n1}$	$-\frac{c_1}{2}k_{sx}+k_na_{n1}^2$	$-\frac{c_1}{2}k_{sx}b_{n1}$	$-\frac{c_1}{2}k_{sx}$	0	k_na_{n1}	$k_nb_{n2}a_{n1}$	$-\frac{c_1}{2}\frac{c_2}{2}k_{sx}-k_na_{n1}a_{n2}$	$\frac{c_1}{2}k_{sx}b_{n2}$
$-k_{sx}b_{n1}$	$k_{sy}a_{n1}$	0	$-\frac{c_1}{2}k_{sy}a_{n1}$	$-\frac{c_1}{2}k_{sx}b_{n1}$	$k_{sy}a_{n1}^2+k_{sx}b_{n1}^2$	$k_{sx}b_{n1}$	$-k_{sy}a_{n1}$	0	$-\frac{c_2}{2}k_{sy}a_{n1}$	$-\frac{c_1}{2}\frac{c_2}{2}k_{sx}-k_na_{n1}a_{n2}$	$-k_{sx}b_{n1}b_{n2}-k_{sy}a_{n1}a_{n2}$
$-k_{sx}$	0	0	0	$-\frac{c_1}{2}k_{sx}$	$k_{sx}b_{n1}$	k_{sx}	0	0	0	$-\frac{c_2}{2}k_{sx}$	$-k_{sx}b_{n2}$
0	$-k_{sy}$	0	$\frac{c_1}{2}k_{sy}$	0	$-k_{sy}a_{n1}$	0	k_{sy}	0	0	0	$k_{sy}a_{n2}$
0	0	$-k_n$	$-k_nb_{n1}$	k_na_{n1}	0	0	0	k_n	k_nb_{n2}	$-k_na_{n2}$	0
0	$-\frac{c_2}{2}k_{sy}$	$-k_nb_{n2}$	$\frac{c_1}{2}k_{sy}a_{n2}$	$\frac{c_1}{2}\frac{c_2}{2}k_{sx}-k_na_{n1}a_{n2}$	$-\frac{c_2}{2}k_{sy}a_{n1}$	0	$\frac{c_2}{2}k_{sy}$	$-k_na_{n2}$	$-k_nb_{n2}a_{n2}$	$-k_na_{n2}b_{n2}$	$\frac{c_2}{2}k_{sy}a_{n2}$
$\frac{c_2}{2}k_{sx}$	0	k_na_{n2}	$k_nb_{n1}a_{n2}$	$\frac{c_1}{2}k_{sx}b_{n2}$	$-\frac{c_2}{2}k_{sx}b_{n1}$	$-\frac{c_2}{2}k_{sx}$	0	k_nb_{n2}	$\frac{c_2}{2}k_{sy}a_{n2}$	$\frac{c_2}{2}k_{sx}b_{n2}$	$\frac{c_2}{2}k_{sx}b_{n2}$
$k_{sx}b_{n2}$	$-k_{sy}a_{n2}$	0	$-k_{sy}a_{n1}a_{n2}-k_{sx}b_{n1}b_{n2}$	$-k_{sy}a_{n1}a_{n2}-k_{sx}b_{n1}b_{n2}$	$-k_{sx}b_{n2}$	$k_{sy}a_{n2}$	0	$-k_na_{n2}$	$-k_nb_{n2}a_{n2}$	$\frac{c_2}{2}k_{sx}b_{n2}$	$k_{sx}b_{n2}^2+k_{sy}a_{n2}^2$

TABLE A.3: Deformation-displacement relationship for one pair of elements connected at the $+y$ face of element 1

-1	0	0	0	$-c_{n1}$	$\frac{b_1}{2}$	1	0	0	0	c_{n2}	$\frac{b_2}{2}$
0	-1	0	c_{n1}	0	$-a_{n1}$	0	1	0	$-c_{n2}$	0	a_{n2}
0	0	-1	$\frac{b_1}{2}$	a_{n1}	0	0	0	1	$\frac{-b_2}{2}$	$-a_{n2}$	0

TABLE A.4: Deformation-displacement relationship for one pair of elements connected at the $+z$ face of element 1

-1	0	0	0	$\frac{-c_1}{2}$	b_{n1}	1	0	0	0	$\frac{-c_2}{2}$	b_{n2}
0	-1	0	$\frac{c_1}{2}$	0	$-a_{n1}$	0	1	0	$\frac{c_2}{2}$	0	a_{n2}
0	0	-1	$-b_{n1}$	a_{n1}	0	0	0	1	b_{n2}	$-a_{n2}$	0

	Incremental displacements δd_1 and δd_2 in global coordinates
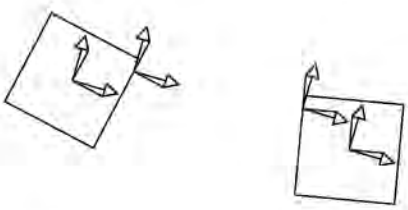	$[T']\{\delta D'_e\}$ Incremental displacements in a common local coordinate frame taken as the average orientation of elements
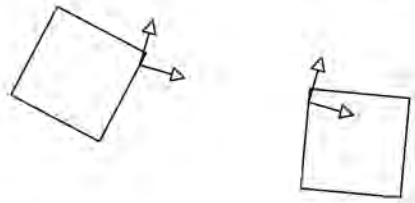	$[B][T']\{\delta D'_e\}$ Incremental spring elongations in a common local coordinate frame taken as the average orientation of elements
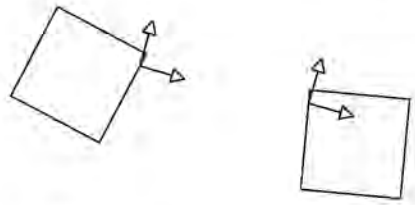	$[k_{edge}][B][T']\{\delta D'_e\}$ Incremental spring forces in a common coordinate frame taken as the average orientation of elements
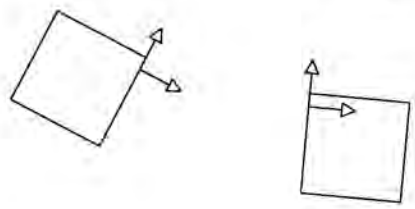	$[R'][k_{edge}][B][T']\{\delta D'_e\}$ Incremental spring forces rotated into a local coordinate frame for each element
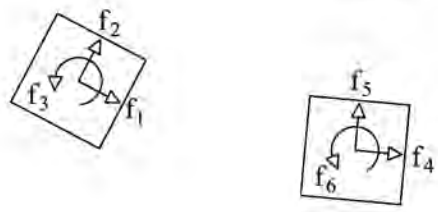	$[B'][R'][k_{edge}][B][T']\{\delta D'_e\}$ Forces and moments at the element determined from forces at the spring location

FIGURE A.1: Determination of the resultant element local forces resulting from forces in interface springs

APPENDIX B: COMPILATION OF EXPERIMENTAL RESULTS

B.1 Camera Specifications

TABLE B.1: Settings for the high-speed camera during open-arena blast testing

Test	Frame Rate (fps)	Resolution (pixels)
1	8113.59	256 x 256
2	8146.64	256 x 256
3	8146.64	256 x 256
4	8146.64	256 x 256
5	8146.64	128 x 256
6	8510.64	128 x 512

B.2 Specifications of Pressure Transducers during Open-Arena Blast Testing

TABLE B.2: Specifications of flush mount pressure transducers and free-air pencil probes

		Sensitivity	Resonant Frequency	Measurement Range
Sensor	Model	mV/kPa (mV/psi)	kHz	MPa (psi)
P1	102B03	0.0750 (0.5168)	>=500	68.9 (10000)
P2	102B	0.1439 (0.9921)	>=500	34.5 (5000)
P3	102B	0.1418 (0.9775)	>=500	34.5 (5000)
P4	102A04	0.7246 (4.996)	>=500	6.9 (1000)
P5	102B03	0.0727 (0.5010)	>=500	68.9 (10000)
P6	S102A	0.1395 (0.9616)	>=500	34.5 (5000)
P7	102A03	0.0719 (0.4956)	>=500	68.9 (10000)
P8	102A03	0.0699 (0.4820)	>=500	68.9 (10000)
P9	102B03	0.0733 (0.5052)	>=500	68.9 (10000)
Pencil Probe 1	137A21	0.1478 (1.0190)	>=500	34.5 (5000)
Pencil Probe 2	137A21	0.1435 (0.9892)	>=500	34.5 (5000)

(A) Sensors P5 and P9 were switched during Shot 1

B.3 Modal Parameter Estimate Sets of Glass Lite Panels

Modal data from every glass lite subjected to experimental blast loading was collected using two uniaxial accelerometers adhered to the surface of the lite. As explained in Chapter 4, averaging was performed across the two sensors to develop individual sets of modal parameter estimates for every lite. Modes are denoted by the number of half wavelengths across the short dimension of the lite (width), followed by the number of half wavelengths in the long dimension of the lite (height)

TABLE B.3: Measured natural frequencies in Hertz of all glass lites subjected to experimental blast loading

Mode		1,1	1,2	2,1	1,3	2,2	1,4	2,3	3,1	2,4	3,2	3,3
Panel 1	Shot 1	30.5	53.0	90.2	93.0	114.6	148.0	155.1	186.1	210.9	208.5	–
Panel 1	Shot 2	34.7	59.2	95.0	99.6	118.6	155.6	158.3	192.0	214.0	217.4	243.7
Panel 1	Shot 3	34.5	58.8	95.1	99.5	118.9	155.7	158.3	194.1	214.2	217.6	243.4
Panel 1	Shot 4	35.9	61.2	96.4	101.3	120.5	157.9	159.7	195.5	214.9	217.9	241.7
Panel 1	Shot 5*	18.2	34.5	53.8	59.2	71.8	94.4	96.9	112.6	133.5	130.5	156.3
Panel 1	Shot 6*	18.2	34.5	53.8	59.4	71.8	94.4	96.9	112.6	133.5	130.5	156.3
Panel 2	Shot 1	27.8	48.9	–	97.8*	111.2	142.5	151.0	181.5	206.8	206.6	247.7
Panel 2	Shot 2	34.3	58.7	93.9	99.0	118.2	155.1	157.5	189.3	212.6	223.6	245.3
Panel 2	Shot 3	32.3	56.3	91.5	96.7	115.5	153.4	155.2	187.3	–	210.7	248.5
Panel 2	Shot 4	33.5	57.6	93.6	97.6	117.9	154.4	156.9	190.9	212.9	221.9	245.6
Panel 2	Shot 5*	17.1	33.5	53.2	58.4	70.9	91.9	96.4	111.8	132.4	129.2	155.5
Panel 2	Shot 6*	17.1	33.5	53.2	58.5	71.0	91.2	96.4	111.8	132.4	129.2	155.6
Panel 3	Shot 1	30.2	53.4	88.6	93.0	112.4	147.2	152.2	184.6	207.7	206.6	247.7
Panel 3	Shot 2	33.9	58.5	93.7	99.1	117.9	155.0	157.4	190.1	213.3	220.3	245.5
Panel 3	Shot 3	33.4	57.9	93.3	98.7	117.5	154.7	157.6	187.8	212.9	221.1	245.2
Panel 3	Shot 4	33.4	57.4	92.9	98.2	117.1	154.2	157.2	191.3	212.7	220.2	245.3
Panel 3	Shot 5*	18.0	33.9	54.0	58.7	71.6	93.5	96.7	112.6	133.0	130.4	156.2
Panel 3	Shot 6*	18.0	33.9	54.0	58.8	71.6	93.5	96.7	112.7	133.0	130.3	156.2
Panel 4	Shot 1	29.9	52.7	87.7	92.8	112.0	147.7	152.3	184.9	208.3	205.9	247.2
Panel 4	Shot 2	34.8	59.8	93.9	100.7	117.6	156.7*	156.8	191.4	212.7	–	245.7
Panel 4	Shot 3	32.5	57.4	91.6	98.0	115.8	154.2	155.4	188.3	211.4	212.3	247.3
Panel 4	Shot 4	32.5	57.3	91.7	97.8	116.5	153.7	156.3	188.7	211.9	210.5	247.1
Panel 4	Shot 5*	16.6	32.8	52.4	57.9	70.2	92.5	95.8	109.2	131.6	128.2	154.7
Panel 4	Shot 6*	17.2	32.8	52.4	57.8	70.2	92.5	95.8	109.2	131.7	128.2	154.7
Panel 5	Shot 1	32.3	56.9	89.0	97.8	113.0	153.6	152.7	185.9	208.6	205.8	246.4
Panel 5	Shot 2	32.4	58.3	90.5	99.4	115.1	156.2	155.4	188.7	211.7	209.6	248.4
Panel 5	Shot 3	32.6	57.0	91.6	97.2	115.4	154.0	155.0	189.2	211.5	210.3	248.5
Panel 5	Shot 4	33.7	58.1	93.0	98.3	116.3	155.2	156.1	188.0	212.6	210.8	248.1
Panel 5	Shot 5*	18.3	34.0	53.4	59.2	70.8	94.1	96.8	107.7	132.9	128.2	154.8
Panel 5	Shot 6	34.7	60.0	93.5	100.9	117.2	157.9	157.5	191.5	213.3	212.4	246.2
Panel 6	Shot 1	29.9	53.2	88.2	93.0	112.6	148.3	152.7	185.8	208.3	207.7	248.0
Panel 6	Shot 2	34.2	58.8	94.2	99.6	118.5	155.3	158.3	192.5	213.4	214.9	243.8
Panel 6	Shot 3	34.4	59.5	94.5	100.4	118.8	156.8	158.6	192.1	214.5	215.1	243.8
Panel 6	Shot 4	33.2	57.2	93.4	97.8	117.1	153.5	156.8	190.3	212.1	212.5	245.2
Panel 6	Shot 5*	16.3	33.3	53.0	58.4	71.6	93.3	97.1	110.3	133.4	130.2	156.5
Panel 6	Shot 6	35.9	60.9	96.4	101.8	120.1	158.5	159.7	195.5	216.1	216.4	241.8

(A) Exclusion from averaging indicated by*

TABLE B.4: Measured percentage modal damping of all glass lites subjected to experimental blast loading

Mode		1,1	1,2	2,1	1,3	2,2	1,4	2,3	3,1	2,4	3,2	3,3
Panel 1	Shot 1	2.5	1.4	1.1	1.2	0.9	0.7	0.7	1.6	1.0	0.6	–
Panel 1	Shot 2	2.4	1.9	1.4	1.2	1.0	0.9	0.8	2.3	0.7	1.6	0.8
Panel 1	Shot 3	2.3	1.7	1.6	1.3	1.0	1.0	0.9	1.7	0.7	1.4	1.1
Panel 1	Shot 4	2.4	2.2	1.6	0.8	1.0	0.8	0.8	0.4	0.7	2.0	0.9
Panel 1	Shot 5*	4.4	1.2	1.2	1.4	0.8	0.9	0.6	1.3	0.6	0.7	0.5
Panel 1	Shot 6*	4.6	1.2	1.2	1.7	0.8	0.9	0.6	1.4	0.6	0.7	0.5
Panel 2	Shot 1	3.2	1.4	–	15.9*	1.0	0.7	0.7	1.1	0.8	0.3	0.6
Panel 2	Shot 2	2.5	2.2	1.3	1.7	1.1	0.8	0.9	0.1	0.7	1.8	0.9
Panel 2	Shot 3	3.2	2.3	1.2	1.4	1.0	0.8	0.8	1.5	–	0.6	0.9
Panel 2	Shot 4	2.7	2.2	1.3	1.8	1.1	0.8	0.8	2.1	0.7	0.4	0.8
Panel 2	Shot 5*	3.9	1.2	1.2	1.0	0.8	2.2	0.6	1.1	0.5	0.6	0.6
Panel 2	Shot 6*	4.0	1.2	1.2	1.0	0.8	2.9	0.6	1.1	0.6	0.6	0.6
Panel 3	Shot 1	2.4	1.3	1.1	1.3	0.8	0.9	0.7	1.9	0.6	0.7	0.5
Panel 3	Shot 2	2.3	1.7	1.5	1.5	1.1	0.9	0.8	0.9	1.1	0.6	1.5
Panel 3	Shot 3	2.5	1.8	1.5	1.3	1.0	0.9	0.8	3.1	0.7	1.8	0.9
Panel 3	Shot 4	3.2	1.8	1.5	1.5	1.1	0.8	0.8	2.1	0.7	1.2	0.6
Panel 3	Shot 5*	2.6	1.2	1.5	0.9	0.8	0.7	0.7	1.5	0.6	0.7	0.5
Panel 3	Shot 6*	2.6	1.2	1.5	0.9	0.9	0.7	0.7	1.5	0.6	0.7	0.5
Panel 4	Shot 1	2.4	1.4	1.3	1.5	1.0	0.8	0.7	1.7	0.6	0.9	0.6
Panel 4	Shot 2	2.2	1.5	1.3	1.3	1.1	0.9*	0.9	2.3	0.7	–	0.8
Panel 4	Shot 3	2.3	1.4	1.2	1.3	1.0	0.8	0.8	1.6	0.6	0.8	0.8
Panel 4	Shot 4	2.3	1.4	1.3	1.2	1.1	0.9	0.8	1.3	0.7	1.0	1.1
Panel 4	Shot 5*	5.5	1.2	1.2	2.2	0.9	0.7	0.6	0.9	0.5	0.7	0.5
Panel 4	Shot 6*	3.9	1.2	1.2	2.3	0.9	0.7	0.6	0.9	0.5	0.7	0.5
Panel 5	Shot 1	2.3	1.4	2.1	1.0	1.1	0.6	0.7	1.8	0.6	1.1	0.7
Panel 5	Shot 2	2.2	1.3	1.0	1.0	0.8	0.7	0.7	1.3	0.7	0.7	1.1
Panel 5	Shot 3	2.4	1.5	1.4	0.8	1.0	0.8	0.8	1.0	0.7	0.8	1.2
Panel 5	Shot 4	2.3	1.9	1.5	2.1	1.2	0.9	0.9	2.2	0.7	0.8	0.9
Panel 5	Shot 5*	4.5	1.2	1.4	0.8	0.9	1.1	0.8	2.2	0.5	0.7	0.5
Panel 5	Shot 6	2.5	1.7	2.4	1.3	1.5	1.0	0.5	1.4	0.8	1.9	1.2
Panel 6	Shot 1	2.6	1.4	1.4	1.7	1.3	0.8	0.7	1.3	0.5	1.4	0.6
Panel 6	Shot 2	2.5	1.4	1.3	1.2	1.0	0.8	0.8	1.8	0.7	2.0	1.0
Panel 6	Shot 3	3.0	1.4	1.3	1.3	1.0	0.9	0.8	1.6	0.7	1.4	0.9
Panel 6	Shot 4	2.5	1.4	1.4	1.4	1.1	0.8	0.9	1.2	0.7	1.8	0.8
Panel 6	Shot 5*	3.2	1.2	1.5	1.4	1.0	0.7	0.6	1.3	0.5	0.7	0.5
Panel 6	Shot 6	2.6	1.4	1.5	1.6	1.1	1.0	0.9	1.8	0.8	1.3	0.8

(A) Exclusion from averaging indicated by*

B.4 Mass Distribution of Glass Debris

TABLE B.5: Measured mass of glass debris across the floor of the test enclosure

Test 1	Grid	1	2	3
Mass (g)	A	1056.3	1403.3	1622.8
Mass (g)	B	2261.4	2686.8	3087.9
Mass (g)	C	14287.9	14594.2	12100.4
Test 2	Grid	1	2	3
Mass (g)	A	2344.8	2261.3	2359.6
Mass (g)	B	3241.8	2377.0	2807.7
Mass (g)	C	3448.5	2620.9	3016.7
Test 3	Grid	1	2	3
Mass (g)	A	11473.9	1630.5	35.4
Mass (g)	B	3274.2	617.5	35.4
Mass (g)	C	119.8	49.7	32.1
Test 4	Grid	1	2	3
Mass (g)	A	21.9	207.3	3460.4
Mass (g)	B	20.2	81.4	386.8
Mass (g)	C	11.0	16.2	43.1
Test 5	Grid	1	2	3
Mass (g)	A	209.7	2277.2	2801.4
Mass (g)	B	24.0	116.6	186.2
Mass (g)	C	10.1	24.9	38.9
Test 6	Grid	1	2	3
Mass (g)	A	240.6	5169.3	4000.9
Mass (g)	B	82.3	506.9	936.0
Mass (g)	C	51.0	55.0	90.8

B.5 Summary of Open-Arena Blast Tests

2.5.1 Summary of Test 1

From the perspective of facing the glass lite specimens, the charge was located in line with the center of the enclosure. The description of the charge, including the composition, scale weight, and distances relative the incident pressure probes and central glass lite specimen in the bottom row of lites (Lite 5), are presented in Table B.6.

TABLE B.6: Summary of Test 1

Charge composition	PETN
Parallel distance from Lite (m)	0.00
Perpendicular distance from Lite 5 (m)	1.82
Charge weight (g)	941.20
Distance to PP1 (m)	1.82
Distance to PP2 (m)	1.82

Observable damage from Test 1 is summarized in Table B.7. A photograph of the distribution of glass debris outside of the test enclosure is provided in Figure B.1. A photograph of the distribution of glass debris on the floor of the test enclosure is shown in Figure B.2 along with an aerial view rendering of the debris distribution obtained using the LiDAR scanning system. Low-hazard and high-hazard glass debris captured by the witness panel is shown in a photograph in Figure B.3. A contrasted version of the photograph is also presented to highlight the glass debris embedded in the witness panel.

TABLE B.7: Observable post-blast damage from Test 1

Number of lites broken	6
Name of broken lites	1, 2, 3, 4, 5, 6
Very low hazard debris	Significant
Low hazard debris	Significant
High hazard debris	Significant

FIGURE B.1: Exterior debris field distribution following Test 1

a) Photograph of debris field b) LiDAR rendering of debris field

FIGURE B.2: Interior debris field distribution following Test 1

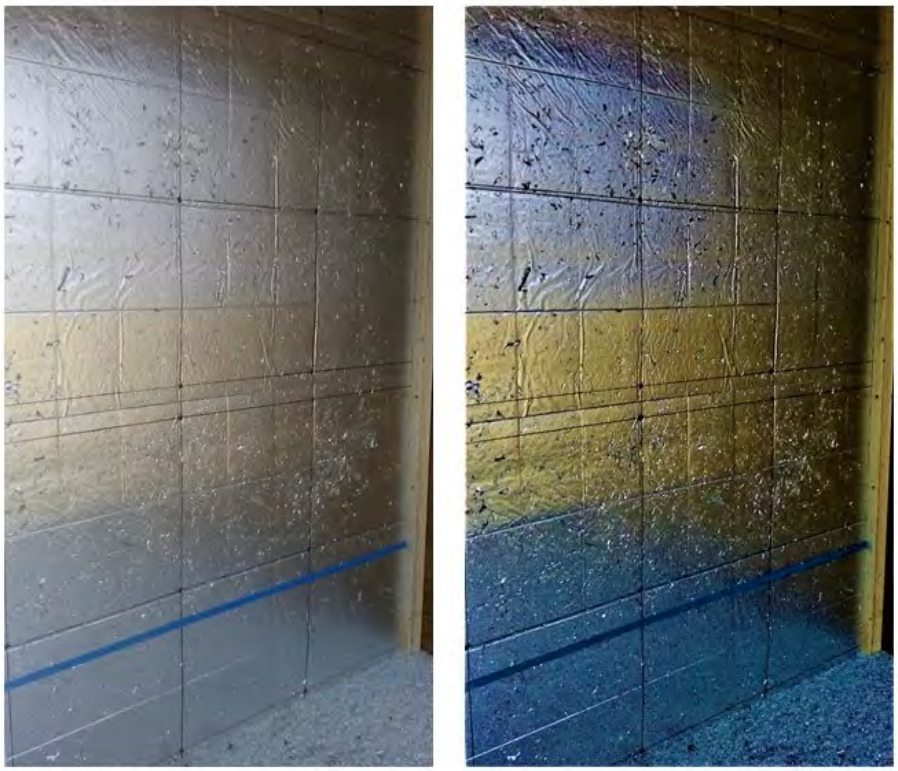

a) In-field photograph b) Contrasted photograph

FIGURE B.3: Glass debris in witness panel following Test 1

2.5.2 Summary of Test 2

From the perspective of facing the glass lite specimens, the charge was located left of center of the enclosure. The description of the charge, including the composition, scale weight, and distances relative the incident pressure probes and central glass lite specimen in the bottom row of lites (Lite 5), are presented in Table B.8.

TABLE B.8: Summary of Test 2

Charge composition	PETN
Parallel distance from Lite (m)	0.85
Perpendicular distance from Lite 5 (m)	3.03
Charge weight (g)	961.62
Distance to PP1 (m)	3.13
Distance to PP2 (m)	1.50

Observable damage from Test 2 is summarized in Table B.9. A photograph of the distribution of glass debris outside of the test enclosure is provided in Figure B.4. A photograph of the distribution of glass debris on the floor of the test enclosure is shown in Figure B.5 along with an aerial view rendering of the debris distribution obtained using the LiDAR scanning system. Low-hazard and high-hazard glass debris captured by the witness panel is shown in a photograph in Figure B.6. A contrasted version of the photograph is also presented to highlight the glass debris embedded in the witness panel.

TABLE B.9: Observable post-blast damage from Test 2

Number of lites broken	6
Name of broken lites	1, 2, 3, 4, 5, 6
Very low hazard debris	Significant
Low hazard debris	Significant
High hazard debris	Moderate

FIGURE B.4: Exterior debris field distribution following Test 2

a) Photograph of debris field

b) LiDAR rendering of debris field

FIGURE B.5: Interior debris field distribution following Test 2

a) In-field photograph b) Contrasted photograph

FIGURE B.6: Glass debris in witness panel following Test 2

2.5.3 Summary of Test 3

From the perspective of facing the glass lite specimens, the charge was located left of the enclosure. The description of the charge, including the composition, scale weight, and distances relative the incident pressure probes and central glass lite specimen in the bottom row of lites (Lite 5), are presented in Table B.10.

TABLE B.10: Summary of Test 3

Charge composition	PETN
Parallel distance from Lite (m)	2.19
Perpendicular distance from Lite 5 (m)	3.07
Charge weight (g)	455.86
Distance to PP1 (m)	3.34
Distance to PP2 (m)	1.99

Observable damage from Test 3 is summarized in Table B.11. A photograph of the distribution of glass debris outside of the test enclosure is provided in Figure B.7. A photograph of the distribution of glass debris on the floor of the test enclosure is shown in Figure B.8 along with an aerial view rendering of the debris distribution obtained using the LiDAR scanning system. Low-hazard and high-hazard glass debris captured by the witness panel was minimal.

TABLE B.11: Observable post-blast damage from Test 3

Number of lites broken	2
Name of broken lites	1, 4
Very low hazard debris	Significant
Low hazard debris	Moderate
High hazard debris	Minimal

FIGURE B.7: Exterior debris field distribution following Test 3

a) Photograph of debris field b) LiDAR rendering of debris field

FIGURE B.8: Interior debris field distribution following Test 3

2.5.4 Summary of Test 4

From the perspective of facing the glass lite specimens, the charge was located to the right of the enclosure. The description of the charge, including the composition, scale weight, and distances relative the incident pressure probes and central glass lite specimen in the bottom row of lites (Lite 5), are presented in Table B.12.

TABLE B.12: Summary of Test 4

Charge composition	ANFO
Parallel distance from Lite 5 (m)	1.73
Perpendicular distance from Lite 5 (m)	2.44
Charge weight (g)	707.60
Distance to PP1 (m)	2.39
Distance to PP2 (m)	2.37

Observable damage from Test 4 is summarized in Table B.13. A photograph of the distribution of glass debris outside of the test enclosure is provided in Figure B.9. A photograph of the distribution of glass debris on the floor of the test enclosure is shown in Figure B.10 along with an aerial view rendering of the debris distribution obtained using the LiDAR scanning system. Low-hazard and high-hazard glass debris captured by the witness panel is shown in a photograph in Figure B.11. A contrasted version of the photograph is also presented to highlight the glass debris embedded in the witness panel.

TABLE B.13: Observable post-blast damage from Test 4

Number of lites broken	2
Name of broken lites	3, 6
Very low hazard debris	Significant
Low hazard debris	Moderate
High hazard debris	Minimal

FIGURE B.9: Exterior debris field distribution following Test 4

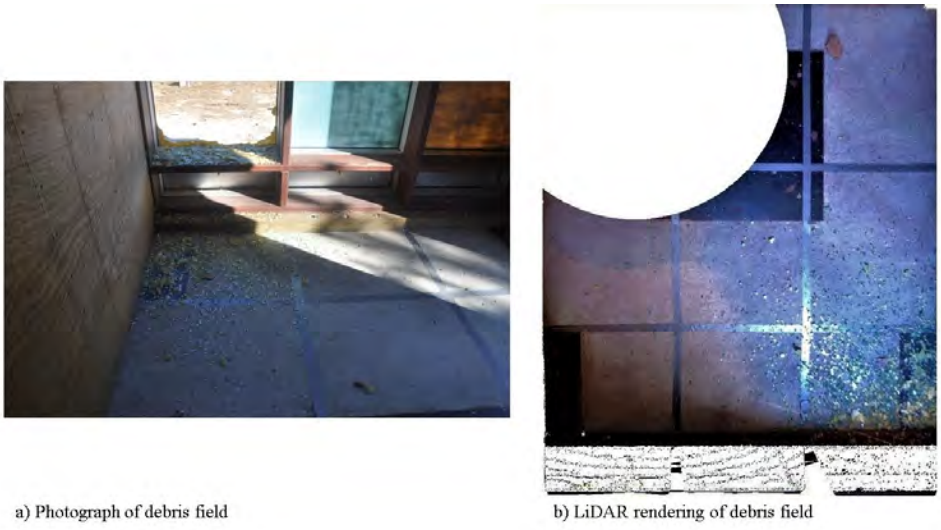

FIGURE B.10: Interior debris field distribution following Test 4

a) In-field photograph b) Contrasted photograph

FIGURE B.11: Glass debris in witness panel following Test 4

2.5.5 Summary of Test 5

From the perspective of facing the glass lite specimens, the charge was located right of center of the enclosure. The description of the charge, including the composition, scale weight, and distances relative the incident pressure probes and central glass lite specimen in the bottom row of lites (Lite 5), are presented in Table B.14.

TABLE B.14: Summary of Test 5

Charge composition	ANFO
Parallel distance from Lite 5 (m)	0.85
Perpendicular distance from Lite 5 (m)	2.72
Charge weight (g)	712.14
Distance to PP1 (m)	1.22
Distance to PP2 (m)	1.29

Observable damage from Test 5 is summarized in Table B.15. A photograph of the distribution of glass debris outside of the test enclosure is provided in Figure B.12. A photograph of the distribution of glass debris on the floor of the test enclosure is shown in Figure B.13 along with an aerial view rendering of the debris distribution obtained using the LiDAR scanning system. Low-hazard and high-hazard glass debris captured by the witness panel was minimal.

TABLE B.15: Observable post-blast damage from Test 5

Number of lites broken	2
Name of broken lites	5, 6
Very low hazard debris	Significant
Low hazard debris	Moderate
High hazard debris	Minimal

FIGURE B.12: Exterior debris field distribution following Test 5

a) Photograph of debris field

b) LiDAR rendering of debris field

FIGURE B.13: Interior debris field distribution following Test 5

2.5.6 Summary of Test 6

From the perspective of facing the glass lite specimens, the charge was located right of center of the enclosure. The description of the charge, including the composition, scale weight, and distances relative the incident pressure probes and central glass lite specimen in the bottom row of lites (Lite 5), are presented in Table B.16.

TABLE B.16: Summary of Test 6

Charge composition	ANFO
Parallel distance from Lite 5 (m)	0.43
Perpendicular distance from Lite 5 (m)	2.40
Charge weight (g)	721.21
Distance to PP1 (m)	1.22
Distance to PP2 (m)	1.22

Observable damage from Test 5 is summarized in Table B.17. A photograph of the distribution of glass debris outside of the test enclosure is provided in Figure B.14. A photograph of the distribution of glass debris on the floor of the test enclosure is shown in Figure B.15 along with an aerial view rendering of the debris distribution obtained using the LiDAR scanning system. Low-hazard and high-hazard glass debris captured by the witness panel was minimal.

TABLE B.17: Observable post-blast damage from Test 6

Number of lites broken	3
Name of broken lites	3, 4, 5
Very low hazard debris	Significant
Low hazard debris	Moderate
High hazard debris	Minimal

FIGURE B.14: Exterior debris field distribution following Test 6

a) Photograph of debris field

b) LiDAR rendering of debris field

FIGURE B.15: Interior debris field distribution following Test 6

B.6 Predicted and Measured Reflected Pressures and Impulses from Experimental Blast Testing

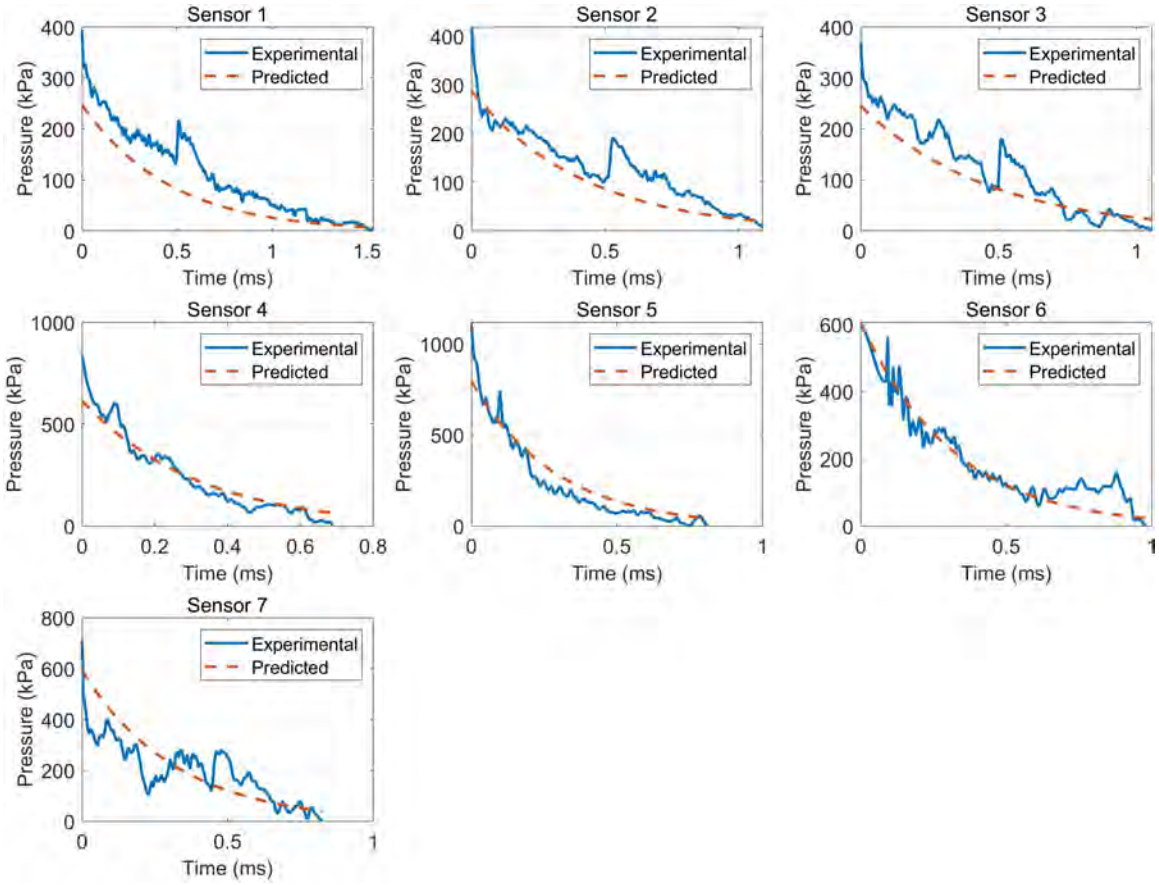

FIGURE B.16: Comparison of the measured reflected pressures and the predicted pressures obtained using the optimized charge weight for Test 1

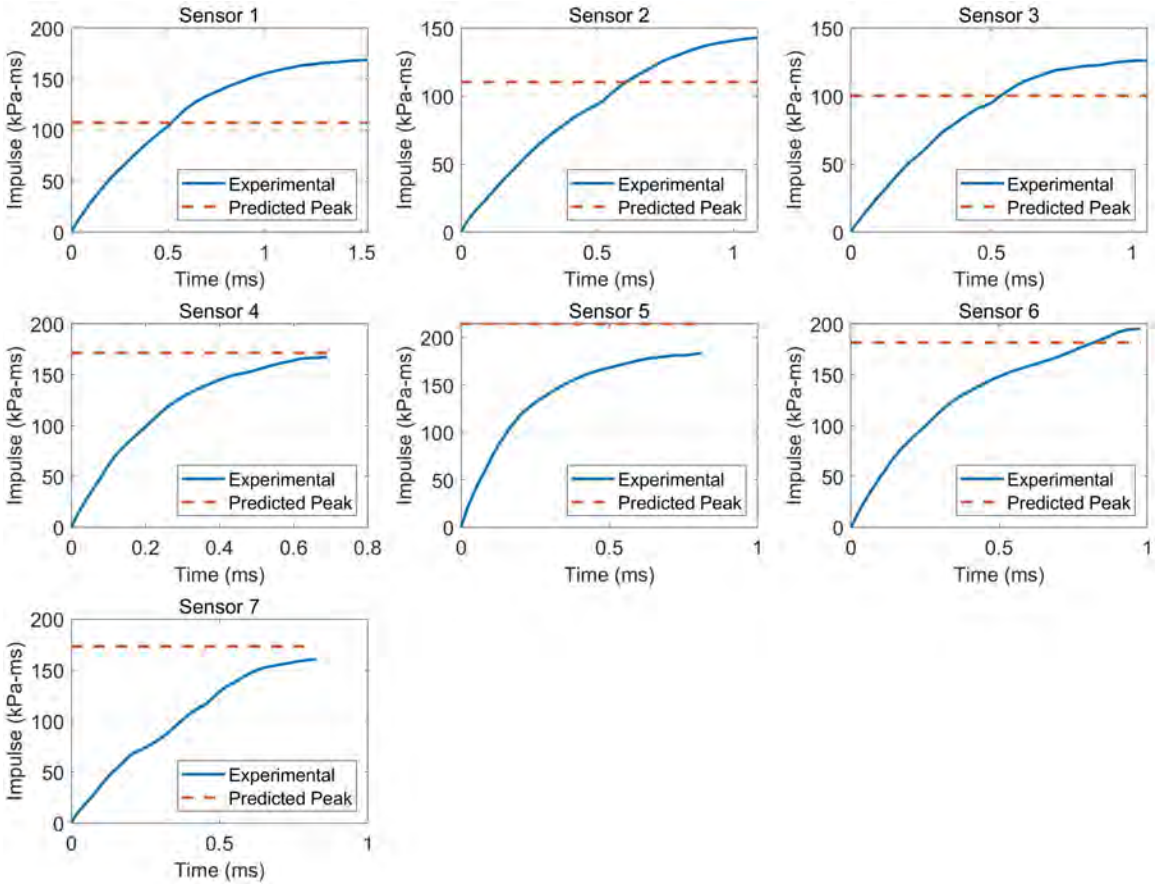

FIGURE B.17: Comparison of the experimentally determined reflected impulses and the peak predicted impulses obtained using the optimized charge weight for Test 1

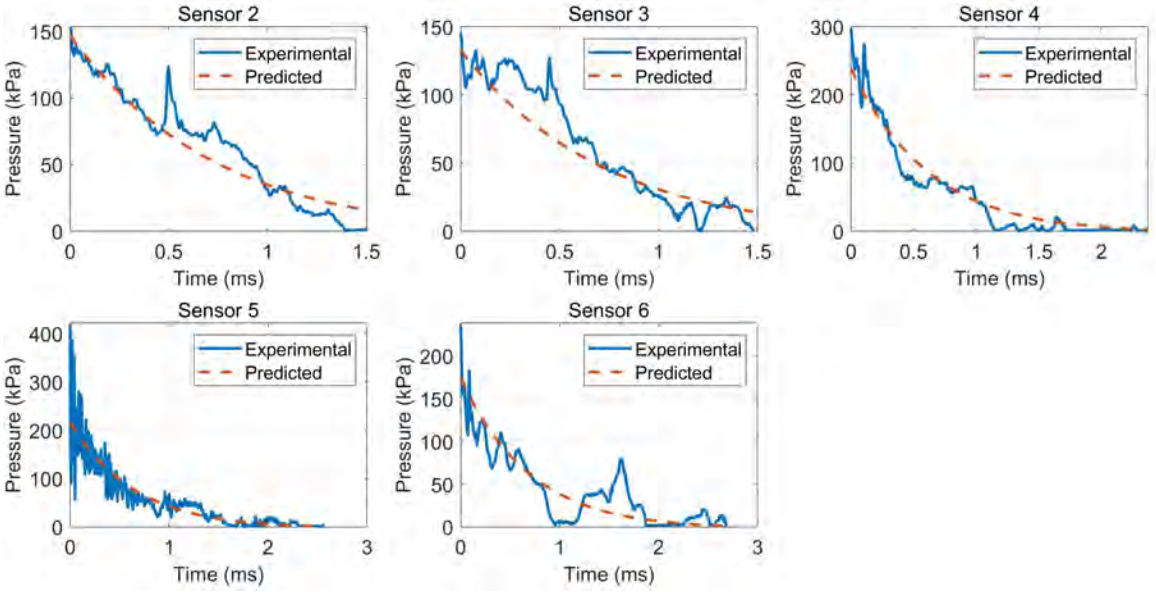

FIGURE B.18: Comparison of the measured reflected pressures and the predicted pressures obtained using the optimized charge weight for Test 2

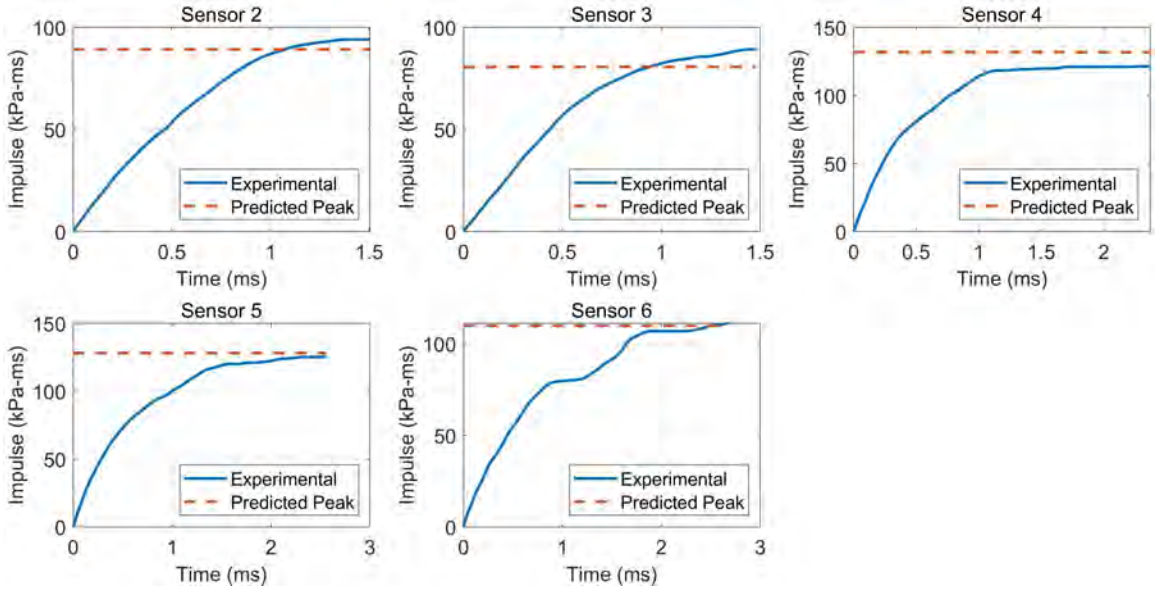

FIGURE B.19: Comparison of the experimentally determined reflected impulses and the peak predicted impulses obtained using the optimized charge weight for Test 2

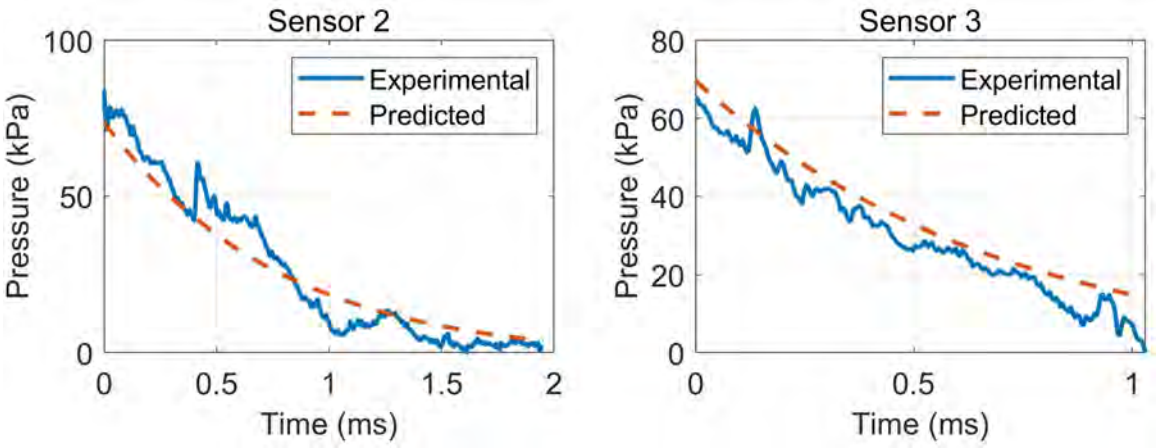

FIGURE B.20: Comparison of the measured reflected pressures and the predicted pressures obtained using the optimized charge weight for Test 3

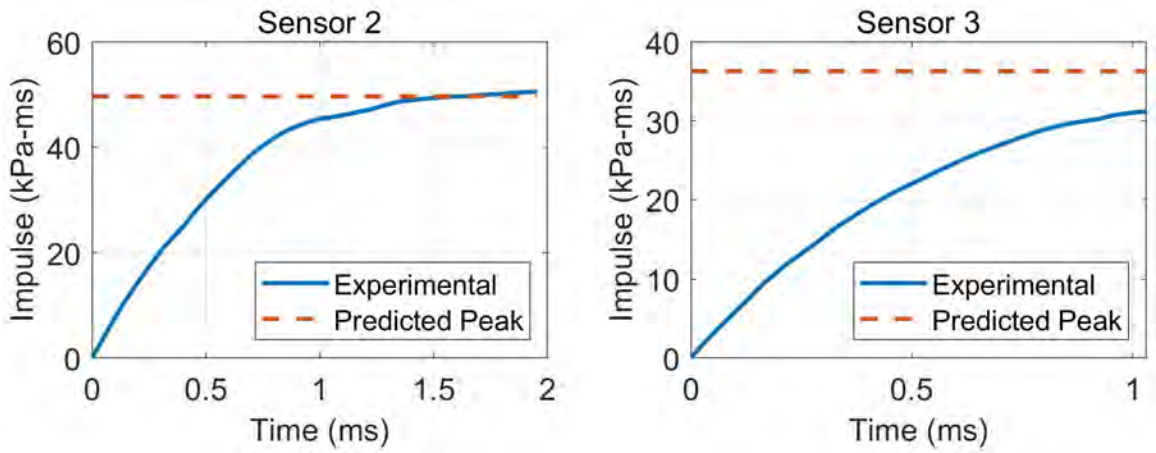

FIGURE B.21: Comparison of the experimentally determined reflected impulses and the peak predicted impulses obtained using the optimized charge weight for Test 3

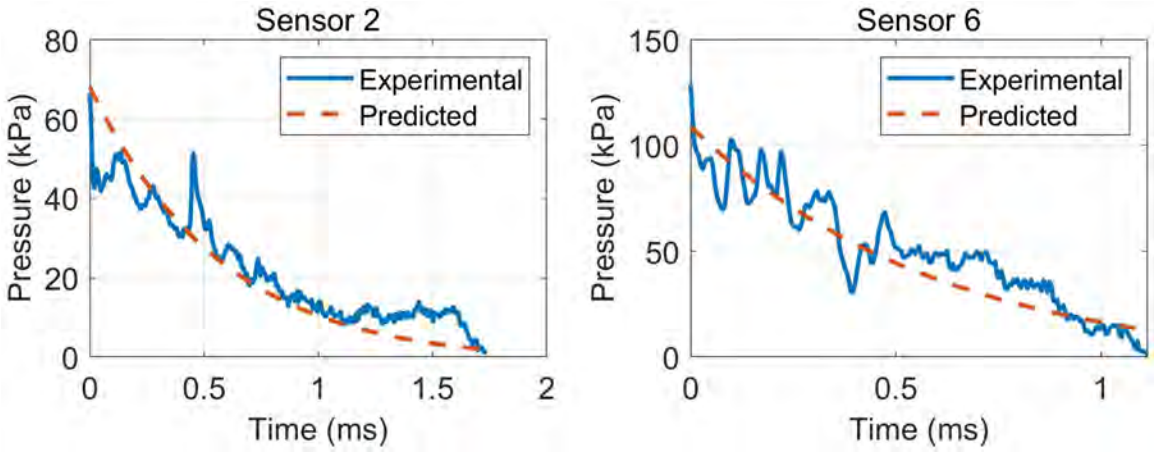

FIGURE B.22: Comparison of the measured reflected pressures and the predicted pressures obtained using the optimized charge weight for Test 4

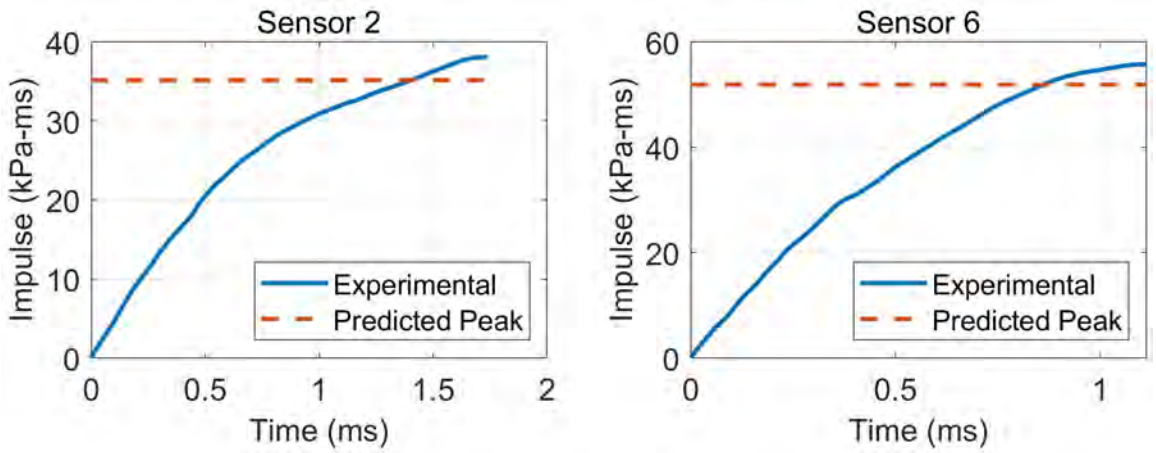

FIGURE B.23: Comparison of the experimentally determined reflected impulses and the peak predicted impulses obtained using the optimized charge weight for Test 4

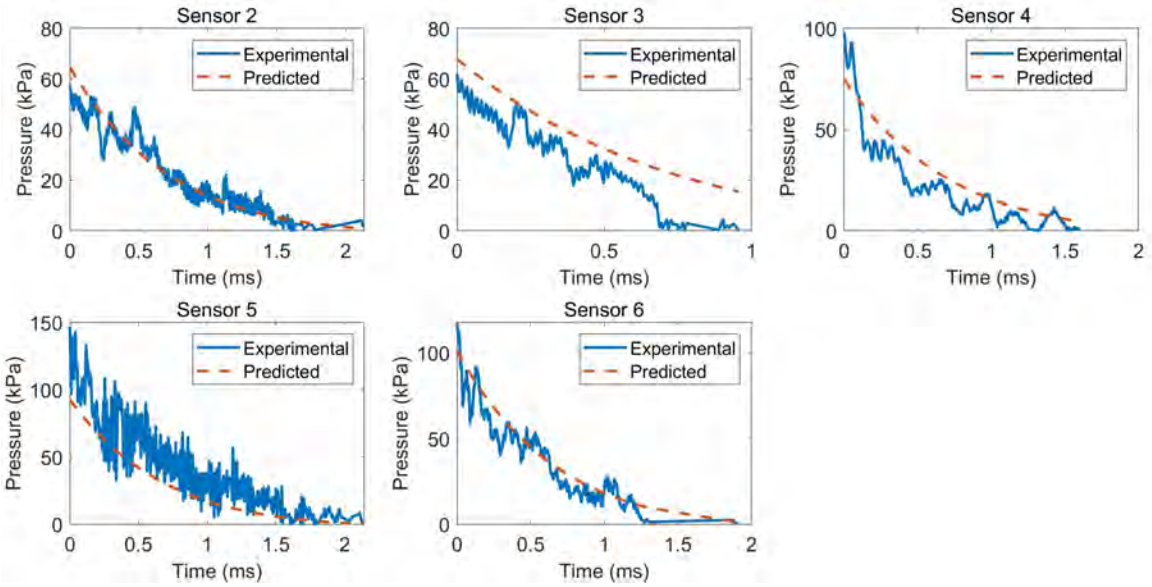

FIGURE B.24: Comparison of the measured reflected pressures and the predicted pressures obtained using the optimized charge weight for Test 5

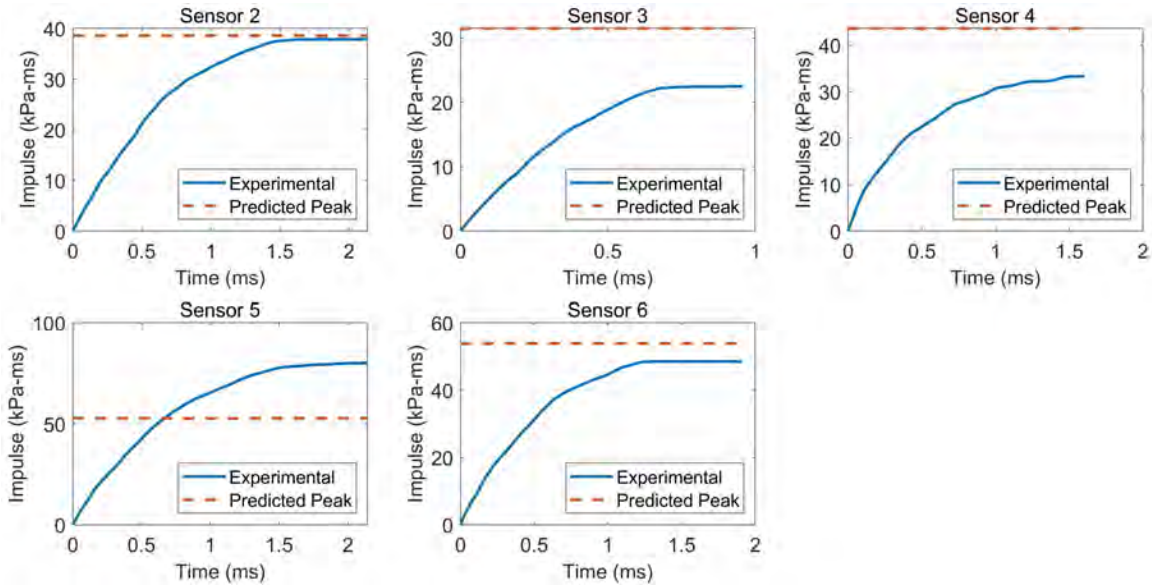

FIGURE B.25: Comparison of the experimentally determined reflected impulses and the peak predicted impulses obtained using the optimized charge weight for Test 5

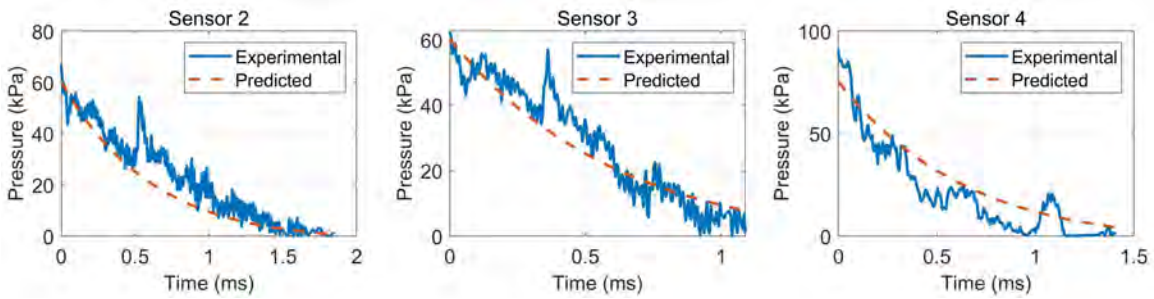

FIGURE B.26: Comparison of the measured reflected pressures and the predicted pressures obtained using the optimized charge weight for Test 6

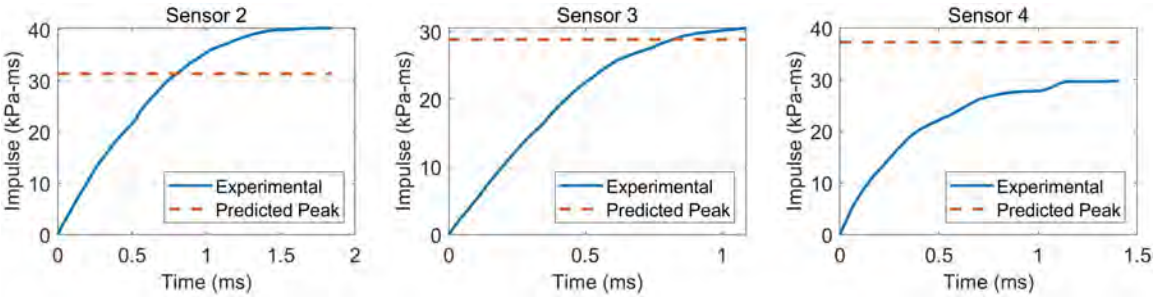

FIGURE B.27: Comparison of the experimentally determined reflected impulses and the peak predicted impulses obtained using the optimized charge weight for Test 6

APPENDIX C: DISTRIBUTION OF THE PEAK REFLECTED PRESSURE, CONSTANT B_I, TIME OF ARRIVAL, AND POSITIVE PHASE LOADING DURATION IN THE AEM SIMULATIONS FOR EACH SCENARIO OF OPEN-ARENA BLAST TESTING

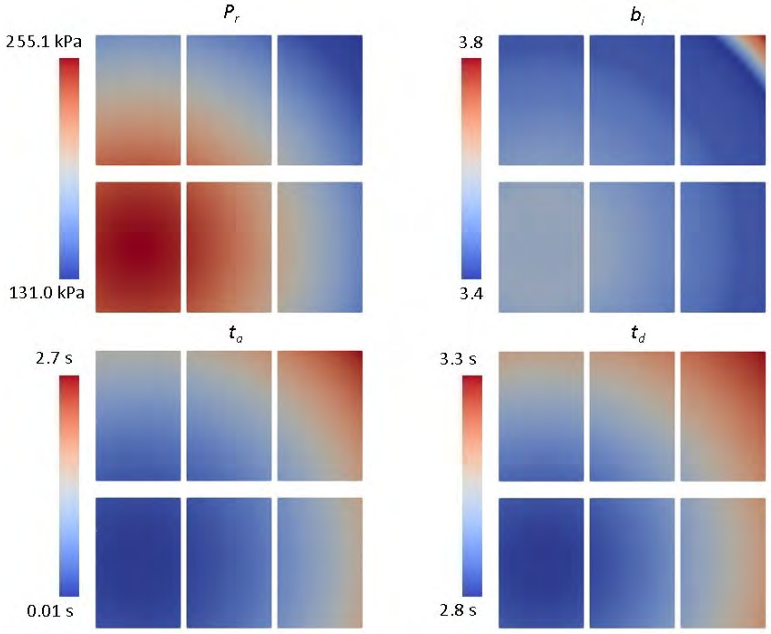

FIGURE C.1: Predicted distribution of P_r, b_i, t_a, and t_d across the Applied Elements using the charge properties from Test 2

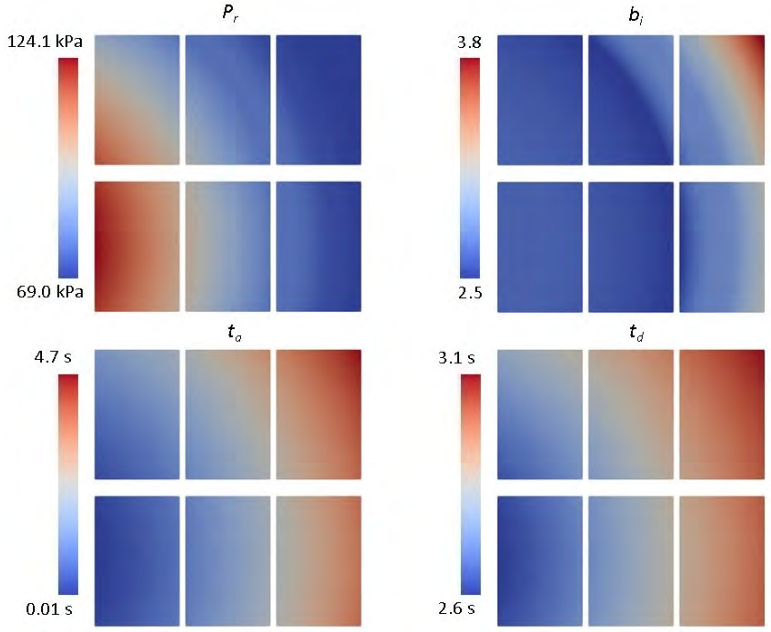

FIGURE C.2: Predicted distribution of P_r, b_i, t_a, and t_d across the Applied Elements using the charge properties from Test 3

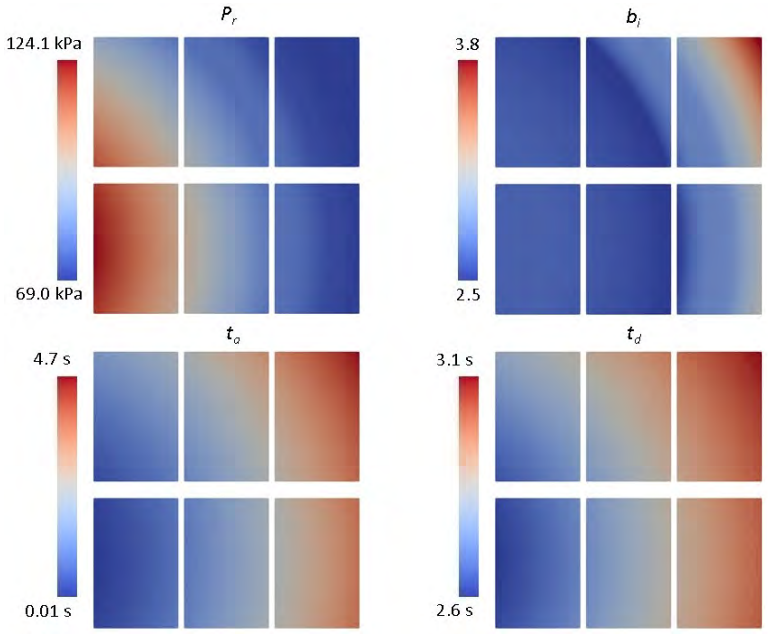

FIGURE C.3: Predicted distribution of P_r, b_i, t_a, and t_d across the Applied Elements using the charge properties from Test 4

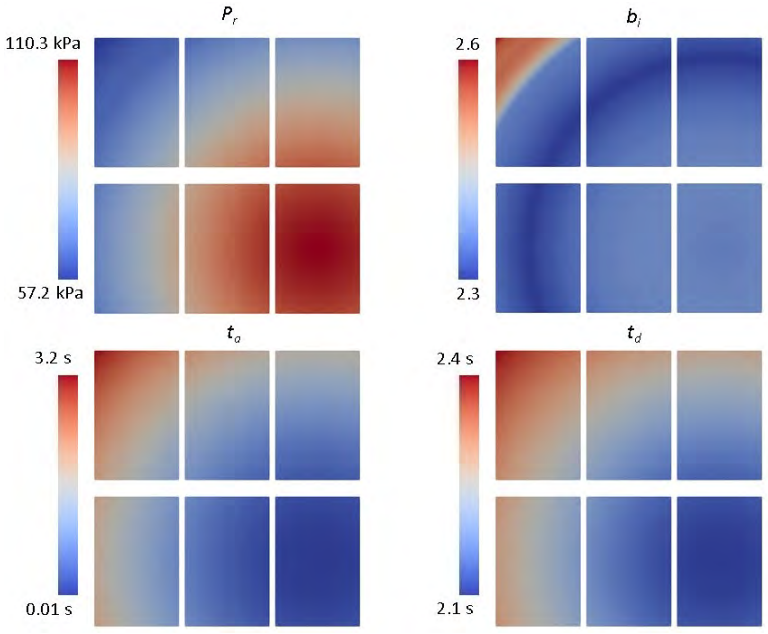

FIGURE C.4: Predicted distribution of P_r, b_i, t_a, and t_d across the Applied Elements using the charge properties from Test 5

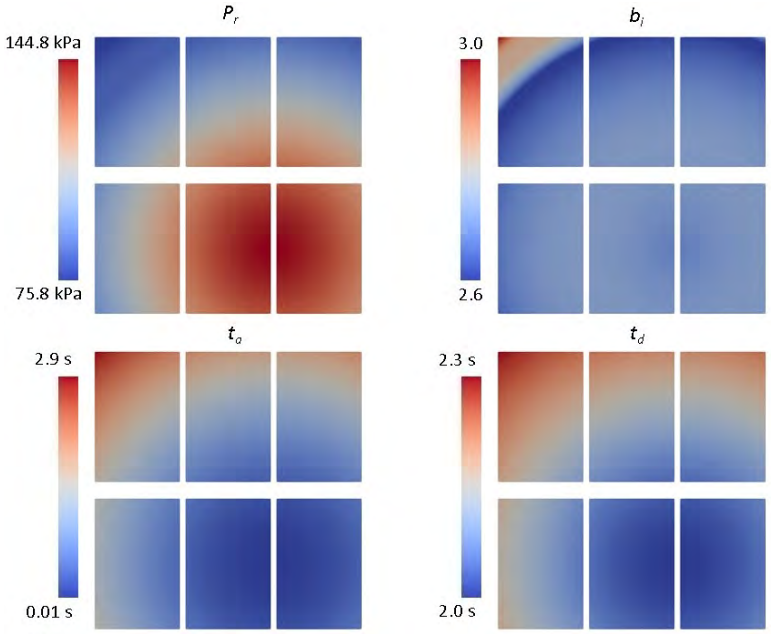

FIGURE C.5: Predicted distribution of P_r, b_i, t_a, and t_d across the Applied Elements using the charge properties from Test 6

APPENDIX D: PREDICTED EQUIVALENT PRINCIPAL STRESSES, LOAD DURATION, AND BIAXIAL STRESS CORRECTION FACTOR PREDICTED USING THE AEM SIMULATIONS OF BLAST LOADING FOR PROBABILISTIC ANALYSIS

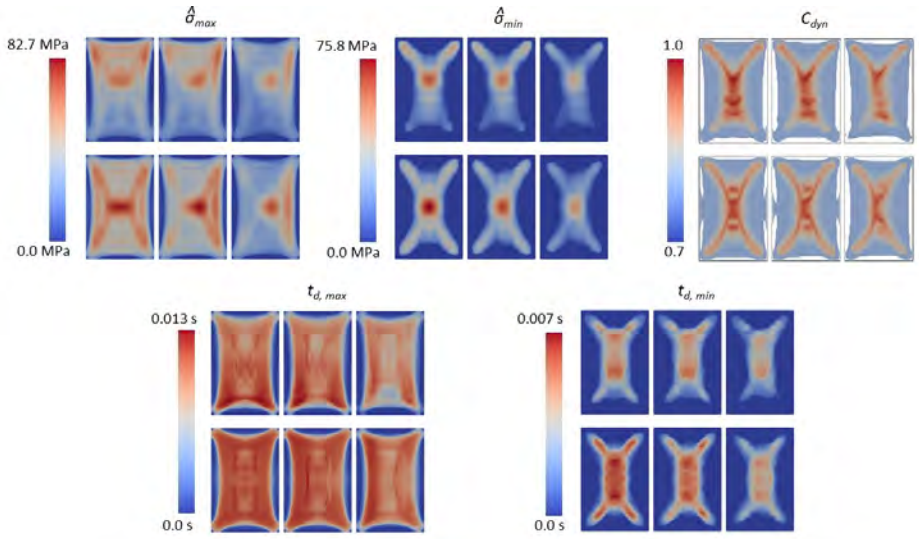

FIGURE D.1: Predicted distribution of $\hat{\sigma}_{max}$, $\hat{\sigma}_{min}$, $t_{d,max}$, $t_{d,min}$, and C_{dyn} across the tensile surface of the glass lites using the calibrated AEM model for Test 2

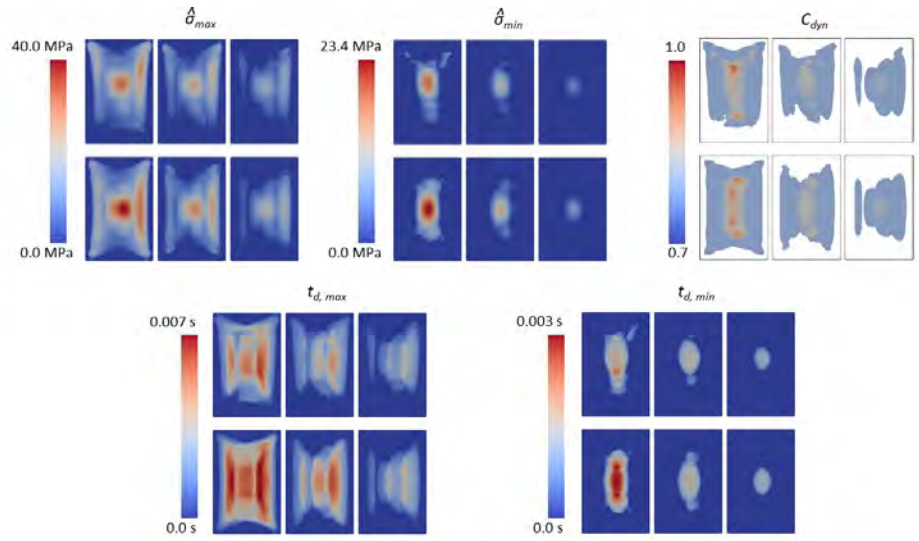

FIGURE D.2: Predicted distribution of $\hat{\sigma}_{max}$, $\hat{\sigma}_{min}$, $t_{d,max}$, $t_{d,min}$, and C_{dyn} across the tensile surface of the glass lites using the calibrated AEM model for Test 3

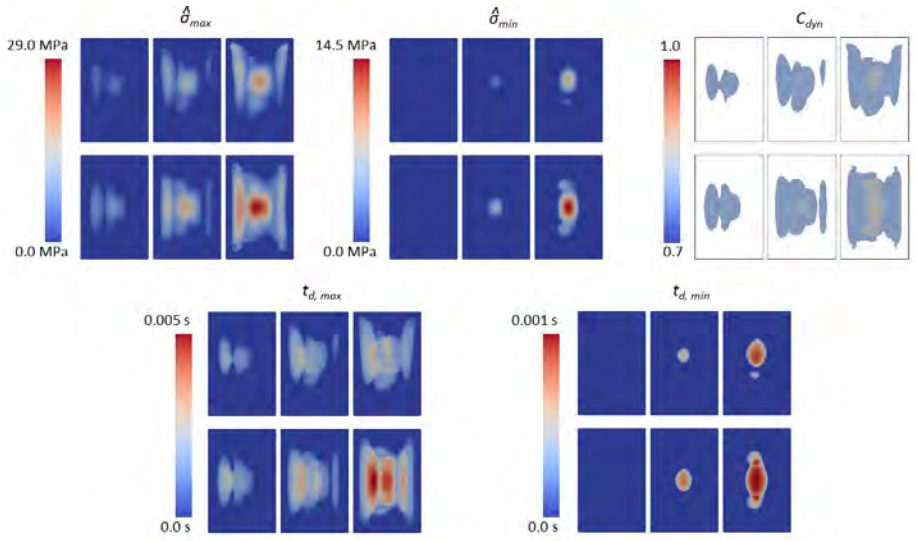

FIGURE D.3: Predicted distribution of $\hat{\sigma}_{max}$, $\hat{\sigma}_{min}$, $t_{d,max}$, $t_{d,min}$, and C_{dyn} across the tensile surface of the glass lites using the calibrated AEM model for Test 4

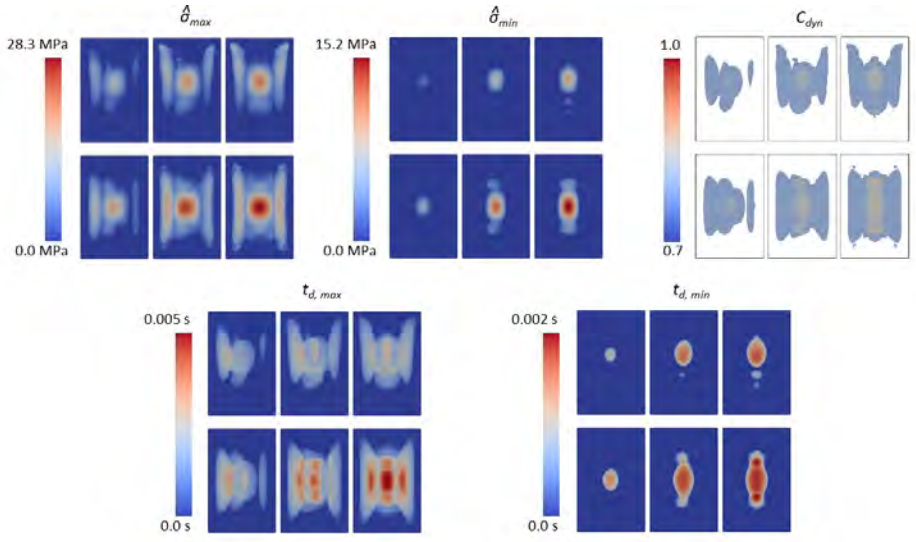

FIGURE D.4: Predicted distribution of $\hat{\sigma}_{max}$, $\hat{\sigma}_{min}$, $t_{d,max}$, $t_{d,min}$, and C_{dyn} across the tensile surface of the glass lites using the calibrated AEM model for Test 5

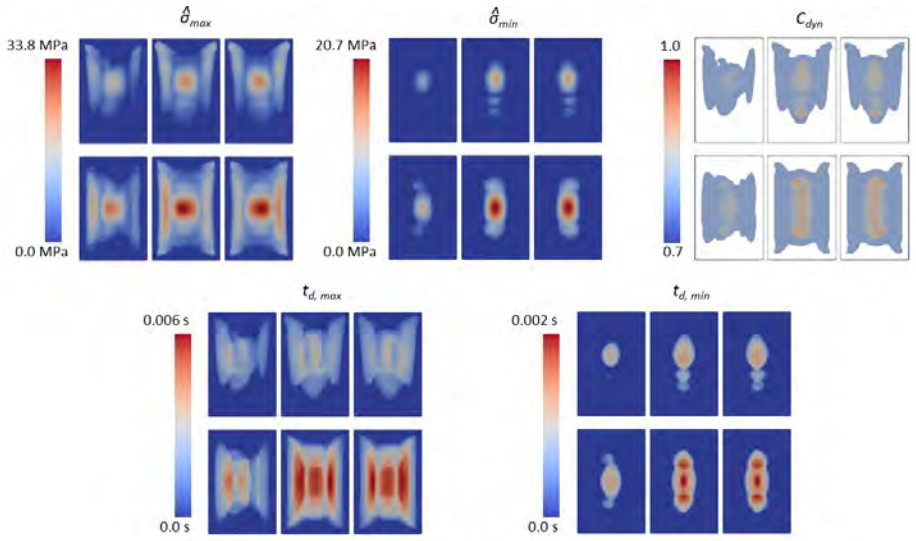

FIGURE D.5: Predicted distribution of $\hat{\sigma}_{max}$, $\hat{\sigma}_{min}$, $t_{d,max}$, $t_{d,min}$, and C_{dyn} across the tensile surface of the glass lites using the calibrated AEM model for Test 6

APPENDIX E: RENDERINGS OF THE PREDICTED FRACTURE, FRAGMENTATION, AND DEBRIS FIELD FORMATION OF THE GLASS LITES UNDER BLAST LOADING

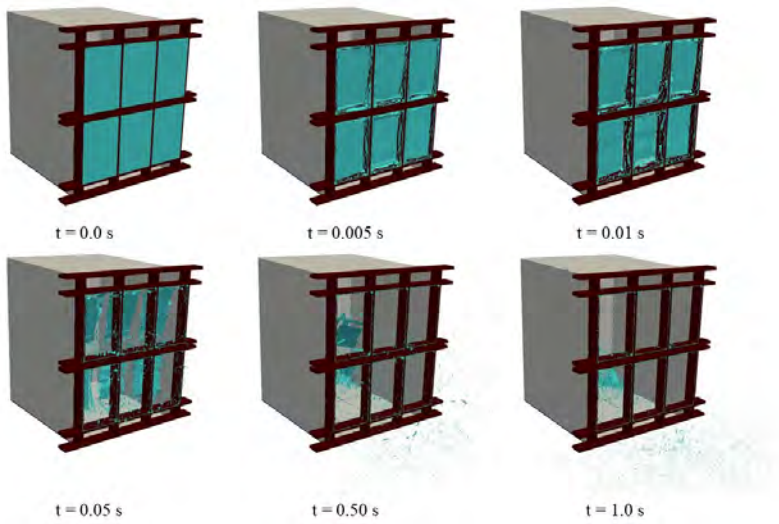

FIGURE E.1: Progressive renderings of the fracture, fragmentation, and debris field formation predicted for Test 1

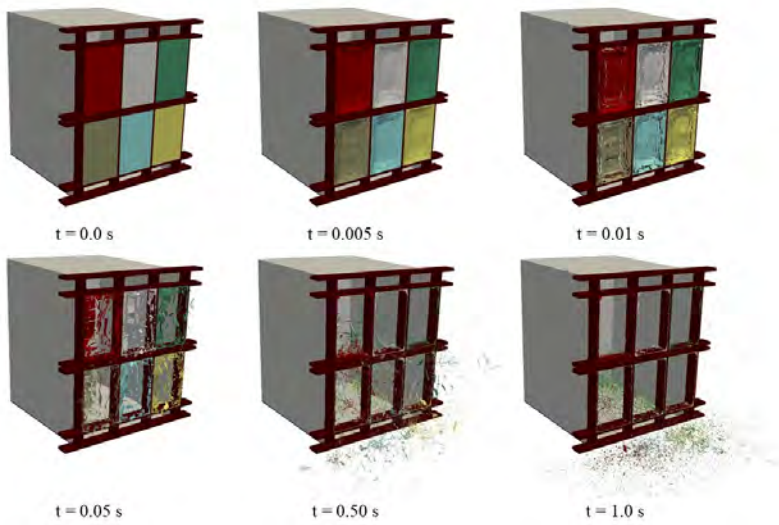

FIGURE E.2: Progressive renderings of the fracture, fragmentation, and debris field formation predicted for Test 2

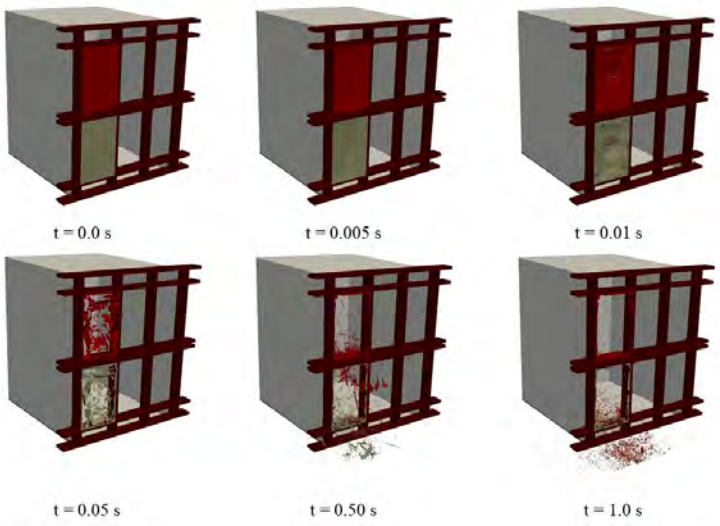

FIGURE E.3: Progressive renderings of the fracture, fragmentation, and debris field formation predicted for Test 3

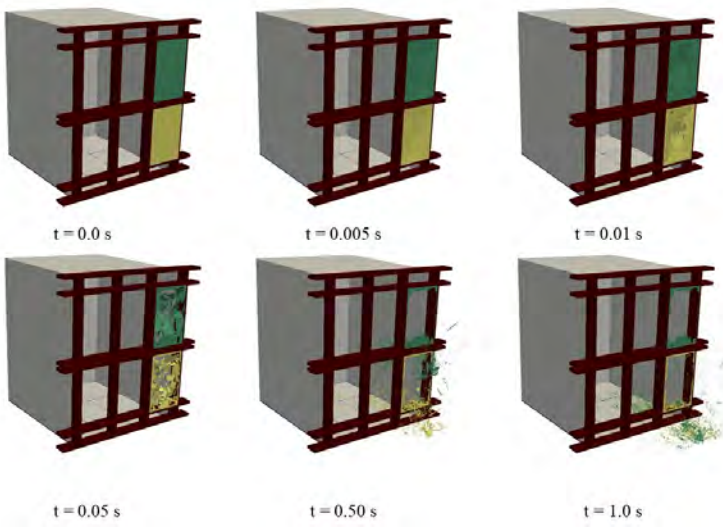

FIGURE E.4: Progressive renderings of the fracture, fragmentation, and debris field formation predicted for Test 4

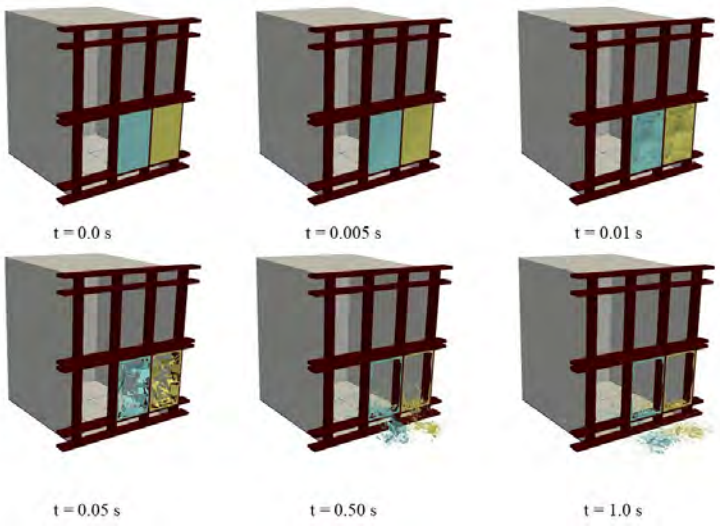

FIGURE E.5: Progressive renderings of the fracture, fragmentation, and debris field formation predicted for Test 5

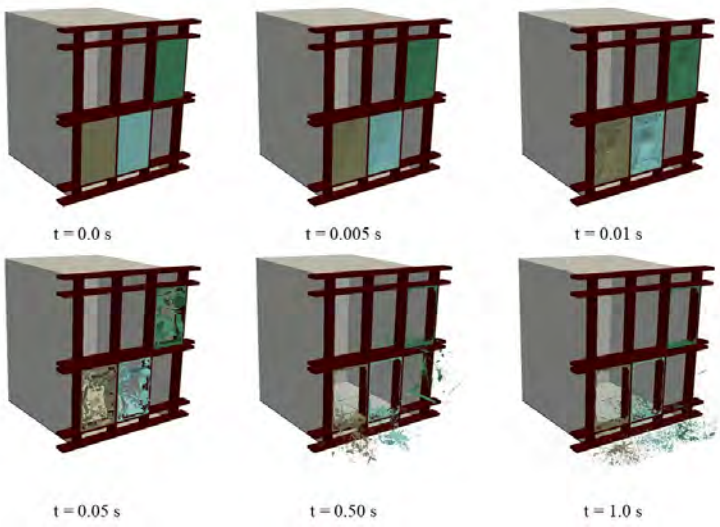

FIGURE E.6: Progressive renderings of the fracture, fragmentation, and debris field formation predicted for Test 6